Synergistic Effects of Volumetric Defects and Notch Geometry on the Fatigue Behavior of Additively Manufactured Metallic Materials

by

Arun Poudel

A dissertation submitted to the Graduate Faculty of
Auburn University
in partial fulfillment of the
requirements for the Degree of
Doctor of Philosophy

Auburn, Alabama
May 10, 2025

Keywords: Additive Manufacturing, Notch Fatigue Behavior, Defect Criticality, Non-destructive Inspection, Short Crack Growth Behavior

Approved by

Nima Shamsaei, Chair, Philpott-WestPoint Stevens Distinguished Professor of Mechanical Engineering
Shuai Shao, Co-chair, McWane Associate Professor of Mechanical Engineering
Robert L. Jackson, Professor of Mechanical Engineering
Jingyi Zheng, Assistant Professor of Mathematics and Statistics
Jia Liu, Associate Professor of Industrial and Systems Engineering

Abstract

In this dissertation, the synergistic effects of volumetric defects and notch geometry on the fatigue behavior of additively manufactured (AM) metallic materials were investigated. Factors influencing fatigue crack initiation and short crack growth behavior were identified and assessed. Both experimental and numerical techniques were utilized to understand the notch fatigue behavior. During experimentation, AlSi10Mg and 17-4 precipitation hardening (PH) stainless steel (SS) specimens with varying geometry types (cylindrical and flat), notch root radii, ρ, ligament widths, w, and volumetric defect contents were used. These specimens were tested under uniaxial cyclic loading, and their fracture surfaces were analyzed to identify the crack initiation site and investigate the fatigue failure mechanisms in different notch configurations. Irrespective of the material or the geometry type, *ρ0.1* (specimens with ρ of 0.1 mm) showed shorter fatigue lives with lower scatter compared to *ρ5* and *ρ50* specimens. For *ρ0.1* specimens, significant cyclic plastic damage at the notch root, due to the high stress concentration, caused critical crack initiations.

For cylindrical specimens, *ρ5* and *ρ50* showed similar fatigue lives for AlSi10Mg; however, for 17-4 PH SS, the latter showed longer fatigue lives. It was likely due to the influence of wider variation in the critical defect features in AlSi10Mg than 17-4 PH SS, on the crack initiation behavior. Notch geometry as well as the critical defect's size and location (within the cross-section and height relative to the notch root plane) influenced the fatigue behavior of cylindrical notched specimens. In the case of flat specimens, there was an additional influence of microstructure on the fatigue behavior of near-defect free 17-4 PH SS specimens. Delta ferrites (δ-Fe) acted as weak points in the microstructure, resulting in the formation of microcracks, and

eventually crystallographic facets as the crack initiation site. Larger *w* resulted in shorter fatigue lives for *ρ0.1* and *ρ5* AlSi10Mg and 17-4 PH SS flat specimens. Specimens with *w* of 10 mm induced higher cyclic plastic damage at the notch root than 5 mm, thus promoting crack initiation and early failure. In specimens with minimal plasticity at the notch root, i.e., *ρ5* and *ρ50* specimens, mode-I stress intensity factor (SIF) of critical features calculated based on linear elastic fracture mechanics (LEFM), i.e., Murakami's approach, correlated well with experimental fatigue lives. However, in specimens with significant plasticity at the notch root, i.e., *ρ0.1* specimens, equivalent plastic strain at the notch root correlated well with the experimental fatigue lives.

Based on LEFM, fatigue criticality of volumetric defects in AlSi10Mg and 17-4 PH SS notched specimens were assessed using a non-destructive technique, i.e., X-ray computed tomography (XCT). Assuming a defect-crack equivalency and accounting for local stress fields using linear elastic finite element analysis, mode-I SIF of defects detected via XCT was calculated and used to represent their fatigue criticality. For validation, *ρ5* and *ρ50* cylindrical and flat specimens were XCT scanned and tested; all crack initiating defects fell within the 99.3 percentile of the highest SIF defects in the respective notched specimens for AlSi10Mg and 17-4 PH SS.

The behavior of short cracks initiated from the volumetric defects, including their growth and arrest, under the influence of the notch stress fields, were believed to have a significant influence on the fatigue lives of notch members. Utilizing a numerical modeling technique, the short crack growth behavior of cracks initiating from volumetric defects in notched specimens was investigated. It utilized the effective SIF of cracks, put forth by El-Haddad, to assess the short crack growth behavior. Notch geometry, defect's size, shape, and location influenced crack arrest behavior. The minimum effective SIF of cracks, at the crack arrest, was used to obtain the fatigue

notch factor. Utilizing the fatigue notch factor-based framework, fatigue lives of flat notched specimens with varying ρ were predicted. This was validated using laser powder bed fused AlSi10Mg and 17-4 PH SS flat notched specimens with ρ of 5 mm and 50 mm. For AlSi10Mg, 95% of all fatigue life predictions fell within the scatter band of 3, and 100% for 17-4 PH SS.

Acknowledgments

I would like to express my sincere gratitude to my advisors, Dr. Nima Shamsaei (Chair) and Dr. Shuai Shao (Co-chair) for their invaluable guidance and support throughout my graduate studies. The successful and timely completion of all projects was largely due to their mentorship and depth of knowledge in the field. In addition, I would like to thank Dr. Robert L. Jackson, Dr. Jingyi Zheng, and Dr. Jia Liu for serving on my committee and providing feedback on my research. I would like to offer my sincere appreciation to my family, friends, and colleagues at the National Center for Additive Manufacturing Excellence, without whom this journey would not have been possible. Last but not least, I would like to acknowledge the sponsors of my research, the U.S. Department of Commerce, National Institute of Standards and Technology (NIST) under award no. NIST-70NANB19H170, the National Science Foundation (NSF) under awards no. 1919818 and 2319690, the Federal Aviation Administration (FAA) under awards no. FAA-12-C-AM-AU-003 and FAA-12-C-AM-AU-A2, and the U.S. Army under award no. W56HZV-17-C-0095.

Table of Contents

List of Tables

List of Figures

Abbreviations

AM	Additive manufacturing/additively manufactured
ANOVA	Analysis of variance
ASED	Average strain energy density
BSE	Backscattered secondary electron
CA	Condition A
CM	Conventional manufacturing/conventionally manufactured
CDF	Cumulative density function
CNC	Computer numerical control
EBSD	Electron backscatter diffraction
EDM	Electrical discharge machining
EPFEA	Elasto-plastic finite element analysis
HCF	High cycle fatigue
HT	Heat treatment/heat treated
IPF	Inverse pole figure
KAM	Kernel average misorientation
LEFEA	Linear elastic finite element analysis
LEVS	Largest extreme value statistics
LoF	Lack-of-fusion
LP	Longitudinal plane
L-PBF	Laser powder bed fusion/laser powder bed fused
MCF	Mid-cycle fatigue
PDF	Probability density function
PH	Precipitation hardening
REC	Recommended
RP	Radial plane
SEM	Scanning electron microscope
SIF	Stress intensity factor
SR	Stress relieving/stress relieved
SS	Stainless steel
TCD	Theory of critical distance
UH	Underheating/underheated
UTS	Ultimate tensile strength
XCT	X-ray computed tomography

Nomenclatures

$\sqrt{area}$	Square root of projected area of a defect on the loading plane
a	Crack length
a_0	El-Haddad's material-dependent parameter
A	Nominal cross-sectional area at the notch root
C_2 and α	Murakami's material-dependent parameters
d	Notch depth
δ-Fe	Delta ferrite
e	Centroidal distance between two neighboring defects
F	Crack geometry factor
F_α	Crack geometry factor depending on notch configuration
r and h	Radius and half-height of the defect
h_{center}	Distance of the crack initiation site from the notch root plane
h_0	Total height of the notch geometry
HV	Vickers hardness
ΔK_{eff}	Effective mode-I stress intensity factor range
$(\Delta K_{eff})_{norm}$	Normalized effective mode-I stress intensity factor range
ΔK_I	Mode-I stress intensity factor range
$K_{I(Max.)}$	Maximum mode-I stress intensity factor during a loading cycle
K_t	Elastic stress concentration factor at the notch root
$K_{t(local)}$	Local elastic stress concentration factor
l	Distance from the notch surface
l_M	Material characteristic length
θ and γ	Transition functions
R	Stress ratio
w	Ligament width
Y	Murakami's location-dependent factor
ρ	Notch root radius
$\sigma_{Max.}$	Maximum nominal stress
σ_e^{defect}	Fatigue limit of the material with defects

1 Introduction

Additive manufacturing (AM), utilizing the layer-by-layer fabrication strategy, escapes the limitations typically imposed on conventional manufacturing (CM) processes such as casting, rolling, molding, machining, etc. to fabricate complex mechanical components. AM enables the fabrication of intricate, customizable, and integrated mechanical components containing features such as notches, lattices, internal channels, etc., which were previously thought to be near-impossible or very costly to manufacture using CM processes [1–3]. AM also allows environmentally sustainable fabrication—by lowering material waste and energy usage—with lower lead time, even at remote locations where the application of CM might be limited [4,5]. These tremendous advantages of AM over CM are not without its challenges. The as-built or as-fabricated additive manufactured (AM) parts inherently contain rough surface texture, ubiquitous presence of volumetric defects, residual stresses, directional microstructure, etc., to name a few [6,7]. These features have been reported to either deteriorate or cause significant scatter to (or both) the mechanical behavior, especially fatigue behavior, of AM parts [8–19]. Such effects are further exacerbated by the presence of notches; notch geometry acts as a stress concentrator and promotes crack initiation, during cyclic loading conditions.

Several studies have investigated different methods to mitigate the adverse effects of such inherent AM features on the fatigue behavior of metallic materials. Detrimental effects from high surface roughness (acting as micro-notches) are minimized by utilizing different surface treatments such as shot-peening, electrochemical polishing, machining, sandblasting, hand-polishing, etc. [20–23]. For instance, the fatigue strength of laser-powder bed fused (L-PBF) AlSi10Mg specimens increased by 1540% after treating the specimens' surfaces with ceramic shot peening [24]. Similarly, residual stresses are minimized, and directional microstructures are

resolved/homogenized by utilizing different types of heat treatments [25–27]. However, in the case of volumetric defects, they are ubiquitously present and near impossible to completely eradicate from AM parts. During loading, volumetric defects act as micro-stress concentrators and influence the crack initiation and the short crack growth behavior [28–30]. During AM of a complex part, the occurrence of macro notch-like features is inevitable [31]. Hence, this dissertation focuses on the complex interaction between the stress fields of macro-notches and volumetric defects (micro-notches) that affect fatigue crack initiation and short crack growth behavior.

For un-notched machined/polished AM specimens, the fatigue crack initiation is influenced by volumetric defect features such as size, morphology, and location [32–34]. The variation of these defect features resulted in a wide scatter/uncertainty in the fatigue lives of AM specimens [35]. In the presence of notches, this uncertainty is expected to increase, considering an additional influence from the interaction between the stress fields of notch geometry and defects. Such uncertainty/unpredictability of the mechanical behavior of AM parts makes the qualification process difficult and poses a huge challenge for their industry-wide adoption, especially for fatigue-critical applications [36,37]. To resolve this issue, structure (micro-/defect)-property (fatigue) relationships for different configurations of AM notched members need to be thoroughly investigated. Fatigue critical features need to be identified, and their respective criticality need to be assessed to understand their effects on the fatigue behavior (crack initiation and short crack growth behavior).

1.1 Motivation and background information

Several studies have investigated the cyclic performances and failure mechanisms of AM metallic notched specimens. While a majority of these studies are focused on notched specimens

with as-fabricated surface conditions [38–47], the studies on machined/polished (M/P) notched specimens, where notch geometry and defects synergistically influence the fatigue behavior, are very limited [28,48–51]. In general, the fatigue failure mechanisms in M/P notched specimens show great dependency on notch geometry (notch root radius, ρ). In notches with small ρ, ranging between 0.2 mm and 2 mm, the high stress concentration due to the notch geometry induces severe cyclic plastic damage at the notch root, thus promoting crack initiation from the notch root and early failures [48,52]. However, in notches inducing low stress concentrations at the notch root, fatigue cracks typically initiate from either surface-exposed or near-surface volumetric defects [28]. Several studies have reported fatigue crack initiations from volumetric defects at different locations in the notched specimens, i.e., notch surface, corner, and lateral surface [29,38,44,49,53]. This illustrates the influence of volumetric defect features on fatigue crack initiation, and thus on overall fatigue behavior. However, volumetric defect features influencing the fatigue behavior of a wide range of notch geometries (including different specimen types, notch root radii, ligament widths, etc.) remain elusive. In addition, the fatigue criticality assessment based on volumetric defect features is needed but is currently missing in the literature. These influences of defect and notch features on the fatigue behavior may change with the change in the material and the underlying microstructure.

In defect-insensitive materials or materials with relatively low defect contents, notch geometry and volumetric defect features compete with microstructural heterogeneity to initiate critical fatigue cracks. Microstructural features such as large grains or weak and brittle phases such as delta ferrites (δ-Fe), induce strain localization, resulting in the formation of microcracks [54–56]. For instance, large grains in Inconel 718 microstructure induced persistent slip bands (PSBs) and resulted in the formation of crystallographic facets as the fatigue crack initiation site despite

the presence of some moderate sized defects [54]. Additionally, a brittle δ-Fe phase in the microstructure deteriorated the fatigue behavior of austenitized steel by promoting microcracks formation and eventually, fatigue failure [55]. This illustrates the influence of microstructural features on fatigue critical crack initiations. However, such influences of microstructural heterogeneities on the fatigue behavior of different configurations of notched specimens with different volumetric defect contents still remain elusive.

To accelerate the use of complex AM parts with notch-like features for fatigue-critical applications, a detailed understanding of their fatigue behaviors and failure mechanisms is needed. In addition to identifying the factors influencing the fatigue behavior, their corresponding criticality needs to be assessed/quantified. This allows for prompt and accurate non-destructive inspection (NDI) of AM parts for fatigue-critical applications. An assessment based on NDI aids the qualification process; however, such an assessment technique is not available in the current literature. Furthermore, a defect-/notch-sensitive fatigue model, that can predict the fatigue lives of AM notched specimens, is cardinal and of paramount importance. Such a fatigue model will reduce the need for repetitive mechanical testing, thus saving time, material, and resources. In the current literature, to depict the fatigue behavior of notched specimens, fatigue models utilizing average strain energy density (ASED) criterion, theory of critical distance (TCD), Murakami's model, etc. have been used; however, these models have only been shown to be applicable to notched parts in as-fabricated surface conditions. For instance, the ASED criterion showed a good correlation with the fatigue lives of as-built Ti-6Al-4V, Co-Cr-Mo, 7075-T6, 42CrMo4+QT, etc. notched specimens [45,56–58]. Similarly, TCD, i.e., point method, line method, and area method, predicted the fatigue lives of L-PBF as-built Ti-6Al-4V notched specimens within the scatter band of 5 [59]. Similarly, Murakami's approach predicted the fatigue limits of L-PBF as-built IN718

notched specimens with reasonable accuracy[60]. While the existing approaches are effective for as-built notched specimens, they do not account for the influence of local crack initiation sites such as volumetric defects or microstructural features on the fatigue behavior. The influence of different volumetric defects or microstructural features such as their sizes, shapes, and locations, on fatigue crack initiation and short crack growth behavior is needed but is missing in the literature.

To investigate the effect of notch geometry on the short crack growth behavior, Witkin et al. proposed the use of stress intensity factor (SIF) for shallow cracks emanating from the notch roots, i.e., $K_I = Q\sigma_{nom.} K_t\sqrt{\pi a}$, where K_I is the mode-I SIF, Q is the geometry factor, $\sigma_{nom.}$ is the nominal stress in the net cross-section, K_t is the stress concentration factor at the notch root, and a is the crack length [61]. For deep cracks, $K_I = 1.122\ \sigma_{nom.}\sqrt{\pi(d+a)}$ was used, where d is the notch depth. Using a similar concept, Härkegård proposed an interpolation function between shallow and deep cracks, to obtain the mode-I SIF expressions for an arbitrary length crack ahead of the notch root [50]. The interpolation function was used to model the effective SIF, i.e., driving force, of cracks ahead of the notch root. It helped characterize the influence of sharp notch geometry on crack arrest, and thus on short crack growth behavior. However, modeling of the synergistic influence of notch geometry and volumetric defect features such as its size, shape, and location on the crack arrest and short crack growth behavior for cracks initiating from defects is still missing in the literature. To summarize, the understanding of the synergistic influence of notch geometry and volumetric defects on fatigue crack initiation and short crack growth behavior of AM metallic materials is very limited and contains many research gaps, which need to be fulfilled to assist the qualification of complex AM parts for fatigue critical applications.

1.2 Project goal, objectives, and tasks

The overall goal of this dissertation is to understand the synergistic effects of volumetric defects and notch geometry on the fatigue behavior of additively manufactured metallic materials. Two materials, AlSi10Mg and 17-4 precipitation (PH) stainless steel (SS), are selected based on the differences in their tensile strengths; it leads to different sensitivity to the presence of volumetric defects and notch geometry for fatigue crack initiation. The proposed goal is divided into several objectives. The **first objective**, addressed in Chapter 2 and Chapter 3, is identifying the factors influencing the fatigue behavior of cylindrical and flat notched specimens with varying ρ and ligament widths (w). AlSi10Mg and 17-4 PH SS specimens with varying notch root radii (ρ of 0.1, 5, and 50 mm), ligament widths (only for flat specimens with ρ of 0.1 and 5 mm, i.e., w of 5 and 10 mm), and defect contents are used. Uniaxial fatigue tests are conducted, and failure mechanisms are investigated to identify the features influencing the fatigue behavior of cylindrical and flat notched specimens. For this objective, it was hypothesized that the criticality of volumetric defects on fatigue crack initiation increases with increasing notch root radii (*Hypothesis 1a*). Secondly, larger ligament width, inducing higher stress concentration, results in shorter fatigue life (*Hypothesis 1b*).

The **second objective**, addressed in Chapter 4, is assessing the fatigue criticality of volumetric defects in notched specimens via a non-destructive approach. In this study, specimens from the first objective are utilized; these specimens are X-ray computed tomography (XCT) scanned and tested. Linear elastic fracture mechanics (LEFM), Murakami's approach, was used to calculate the mode-I stress intensity factor (SIF) of volumetric defects, and the SIF was used to represent their fatigue criticality. For validation, the highest SIF defect within the XCT scan volume was compared with the critical defect observed via fractography, for cylindrical and flat

AlSi10Mg and 17-4 PH SS specimens. It is hypothesized that the mode-I stress intensity factor of defects, calculated by correcting for the notch stress field, can rank the fatigue criticality of defects in notched specimens (*Hypothesis 2a*). Secondly, driven by the stress concentration, smaller defects closer to the notch root plane can be more fatigue critical than larger defects away from it (*Hypothesis 2b*).

Finally, the **third objective**, addressed in Chapter 5, is modeling the synergistic effects of notch geometry & volumetric defects on the short crack growth behavior via a numerical approach. A parametric study is conducted to quantify the effects of notch geometry and defect features on the crack driving force, i.e., mode-I SIF, using linear elastic finite element analysis (LEFEA). LEFEA results are used in conjunction with El-Haddad's approach to calculate the effective SIF of cracks initiating from defects. The trends of effective SIF of cracks are utilized to compare the crack arrest and the short crack growth behavior among different notch-defect configurations. The minimum effective SIF, at crack arrest, is used to obtain the fatigue notch factor. Finally, the fatigue lives of flat notched specimens are predicted using a fatigue notch factor-based framework. It is hypothesized that features such as notch geometry, defect's size, shape, and location affect the effective SIF of cracks initiating from defects (*Hypothesis 3a*). Also, the minimum effective SIF, at crack arrest, can be used to obtain the fatigue notch factor, corresponding to critical defects residing in notched specimens (*Hypothesis 3b*).

1.3 Broader impact

This dissertation offers a comprehensive understanding as well as modeling approaches for the synergistic effects of volumetric defects and notch geometry on the fatigue behavior of AM notched specimens. In addition to achieving the goal and objectives, this dissertation work is

expected to make broader impacts on related research fields and industry. These broader impacts are as follows. The **first objective** identifies the factors influencing the fatigue behavior of cylindrical and flat notched specimens with varying geometries (notch root radius and ligament width) and defect contents. The identified features mainly influence the crack initiation behavior in notched specimens. This knowledge can be used to additively manufacture mechanical components with low criticality notch and defect features, for high-cycle fatigue applications. The **second objective** assesses the fatigue criticality of volumetric defects in notched specimens via a non-destructive approach. This can assist in the production of high-quality AM parts by characterizing and assessing the fatigue critical defects and optimizing different process variables, during fabrication, to remove them. This will reduce the overall cost of production and lower the uncertainties (variability/scatter) in their mechanical behavior.

The **third objective** models the influence of notch geometry and volumetric defect features on the short crack growth behavior via a numerical approach. This approach is useful in determining the effects of critical features on crack arrest, and thus on overall fatigue behavior. This will help AM users to analyze and compare the criticality of different notch and defect features, based on their effect on the short crack growth behavior. The availability of a numerical approach will reduce the need for extensive fatigue testing to obtain the fatigue performances of different notch configurations. Additionally, the expressions for elastic mode-I SIF of cracks initiating from defects in different notch configurations, developed in this study, can be used to model different notch-defect configurations and for different materials; this will help characterize AM parts better for fatigue critical applications. Overall, this dissertation work will generate fatigue data and fractography information for different configurations of AlSi10Mg and 17-4 PH SS notched specimens for the AM community to use.

2 Fatigue Behavior of Additively Manufactured Cylindrical Notched Specimens: The Effect of Volumetric Defects

2.1 Abstract

This study investigated the synergistic effects of volumetric defects and notch geometry on the fatigue behavior of laser powder bed fused AlSi10Mg and 17-4 precipitation hardening (PH) stainless steel (SS) cylindrical notched specimens. Among the considered notch root radii, ρ, of 0.1, 5, and 50 mm, 0.1 mm showed the shortest fatigue lives. All fatigue cracks initiated from the notch root for ρ 0.1 mm and from volumetric defects or turning grooves for ρ 5 mm and 50 mm specimens. The mode-I stress intensity factor, taking into account the synergistic influence of notch geometry, defects' size, and location, was found to correlate well with experimental fatigue lives of AlSi10Mg and 17-4 PH SS notched specimens.

Keywords

Laser powder bed fusion (L-PBF/LB-PBF); Notch fatigue behavior; Defect criticality; AlSi10Mg; 17-4 PH SS

2.2 Introduction

The layer-by-layer deposition of feedstock enables additive manufacturing (AM) processes to fabricate intricate and complex mechanical components, with lattice structures, topology-optimized surfaces, and internal cooling channels, to name a few [62–64], with a lower lead time, minimal material waste, and lower energy consumption compared to conventional manufacturing processes [65]. Such an ability of AM to fabricate geometrically complex components makes the occurrence of notches inevitable [66]. However, the usage of additively manufactured (AM) notched components for fatigue-critical applications present several non-trivial challenges that impact its industry-wide adoption [67,68]. Two of the most prominent ones are the ubiquitous presence of volumetric defects and high surface roughness in AM parts [69–71]. While the micro-notches constituting the surface texture can promote fatigue crack initiation [72–74], their effects can be remedied by surface treatments [75–78]. Volumetric defects, on the other hand, are also well acknowledged to accelerate the fatigue crack nucleation and impact short crack growth [79,80] and are near-impossible to eliminate completely. Therefore, these defects will be the emphasis of this work. In the presence of macro-notches, the stress fields of volumetric defects and the notches can interact, leading to complex fatigue behaviors of notched members [48,49,56,81] that are difficult to predict. This difficulty is in spite of the significant existing knowledge on the relatively isolated effects of notches and volumetric defects [82–86].

Limited literature on the synergistic effects of macro-notch and volumetric defects on the fatigue behavior seems to suggest the dominance of either notches or volumetric defects as the primary fatigue crack initiation sites in the presence of very sharp and very blunt notches, respectively [28,39,87–92]. For instance, in sharply notched specimens, typically with notch root radius, ρ, ranging approximately from 0.2 mm to 2 mm, the stress concentrations generated by the

notches are often overwhelming and fatigue failures are typically from the notch roots. This behavior has previously been seen in laser powder bed fused (L-PBF) Inconel 718 [38], Ti-6Al-4V [28], AlSi10Mg [39], and 316L stainless steel (SS) [93]. In such cases, conventional notch approaches, such as the theory of critical distance, average strain energy densities, and gradient elasticity, have been shown effective to assess the fatigue behavior of AM notched members [46,82]. In bluntly notched specimens with comparatively low stress concentration at the notch root, volumetric defects often emerge to play a role during fatigue crack initiation. For instance, L-PBF 316L SS specimens with an internal circular notch showed fatigue cracks initiation from lack-of-fusions (LoFs) [29]. In this case, the fatigue behavior of the specimens should approach that of the smooth specimens and, in principle, can be described well by defect-sensitive fatigue models incorporating notch stress fields [94,95].

Although the literature suggests a transition of fatigue failure of notched AM parts from notch-critical to volumetric defect-critical with the change in the notch geometry from sharp to blunt, the understanding of the synergistic effects of notch geometry and volumetric defects on the fatigue behavior is still limited. Specifically, the factors governing such a transition, in the context of the complex interplay between notch geometry, volumetric defects, and material, are largely unexplored. For instance, features of volumetric defects such as size, shape, location, etc. affect their stress field [85,96], and are known to affect the fatigue behavior of a smooth specimen. However, how this influence, i.e., the criticality of volumetric defects, is affected by the stress field, imposed by macro-notches, is not well understood. Furthermore, the criticalities of notches and volumetric defects may vary depending on the material which may possess vastly different strength and ductility [97,98], as these properties heavily influence the localized cyclic plasticity occurring in the material leading to crack initiation and growth [99]. Therefore, such an

understanding of factors influencing the fatigue behavior and failure mechanisms in notched members of different AM metallic materials is indeed needed before these parts can be deployed in fatigue critical applications.

This study therefore investigates the effects of notch geometry and volumetric defects on the fatigue behavior of L-PBF AlSi10Mg and 17-4 PH SS. AlSi10Mg and 17-4 PH SS differ in their tensile strength and ductility, which induces different levels of fatigue sensitivity to the presence of volumetric defects and notches. Furthermore, these materials have different industrial applications; AlSi10Mg has an appealing specific strength and is relatively economical, whereas 17-4 PH SS offers excellent corrosion resistance, high strength, and good weldability [100–102]. The synergistic effects of notches and volumetric defects on fatigue behavior are thoroughly analyzed by inducing different populations of volumetric defects in cylindrical specimens with varying notch root radii. A comprehensive characterization of the microstructure, defect content, fatigue behavior, and failure mechanisms is conducted for both L-PBF AlSi10Mg and 17-4 PH SS. Furthermore, linear elastic finite element analysis (LE-FEA) is employed to analyze/quantify the local stress field of notches of different configurations. This article is arranged as follows: Section 2 discusses the experimental setup including the fabrication methods, feedstocks, and heat treatment (HT) schedules; Section 3 presents the results including the microstructure and defect content (Section 3.1), and fatigue behavior and fractography (Section 3.2); Section 4 discusses the factors influencing the fatigue behavior of notched specimens (Section 4.1), the stress distribution near notches of different configurations (Section 4.2), and the relationship between the calculated effective stress intensity factors (SIF) and the fatigue lives (Section 4.3). Finally, conclusions are drawn in Section 5.

2.3 Materials and methods

AlSi10Mg and 17-4 PH SS cylindrical bars of diameter 12 mm were fabricated using the L-PBF AM process in a vertical orientation, perpendicular to the build plate. The build layouts for AlSi10Mg fabricated using Renishaw RenAM 500Q Flex and for 17-4 PH SS using 3D SYSTEMS DMP Flex 350B machine are shown in **Figs. 1** (a & b). As a note, only cylindrical bars shown in the layouts were used in this work; the rectangular blocks were intended for a different study. The recommended key process parameters for both AlSi10Mg and 17-4 PH SS in their respective AM machines are shown in **Table 1**. In addition, the chemical compositions of the feedstocks, AlSi10Mg powder supplied by Renishaw, Inc., and 17-4 PH SS Type A powder supplied by 3D SYSTEMS, Inc., are listed in **Table 2**.

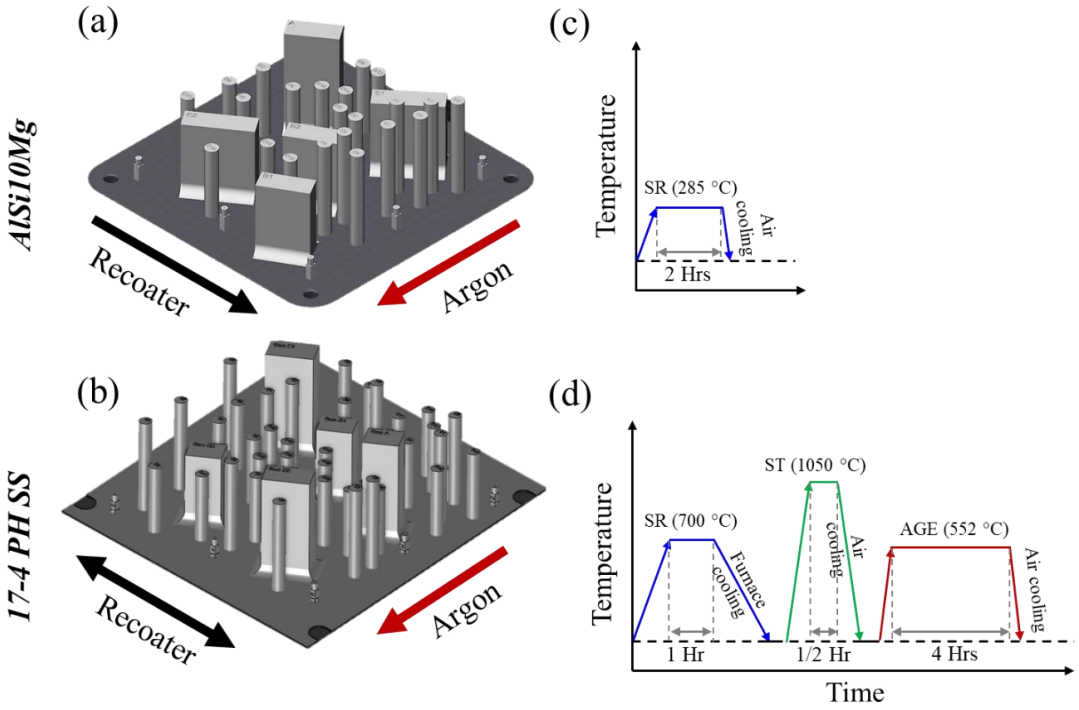

Fig. 1 (a & b) Build layouts and (c & d) heat treatment schedules for AlSi10Mg and 17-4 PH SS, respectively. Directions for inert argon gas flow and recoater movement are shown using arrows in (a & b). The double headed arrow in (b) indicates recoater movement in 3D SYSTEMS (17-4 PH SS) which has feedstock chambers on both sides of the build platform.

Table 1 Recommended key process parameters for AlSi10Mg in RenAM 500Q Flex and 17-4 PH SS in 3D SYSTEMS DMP Flex 350B.

Material	Laser power (W)	Laser speed (mm/s)	Layer thickness (µm)	Hatch distance (µm)	Layer rotation angle (°)	Scan strategy
AlSi10Mg	350	1800	30	100	67	Stripe
17-4 PH SS	245	910	30	120	67	Stripe

Table 2 Chemical composition of the AlSi10Mg powder supplied by Renishaw, Inc., and 17-4 PH SS powder supplied by 3D SYSTEMS, Inc.

AlSi10Mg	Element	Al	Si	Mg	N	Fe	Zn	Cu	Mn	Ni	Pb
	wt. %	Bal.	9.6	0.38	0.2	0.18	0.1	0.05	0.01	0.01	0.01
17-4 PH SS	Element	Fe	Cr	Ni	Cu	Mn	Si	Nb+Ta	C	P	S
	wt. %	Bal.	16.25	4	4	1	1	0.3	0.07	0.04	0.03

Two batches of specimens were fabricated for each AlSi10Mg and 17-4 PH SS. For each material, one batch was fabricated using the manufacturer's recommended process parameters while the other batch was fabricated in the underheating condition, i.e., energy input lower than the recommended, to induce more and larger LoFs. To establish the underheating condition, the laser speed was increased by 10% for AlSi10Mg while the laser power was decreased by 20% and the laser speed was increased by 20% for 17-4 PH SS. Different variations in process parameters were implemented for the two alloys (which had different thermal physical properties) to induce adequate, yet reasonable, amount of LoFs. For simplicity, specimens fabricated using recommended and LoF-inducing process parameters will be referred to as Rec. and LoF specimens in the following sections of this manuscript. After fabrication, the cylindrical bars were heat treated (HT) in an Ar atmosphere to prevent oxidation and surface decarburization following the schedules shown in **Figs. 1** (c & d). The AlSi10Mg bars, according to the AMS 2771 standard [103], were stress relieved (SR) at 285 °C for 2 hours followed by air cooling. On the other hand, the 17-4 PH SS bars were SR at 700 °C for an hour, followed by Condition A (CA) solution treatment at 1050 °C for half an hour, and aging at 552 °C for 4 hours, i.e., H1025. The CA-H1025 HT for 17-4 PH

SS was in accordance with the ASTM A693 [104] standard. During the HT, the temperature inside the furnace was monitored using an external thermocouple, placed in the vicinity of specimens, and maintained at ±5 °C of the intended temperature.

The HT bars were machined with a computerized numerical controlled (CNC) lathe into cylindrical specimens with notches of three different notch root radii, 0.1 mm, 5 mm, and 50 mm. The specimens with ρ of 0.1 mm and 5 mm had a 90° notch opening angle. The geometries and dimensions of the notch configurations are shown in **Fig. 2**. It is worth mentioning that the notch geometries are not in accordance with any standard. After machining, ρ 5 mm and ρ 50 mm specimens were hand-polished using sandpapers with grits ranging from P240 to P1200. However, the hand-polishing, i.e., fine sanding, of ρ 0.1 mm specimens was challenging due to the constraints imposed by their notch geometry; the specimens remained in the as-machined surface condition. The uniaxial force-controlled fatigue tests were conducted on these notched specimens, at room temperature. MTS landmark servohydraulic test frames with 25 kN load cells were used to test AlSi10Mg and 100 kN to test 17-4 PH SS specimens. The fatigue loading was performed under tension-tension conditions, i.e., stress ratio, R, of 0.1. The maximum nominal stresses of amplitudes ranging from 100 MPa to 150 MPa were applied on AlSi10Mg, and from 800 MPa to 1200 MPa on 17-4 PH SS specimens. Such a wide range of stresses were applied to get insights into low-cycle as well as mid-to high-cycle fatigue behavior of notched specimens with varying ρ. The nominal stresses were calculated based on the smallest cross-section at the notch root plane, i.e., a diameter of 5 mm, for all notched specimens.

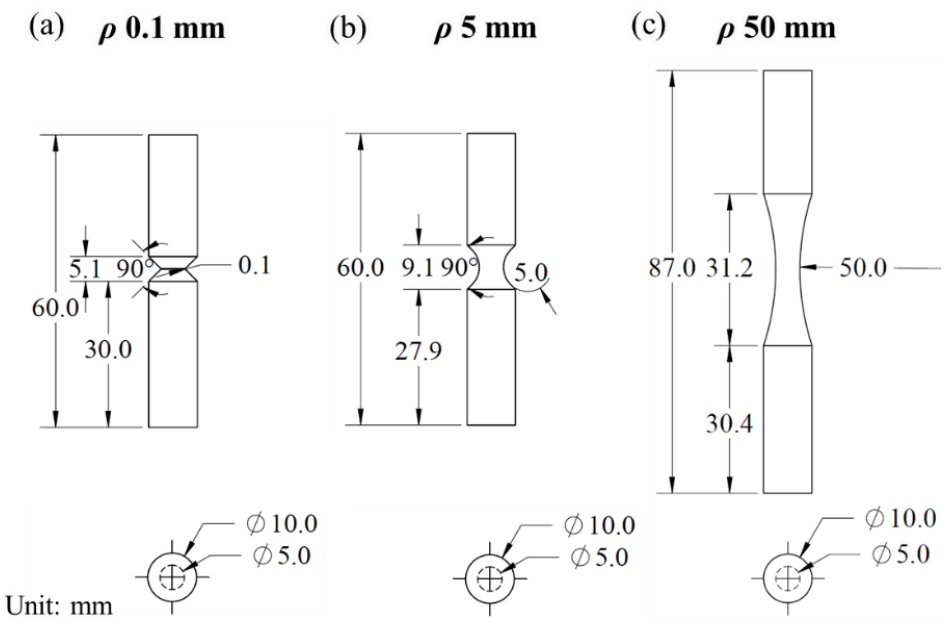

Fig. 2 Geometries and dimensions of cylindrical notched specimens with notch root radii of (a) 0.1 mm, (b) 5 mm, and (c) 50 mm. All dimensions are in mm.

Fractography was performed to investigate the fatigue failure mechanisms in different notch configurations using a Zeiss Crossbeam 550 scanning electron microscope (SEM) equipped with an electron backscatter diffraction (EBSD), backscattered secondary electron (BSE), and electron dispersive spectroscopy (EDS) detectors. The SEM was also used for the microstructural characterization of AlSi10Mg and 17-4 PH SS on both longitudinal plane (LP), i.e., the plane parallel to the build direction, and radial plane (RP), i.e., the plane perpendicular to the build direction. Samples were extracted and mounted in a cold-set epoxy resin and then ground and polished using different grit sandpapers in accordance with ASTM E3 [105], for metallography. The mirror-surface finish was obtained by polishing the mounts in colloidal silica on a chemo-met pad and then on a GIGA-1200 vibratory polisher. Furthermore, defect contents in Rec. and LoF specimens for both AlSi10Mg and 17-4 PH SS were analyzed/characterized using the ZEISS Xradia 620 Versa X-ray computed tomography (XCT) machine. The scans resulted in a voxel size of 6.5 µm; any defects smaller than 20 µm were discarded to avoid false detection from noise.

2.4 Results

2.4.1 Microstructure and defect content

The BSE images and inverse pole figure (IPF) maps for heat treated, i.e., SR for AlSi10Mg and CA-H1025 for 17-4 PH SS, samples, representing both longitudinal and radial planes of the specimens, are shown in **Fig. 3**. For AlSi10Mg, a bimodal grain structure, i.e., long columnar grains oriented along the build direction and fine equiaxed grains, was observed throughout the microstructure (see **Figs. 3**(c & f)). The locations for the fine equiaxed grains in the microstructure are pointed out using a red arrow in **Fig. 3**(c). These regions are typically seen near the melt pool boundaries [106,107] and can be attributed to the higher cooling rates/higher temperature gradients at the melt pool boundaries than the center of the melt pools. Furthermore, **Figs. 3**(b & e) show the presence of vast Si-rich networks in SR AlSi10Mg, as confirmed using EDS analysis (see **Fig. 4**(a)). Similar observations were made in previous studies on SR L-PBF AlSi10Mg [107,108]. Additionally, microscopy performed on the LoF batch AlSi10Mg sample showed no significant differences in the microstructure compared to the Rec. batch.

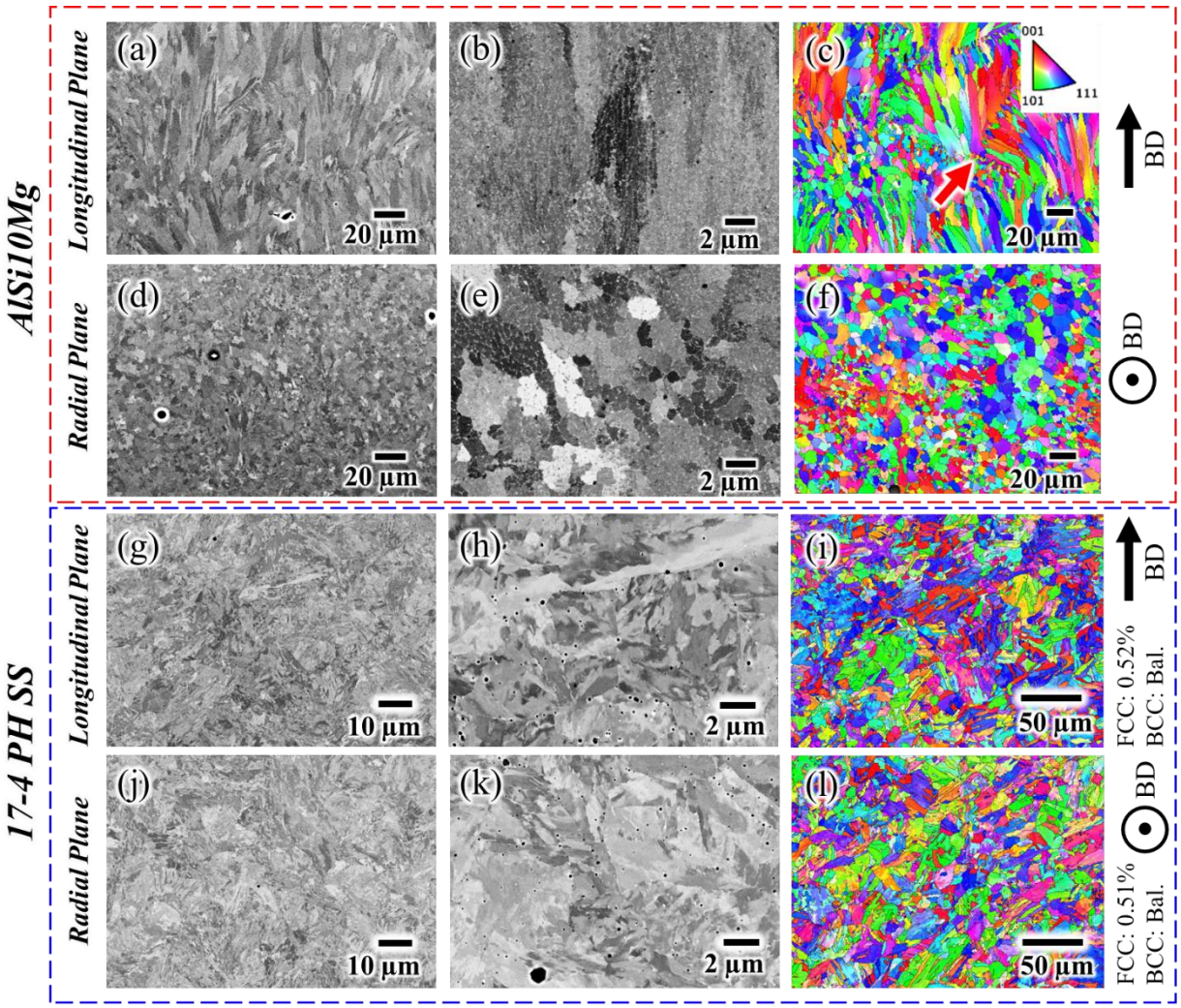

Fig. 3 BSE images and IPF maps of L-PBF AlSi10Mg and 17-4 PH SS: (a-c) AlSi10Mg (LP), (d-f) AlSi10Mg (RP), (g-i) 17-4 PH SS (LP), (j-l) 17-4 PH SS (RP). The red arrow points to an area with fine equiaxed grains, most likely the melt pool boundaries, in AlSi10Mg.

The CA-H1025 treated 17-4 PH SS showed fully homogenized martensitic microstructure in both LP and RP (see **Figs. 3**(g-l)). The BSE images show the presence of fine laths in the microstructure. A similar microstructure for CA-H1025 L-PBF 17-4 PH SS has previously been reported [109–111]. Interestingly, within the microstructure, globular precipitates rich in Nb, Si, S, Cu, and O were observed (see **Fig. 4**(b)). In addition, the kernel average misorientation (KAM) map in **Fig. 4**(c) suggests the presence of delta ferrites, δ-Fe, in the microstructure. The KAM map shows the local lattice misorientation and the absence of misorientation in certain regions of the

microstructure hints towards the presence of δ-Fe. The higher misorientation in the martensitic matrix is primarily due to the prevalence of fine martensitic laths in the nanoscale which typically have 2º-5º misorientation with their immediate neighbors [109,112,113]. In contrast, δ-Fe typically forms during annealing at intermediate temperatures and is free of laths, dislocations, and the local misorientation. The formation of δ-Fe might have occurred during the CA-H1025 heat treatment conducted in this study. In a previous study, the presence of δ-Fe phase in the martensitic matrix has been reported for CA-H900 treated 17-4 PH SS [110].

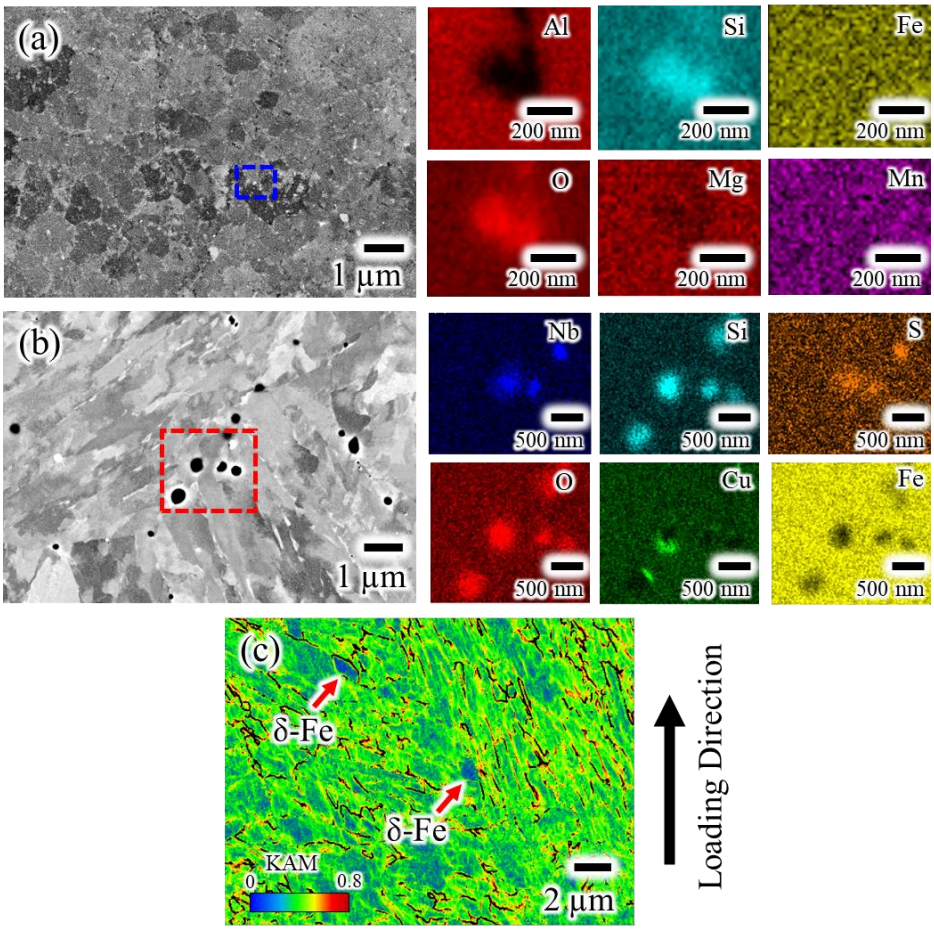

Fig. 4 EDS elemental maps for (a) AlSi10Mg and (b) 17-4 PH SS. (c) KAM map for a CA-H1025 treated 17-4 PH SS sample.

The visualization of volumetric defects in L-PBF AlSi10Mg and 17-4 PH SS detected via XCT is presented in **Fig. 5**; the corresponding size analyses are shown in **Table 3**. For AlSi10Mg,

the specimens in both Rec. and LoF batch had considerable defects. On the other hand, the defect content varied greatly between the Rec. and LoF batches for 17-4 PH SS; Rec. specimens had minimal, while LoF had significantly higher defect content (see **Figs. 5**(c & d)). One-way Analysis of Variance (ANOVA) tests were conducted on ρ 50 mm AlSi10Mg and 17-4 PH SS specimens to determine if there was a statistical difference between the sizes of the defects in Rec. and LoF batches. The p-values, which signify the probability of the means between Rec. and LoF batches are statistically similar if greater than 0.05, were found to be 0.34 and 2.2E-16, for AlSi10Mg and 17-4 PH SS, respectively. This suggests a similarity in the defect sizes between Rec. and LoF batches for AlSi10Mg but a significant difference for 17-4 PH SS. The average volumetric defect content quantified in terms of relative density, number of defects larger than 50 µm, 90^{th} percentile size, and maximum defect size for the specimens shown in **Fig. 5** are listed in **Table 3**. It is worth mentioning that all defects smaller than 20 µm were removed from the analysis to avoid false detection from noise. Relative densities for Rec. and LoF batch AlSi10Mg specimens were 99.768% and 99.624% while it was 99.999% and 99.936% for 17-4 PH SS, respectively. Furthermore, the maximum defect sizes in AlSi10Mg and 17-4 PH SS specimens were, respectively, 462 µm and 50 µm for Rec. condition, and 639 µm and 287 µm for LoF condition.

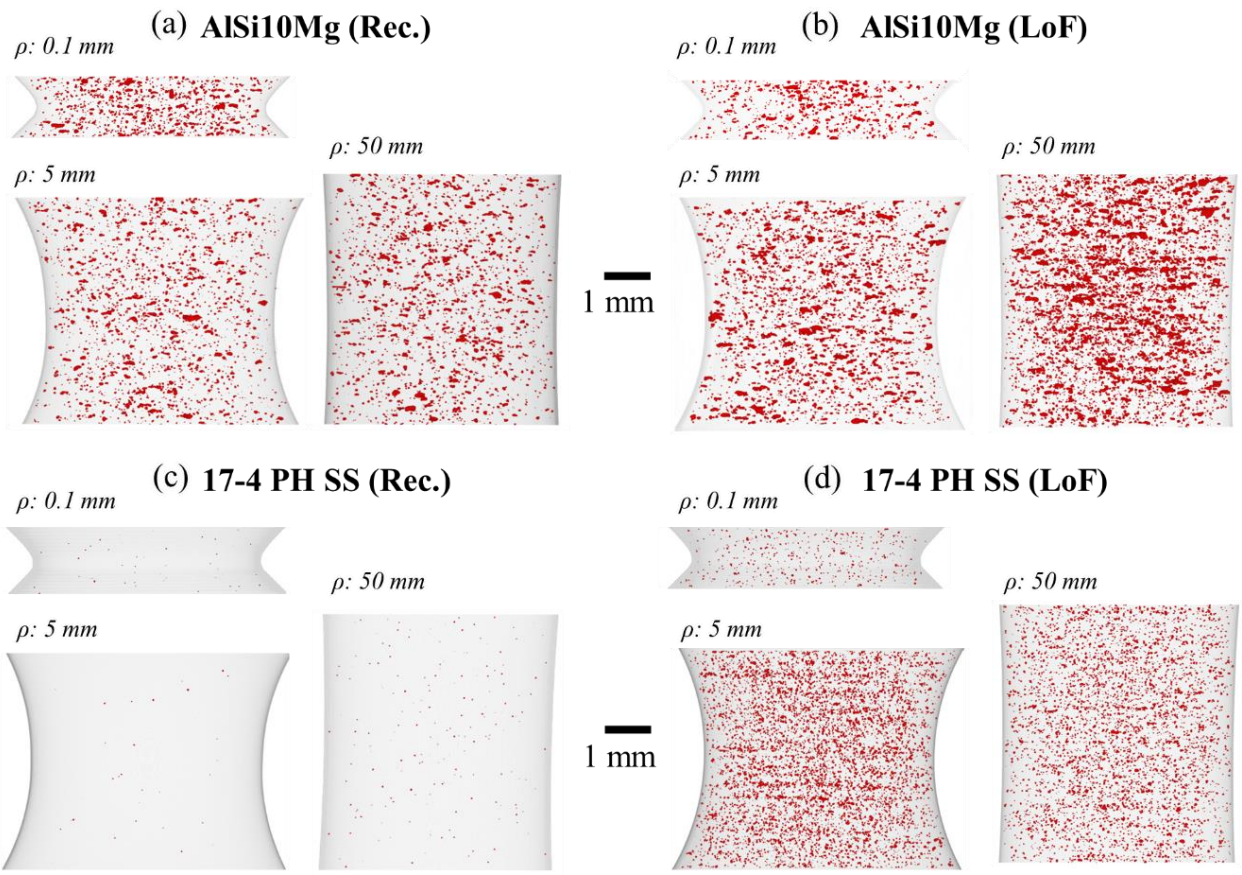

Fig. 5 Visualization of volumetric defects in L-PBF notched specimens: (a) AlSi10Mg (Rec.), (b) AlSi10Mg (LoF), (c) 17-4 PH SS (Rec.), and (d) 17-4 PH SS (LoF).

Table 3 Average defect content quantified in terms of relative density, number of defects larger than 50 µm, 90th percentile size, and maximum defect size in the specimens shown in **Fig. 5**. As a note, the defect content was averaged among ρ 0.1 mm, 5 mm, and 50 mm specimens from each batch and for each material.

AlSi10Mg	Rec.	LoF
Relative Density, %	99.768 ± 0.085	99.624 ± 0.128
No. of Defects > 50 µm	666 ± 268	1152 ± 871
90th Percentile Size, µm	96 ± 2	99 ± 3
Max. Defect Size, µm	462 ± 39	639 ± 97
17-4 PH SS	Rec.	LoF
Relative Density, %	99.999 ± 0.0003	99.936 ± 0.052

No. of Defects > 50 µm	0	740 ± 609
90^{th} Percentile Size, µm	39 ± 4	57 ± 5
Max. Defect Size, µm	50 ± 3	287 ± 72

2.4.2 Fatigue behavior and fractography

The stress-life fatigue plots for AlSi10Mg and 17-4 PH SS notched cylindrical specimens are presented in **Figs. 6**(a & b) and **Figs. 6**(d & e), respectively. The comparison of fatigue data for each alloy under different fabrication conditions is provided in **Figs. 6**(c & f). Irrespective of the material or the fabrication condition, i.e., either Rec. or LoF, ρ 0.1 mm notches induced the shortest fatigue lives at all stress levels. Furthermore, in each material, the fatigue lives of Rec. and LoF batch ρ 0.1 mm specimens were similar (see **Figs. 6**(c & f)), indicating a similar failure mechanism. Interestingly, for AlSi10Mg, not a clear difference in the fatigue lives was observed either between ρ 5 mm and 50 mm or between Rec. and LoF batch specimens. In addition, a considerable scatter in the fatigue lives of AlSi10Mg specimens was present for ρ 5 mm and 50 mm, as opposed to ρ 0.1 mm (see **Figs. 6**(a & b)). For ρ 5 mm and 50 mm, the scatter was considerably smaller at a higher stress level, i.e., 150 MPa, as compared to lower ones, such as 125 MPa and 100 MPa. As most of the fatigue lives in the high cycle fatigue regime is typically spent on crack initiation, such a large scatter at those levels suggested a variation in the characteristics of crack initiating sites.

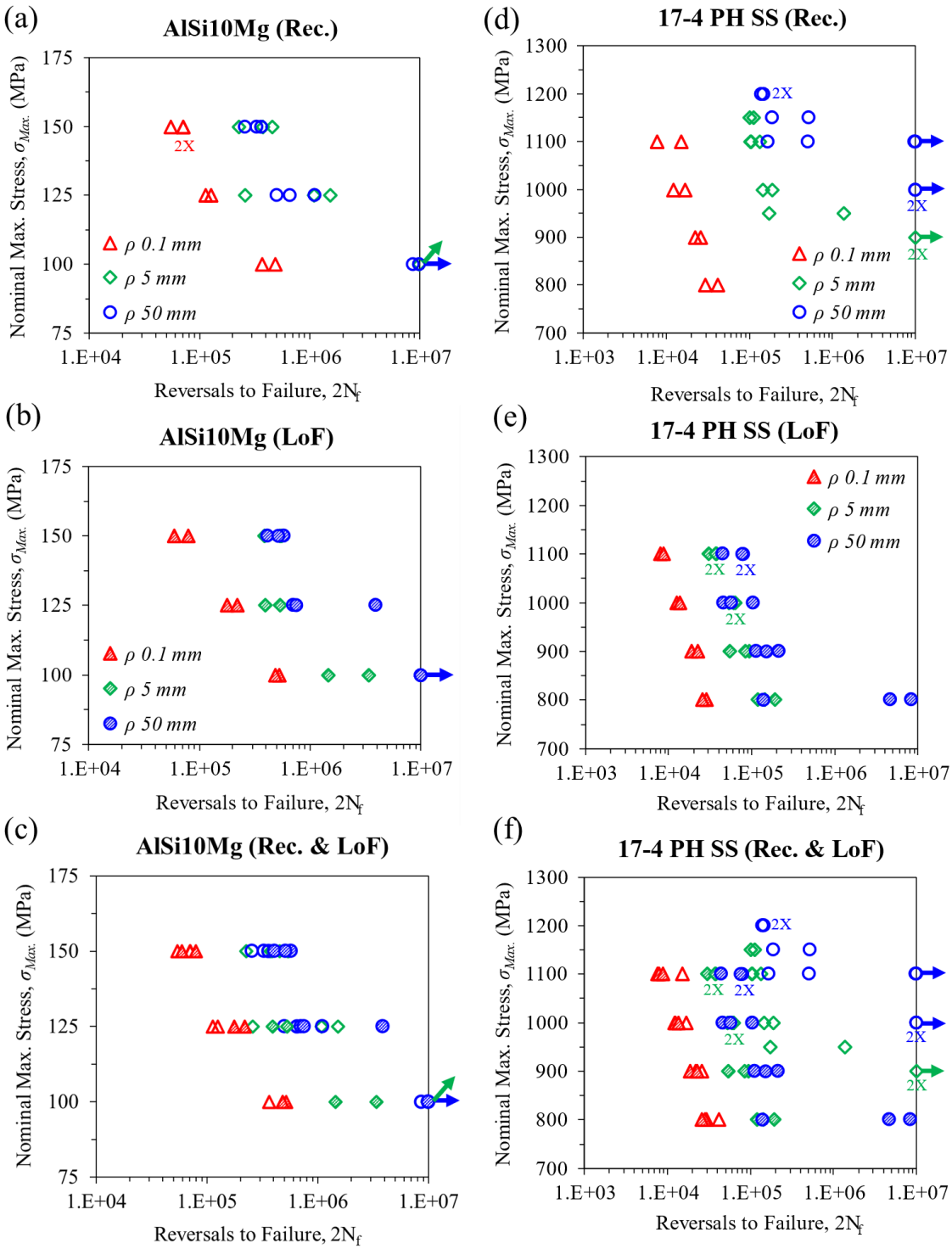

Fig. 6 Stress-life fatigue plots of L-PBF cylindrical notched specimens with different notch root radii, fabricated using different process parameters: (a) AlSi10Mg (Rec.), (b) AlSi10Mg (LoF), (c) AlSi10Mg (a comparison between Rec. and LoF), (d) 17-4 PH SS (Rec.), (e) 17-4 PH SS (LoF), and (f) 17-4 PH SS (a comparison between Rec. and LoF). As a note, the legends used in (a) and (b) are applicable for (c), and the same with (d) and (e) for (f).

On the other hand, for 17-4 PH SS, there was a clear difference in the fatigue lives between the ρ 5 mm and 50 mm notched specimens. **Figures 6**(d & e) clearly show longer fatigue lives of ρ 50 mm specimens over 5 mm for the Rec. batch, although this is less pronounced for the LoF batch. The Rec. batch ρ 50 mm specimens reached run-out, i.e., fatigue lives exceeding 10^7 reversals, at 1100 MPa, while ρ 5 mm reached run-out at 900 MPa. Between the Rec. and LoF batches, the former showed longer fatigue lives at all stress levels than the latter. However, the scatter in the fatigue lives of LoF specimens was smaller than the Rec. ones (see **Fig. 6**(f)). This may be due to the larger defect populations in LoF specimens, resulting in a higher likelihood of critical defects with similar detrimental effects in all specimens.

Detailed fractography was performed on the fracture surfaces to investigate the fatigue failure mechanisms in AlSi10Mg and 17-4 PH SS specimens with different notch root radii. A representative fracture surface from each notch configuration is shown in **Fig. 7**. Irrespective of the material, all fatigue cracks initiated from the notch root for ρ 0.1 mm and from a localized region such as a volumetric defect or a turning groove for ρ 5 mm and 50 mm specimens. For ρ 0.1 mm specimens, a severe and consistent influence from notch geometry, causing the fatigue crack initiation from multiple sites along the notch root (see **Fig. 7**(a & b)), most likely resulted in a minimal scatter of their fatigue lives. Specifically, since volumetric defects didn't have any influence over the fatigue behavior of ρ 0.1 mm specimens, the fatigue lives for both Rec. and LoF batches were similar (see **Figs. 6**(c & f)). In the cases of AlSi10Mg specimens with ρ 5 mm and 50 mm notches, all fatigue critical cracks initiated from a localized region, i.e., irregular shaped (flat) LoFs. The wide scatter in their fatigue lives, shown in **Fig. 6**(c), is likely due to the variation in LoFs' critical features. Additionally, the presence of large volumetric defects with similar

detrimental effects in both Rec. and LoF batch AlSi10Mg specimens has likely resulted in their similar fatigue lives.

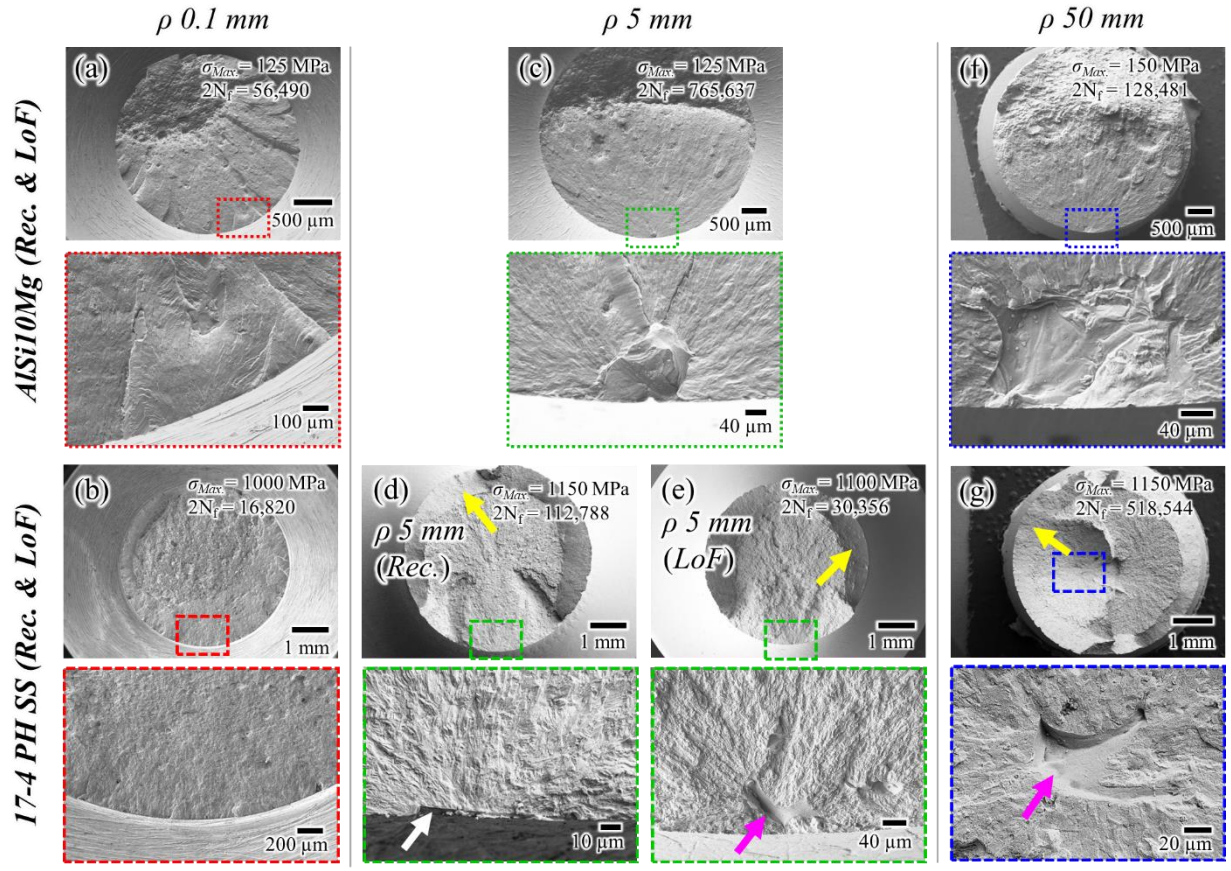

Fig. 7 Fractography images showing the fatigue crack initiation sites in specimens with notch root radii of (a & b) 0.1 mm, (c-e) 5 mm, and (f & g) 50 mm, for AlSi10Mg (Rec. & LoF) and 17-4 PH SS (Rec. & LoF), respectively. (d) and (e), respectively, show the fracture surfaces for ρ 5 mm specimens from Rec. and LoF 17-4 PH SS batches. Yellow, white, and magenta arrows, respectively, point to the shear lips, crack initiating turning groove, and volumetric defects.

In the case of 17-4 PH SS, all fatigue cracks initiated from LoFs in ρ 50 mm, and from both LoFs and turning grooves in ρ 5 mm specimens. The Rec. batch of ρ 5 mm specimens had very low defect count (see **Fig. 5**(c)), and the fatigue cracks initiated from the turning grooves (see **Fig. 7**(d)). The grooves likely were not adequately removed during polishing given the geometrical constraints imposed by the ρ 5 mm notch geometry. In LoF specimens, a dense defect population likely promoted fatigue crack initiation and failures resulting in shorter fatigue lives than Rec.

ones. Further discussion on the factors influencing the fatigue crack initiation behavior in notched specimens is included in **Section 4.1**. Additionally, for 17-4 PH SS, shear lips (indicated using yellow arrows in **Fig. 7**) were observed in the final fracture region of ρ 5 mm and 50 mm specimens. These shear lips have most likely formed when the major fatigue cracks reached the specimens' surface and led to fracture under plane stress condition.

2.5 Discussion

2.5.1 Factors influencing the fatigue behavior of notched specimens

For ρ 0.1 mm specimens, fractography revealed the fatigue crack initiation from the notch roots, implying the notch geometry was the sole factor influencing its crack initiation behavior for both AlSi10Mg and 17-4 PH SS. During cyclic loading, due to the high stress concentration, severe cyclic plasticity occurred at the notch root of ρ 0.1 mm specimens that promoted crack initiation and led to their early fatigue failures. However, in the cases of ρ 5 mm and 50 mm specimens, volumetric defects and turning grooves also played a role in fatigue crack initiation (see **Figs. 7**(c-g)). The size of the critical volumetric defects was quantified using Murakami's approach, i.e., $\sqrt{area}$ [114], and presented in **Figs. 8**(a & b), respectively, for AlSi10Mg and 17-4 PH SS. For an internal defect, $\sqrt{area}$ was calculated as the square root of area of the convex hull around the defects' projection on the loading plane and, for a surface defect, this convex hull included part of specimen perimeter adjacent to the surface. In the case of turning grooves, their aspect ratio (i.e., the ratio of their span along the specimens' tangential direction to their depth along the radial direction) was typically high. As such, the size of the turning grooves was calculated as, $\sqrt{area} = \sqrt{10}\, t_{max.}$, where $t_{max.}$ was the maximum depth of the groove [115]. It is worth mentioning that, in the case of multiple crack initiations observed on a single fracture surface, the crack-initiating defect with the largest $\sqrt{area}$ was considered for analysis. For AlSi10Mg in **Fig. 8**(a), at 150 MPa,

the fatigue life appeared to follow a general trend of shorter fatigue life with larger critical defect size for both ρ 5 mm and 50 mm specimens. However, such a trend didn't exist at lower stress levels, indicating the influence of factors other than defect size only. In comparison, for 17-4 PH SS, a general trend of larger critical defects giving rise to shorter fatigue lives appeared to be visible at all stress levels with a few exceptions (see **Fig. 8**(b)).

The size distributions of the critical defects in ρ 5 mm and 50 mm specimens were further analyzed using the largest extreme value statistics (LEVS). The critical defects' sizes were found to follow Gumbel distribution, as shown using the reduced variate plots with $R^2 > 0.8$ in **Figs. 8**(c & d). The reduced variate, *Y*, was obtained using,

$$Y_i = -ln\,(-\,ln(i\,/\,N+1)), \tag{1}$$

where *i* and *N* are, respectively, the rank and the total number of defects used during the analysis [116]. Furthermore, the corresponding cumulative and probability density functions (CDF and PDF) for the critical defects in ρ 5 mm and 50 mm notched specimens were analyzed in accordance with the ASTM E2283 standard [40] and presented in **Figs. 8**(e & f). For both AlSi10Mg and 17-4 PH SS, the mean critical defects' sizes in ρ 50 mm were slightly larger than in ρ 5 mm specimens (see PDF curves in **Figs. 8**(e & f). This is likely due to the higher probability for larger defects to exist in the larger volume of material experiencing elevated stress at the notch root of ρ 50 mm than 5 mm. Regarding the variation of defects' sizes in AlSi10Mg, ρ 50 mm specimens showed a smaller variation, resulting in a narrower PDF curve compared to ρ 5 mm. This could be due to the higher likelihood of defects of similar sizes becoming fatigue critical in the ρ 50 mm specimens because of their larger volume of material that experiences the stress concentration. However, in the case of 17-4 PH SS, turning grooves often served as the fatigue critical feature in ρ 5 mm specimens (8 out of 39 failed specimens), and the size of these grooves were quite similar and

small (see the markers pointed by the green arrow in **Fig. 8**(d)). This likely resulted in a narrower PDF curve for ρ 5 mm than 50 mm 17-4 PH SS specimens.

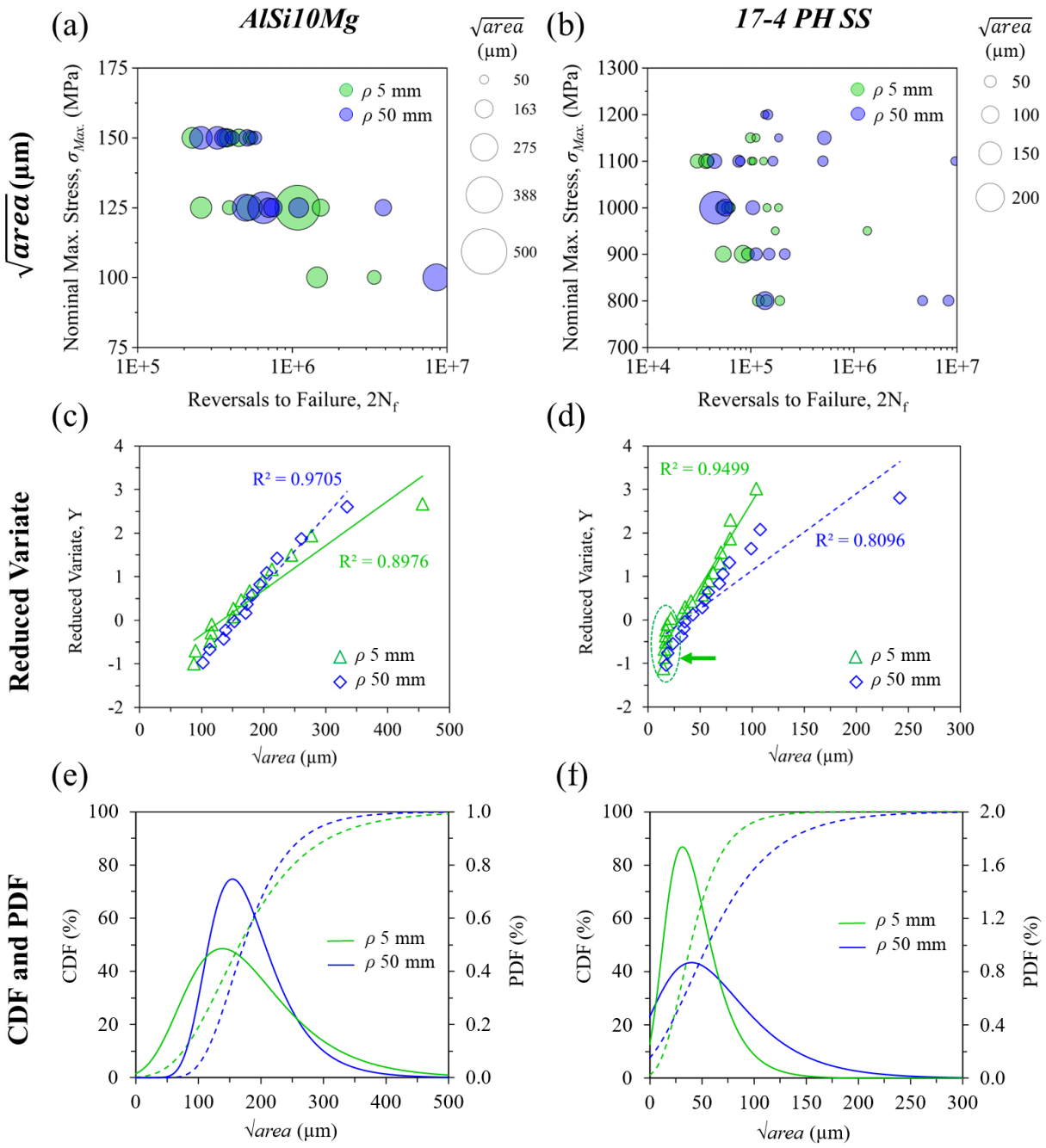

Fig. 8 (a & b) Stress-life fatigue plots with markers' size scaled according to the critical defects' size, (c & d) reduced variate plots, and (e & f) CDF and PDF plots according to LEVS, for AlSi10Mg and 17-4 PH SS, respectively.

Further analysis was performed to identify the factors that could correlate well with the fatigue lives of the notched specimens. On that front, the height of crack initiation relative to the notch root plane, i.e., the loading plane through the smallest cross-section, was obtained, and presented as box plots in **Figs. 9**(a & b). For both AlSi10Mg and 17-4 PH SS, the relative height of crack initiation, h_{center}/h_0 where h_{center} is the distance of the crack initiation site from the notch root plane and h_0 is the total height of the notch geometry (see schematics in **Fig. 9**), for ρ 5 mm and 50 mm specimens showed some scatter but had their means near the notch root plane. The absolute height of crack initiation, i.e., h_{center}, for ρ 50 mm varied in a wider range compared to ρ 5 mm specimens. For AlSi10Mg, h_{center} varied in the range of approximately ±4.2 mm for ρ 50 mm and ±2.1 mm for ρ 5 mm, and for 17-4 PH SS, it ranged approximately ±3.7 mm for ρ 50 mm and ±1.1 mm for ρ 5 mm. Such wider variation for ρ 50 mm specimens is likely due to the larger material volumes experiencing elevated stresses at the notch root compared to ρ 5 mm.

The relative height of crack initiation for each fatigue test plotted against fatigue life is shown in **Figs. 9**(c & d). For both AlSi10Mg and 17-4 PH SS, the scatter in the relative height of crack initiation increased with increasing fatigue life. Several instances were seen, where specimens with critical defects of similar sizes or even larger sizes farther away from the notch root plane showed longer fatigue lives compared to the specimens closer to the notch root plane. This confirmed the influence of stress concentration from the notches on the fatigue crack initiation behavior for ρ 5 mm and 50 mm specimens. This observation, while distinct for AlSi10Mg, is less pronounced for 17-4 PH SS, as seen in **Fig. 9**(d). It is likely due to wider range of volumetric defect sizes in AlSi10Mg compared to 17-4 PH SS—ranges from 20 µm to 639 µm in AlSi10Mg and from 20 µm to 287 µm in 17-4 PH SS (see **Table 3**)—might have increased the likelihood of crack initiation from larger defects, and those located farther away from the notch root plane in

AlSi10Mg. The additional presence of turning grooves at the notch root that were not adequately polished away in the ρ 5 mm 17-4 PH SS specimens likely contributed to their less scatter in relative height of crack initiation. Nevertheless, the understanding of the influence of notch geometry on the fatigue crack initiation was of paramount importance and needed to be quantified.

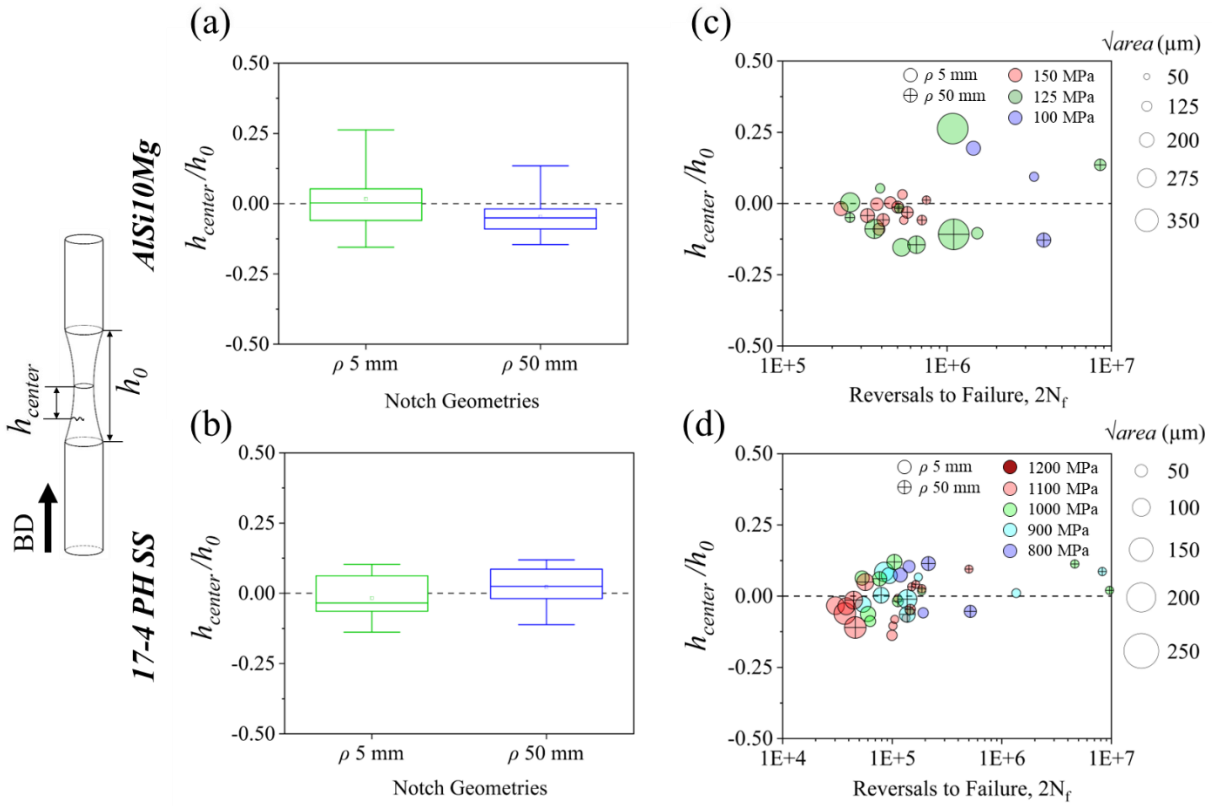

Fig. 9 Box plots showing the relative height of crack initiation for (a) AlSi10Mg and (b) 17-4 PH SS notched specimens. The relative height of crack initiation plotted against the fatigue lives of notched specimens tested at different stress levels for (c) AlSi10Mg and (d) 17-4 PH SS.

2.5.2 Utilizing LE-FEA to analyze the local stress field in notched specimens

Linear elastic finite element analysis (LE-FEA) was performed to calculate the stress distribution in different notched specimens, i.e., ρ of 0.1 mm, 5 mm, and 50 mm. A two-dimensional axisymmetric finite element model (as illustrated in **Figs. 10**(a-c)) was created for each configuration in the ABAQUS® software. Further details on the methodology used during

the LE-FEA are provided in the **Suppl. Mater. Section S1**. The normal stresses along the loading direction were extracted from seven different heights relative to the notch root plane.

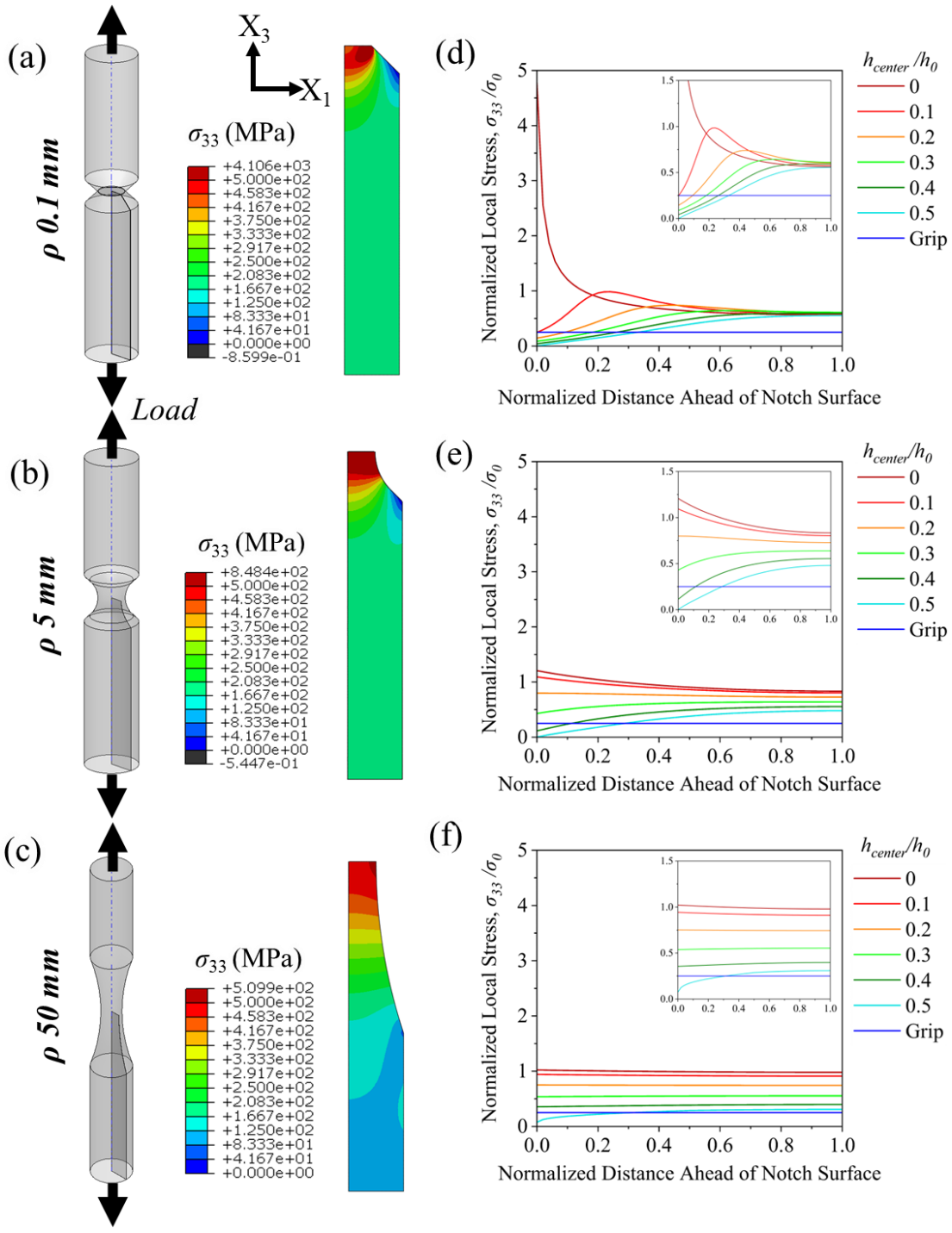

Fig. 10 Notch geometries and stresses at different heights in specimens with ρ of (a, d) 0.1 mm, (b, e) 5 mm, and (c, f) 50 mm, respectively. Black arrows point to the applied loading direction. Stress contour plots for each notch configuration are also shown. The x-axis in (d-f) represents the

distance ahead of the notch surface normalized by the distance from the notch surface to the axisymmetric axis.

Normal stresses, σ_{33},—along the loading direction—normalized by the nominal stress at the smallest cross-section ($\sigma_0 = P/A$, where P is the remotely applied axial load and A is the cross-sectional area at the notch root), at different relative heights, h_{center}/h_0, and distances ahead of the notch surface are shown in **Figs. 10**(d-f). As expected, notched specimens with smaller notch root radii showed higher local stresses and higher stress gradients ahead of the notch root and vice versa. Stress concentration factors, K_t, for ρ 0.1 mm, 5 mm, and 50 mm, at their notch roots were found to be 4.77, 1.21, and 1.02, respectively. At different relative heights, the local stress varied and became very small in the vicinity of the shoulder (see stress contour plots in **Fig. 10**). This caused the normalized stress trend ahead of the notch surfaces to vary among different relative heights. Mathematical fittings have been performed on the curves shown in **Fig. 10**, for which the details are provided in the **Suppl. Mater. Section S1**.

2.5.3 Quantifying the synergistic effect of notches and volumetric defects with mode-I stress intensity factor

Factors such as notch geometry, critical defects' size, and location were found to influence the fatigue crack initiation, and thus, the overall fatigue life of AlSi10Mg and 17-4 PH SS cylindrical notched specimens in the mid to high cycle fatigue regimes. For ρ 5 mm and 50 mm specimens, fatigue cracks initiated from either volumetric defects or turning grooves. Treating these defects as crack nuclei, their detrimental effects can be quantified by the mode-I SIF with the consideration of the local stresses elevated by the notch, i.e.,

$$K_{I(Max.)} = Y\,\sigma_{Max.}\,K_{t(local)}\sqrt{\pi\sqrt{area}}\,, \tag{3}$$

where $K_{I(Max.)}$ is the maximum mode-I SIF of cracks during a loading cycle, *Y* is the Murakami's location-dependent factor (0.5 for internal and 0.65 for surface defects [114]), $\sigma_{Max.}$ is the maximum applied nominal stress during a loading cycle, $K_{t(local)}$ is the local elastic stress concentration factor (i.e., the σ_{33}/σ_0 presented in **Fig. 10**) based on the location of the crack initiating defect. The elastic stress field was considered to comply with one of the key assumptions for the validity of SIF, i.e., the material undergoes elastic deformation.

For ρ 0.1 mm specimens, the detrimental effects of the notches can be quantified by calculating the SIF of virtual, microstructurally small cracks initiated from the notch root surface. For AlSi10Mg, considering that the microstructural boundaries, i.e., grain boundaries, are effective barriers for the growth of microstructurally small cracks, the characteristic length of the virtual crack, l_M, should be its grain size. Similarly, for 17-4 PH SS, l_M should be the lath packet size; however, several studies have suggested δ-Fe as weak points [117,118] that can act as a potential initiation site. In this study, the sizes of the lath packets and δ-Fe were comparable. The SIF can be calculated as

$$K_{I(Max.)} = Y\,\sigma_{Max.}\,K_{t(local)}\,\sqrt{\pi l_M}\,. \tag{2}$$

Here, $K_{t(local)}$ was evaluated in accordance with the theory of critical distance (TCD), i.e., at l_M distance ahead of the notch root [82,119]. TCD assesses the detrimental effect of notches by considering the elastic stresses at a certain distance, line, area, or volume—based on the method used—ahead of the notch root. The l_M for AlSi10Mg and 17-4 PH SS were found to be 15 µm and 8 µm, respectively. For AlSi10Mg, l_M was obtained by measuring the average grain size in the radial direction, i.e., the direction of crack growth, and for 17-4 PH SS, it was calculated as the

average minimum axis of fitted ellipses for the lath packets in the martensitic microstructure (see **Fig. 3**).

The obtained SIF, $K_{I(Max.)}$, for AlSi10Mg notched specimens are shown in the stress-life plot as marker sizes as well as plotted against the fatigue lives in **Fig. 11**. In general, higher SIF corresponded to lower fatigue lives. It is interesting to note that data points for ρ of 0.1 mm, 5 mm, and 50 mm having similar SIF showed similar fatigue lives. This further confirmed the applicability of SIF to assess the criticalities of crack initiating features for both sharply and bluntly notched specimens. However, there was some scatter present in the SIF trend against the fatigue lives, especially for ρ 50 mm specimens (see **Fig. 11**(b)). Therefore, fractography images of three ρ 50 mm specimens, i.e., *X*, *Y*, and *Z*, having similar SIF but very different fatigue lives are shown in **Figs. 11**(c-e). Specimen *Z* had a much longer fatigue life than specimens *X* and *Y*; almost 8 times the fatigue life of specimen *Y*, and almost 21 times the fatigue life of specimen *X*. This is most likely due to the influence of volumetric defects' morphology on the local stress field, and thus, on fatigue crack initiation. Specimens *X* and *Y* had similar projected critical defect shapes (see **Figs. 11**(a & b)); however, the critical defect in specimen *Z* had two arms-like features (see **Fig. 11**(c)). During loading, cracks initiating from the region with arms-like features have significantly low SIF compared to the core region of the defect, thus imparting minimal influence on the crack initiation behavior [120]. Hence, these protrusions/arms in the defect morphology most likely were less detrimental and played an insignificant role during fatigue crack initiation, leading to an overestimation of the critical defect size measured using Murakami's approach, i.e., $\sqrt{area}$ [120].

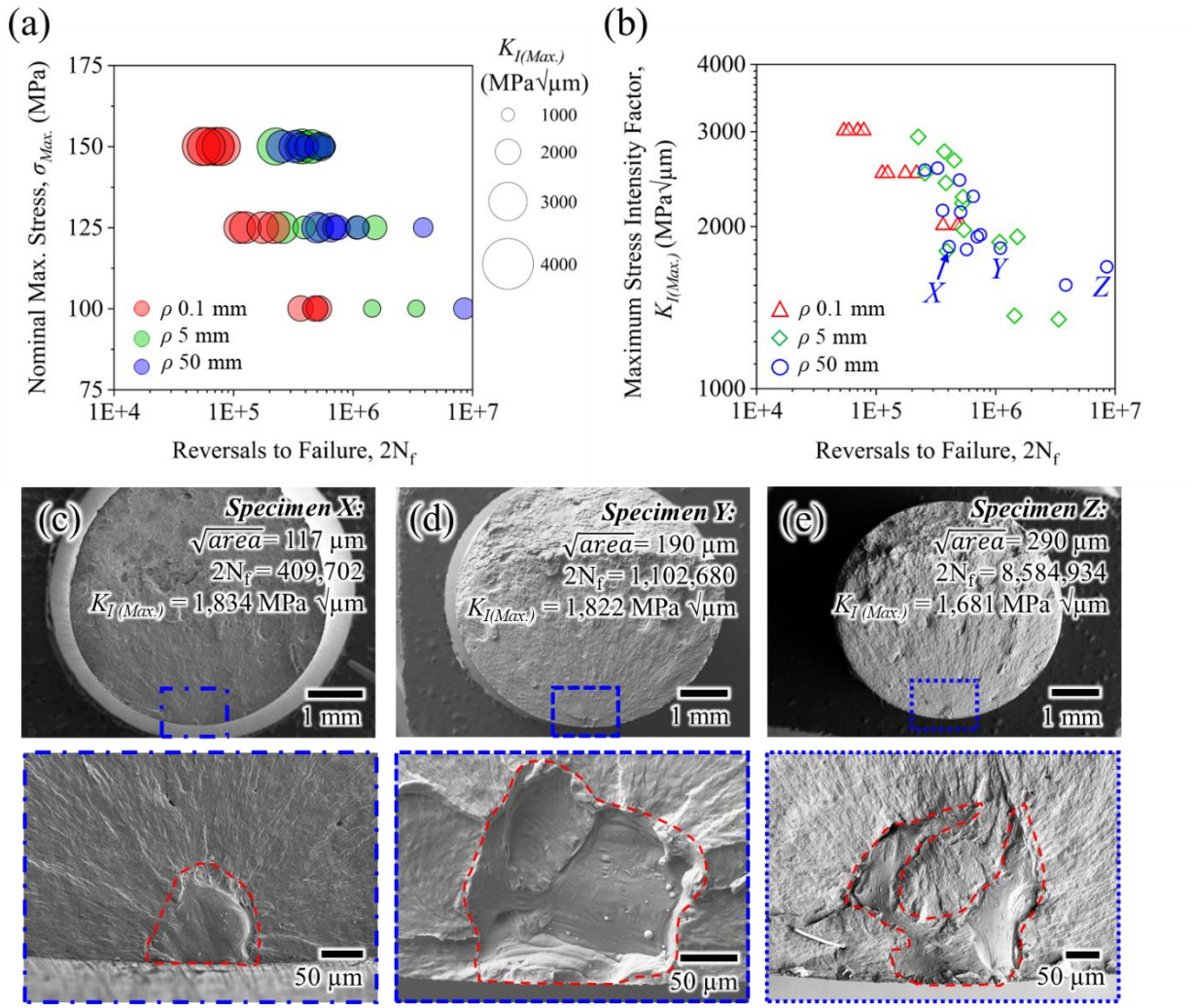

Fig. 11 (a) Stress-life plot with SIF as marker sizes and (b) SIF-fatigue life plot for AlSi10Mg notched specimens. Fractography images for specimens (c) *X*, (d) *Y*, and (e) *Z*.

For 17-4 PH SS, the stress-life plot with SIF indicated as the size of circular markers and SIF-fatigue life plot are shown in **Fig. 12**. In general, the trend for 17-4 PH SS was similar to AlSi10Mg; higher SIF led to shorter fatigue lives. **Figure 12**(a) shows a consistent SIF-fatigue life trend irrespective of the notch configuration at all stress levels except for a few outliers, particularly for ρ 5 mm; one of such outliers is pointed to using a magenta arrow in **Fig. 12**(a). Most of these anomalies had lower SIF compared to other specimens having similar fatigue lives. These specimens had fatigue crack initiation from small turning grooves, hence the lower SIF

compared to specimens with crack initiation from volumetric defects. These cases are better represented as square green markers in **Fig. 12**(b).

Fractography images for one of such abnormal specimens, i.e., specimen *X* indicated in **Fig. 12**(b), with fatigue crack initiation from a turning groove is shown in **Fig. 12**(c). Additionally, a larger scatter was seen in the SIF-fatigue life trend among specimens with crack initiation from volumetric defects compared to specimens with initiations from either notch roots or turning grooves. This is especially obvious for ρ 50 mm specimens. As shown in **Figs. 12**(d & e), specimen *Z*, having a similar SIF, exhibited 44 times longer fatigue life compared to the one for specimen *Y*. This could again be explained by the differences in critical defects' morphology between specimens *Y* and *Z*. The core region, i.e., the region except for arms/protrusions, of the defect in specimen *Z* was significantly smaller than in specimen *Y*. As discussed before for AlSi10Mg, these arms in the projected defect morphology likely had an insignificant impact on fatigue crack initiation, which was overestimated by the Murakami's $\sqrt{area}$. The effect from defect morphology could also have been affected by the differences in the exposure of critical defects to the notch surface for both specimens *Y* and *Z*. The higher exposure of the core region of the critical defect in specimen *Y* could have promoted crack initiation and led to early fatigue failure compared to specimen *Z*. Such variation in the defect morphology and exposure to the surface could have influenced the local stress fields, and thus, the fatigue crack initiation behavior.

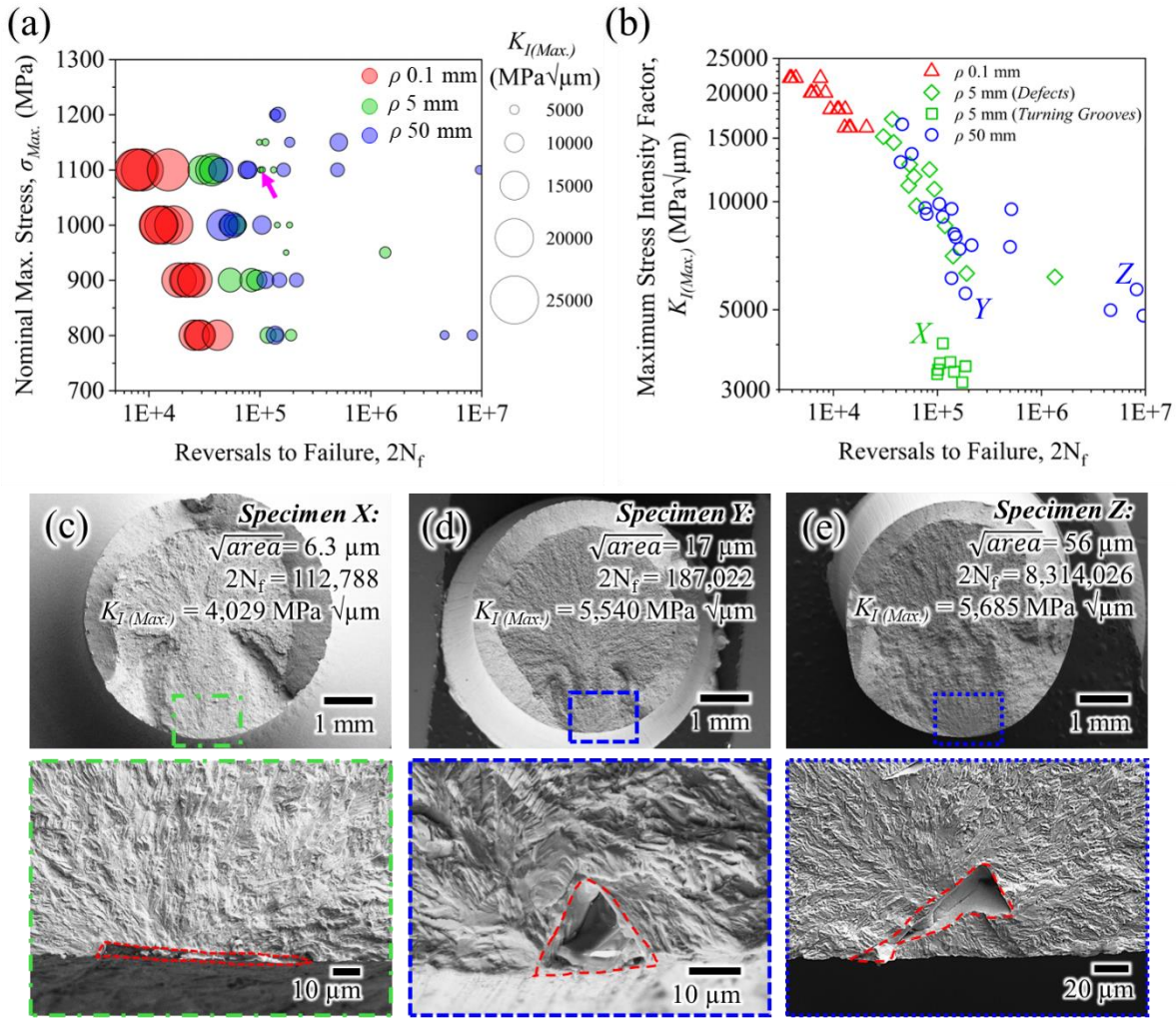

Fig. 12 (a) Stress-life plot with SIF as marker sizes and (b) SIF-fatigue life plot for 17-4 PH SS notched specimens. Fractography images for specimens (c) *X*, (d) *Y*, and (e) *Z*. The magenta arrow points to one of the ρ 5 mm specimens with crack initiation from turning grooves.

2.6 Conclusions

This work investigated the synergistic effects of volumetric defects and notch geometry on the fatigue behavior of cylindrical notched specimens. The primary factors influencing the fatigue crack initiation behavior were identified and quantified for different notch configurations of AlSi10Mg and 17-4 PH SS specimens. The following conclusions were drawn:

1. For AlSi10Mg and 17-4 PH SS, fatigue lives for ρ 0.1 mm notched specimens were inferior to ρ 5 mm and 50 mm counterparts at all stress levels, had the lowest scatter, and were insensitive to the presence of volumetric defects.
2. For ρ 0.1 mm specimens, fatigue cracks initiated from the notch root, while it was from volumetric defects or turning grooves for ρ 5 mm and 50 mm. This suggested the existence of a critical notch root radius above and below which the defects/grooves and the notch geometry, respectively, dominated the fatigue crack initiation behavior.
3. Overall, features such as notch geometry, defects' size, and location influenced the fatigue behavior of ρ 5 mm and 50 mm notches. Smaller notch root radius, larger defects, and defects closer to the surface and the notch root plane were found to be more detrimental to the fatigue behavior.
4. The mode-I stress intensity factor (SIF) obtained for the virtual cracks in ρ 0.1 mm and for volumetric/surface defects in ρ 5 mm and 50 mm specimens accounted for the primary factors influencing the fatigue crack initiation behavior in the notched specimens. SIF showed an inverse relationship with the experimental fatigue lives of AlSi10Mg and 17-4 PH SS specimens.

Overall, this study identified and quantified the primary factors influencing the fatigue behavior of AlSi10Mg and 17-4 PH SS notched specimens. This understanding can be leveraged to design and fabricate low-criticality notch features, having lower stress concentrations and the presence of fewer and smaller defects in the critical region, in complex AM parts. Additionally, the methodology presented in this work can be used to analyze and compare the critical effects of notch geometry and volumetric defect features on the fatigue crack initiation behavior. The

influence of additional factors such as volumetric defects' morphology and orientation with respect to the notch surface, on the fatigue behavior remains to be investigated.

3 Edge Notches in Additive Manufacturing: Influence of Volumetric Defects and Microstructure on the Fatigue Behavior

3.1 Abstract

This study investigated the fatigue behavior of additively manufactured flat, edge-notched AlSi10Mg and 17-4 precipitation hardening (PH) stainless steel (SS) specimens. Specimens with varying notch root radii, ρ, ligament widths, w, and defect contents were subjected to uniaxial cyclic loading. For AlSi10Mg, notch geometry and volumetric defect features such as size and location (within the rectangular cross-section and at different heights relative to the notch root plane) influenced the fatigue behavior. On the other hand, for 17-4 PH SS, there was an additional influence of the microstructural features on the fatigue behavior. In near defect-free 17-4 PH SS specimens, delta ferrite (δ-Fe) phase acted as weak points in the microstructure, promoting crack initiation and short crack growth along δ-Fe-martensite interfaces to form crystallographic facets, leading to fatigue failures. Larger w resulted in shorter fatigue lives for specimens with ρ of 0.1 mm and 5 mm. Compared to the w of 5 mm, 10 mm induced higher plastic damage at the notch root, thus promoting early crack initiation and failures. For notched specimens with negligible plasticity at the notch root, the mode-I stress intensity factor exhibited a correlation with the experimental fatigue lives. On the other hand, for specimens experiencing significant plasticity at the notch root, the equivalent plastic strain showed a correlation with the experimental fatigue lives.

Keywords

Additive manufacturing; Fatigue behavior; Flat notched specimens; Defect criticality; 17-4 PH stainless steel; AlSi10Mg

3.2 Introduction

Edge notches and their variants, such as surface-holes, are widely present in additively manufactured (AM) structures. These notches include, for example, the perforations and fir-tree roots in gas turbine blades and the screw holes in mounting brackets [121–124]. Under service, these notches generate stress concentrations and are often life-limiting features of mechanical components [121,123,125–127]. For conventionally manufactured components, prevailing treatments of these notches have focused on the behavior of short, through-the-thickness cracks initiating from various notch geometries, such as U and V notches, and have relied on two dimensional elastic solutions of notch stress fields [128–131]. On a few occasions, the behavior of non-through-thickness cracks, such as semi-circular/semi-elliptical cracks at the notch root surfaces or notch root corners, have been investigated, revealing more critical effects of the corner cracks [132–134]. Nevertheless, although such notch treatments may be adequate for conventionally manufactured components, they may not be capable of fully capturing the AM materials' complexities in the interactions between the ubiquitously present volumetric defects and the notches.

Unlike grooves or shoulders on cylindrical parts, edge notches (or surface holes) in flat members present a unique combination of stress concentration and surface boundary conditions, i.e., the notch surface is perpendicular to the lateral free surfaces. The lateral free surfaces are subjected to less constraints from the surrounding materials, and in the presence of the volumetric defects in AM materials [69], are more prone to fatigue crack initiation. As such, for AM parts containing edge notches, complex competitions are at play between volumetric defects and notches, as well as among volumetric defects located at the notch root, part interior at different heights from the notch root, and lateral free surface, with regards to their criticality on fatigue

crack initiation. Such competitions are further obscured if multiple notches are present, and their stress fields interact [41,135]. Understandings regarding the synergistic effects of edge notches and volumetric defects have been lacking. Furthermore, in AM parts derived from well-optimized process conditions or hot isostatically pressed or the ones made from defect-insensitive materials, fatigue cracks often initiate from microstructural heterogeneities rather than volumetric defects [136,137]. In these cases, microstructural features such as large grains (where the formation of persistent slip bands is easier [54,138,139]) and weak and brittle phases (e.g., delta-ferrite in steels [55]), can act analogously to volumetric defects in the competition with notches and lateral free surfaces. In this regard, understandings on the edge notches are again lacking in literature.

This study therefore aims to address the research gaps by investigating the fatigue behavior of flat, edge-notched AM specimens with varying geometry (notch root radius and ligament width) as well as defect content made of AlSi10Mg and 17-4 precipitation hardening (PH) stainless steel (SS). These materials are selected based on their varying sensitivity to volumetric defects and notch geometry for fatigue crack initiation [140–143]. Detailed characterization of defect content, microstructure, fatigue behavior, and failure mechanisms are performed. Factors affecting the fatigue behavior of the notched specimens are identified and assessed. This article is arranged as follows: Section 2 details the experimental methods including fabrication, heat treatment, and notch geometries; Section 3 presents the microstructure and defect content analysis (Section 3.1), and the fatigue behavior of notched specimens with varying notch root radii and ligament widths (Section 3.2); Section 4 discusses the overall effect of notch geometry on fatigue behavior (Section 4.1), fatigue crack initiation mechanisms in different notch configurations (Section 4.2), and an approach to quantify the synergistic effects of volumetric defects and notch geometry on the fatigue behavior of flat notched specimens (Section 4.3); Finally, Section 5 draws conclusions.

3.3 Materials and method

Rectangular blocks of dimension 90 mm × 60 mm × 38 mm were fabricated using laser powder bed fusion (L-PBF) machines for two materials, Renishaw RenAM 500Q Flex for AlSi10Mg, and 3D SYSTEMS DMP Flex 350B for 17-4 PH SS. For each material, two batches of blocks were fabricated, one using the recommended process parameters, namely REC, and another by altering the process parameters to induce underheated conditions, namely UH. For AlSi10Mg, underheating was induced by reducing the laser power by 10%, and for 17-4 PH SS, it was achieved by decreasing the laser power by 20% and increasing the laser speed by 20%. Different percentage variations of the process parameters between AlSi10Mg and 17-4 PH SS were applied to induce reasonable amount of lack-of-fusion (LoF) defects. The process parameters for both materials and fabrication conditions are listed in **Table 4**.

Table 4 Recommended and underheated process parameters for AlSi10Mg in RenAM 500Q Flex and 17-4 PH SS in 3D SYSTEMS DMP Flex 350B.

Material	Condition	Laser power (W)	Laser speed (mm/s)	Layer thickness (µm)	Hatch distance (µm)	Layer rotation angle (°)	Scan strategy
AlSi10Mg	REC	350	1800	30	100	67	Stripe
	UH	315					
17-4 PH SS	REC	245	910	30	120	67	Stripe
	UH	196	1092				

After fabrication, the rectangular blocks were stress relieved (SR) prior to removal from the build plate. AlSi10Mg was SR at 285 °C for 2 hours followed by air cooling while 17-4 PH SS at 700 °C for an hour followed by furnace cooling. Furthermore, 17-4 PH SS blocks, after removal from the build plate, were annealed at 1050 °C for half an hour followed by air cooling, i.e., Condition A (CA), and aged at 552 °C for 4 hours, followed by air cooling, i.e., H1025. The CA-H1025 heat treatment (HT) schedule for 17-4 PH SS was in accordance with ASTM A693 standard

[104]. During the HT, the furnace temperature was monitored using a thermocouple, placed in the vicinity of the fabricated blocks, and was maintained at ±5 °C of the desired temperature.

The heat treated (HT) blocks were machined into flat, edge-notched geometries shown in **Fig. 13**, using wire electrical discharge machining (EDM). Detailed dimensions of the notched specimens are provided in **Fig. S1** of the **Suppl. Mater. Section S1**. During EDM, the specimens were extracted so that the loading direction was along the build direction. For each batch, i.e., REC or UH, and for each material, two sets of specimens were extracted, one with varying notch root radii, ρ, i.e., 0.1 mm, 5 mm, and 50 mm, and another with varying ligament widths, w, i.e., 5 mm and 10 mm, only for root radii of 0.1 mm and 5 mm. For simplicity, in the remaining sections of this article, a notched specimen with a ligament width of 5 mm and a notch root radius of 0.1 mm is referred to as *w5 ρ0.1*, and the same nomenclature convention is used for all other configurations. The *ρ0.1* and *ρ5* specimens had a notch opening angle of 90°. After EDM, the lateral surfaces of *ρ0.1* specimens and both notch and lateral surfaces of *ρ5* and *ρ50* specimens were hand-polished using Si-C paper with reducing grits from P240 to P1200, while notch surfaces of *ρ0.1* specimens were left unpolished. Hand polishing of notch surfaces in *ρ0.1* was challenging due to the constraints posed by its sharp notch geometry. Uniaxial force-controlled fatigue tests were conducted with a stress ratio of 0.1 using MTS servohydraulic test frames with a load cell of 25 kN for AlSi10Mg and 100 kN for 17-4 PH SS. The nominal maximum stresses of 100, 125, and 150 MPa were applied on AlSi10Mg, and 700, 800, and 900 MPa on 17-4 PH SS specimens. The force was calculated based on the nominal, minimum cross-sectional area in the specimen. At least three specimens were tested per material, per geometry, and per fabrication condition, at each stress level.

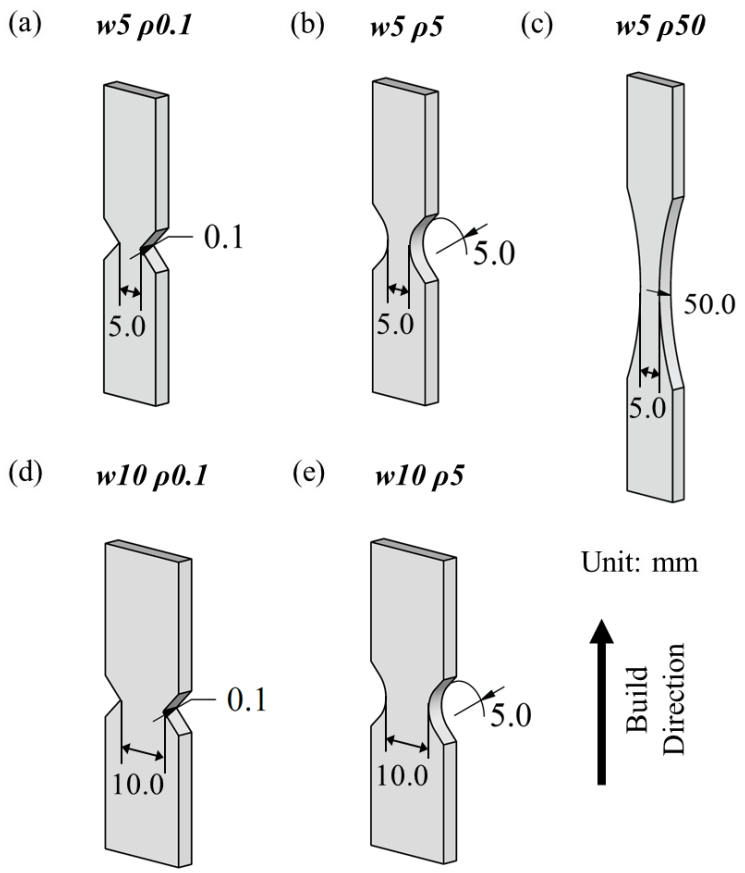

Fig. 13 Geometries of flat notched specimens with varying ligament widths, *w*, and notch root radii, *ρ*: (a) *w5 ρ0.1*, (b) *w5 ρ5*, (c) *w5 ρ50*, (d) *w10 ρ0.1*, and (e) *w10 ρ5*.

After fatigue failure, the critical crack initiation site in each specimen was identified using a Zeiss Crossbeam 550 scanning electron microscope (SEM). Utilizing the SEM equipped with electron backscatter diffraction (EBSD) detectors, microstructural characterization of HT AlSi10Mg and 17-4 PH SS was performed. Metallography coupons were prepared by mounting the samples in an epoxy resin and polishing them progressively using reducing grit SiC sandpapers, a Chemo-met pad, and a GIGA-1200 vibratory polisher for a mirror surface finish [105]. Volumetric defect content within the flat notched specimens was detected and quantified using a ZEISS Xradia 620 Versa X-ray computed tomography (XCT) machine. Defects smaller than 3 times the voxel size, i.e., defect size of 20 μm, were filtered out from the analysis to reduce noise-related misdetections.

3.4 Results

3.4.1 Microstructure and defect content

Micrographs obtained utilizing the EBSD technique in the longitudinal plane, i.e., plane parallel to the build direction, of SR AlSi10Mg and CA-H1025 17-4 PH SS are shown in **Fig. 14**. IPF map for SR AlSi10Mg showed the presence of bimodal grain structure, long columnar grains oriented approximately along the build direction and fine equiaxed grains (see **Fig. 14**(a)). Such long columnar grains are typical of fusion-based additive manufacturing (AM) processes [144]. Furthermore, fine equiaxed grains (shown using a magenta arrow in **Fig. 14**(a)) are indicative of regions near the melt pool boundaries. These features have previously been reported and are typical of L-PBF AlSi10Mg in as-fabricated and SR conditions [107,145,146]. On the other hand, CA-H1025 treated 17-4 PH SS showed a fully homogenized martensitic microstructure (see **Fig. 14**(b)); this is in agreement with the observation reported for L-PBF CA-H1025 treated 17-4 PH SS in the literature [147]. Delta ferrite (δ-Fe) was observed in the 17-4 PH SS microstructure, as indicated by the high magnification kernel average misorientation (KAM) map. Regions, as indicated by red arrows in **Fig. 14**(c), show low misorientations compared to the surrounding martensitic matrix. KAM values are typically high in martensite due to the inherent strain incurred during the martensitic transformation; however, due to the diffusional transformation to δ-Fe, its internal strain is much lower compared to the martensitic laths. Large δ-Fe measuring about 8 μm were found within the microstructure (see **Fig. 14**(c)). It is worth mentioning that there were no significant differences in the microstructure between REC and UH specimens for AlSi10Mg and 17-4 PH SS. Further details on the microstructural characterization including backscattered electron micrographs for AlSi10Mg and 17-4 PH SS are provided in **Suppl. Mater. Section S2**.

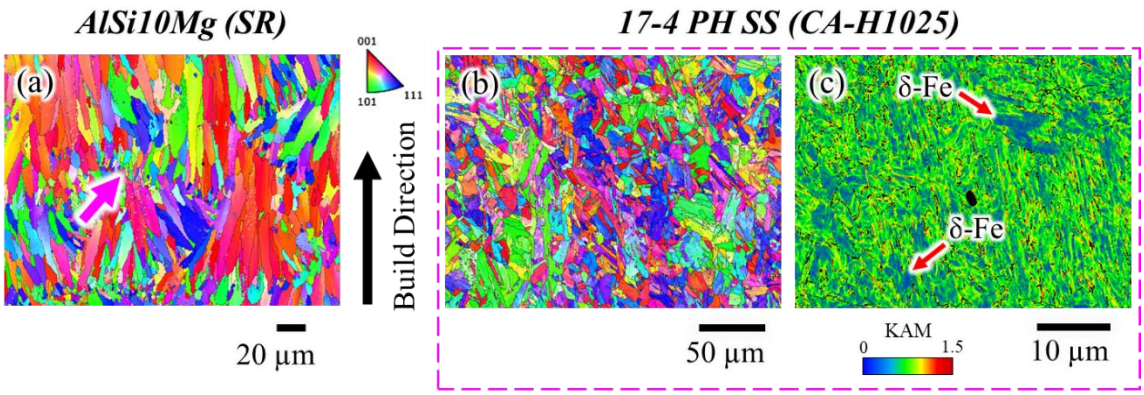

Fig. 14 IPF maps of heat treated (a) AlSi10Mg and (b) 17-4 PH SS, in the longitudinal plane. (c) High magnification KAM map showing the presence of δ-Fe. Magenta and red arrows point to fine grains near the melt pool boundaries in AlSi10Mg and δ-Fe in 17-4 PH SS, respectively.

The volumetric defects in a few representative *w5 ρ5* specimens for both AlSi10Mg and 17-4 PH SS are visualized in **Fig. 15**. Different sizes of volumetric defects were found near the notch surface, lateral surface, and internal (embedded) locations. Between REC and UH specimens, the defect content was comparable for AlSi10Mg, while it was significantly different for 17-4 PH SS. A very low defect content was observed for the REC 17-4 PH SS specimens. The statistical difference in the defect content between REC and UH specimens was confirmed using one-way analysis of variance (ANOVA) tests for AlSi10Mg and 17-4 PH SS. The p-values were respectively found to be 0.56 and 1.3E-18 for AlSi10Mg and 17-4 PH SS. With p-values higher than 0.05 suggesting similarity in the defect sizes, defect content was statistically similar for AlSi10Mg and different for 17-4 PH SS. In terms of defect sizes (equivalent spherical diameter), AlSi10Mg showed a wider variation ranging from 20 µm (limitations due to XCT resolution) to 209 µm compared to 17-4 PH SS, which ranged from 20 µm to 84 µm. Further details on the defect content, quantified in terms of relative density, number of defects larger than 50 µm, 90th percentile defect size, and maximum defect size, are provided in **Suppl. Mater. Section S2**. For both materials, the defect content in *w5* and *w10* specimens was assumed to be similar, considering their EDM extraction from the same fabricated blocks.

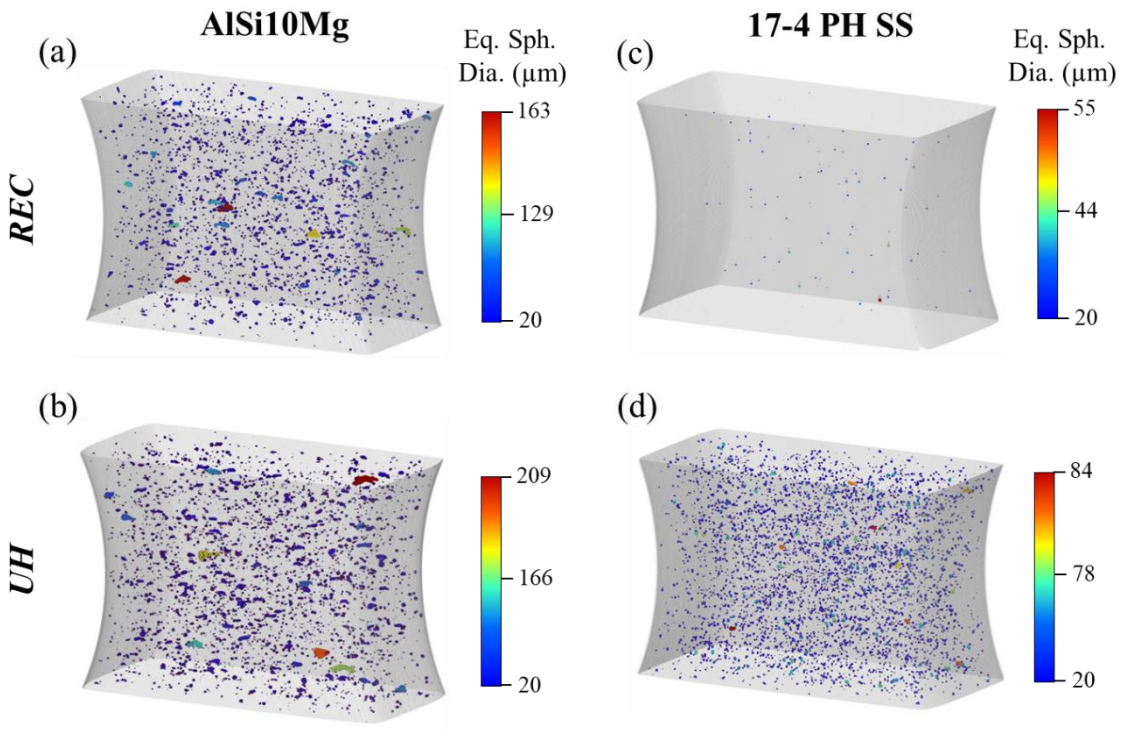

Fig. 15 Visualization of volumetric defects in different configurations of L-PBF *w5 ρ5* notched specimens: (a) AlSi10Mg (REC), (b) AlSi10Mg (UH), (c) 17-4 PH SS (REC), and (d) 17-4 PH SS (UH). Note, volumetric defects are color-coded according to their equivalent spherical diameter.

3.4.2 Fatigue behavior

The stress-life fatigue plots comparing REC and UH specimens with varying notch root radii for AlSi10Mg and 17-4 PH SS are, respectively, shown in **Figs. 4**(a & b). It is worth mentioning that **Fig. 16** only presents data for specimens with the same constant ligament width of 5 mm. The stress-life data for *w5 ρ0.*1, *w5 ρ5*, and *w5 ρ50* AlSi10Mg and 17-4 PH SS specimens are listed in **Table 5** and **Table 6**. Irrespective of the material or the fabrication condition, i.e., either REC or UH, *ρ0.1* specimens had the shortest fatigue lives compared to *ρ5* and *ρ50* at all stress levels (see **Fig. 16**). In addition, there were no significant differences in the fatigue lives between REC and UH *ρ0.1* specimens for either AlSi10Mg or 17-4 PH SS. Such comparable fatigue lives suggested a prevalence of the identical fatigue failure mechanism in REC and UH specimens. On the other hand, for *ρ5* and *ρ50* AlSi10Mg specimens, the scatter in the fatigue lives

was considerably higher than *ρ0.1* at all stress levels (see **Fig. 16**(a)). For AlSi10Mg, no clear difference in the fatigue lives was observed between *ρ5* and *ρ50* specimens; there was no clear difference between REC and UH specimens either. The presence of wide scatter in the mid-to high-cycle fatigue lives of AlSi10Mg hinted at the variation in the critical features of crack initiation sites.

For 17-4 PH SS, in contrast to AlSi10Mg, there was a clear difference in the fatigue lives between *ρ5* and *ρ50* specimens (see **Fig. 16**(b)). The average fatigue lives of *ρ50* specimens were longer than *ρ5* at all stress levels. The *ρ50* specimens reached run-out, i.e., the fatigue life of 10^7 reversals or higher, at 800 MPa (shown using blue arrows in **Fig. 16**(b)), while all *ρ5* specimens failed even at 700 MPa. Furthermore, for *ρ5* and *ρ50*, there was a clear difference in the fatigue lives between REC and UH specimens. As expected, REC specimens having lower defect content (see **Figs. 3**(c & d)) exhibited longer fatigue lives than the UH ones at all stress levels. Interestingly, the UH specimens, where the crack initiation was expected to be from the induced LoF defects, had lower scatter in their fatigue lives than REC specimens at all stress levels. For REC *ρ5* and *ρ50* specimens, the scatter in the fatigue lives increased with decreasing stress levels (see **Fig. 16**(b)).

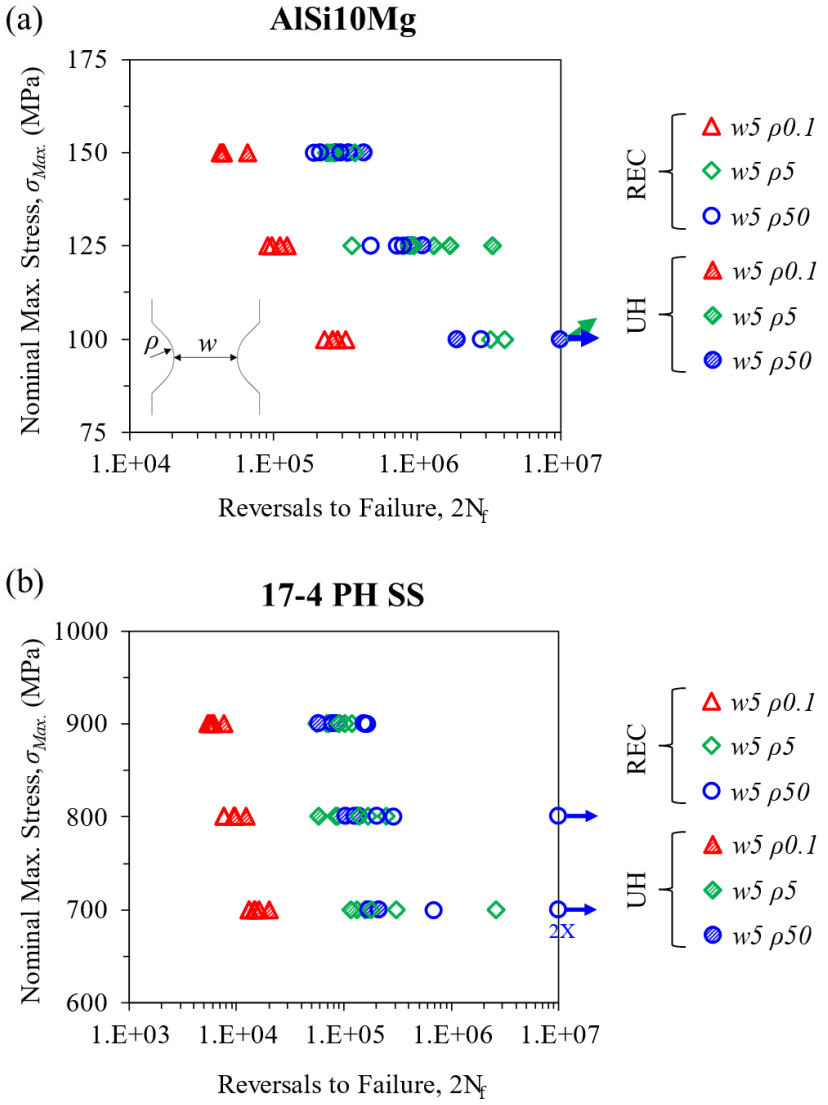

Fig. 16 Stress-life plots for L-PBF flat notched specimens with varying notch root radii: (a) AlSi10Mg (REC and UH) and (b) 17-4 PH SS (REC and UH).

Table 5 Uniaxial fatigue test results for *w5 ρ0.*1, *w5 ρ5*, and *w5 ρ50* AlSi10Mg specimens fabricated under REC and UH conditions.

AlSi10Mg (REC)				AlSi10Mg (UH)			
ID	*w* & ρ	$\sigma_{Max.}$ (MPa)	$2N_f$ (Reversals)	ID	*w* & ρ	$\sigma_{Max.}$ (MPa)	$2N_f$ (Reversals)
REC_1	*w5 ρ0.1*	100	229,384	UH_1	*w5 ρ0.1*	100	260,136
REC_2	*w5 ρ0.1*	100	319,592	UH_2	*w5 ρ0.1*	100	283,732
REC_3	*w5 ρ0.1*	100	311,638	UH_3	*w5 ρ0.1*	100	281,468
REC_4	*w5 ρ0.1*	125	93,006	UH_4	*w5 ρ0.1*	125	112,488
REC_5	*w5 ρ0.1*	125	99,044	UH_5	*w5 ρ0.1*	125	124,886
REC_6	*w5 ρ0.1*	125	98,035	UH_6	*w5 ρ0.1*	125	113,564

REC_7	*w5 ρ0.1*	150	43,414	UH_7	*w5 ρ0.1*	150	45,186
REC_8	*w5 ρ0.1*	150	44,434	UH_8	*w5 ρ0.1*	150	66,540
REC_9	*w5 ρ0.1*	150	44,398	UH_9	*w5 ρ0.1*	150	44,980
REC_10	*w5 ρ5*	100	3,256,880	UH_10	*w5 ρ5*	100	>10,000,000
REC_11	*w5 ρ5*	100	4,112,788	UH_11	*w5 ρ5*	100	>10,000,000
REC_12	*w5 ρ5*	100	>10,000,000	UH_12	*w5 ρ5*	100	>10,000,000
REC_13	*w5 ρ5*	125	352,052	UH_13	*w5 ρ5*	125	1,321,660
REC_14	*w5 ρ5*	125	885,952	UH_14	*w5 ρ5*	125	1,694,142
REC_15	*w5 ρ5*	125	949,164	UH_15	*w5 ρ5*	125	3,383,468
REC_16	*w5 ρ5*	150	247,250	UH_16	*w5 ρ5*	150	237,446
REC_17	*w5 ρ5*	150	263,712	UH_17	*w5 ρ5*	150	265,080
REC_18	*w5 ρ5*	150	369,506	UH_18	*w5 ρ5*	150	274,998
REC_19	*w5 ρ50*	100	2,809,784	UH_19	*w5 ρ50*	100	1,894,412
REC_20	*w5 ρ50*	100	>10,000,000	UH_20	*w5 ρ50*	100	>10,000,000
REC_21	*w5 ρ50*	100	>10,000,000	UH_21	*w5 ρ50*	100	>10,000,000
REC_22	*w5 ρ50*	125	474,710	UH_22	*w5 ρ50*	125	890,046
REC_23	*w5 ρ50*	125	721,150	UH_23	*w5 ρ50*	125	938,542
REC_24	*w5 ρ50*	125	792,750	UH_24	*w5 ρ50*	125	1,108,168
REC_25	*w5 ρ50*	150	190,624	UH_25	*w5 ρ50*	150	272,842
REC_26	*w5 ρ50*	150	214,062	UH_26	*w5 ρ50*	150	335,756
REC_27	*w5 ρ50*	150	297,028	UH_27	*w5 ρ50*	150	428,260

Table 6 Uniaxial fatigue test results for *w5 ρ0.*1, *w5 ρ5*, and *w5 ρ50* 17-4 PH SS specimens fabricated under REC and UH conditions.

17-4 PH SS (REC)				17-4 PH SS (UH)			
ID	*w* & *ρ*	$\sigma_{Max.}$ (MPa)	$2N_f$ (Reversals)	ID	*w* & *ρ*	$\sigma_{Max.}$ (MPa)	$2N_f$ (Reversals)
REC_1	*w5 ρ0.1*	700	13,142	UH_1	*w5 ρ0.1*	700	14,688
REC_2	*w5 ρ0.1*	700	13,226	UH_2	*w5 ρ0.1*	700	14,938
REC_3	*w5 ρ0.1*	700	16,234	UH_3	*w5 ρ0.1*	700	20,120
REC_4	*w5 ρ0.1*	800	7,574	UH_4	*w5 ρ0.1*	800	9,574
REC_5	*w5 ρ0.1*	800	7,614	UH_5	*w5 ρ0.1*	800	9,648
REC_6	*w5 ρ0.1*	800	9,466	UH_6	*w5 ρ0.1*	800	12,284
REC_7	*w5 ρ0.1*	900	5,424	UH_7	*w5 ρ0.1*	900	5,916
REC_8	*w5 ρ0.1*	900	5,494	UH_8	*w5 ρ0.1*	900	6,138
REC_9	*w5 ρ0.1*	900	5,794	UH_9	*w5 ρ0.1*	900	7,572
REC_10	*w5 ρ5*	700	178,434	UH_10	*w5 ρ5*	700	117,446
REC_11	*w5 ρ5*	700	305,802	UH_11	*w5 ρ5*	700	133,034
REC_12	*w5 ρ5*	700	2,630,734	UH_12	*w5 ρ5*	700	157,964
REC_13	*w5 ρ5*	800	138,534	UH_13	*w5 ρ5*	800	58,108
REC_14	*w5 ρ5*	800	166,244	UH_14	*w5 ρ5*	800	83,222

REC_15	*w5 ρ5*	800	247,938	UH_15	*w5 ρ5*	800	88,492
REC_16	*w5 ρ5*	900	90,452	UH_16	*w5 ρ5*	900	56,280
REC_17	*w5 ρ5*	900	101,932	UH_17	*w5 ρ5*	900	69,764
REC_18	*w5 ρ5*	900	119,496	UH_18	*w5 ρ5*	900	72,516
REC_19	*w5 ρ50*	700	681,664	UH_19	*w5 ρ50*	700	169,800
REC_20	*w5 ρ50*	700	>10,000,000	UH_20	*w5 ρ50*	700	173,246
REC_21	*w5 ρ50*	700	>10,000,000	UH_21	*w5 ρ50*	700	212,112
REC_22	*w5 ρ50*	800	205,274	UH_22	*w5 ρ50*	800	104,002
REC_23	*w5 ρ50*	800	286,690	UH_23	*w5 ρ50*	800	125,334
REC_24	*w5 ρ50*	800	>10,000,000	UH_24	*w5 ρ50*	800	137,242
REC_25	*w5 ρ50*	900	152,826	UH_25	*w5 ρ50*	900	58,464
REC_26	*w5 ρ50*	900	156,548	UH_26	*w5 ρ50*	900	79,218
REC_27	*w5 ρ50*	900	163,902	UH_27	*w5 ρ50*	900	86,990

The stress-life plots comparing *ρ0.1* and *ρ5* notched specimens with varying ligament widths, i.e., *w5* and *w10*, for AlSi10Mg and 17-4 PH SS are shown in **Fig. 17**. The stress-life data for *w10 ρ0.1* and *w10 ρ5* AlSi10Mg and 17-4 PH SS specimens are listed in **Table 7** and **Table 8**. Regardless of stress level and material condition (i.e. REC or UH), *w10* specimens, i.e., the ones with ligament width of 10 mm, had shorter fatigue lives by an order of magnitude compared to *w5* specimens for either alloy. For all configurations, the slope of the stress-life data as well as the scatter in the fatigue lives between *w5* and *w10* specimens were comparable (see **Fig. 17**).

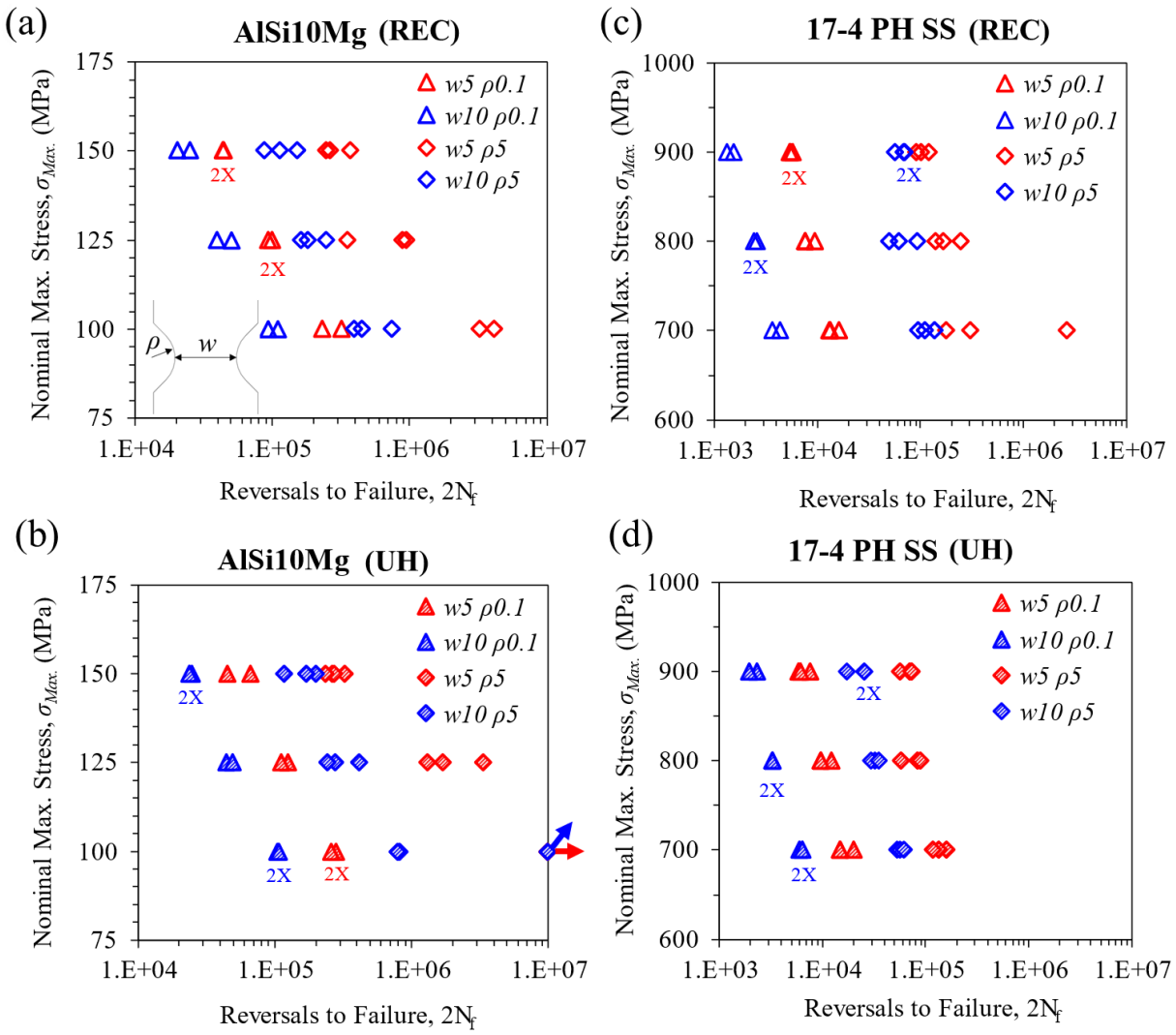

Fig. 17 Stress-life plots for L-PBF flat notched specimens with varying ligament widths: (a) AlSi10Mg (REC), (b) AlSi10Mg (UH), (c) 17-4 PH SS (REC), and (d) 17-4 PH SS (UH).

Table 7 Uniaxial fatigue test results for *w10 ρ0.*1 and *w10 ρ5* AlSi10Mg specimens fabricated under REC and UH conditions.

AlSi10Mg (REC)				AlSi10Mg (UH)			
ID	*w* & *ρ*	$\sigma_{Max.}$ (MPa)	$2N_f$ (Reversals)	ID	*w* & *ρ*	$\sigma_{Max.}$ (MPa)	$2N_f$ (Reversals)
REC_28	*w10 ρ0.1*	100	93,876	UH_28	*w10 ρ0.1*	100	105,558
REC_29	*w10 ρ0.1*	100	108,994	UH_29	*w10 ρ0.1*	100	106,908
REC_30	*w10 ρ0.1*	100	94,658	UH_30	*w10 ρ0.1*	100	106,433
REC_31	*w10 ρ0.1*	125	39,890	UH_31	*w10 ρ0.1*	125	44,696
REC_32	*w10 ρ0.1*	125	50,110	UH_32	*w10 ρ0.1*	125	49,064
REC_33	*w10 ρ0.1*	125	41,845	UH_33	*w10 ρ0.1*	125	45,021

REC_34	*w10 ρ0.1*	150	20,464	UH_34	*w10 ρ0.1*	150	23,650
REC_35	*w10 ρ0.1*	150	25,006	UH_35	*w10 ρ0.1*	150	25,042
REC_36	*w10 ρ0.1*	150	21,056	UH_36	*w10 ρ0.1*	150	23,758
REC_37	*w10 ρ5*	100	396,884	UH_37	*w10 ρ5*	100	802,252
REC_38	*w10 ρ5*	100	445,826	UH_38	*w10 ρ5*	100	825,014
REC_39	*w10 ρ5*	100	737,108	UH_39	*w10 ρ5*	100	>10,000,000
REC_40	*w10 ρ5*	125	163,058	UH_40	*w10 ρ5*	125	245,284
REC_41	*w10 ρ5*	125	181,208	UH_41	*w10 ρ5*	125	278,258
REC_42	*w10 ρ5*	125	247,114	UH_42	*w10 ρ5*	125	420,032
REC_43	*w10 ρ5*	150	87,248	UH_43	*w10 ρ5*	150	117,840
REC_44	*w10 ρ5*	150	112,766	UH_44	*w10 ρ5*	150	170,346
REC_45	*w10 ρ5*	150	151,518	UH_45	*w10 ρ5*	150	200,832

Table 8 Uniaxial fatigue test results for *w10 ρ0.*1 and *w10 ρ5* 17-4 PH SS specimens fabricated under REC and UH conditions.

AlSi10Mg (REC)				AlSi10Mg (UH)			
ID	*w* & *ρ*	$\sigma_{Max.}$ (MPa)	$2N_f$ (Reversals)	ID	*w* & *ρ*	$\sigma_{Max.}$ (MPa)	$2N_f$ (Reversals)
REC_28	*w10 ρ0.1*	700	3,674	UH_28	*w10 ρ0.1*	700	6,010
REC_29	*w10 ρ0.1*	700	4,314	UH_29	*w10 ρ0.1*	700	6,324
REC_30	*w10 ρ0.1*	700	3,851	UH_30	*w10 ρ0.1*	700	6,302
REC_31	*w10 ρ0.1*	800	2,402	UH_31	*w10 ρ0.1*	800	3,274
REC_32	*w10 ρ0.1*	800	2,562	UH_32	*w10 ρ0.1*	800	3,278
REC_33	*w10 ρ0.1*	800	2,468	UH_33	*w10 ρ0.1*	800	3,265
REC_34	*w10 ρ0.1*	900	1,332	UH_34	*w10 ρ0.1*	900	1,948
REC_35	*w10 ρ0.1*	900	1,530	UH_35	*w10 ρ0.1*	900	2,320
REC_36	*w10 ρ0.1*	900	1,358	UH_36	*w10 ρ0.1*	900	1,998
REC_37	*w10 ρ5*	700	94,738	UH_37	*w10 ρ5*	700	53,550
REC_38	*w10 ρ5*	700	111,310	UH_38	*w10 ρ5*	700	56,436
REC_39	*w10 ρ5*	700	138,384	UH_39	*w10 ρ5*	700	62,080
REC_40	*w10 ρ5*	800	49,980	UH_40	*w10 ρ5*	800	29,622
REC_41	*w10 ρ5*	800	61,956	UH_41	*w10 ρ5*	800	32,332
REC_42	*w10 ρ5*	800	93,426	UH_42	*w10 ρ5*	800	35,458
REC_43	*w10 ρ5*	900	56,878	UH_43	*w10 ρ5*	900	17,250
REC_44	*w10 ρ5*	900	68,078	UH_44	*w10 ρ5*	900	25,168
REC_45	*w10 ρ5*	900	70,406	UH_45	*w10 ρ5*	900	25,430

3.5 Discussion

3.5.1 Overall effect of notch geometry on fatigue behavior

Different notch geometries, depending on their features such as ρ and w, induce different levels of stress concentration at the notch root. Under cyclic loading, this can result in an accumulation of cyclic plastic damage at the notch root to different extents, that promotes crack initiation and leads to fatigue failure. Such an influence from the notch geometry may have governed the ordering of fatigue lives for AlSi10Mg and 17-4 PH SS flat notched specimens shown in **Fig. 16** and **Fig. 17**. To quantify the plastic deformation at the notch root, influencing the fatigue crack initiation behavior of varying ρ and w specimens, elasto-plastic finite element analysis (EPFEA) was performed for both AlSi10Mg and 17-4 PH SS specimens.

EPFEA was performed on two-dimensional finite element models in the ABAQUS® software for *w5 ρ0.1, w5 ρ5, w5 ρ50, w10 ρ0.1,* and *w10 ρ5* configurations in plane stress condition, considering small thickness (3 mm) of the specimens. Utilizing the symmetric boundary conditions, only $1/4^{th}$ of the full geometries, as shown in **Fig. S4** of the **Suppl. Mater. Section S3**, was modeled. The material parameters, i.e., modulus of elasticity and true stress-plastic strain data, for AlSi10Mg and 17-4 PH SS were obtained from the tensile test conducted in accordance with ASTM E8 standard [148]. Force to generate the nominal stresses of 100, 125, and 150 MPa, were applied on the grip ends of the finite element models for AlSi10Mg, and 700, 800, and 900 MPa for 17-4 PH SS. Further details on the methodology used for the EPFEA are provided in **Suppl. Mater. Section S3**. As a result, the equivalent plastic strains (PEEQ), indicative of plasticity in the model, were extracted from regions ahead of the notch surface, at the notch root plane, and presented in **Fig. 18**. Note that, for *w5 ρ50* specimens, no plasticity was observed at the notch root, therefore, the results were not shown.

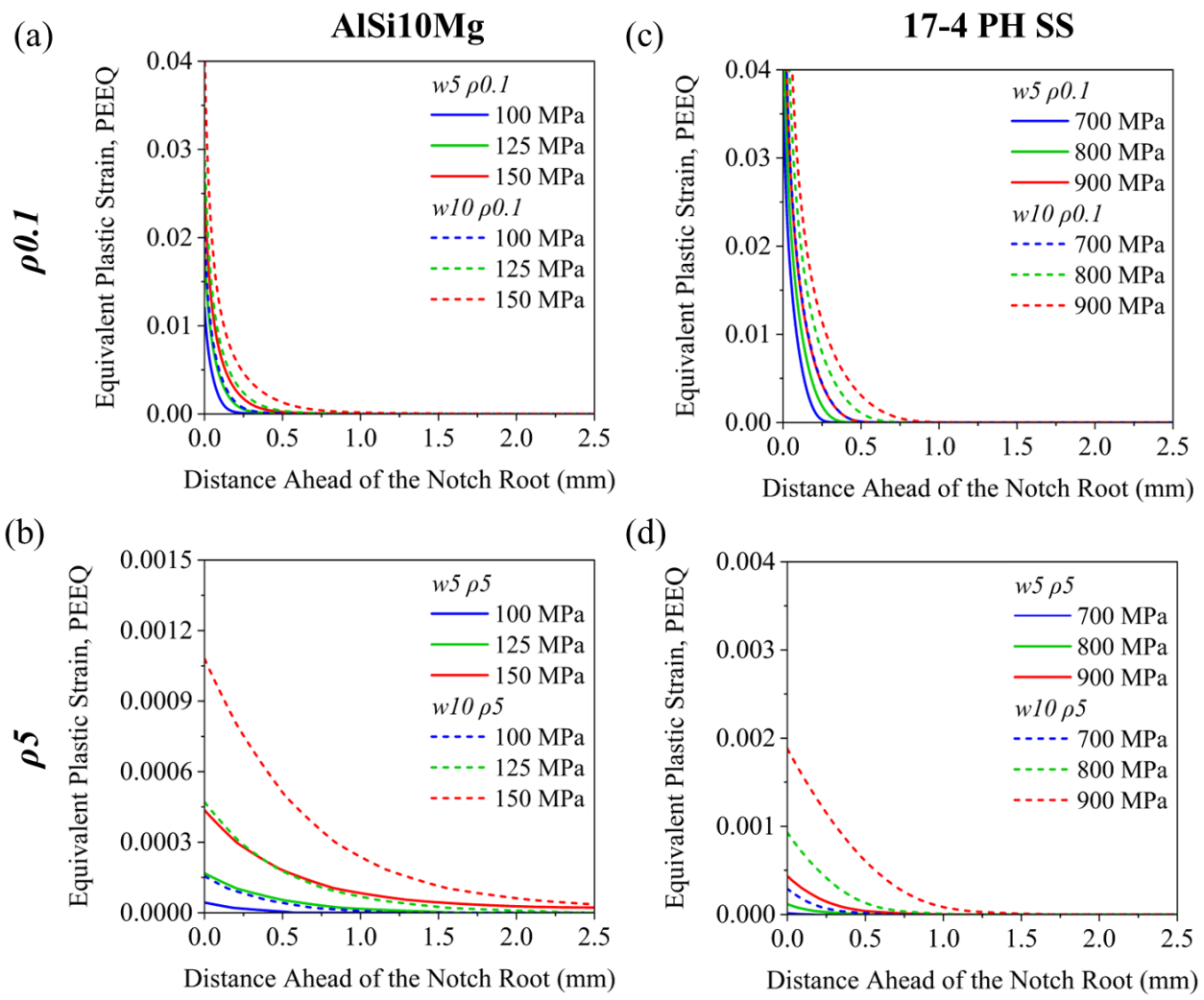

Fig. 18 Equivalent plastic strain (PEEQ) ahead of the notch surface, at the notch root plane, for *ρ0.1* and *ρ5* specimens with varying ligament widths for (a & b) AlSi10Mg and (c & d) 17-4 PH SS, at different stress levels.

In general, *ρ0.1* specimens generated significantly higher PEEQ values at the notch root compared to *ρ5*, irrespective of the *w* or the material at all stress levels. While *ρ0.1* specimens showed plastic strains of ~ 5% at the notch root, *ρ5* showed less than 0.2%, at the highest nominal stress (150 MPa for AlSi10Mg and 900 MPa for 17-4 PH SS). During cyclic loading, severe plastic damage likely accumulated at the notch root of *ρ0.1* specimens, which promoted crack initiation and led to shorter fatigue lives with lower scatter compared to *ρ5* and *ρ50* (see **Fig. 16**). Regarding the effect of *w*, for both *ρ0.1* and *ρ5*, *w10* showed a slightly higher PEEQ at the notch root than

w5, for both AlSi10Mg and 17-4 PH SS, at all stress levels. At the highest nominal stress, *w5 ρ5* specimens showed plastic strains of less than 0.05% for either material, while *w10 ρ5* induced slightly higher plastic strains of ~0.1% and ~0.2% for AlSi10Mg and 17-4 PH SS, respectively. During cyclic loading, higher plasticity at the notch root of the *w10* specimens accumulated more plastic damage at the notch root, thus making fatigue crack initiation faster than the one in the *w5* counterparts. Such an ease of fatigue crack initiation in *w10* specimens, leading to an early fatigue failure, was likely the reason behind their shorter fatigue lives than *w5* ones (see **Fig. 17**).

For *ρ0.1* AlSi10Mg specimens, PEEQ profiles for *w5* at 150 MPa (red solid line in **Fig. 18**(a)) and *w10* at 125 MPa (green dashed line in **Fig. 18**(a)) were comparable, and, interestingly, these specimens had similar fatigue lives, shown in **Figs. 5**(a & b). The same was true for *w5 ρ0.1* specimens at 125 MPa and *w10 ρ0.1* at 100 MPa. For 17-4 PH SS, PEEQ ahead of the notch root as well as the resulting fatigue lives were similar for *w5 ρ0.1* specimens at 900 MPa and *w10 ρ0.1* at 700 MPa (see **Fig. 18**(c) and **Fig. 17**(c)). Similar observations could be made for *ρ5* specimens of both materials. For instance, *w5 ρ5* AlSi10Mg specimens at 150 MPa and *w10 ρ5* at 125 MPa had similar PEEQ ahead of the notch root as well as overlapping fatigue lives (see **Figs. 17**(a & b)). For both AlSi10Mg and 17-4 PH SS and for both *ρ0.1* and *ρ5* specimens, a higher PEEQ at the notch root corresponded to a shorter fatigue life and vice versa. These observations suggested that plastic strain at the notch root, induced due to an increase in the ligament width, was a governing factor of fatigue lives, especially for *ρ0.1* specimens. To confirm these observations, the PEEQ at the notch roots of *w5* and *w10* specimens were plotted against their experimental fatigue lives for both notch root radii and materials, as shown in **Fig. 19**.

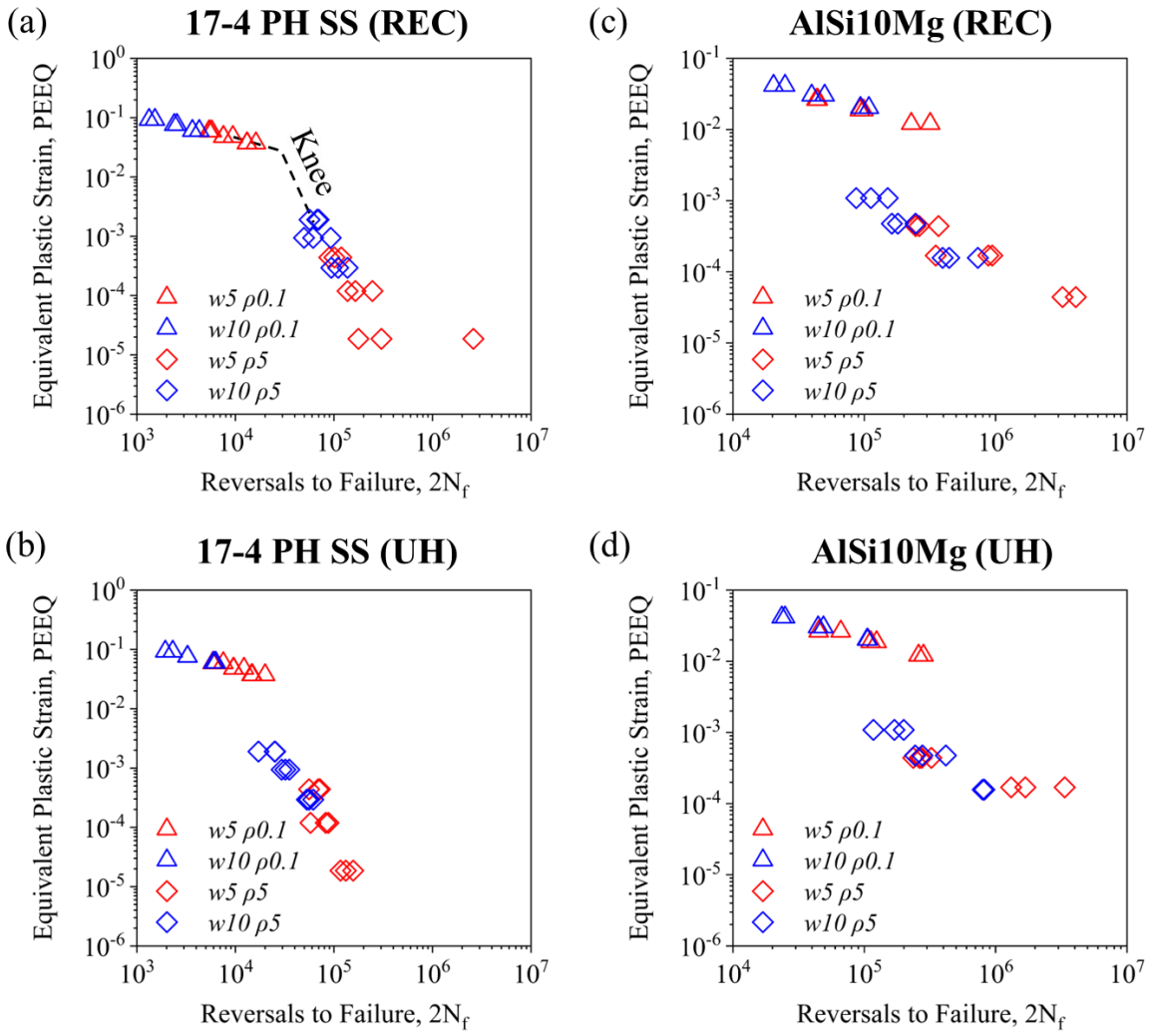

Fig. 19 Equivalent plastic strain (PEEQ)-fatigue life plots for L-PBF flat notched specimens with varying notch root radii and ligament widths: (a) 17-4 PH SS (REC), (b) 17-4 PH SS (UH), (c) AlSi10Mg (REC), and (d) AlSi10Mg (UH).

A clear dependence of experimental fatigue lives on PEEQ is evident in **Fig. 19**. Within the same ρ, a monotonic trend existed, showing a good correlation between *w5* and *w10* specimens. This further confirmed that the more pronounced PEEQ at the notch root was deteriorating the fatigue lives of *w10* specimens. However, between *ρ0.1* and *ρ5* specimens, the PEEQ-life trends were not consistent and showed different slopes, as shown in **Fig. 19**. Due to the variation in slopes in the PEEQ-life trends, a knee was observed between the data points of *ρ0.1* and *ρ5* REC 17-4 PH SS specimens (see **Fig. 19**(a)). The knee appeared to be similar to the one in stress-life plots

[149,150] in double-logarithm scales signifying the transition from the mid cycle fatigue (MCF) to high cycle fatigue (HCF) regimes. However, in the case of UH 17-4 PH SS specimens, the knee was less apparent in the PEEQ-life trends between *ρ0.1* and *ρ5* (see **Fig. 19**(b)). The PEEQ-life trend for *ρ5* (see **Fig. 19**(b)) showed an offset towards shorter fatigue lives. This is likely due to an added influence from localized crack initiating features, resulting in shorter fatigue lives. In the case of AlSi10Mg, the knee was even less apparent than UH 17-4 PH SS specimens. This suggested the prevalence of even more detrimental crack initiating features in AlSi10Mg. In addition, the higher scatter in the fatigue lives of AlSi10Mg compared to 17-4 PH SS specimens (see **Fig. 19**) also suggested that the criticality of these features varied significantly. To gain further insights into the critical features influencing the fatigue behavior, the crack initiation mechanisms in different notch configurations needed to be investigated.

3.5.2 Diverse fatigue crack initiation mechanisms in notched specimens

Fractography was performed to identify the crack initiation sites and investigate the fatigue failure mechanisms in flat notched specimens with varying *ρ* and *w*. For *ρ0.1* notched specimens, critical fatigue cracks initiated from the notch root, irrespective of the ligament width and the material. Representative fractography images for *ρ0.1* AlSi10Mg specimens with *w* of 5 mm and 10 mm are shown in **Figs. 20**(a & d). During cyclic loading, severe stress concentration due to the notch geometry accumulated plastic damage at the notch root, as suggested by PEEQ plots in **Figs. 6**(a & b), thus promoting crack initiation independent of the volumetric defects present in the material and leading to early failures in *ρ0.1* AlSi10Mg and 17-4 PH SS specimens (see **Fig. 16** and **Fig. 17**). Such a crack initiation mechanism in sharp notches (i.e., *ρ0.1* with *w* of 5 mm and 10 mm), likely accumulated sufficient plasticity required for crack initiation only from the stress fields due to the notch geometry, resulting in an overlapping PEEQ-life trend for *w5 ρ0.1* and *w10*

ρ0.1 specimens, as shown in **Fig. 19**. Such a strong and consistent influence of notch geometry on the fatigue crack initiation likely resulted in shorter fatigue lives with lower scatter for sharp *ρ0.1* notched specimens.

For blunt notched specimens (i.e., *ρ5* and *ρ50* specimens with *w* of 5 mm and 10 mm), different crack initiation sites, i.e., either volumetric defects or microstructural features, were observed. For AlSi10Mg blunt notches, all fatigue critical cracks initiated from LoF defects, located either at the surface or near-surface. Fractographs for representative blunt notched AlSi10Mg specimens with *w* of 5 mm and 10 mm are shown in **Figs. 20**(b & e). The variation in the critical defect features and their influence on the fatigue crack initiation and resulting fatigue life likely resulted in an increased fatigue scatter at different stress levels (see **Fig. 16**(a) and **Figs. 5**(a & b)). Additionally, the variation in the critical defect features resulted in an overlap between the fatigue lives of *w5 ρ5* and *w5 ρ50* AlSi10Mg specimens, shown in **Fig. 16**(a). Similarly, between *w5 ρ5* and *w10 ρ5* specimens, the scatter in the observed fatigue lives in **Figs. 19**(c & d) was likely due to the wide variation in the defect features such as size and location.

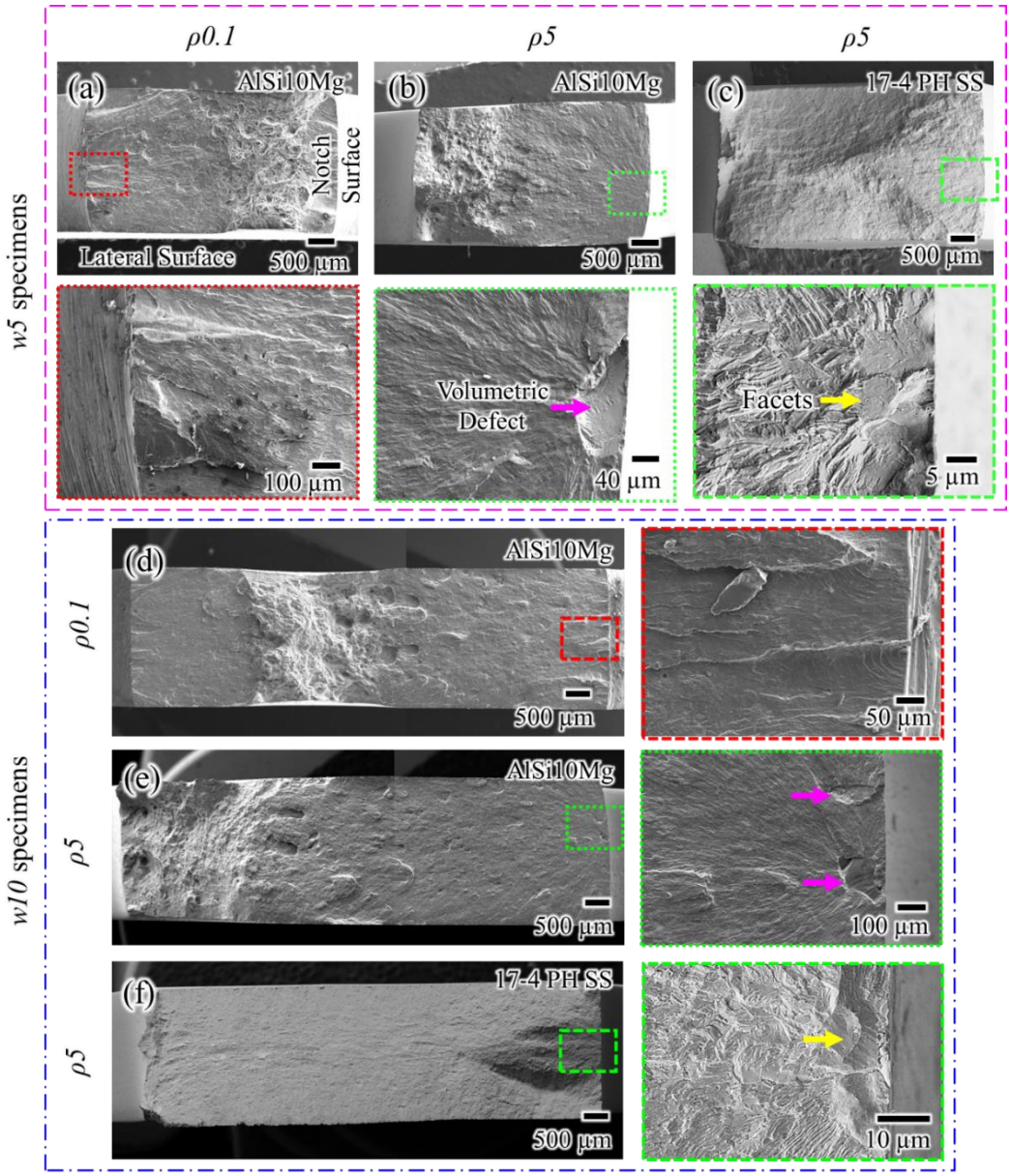

Fig. 20 Fractography images showing critical fatigue crack initiations from the (a & d) notch root and (b & e) volumetric defect in AlSi10Mg, and from (c & f) crystallographic facets in 17-4 PH SS specimens having *w* of 5 mm and 10 mm. Magenta and yellow arrows, respectively, point to critical defects and crystallographic facets.

For 17-4 PH SS, unlike AlSi10Mg, fracture surfaces of blunt notches showed critical crack initiations from both volumetric defects and microstructural features. Specifically, crystallographic facets were observed at the fatigue crack initiation sites in near defect-free REC specimens, and volumetric defects were observed in UH ones. Representative *w5* and *w10* 17-4

PH SS fracture surfaces with crystallographic facets at the fatigue crack initiation site are shown in **Figs. 20**(c & f). The appearance of crystallographic facets in the crack initiation site indicates the transition from defect dominated crack initiation to microstructure dominant. This could be due to the smaller population and size of the volumetric defects induced by the REC condition and the presence of δ-Fe in the 17-4 PH SS microstructure, which are known weak points susceptible to fatigue crack initiation [55,151]. The size of δ-Fe in the microstructure was about 8 μm (see **Fig. 14**(c)), which is significantly smaller than the critical volumetric defects whose size ranged from 45 μm to 204 μm for UH 17-4 PH SS specimens. Nevertheless, compared to volumetric defects, the detrimental effect of δ-Fe was lower, which was likely the reason for the longer fatigue lives of REC compared to UH 17-4 PH SS specimens (see **Fig. 16**(b) and **Figs. 17**(c & d)). The detrimental effects of volumetric defects, lying predominantly at/near the notch root, on the fatigue behavior likely shifted the PEEQ-life trends towards shorter fatigue lives, i.e., accelerated crack initiation, for the UH compared to the REC 17-4 PH SS specimens (see **Figs. 19**(a & b)).

The scatter in the fatigue lives of the UH was lower compared to the REC for 17-4 PH SS blunt notched specimens (see **Fig. 16**(b) and **Fig. 17**(d)). In most of the UH 17-4 PH SS specimens, critical crack initiations were from multiple LoF defects (2 or more). Detailed fractography images of UH 17-4 PH SS specimens are shown in **Fig. S6** and **Fig. S7** in the **Suppl. Mater. Section S4**. Such multiple crack initiation in UH 17-4 PH SS specimens was likely due to the presence of populous and large volumetric defects in them (see **Fig. 15**(d)). The presence of multiple fatigue critical defects in the same specimen, resulting in similar criticality on the fatigue behavior, likely caused shorter fatigue lives with lower scatter for the UH specimens compared to the REC ones. This transition to multiple defect-driven crack initiation, mainly from defects at/near the notch root, apparently caused the PEEQ-life trend in **Fig. 19**(b) to have a lower scatter for UH 17-4 PH

SS specimens compared to AlSi10Mg ones; the size and location of volumetric defects in AlSi10Mg vary within a wider range compared to UH 17-4 PH SS specimens (see **Fig. 15**). It is worth noting that, similar to sharp notches (i.e., the *ρ0.1* specimens), fatigue crack initiation mechanisms were not affected by the ligament width. Higher plasticity at the notch root of *w10* specimens than *w5*, likely promoted the crack initiation behavior, irrespective of the initiation sites, leading to early fatigue failure (see **Fig. 17**).

Fractography revealed critical crack initiation sites (both defects and crystallographic facets) in blunt notches to be either near the notch surface or on the adjacent lateral surfaces, for both AlSi10Mg and 17-4 PH SS. Fatigue crack initiation from defects near notch and lateral surfaces have previously been reported for L-PBF 316L SS and Ti-6Al-4V notched specimens [29,152,153]. For further characterization, the size of the critical volumetric defects was quantified using Murakami's $\sqrt{area}$ approach [114]. For internal defects, $\sqrt{area}$ is the square root of the area of the convex hull around the projected shape of the defect on the loading plane, while for sub-surface defects, the convex hull also includes the area between the defect and the free surface. In the case of multiple crack initiating defects, the defect with the largest $\sqrt{area}$ was considered as the critical defect. The size and location (within the cross-section as well as height relative to the notch root plane) of the critical defects in blunt notches, i.e., *w5 ρ5*, *w10 ρ5*, and *w5 ρ50*, are plotted in **Fig. 21** for both materials. All critical volumetric defects lie either on notch or lateral surfaces (side surfaces), as indicated by defects' minimal distances from free surfaces, for both materials, shown in **Fig. 21**(a). The relative height of the crack initiation (h_{center}/h_0, where h_{center} is the distance between the crack initiation site and the notch root plane, and h_0 is the total height of the notch geometry, schematically shown in **Fig. 21**) showed no height dependency for *w5 ρ5*, *w10 ρ5*, and *w5 ρ50* specimens. The mean relative height of crack initiation was near the

notch root plane (see **Figs. 21**(c & d)). Volumetric defects of different sizes at different locations throughout the edges in rectangular cross-section as well as at different relative heights experience different local stress concentrations due to the notch stress field. Details on the notch stress field in specimens with varying notch geometries are shown in **Fig. 22**. Further details on the critical defect sizes in AlSi10Mg and 17-4 PH SS specimens are presented in **Suppl. Mater. Section S4**.

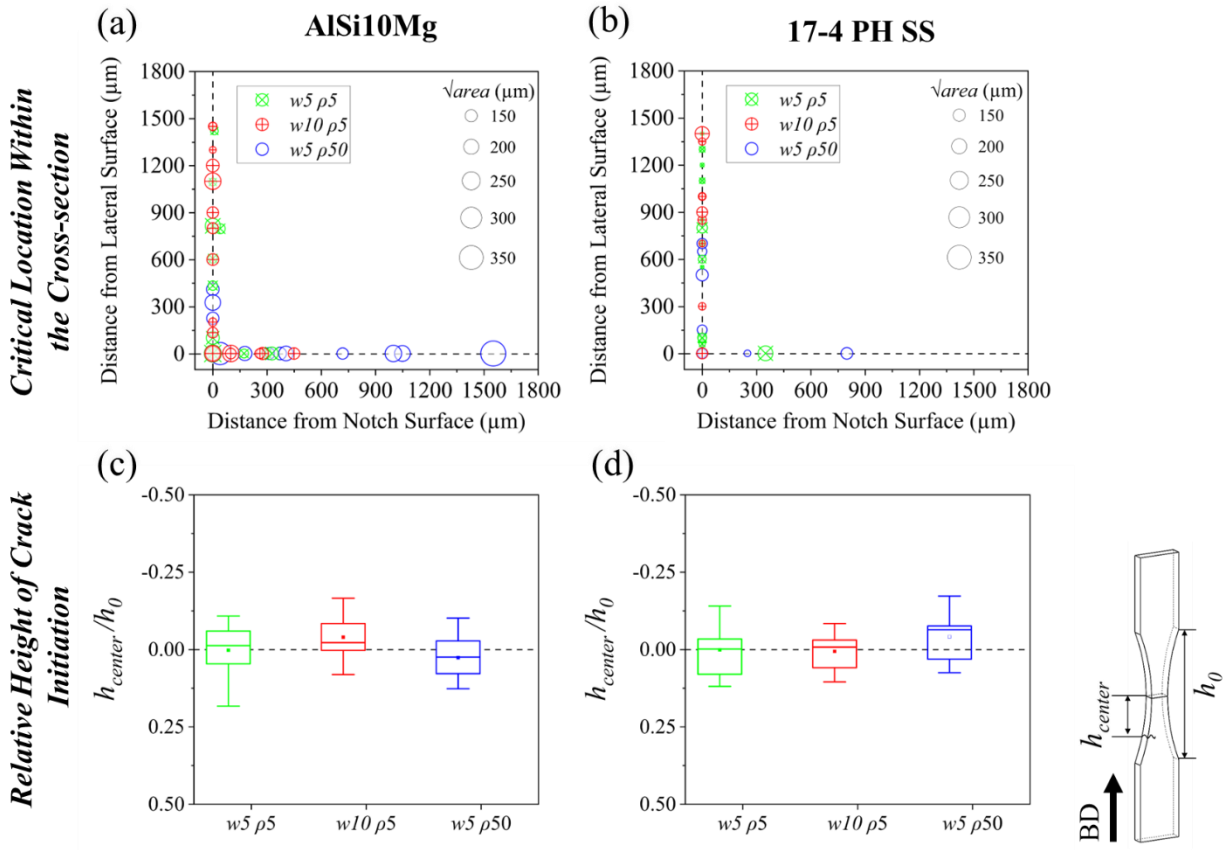

Fig. 21 Plots showing the size and location of the crack initiating volumetric defects in *w5 ρ5*, *w10 ρ5*, and *w5 ρ50* specimens for (a) AlSi10Mg and (b) 17-4 PH SS. The markers are scaled according to the critical defect size, $\sqrt{area}$. Box plots showing the relative height of crack initiation for (c) AlSi10Mg and (d) 17-4 PH SS blunt notched specimens.

3.5.3 Quantifying the synergistic effects of volumetric defects and notch geometry on the fatigue behavior

Linear elastic finite element analysis (LEFEA) was performed using ABAQUS® software to assess the stress concentration near notches. Three-dimensional finite element models were

created for *w5 ρ5*, *w10 ρ5*, and *w5 ρ50* configurations. Details on the methodology used during LEFEA are presented in **Suppl. Mater. Section S5**. For each configuration, the resulting normal stress, σ_{33}, along the loading direction, i.e., X_3, was extracted from seven different heights relative to the notch root plane, h_{center}/h_0. To account for the influence of notch stress fields at critical locations on both notch and lateral surfaces, normal stresses at both center and lateral planes were extracted. The σ_{33} at different relative heights were normalized using the nominal stress at the notch root plane, i.e., $\sigma_{33}/\sigma_0 = \sigma_{33}A/P$, where *A* is the smallest cross-sectional area at the notch root and *P* is the remotely applied load, and presented in **Figs. 22**(a-c) for different notch configurations.

The normal stresses ahead of the notch root for *w10 ρ5* were the highest at the notch root plane, $h_{center}/h_0 = 0$, followed by *w5 ρ5* and *w5 ρ50* configurations. There was a slight difference in the normalized stresses between the center and lateral planes for *w5 ρ5* and *w10 ρ5* configurations. Lateral planes had lower stress compared to the center planes, which was likely due to the plane stress condition experienced by the lateral surface material. For the *w5 ρ50* configuration, the stress concentration was virtually nonexistent, and the normalized stress was near identical for the center and lateral planes (see **Fig. 22**(c)). The normalized stress trend ahead of the notch surface varied among different relative heights. Near the notch root plane, normalized stresses decreased with increasing distance ahead of the notch surface; however, it gradually shifted to an increasing trend for larger relative heights (see **Fig. 22**). The stress concentration factors, K_t, at the notch root for *w10 ρ5*, *w5 ρ5*, and *w5 ρ50* configurations were, respectively, found to be 1.65, 1.33, and 1.03 in the center plane and 1.58, 1.29, and 1.03 in the lateral plane. Mathematical fits for normalized stresses at locations with relative heights, $h_{center}/h_0 \leq 0.3$, for *w5 ρ5*, *w10 ρ5*, and *w5 ρ50* configurations, are provided in **Suppl. Mater. Section S5**.

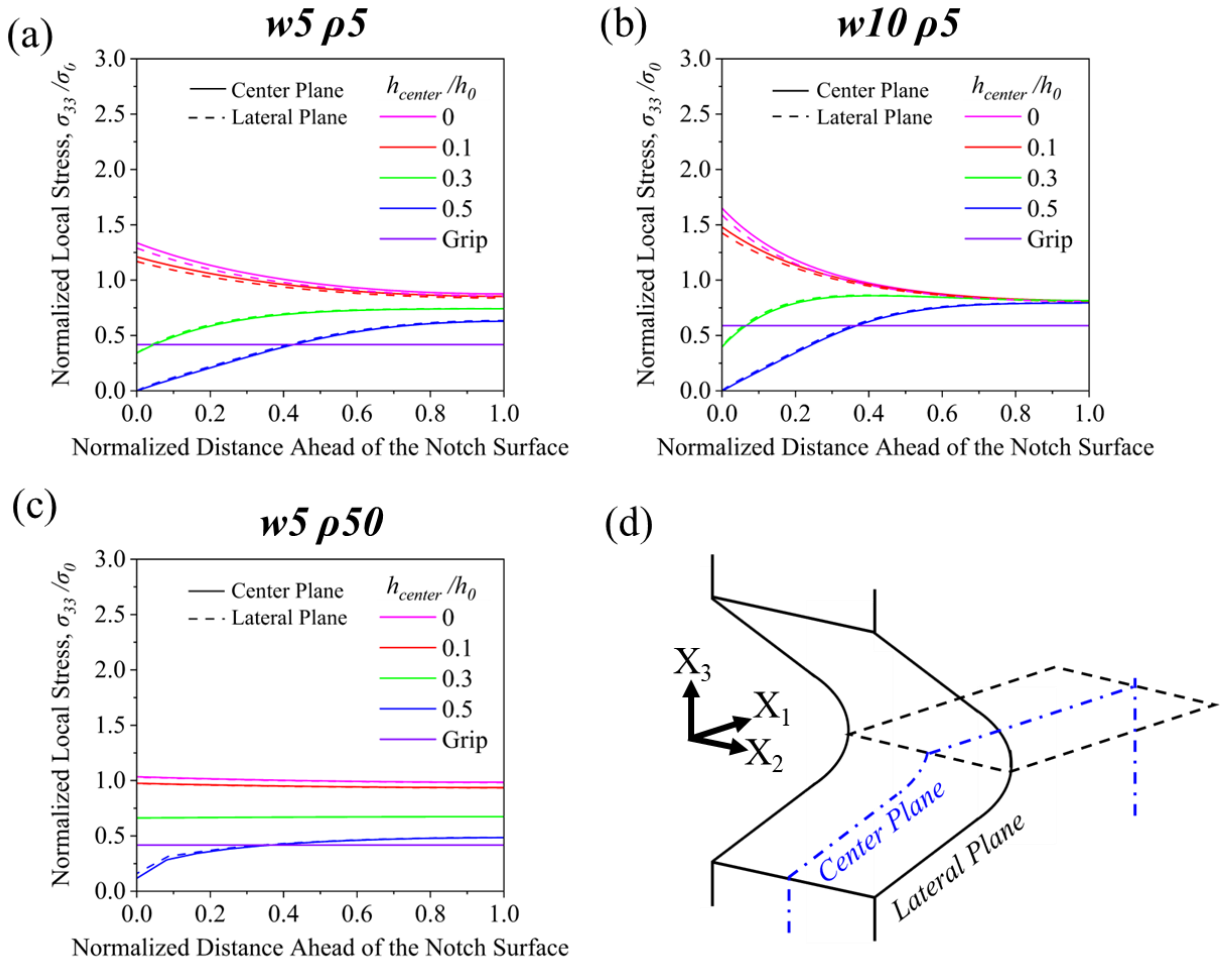

Fig. 22 Normalized stresses at different relative heights and distances ahead of the notch surface in center and lateral planes for (a) *w5 ρ5*, (b) *w10 ρ5*, (c) *w5 ρ50*, configurations. (d) Schematic showing the center and lateral planes in the flat notched specimen.

At the location of each critical crack initiation site, utilizing the results of the LEFEA, the local stress concentration factor, $K_{t(local)}$ shown as σ_{33}/σ_0 in **Fig. 22**, was calculated. **Figure 11** presents the location and size of the critical defects, color-coded in accordance with their $K_{t(local)}$, for *w5 ρ5*, *w10 ρ5*, and *w5 ρ50* AlSi10Mg and 17-4 PH SS specimens. The critical defects with higher $K_{t(local)}$ generally had smaller sizes (see **Fig. 23**). It signified the amplifying effect of the notches on the fatigue criticality of defects (or other crack initiating features), i.e., higher stress

concentration of notches made smaller defects in the vicinity more critical for fatigue crack initiation.

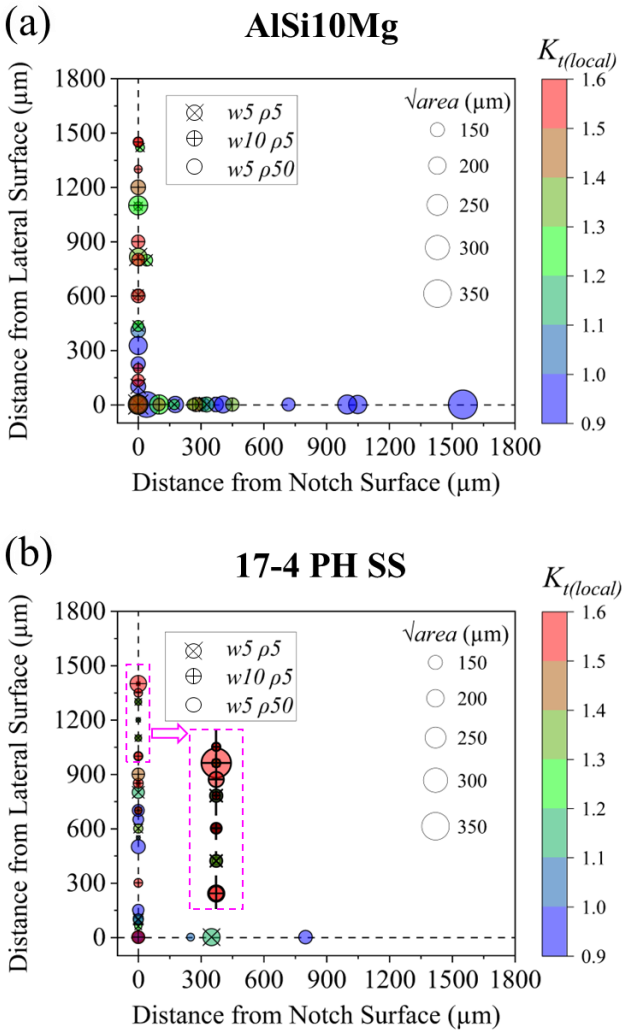

Fig. 23 Plots showing the size and location of critical defects, and the stress concentration they experience in *w5 ρ5*, *w10 ρ5*, and *w5 ρ50* specimens for (a) AlSi10Mg and (b) 17-4 PH SS. The size of the markers is scaled according to the critical defect size, and each marker is color-coded in accordance with $K_{t(local)}$ at the initiation site due to the notch geometry.

The combined/synergistic effects of the influencing factors on the fatigue behavior were quantified by calculating the crack initiating feature's mode-I SIF via linear elastic fracture mechanics (LEFM). Here, the validity of LEFM is established by utilizing EPFEA results, shown in **Fig. 18**, and confirming the presence of minimal or no plasticity at the notch root for the blunt

notched (i.e., *w5 ρ5*, *w10 ρ5*, and *w5 ρ50*) specimens. At the maximum stress levels experienced by the fatigue specimens, the plastic strain at the notch roots of *w5 ρ5* and *w10 ρ5* specimens was less than 0.2% for either material. For *w5 ρ50* specimens, no plasticity was observed. Specifically, for *w5 ρ5*, *w10 ρ5*, and *w5 ρ50* specimens with critical crack initiation from volumetric defects, assuming a defect-crack equivalence, mode-I SIF was calculated using, $K_{I(Max.)} = Y\sigma_{Max.}K_{t(local)}\sqrt{\pi\sqrt{area}}$, where $K_{I(Max.)}$ is the maximum SIF during a loading cycle, *Y* is the Murakami's location-dependent factor (0.65 for surface and 0.5 for internal defects), $\sigma_{Max.}$ is the maximum applied nominal stress, and $K_{t(local)}$ is the local stress concentration factor presented as σ_{33}/σ_0 in **Fig. 22**. Here, $\sqrt{area}$, measured in accordance with Murakami's approach, accounts for the critical defect size, while *Y* and $K_{t(local)}$ account for the location of the critical defect within the rectangular cross-section, the relative height of crack initiation, and the notch geometry.

In the case of critical crack initiation from microstructural features, i.e., for REC *w5 ρ5*, *w10 ρ5*, and *w5 ρ50* 17-4 PH SS specimens with crystallographic facets as the crack initiation site, a similar approach, $K_{I(Max.)} = Y\,\sigma_{Max.}\,K_{t(local)}\,\sqrt{\pi l_M}$, where l_M is the material characteristics length, was used to calculate the mode-I SIF. In the absence of abundant volumetric defects, δ-Fe likely acted as the weak point and led to the formation of microcracks. Considering the ease for micro-cracks to initiate from larger δ-Fe, l_M for 17-4 PH SS was estimated to be 8 µm, i.e., the size of the largest δ-Fe shown in **Fig. 14**(c). This is consistent with the observation made in **Figs. 20**(c & f), where the size of each facet is ~8 µm. In this scenario, $K_{I(Max.)}$ represents the detrimental effect of l_M-sized virtual cracks on the fatigue behavior of *w5 ρ5*, *w10 ρ5*, and *w5 ρ50* 17-4 PH SS specimens. It should be noted that the SIF calculation assumes the presence of a crack in the specimen; however, in specimens with crack initiation from δ-Fe, no such crack is expected to

have existed prior to fatigue loading. It required a certain number of cycles to induce strain localization around δ-Fe and form microcracks leading to the formation of crystallographic facets. As such, the SIF calculated with l_M corresponds to these cracks formed from δ-Fe. The SIF obtained for *w5 ρ5*, *w10 ρ5*, and *w5 ρ50* specimens are presented as marker sizes in the stress-life plots in **Figs. 24**(a & b) and plotted against the experimental fatigue lives in **Figs. 24**(c-f), for AlSi10Mg and 17-4 PH SS.

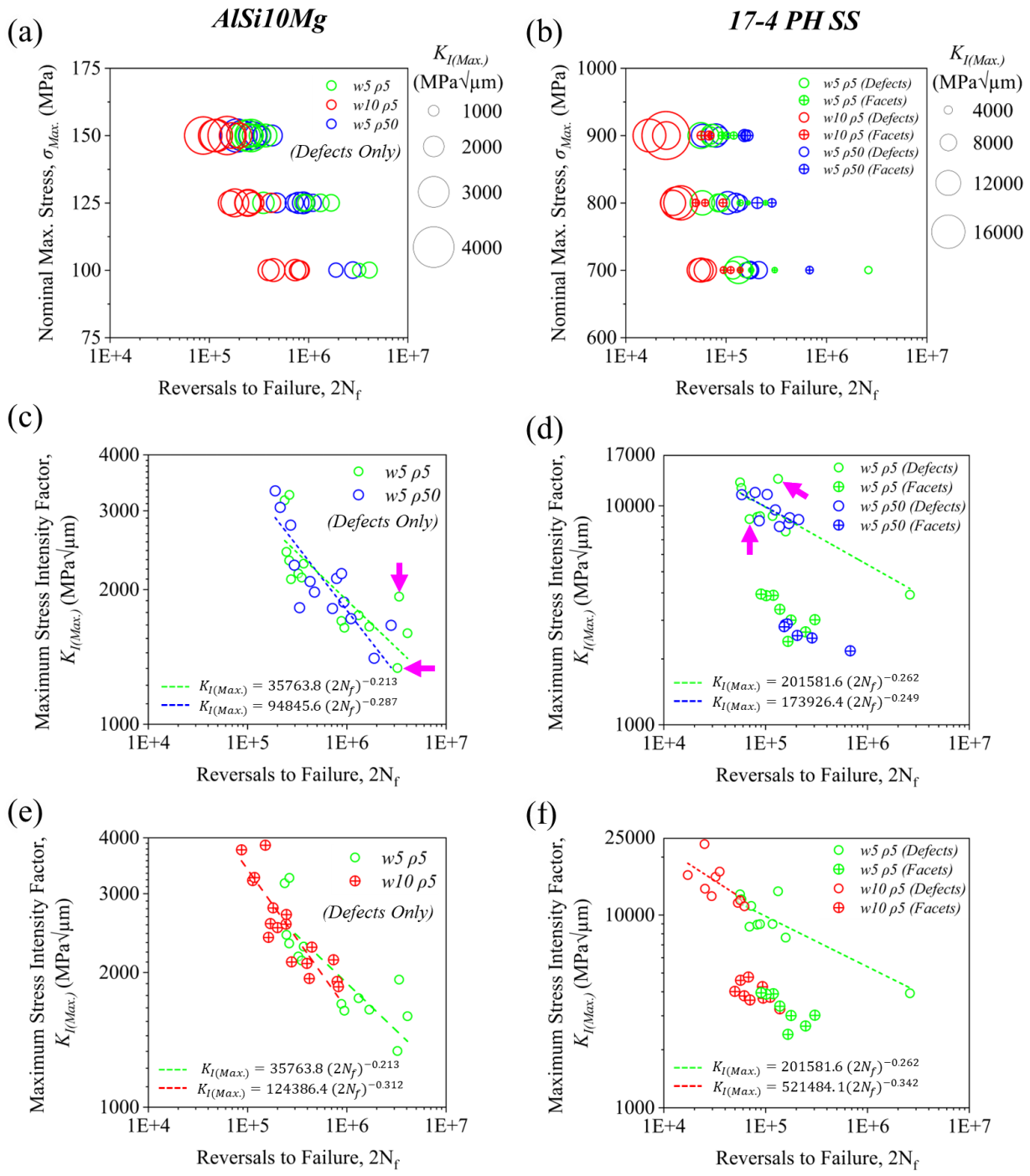

Fig. 24 (a & b) Stress-life fatigue plots with marker sizes scaled according to the SIF of critical features. SIF plotted against the fatigue lives of (c & d) *w5 ρ5* and *w5 ρ50*, and (e & f) *w5 ρ5* and *w10 ρ5* specimens for AlSi10Mg and 17-4 PH SS. Magenta arrows point to those critical defects that are relatively far away from the trend lines in (c & d).

The stress-life plots in **Figs. 24**(a & b) show a decreasing trend for SIF with increasing fatigue lives for both AlSi10Mg and 17-4 PH SS specimens. This trend is especially true at relatively high stress levels, at 150 MPa for AlSi10Mg and 900 MPa for 17-4 PH SS. For a given crack initiation mechanism (either from defects or δ-Fe), *w5 ρ5*, *w10 ρ5*, and *w5 ρ50* specimens showed a consistent SIF-fatigue life trend (see **Figs. 24**(c-f)). For 17-4 PH SS, specimens with crystallographic facets as the crack initiation sites had much lower SIF compared to specimens with crack initiation from equivalent-size volumetric defects at all stress levels. This behavior, suggesting that the δ-Fe has been much more fatigue critical than the volumetric defects of the same size, is evident in the plots in **Figs. 24**(d & f). Power law functions fitted to correlate SIF with the experimental fatigue lives showed a linear trend; fitting functions are presented in the plots shown in **Figs. 24**(c-f). Nevertheless, some scatter was observed in the SIF-life trend for both AlSi10Mg and 17-4 PH SS.

Factors that were not accounted for in the LEFM approach used in this study, such as defect morphology and multiple critical crack initiations, could have influenced fatigue behavior and introduced scatter. The outlying data points in **Figs. 24**(c & d), marked by magenta arrows, were further investigated to identify and confirm the origins of the scatter. For marked data points in **Fig. 24**(c), fractography images show critical defects of varying morphology (see **Figs. 25**(a & b)); however, despite having different SIF, these defects resulted in similar fatigue lives for *ρ5* AlSi10Mg specimens. Branching or arms-like features in the critical defect morphology, shown in **Fig. 25**(b), likely had minimal impact on the fatigue crack initiation, and thus on overall fatigue life [120]. This may have led to an overestimation of its effective defect size measured using Murakami's $\sqrt{area}$ approach, and thus of its SIF. Additionally, for data points marked in **Fig. 24**(d), fractography images show single and multiple crack initiations in *ρ5* 17-4 PH SS specimens

(see **Figs. 13**(c & d)). The specimen shown in **Fig. 25**(d) having multiple crack initiations but with a lower SIF had only half the fatigue life of the specimen shown in **Fig. 25**(c) with a single crack initiation. Multiple crack initiation significantly deteriorated the fatigue lives of notched specimens.

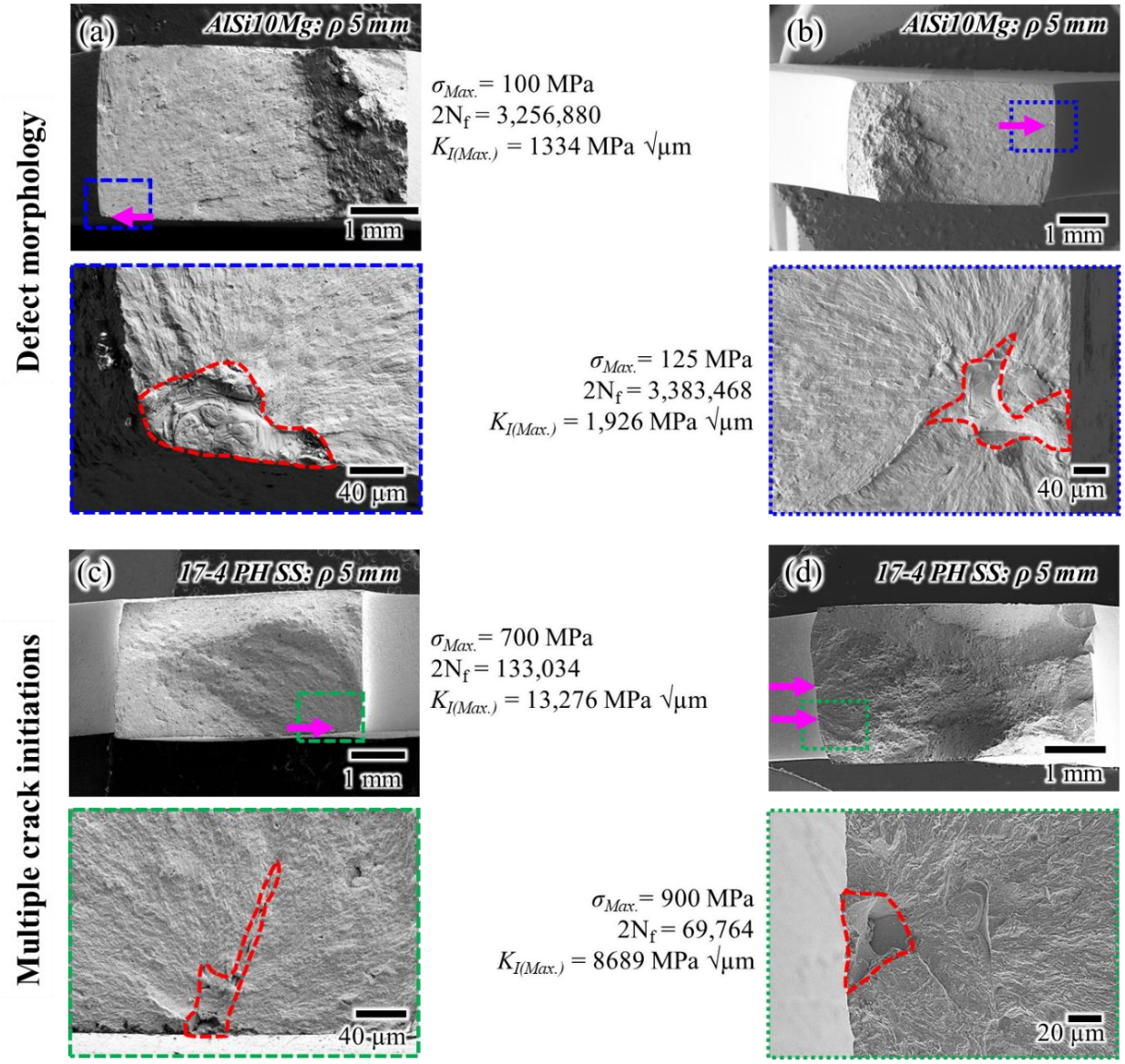

Fig. 25 Fractography images showing (a & b) critical volumetric defects of different morphology and (c & d) multiple crack initiations in AlSi10Mg and 17-4 PH SS flat notched specimens. Magenta arrows point to crack initiating volumetric defects.

3.6 Conclusions

This study investigated the combined effects of edge notches, volumetric defects, and microstructure on the fatigue behavior of additively manufactured AlSi10Mg and 17-4 precipitation hardening (PH) stainless steel (SS). Specimens with varying defect contents, notch root radii, ρ, and ligament widths, w, were subjected to uniaxial fatigue loading. Fracture surfaces were analyzed to investigate the fatigue failure mechanisms and to identify factors influencing the fatigue crack initiation behavior. The combined influence of different factors was quantified and correlated with the experimentally measured fatigue lives of AlSi10Mg and 17-4 PH SS flat notched specimens. The major conclusions derived from this study are listed below.

1. A strong and consistent influence of notch geometry on fatigue crack initiation of *ρ0.1* specimens led to short and low scatter fatigue lives with critical crack initiations from the notch root. Unlike *ρ0.1* specimens, *ρ5* and *ρ50* showed critical crack initiations from localized features, i.e., volumetric defects for AlSi10Mg, and either volumetric defects or delta ferrites (δ-Fe) for 17-4 PH SS.
2. Between *ρ5* and *ρ50* AlSi10Mg specimens, a wide variation in the volumetric defect features resulted in comparable fatigue lives. However, in the case of 17-4 PH SS, for a given crack initiation mechanism (either δ-Fe or defects), *ρ50* clearly showed longer fatigue lives than *ρ5* specimens. This was likely due to similar fatigue criticality of the crack initiation site features, i.e., similar sized δ-Fe or multiple critical volumetric defects, thus revealing the effect of varying notch root radii on the fatigue behavior.
3. Specimens with *w* of 10 mm showed an order of magnitude shorter fatigue lives compared to their 5 mm counterparts. For both *ρ0.1* and *ρ5* specimens, larger *w* accumulated more

cyclic plastic damage at the notch root, which accelerated fatigue crack initiation and led to shorter fatigue lives.

4. For *ρ0.1* specimens with significant plasticity at the notch root, equivalent plastic strain correlated well with the experimental fatigue lives of *w5* and *w10* specimens for both AlSi10Mg and 17-4 PH SS.
5. For *ρ5* and *ρ50* specimens with minimal plasticity at the notch root, the mode-I stress intensity factor calculated using linear elastic fracture mechanics quantified the synergistic effects of notch geometry and defect/microstructural features on the fatigue behavior. SIF correlated well with the experimental fatigue lives as well as defect-related fatigue lives of *w5 ρ5*, *w10 ρ5*, and *w5 ρ50* specimens for both AlSi10Mg and 17-4 PH SS.

This study identified the primary factors influencing the fatigue behavior, especially crack initiation behavior, of flat, edge-notched specimens with varying notch root radii and ligament widths. The understanding of the notch fatigue behavior obtained in this study is useful in assessing the criticalities posed by volumetric defect features, microstructural features, and notch geometries on the fatigue behavior of complex AM parts with notches inducing different levels of plasticity at the notch root.

4 Fatigue Criticality Assessment of Volumetric Defects in Notched Specimens: A Non-destructive Approach

4.1 Abstract

This study utilizes linear elastic fracture mechanics to assess fatigue criticality of volumetric defects in notched specimens with varying geometries. Contrasting to the existing literature, this study assesses the fatigue criticality of defects, prior to fracture, via a non-destructive inspection technique, i.e., X-ray computed tomography (XCT). Treating volumetric defects as cracks, based on Murakami's definition, the approach calculates their Mode-I stress intensity factor (SIF) with their local stresses obtained via linear elastic finite element analysis, and utilizes the SIF to represent their criticality. For validation, cylindrical and flat specimens with notch root radii of 5 mm and 50 mm of AlSi10Mg and 17-4 precipitation hardened stainless steel were fabricated, XCT scanned, and tested under fatigue loading. All crack initiating defects, observed from fractography, fell within the 99.3 percentile of the defects with the highest stress intensity factor in the respective specimens.

Keywords:
Additive manufacturing; Defect criticality; Non-destructive inspection/testing/evaluation (NDI/NDT/NDE); X-ray computed tomography (XCT); Fatigue

4.2 Introduction

Additive manufacturing (AM) processes, such as laser powder bed fusion (L-PBF), are prone to induce volumetric defects in parts, which act as stress concentrators and often are fatigue-critical in surface machined condition [8,140,154,155]. Variation in the defects' geometrical features resulting from slight perturbations in processing conditions can lead to significant scatter in fatigue lives, often well beyond two orders of magnitude in the high cycle fatigue regime [149,156,157]. This suggests that defect content, thus the material properties, can significantly vary from coupons to parts and from one part to another [158–160]. The uncertainties associated with such variations can not only make quantifying defects' critical effects on part's fatigue behavior difficult but also render the conventional, process-lockdown based qualification approaches impractical [161,162]. These challenges are further exacerbated by AM's ability to fabricate geometrically complex parts, which often comprise an abundance of notch-like features [52,141,163,164]. The stress concentration of these features interacts with that of the volumetric defects to potentially accelerate fatigue crack initiation [52,165–168]. Since such an acceleration only affects the defects present in the vicinity of notches, the uncertainty in the fatigue performance of AM parts can be further increased.

The uncertainty of defect content in critical locations of AM parts can be ascertained, at least partially, by the application of an effective non-destructive inspection (NDI) technique, such as X-ray computed tomography (XCT) [169–173]. For instance, modern high-resolution XCT systems can reliably reveal the geometry, size, and spatial distributions of volumetric defects larger than 20 μm in a reasonably sized notch specimen (i.e., a diameter of 5 mm) made of relatively dense material (i.e., 17-4 PH stainless steel (SS)) [170,174,175]. Nevertheless, due to the complex interplay between the stress fields of notches and volumetric defects, quantifying the critical

effects of volumetric defects in the presence of notches remains elusive. Specifically, due to the presence of a decaying stress field away from the notch roots, the existing approaches for notch free members [149,176–179] that categorize defects into internal/surface ones and calculate their stress intensity factors in each category assuming a uniform stress may not be directly applicable.

This study utilizes linear elastic fracture mechanics (LEFM) to assess the fatigue criticality of volumetric defects detected via an NDI technique, i.e., XCT, for the qualification of AM parts. The existing literature utilizes the LEFM approach, such as Murakami's $\sqrt{area}$ approach, to measure the post-fracture critical defect's size and its equivalent SIF [40,48]. Contrasting to the literature, this work assesses the fatigue criticality of defects using a non-destructive technique, enabling the identification of potentially critical defects prior to destructive analysis. Furthermore, this study performed such fatigue criticality assessments for complex AM parts; these parts have different geometry notches in them. In this study, the NDI-based approach relies on XCT to quantify the content of volumetric defects in a part, and finite element method performed on part's computer aided design (CAD) model to analyze the local stress environment of each defect. By treating each defect as a crack equivalent, a defect's criticality is represented by its Mode-I stress intensity factor (SIF) calculated via Murakami's approach, accounting for the local stress. This approach is then validated on two types of notched fatigue specimens (cylindrical and flat) with two notch root radii (5 mm and 50 mm) made of both AlSi10Mg and 17-4 PH SS. For validation, the critical crack initiating defect was identified using fractography for each specimen, matched with the one detected from XCT, and its corresponding SIF, calculated using the NDI-based approach, was compared with the others in the same specimen.

4.3 Method and materials

The procedure to quantify the fatigue criticality of volumetric defects in notched specimens is illustrated in **Fig. 26**. First, the notched specimens were scanned using an XCT technique to extract the volumetric defects' information such as their sizes and locations. To extract defect information, the tomography data was processed to obtain greyscale images, followed by gradient and binary operations, to isolate the defect boundary from the surrounding matrix, as shown in **Fig. 27**(a-c). The boundary filled binarized defect morphology, shown in **Fig. 27**(d), was processed using MATLAB to extract the necessary defect information. Note that this approach slightly overestimates the sizes of the detected volumetric defects. Second, the local stresses at different locations within the notched specimens were quantified using linear elastic finite element analysis (LEFEA).

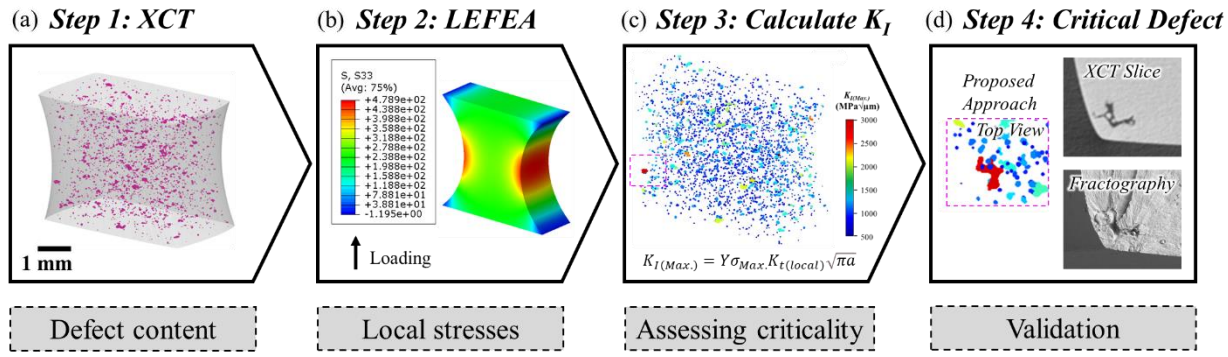

Fig. 26 Diagram showing different steps to quantify the fatigue criticality of volumetric defects in notched specimens: (a) Defect content quantified via XCT, (b) local stresses analyzed via LEFEA, (c) SIF calculated using LEFM, and (d) validation performed using fractography.

LEFEA was performed using ABAQUS® software for ρ *5 mm* and ρ *50 mm* cylindrical and flat specimens. It is worth mentioning that the finite element (FE) models and the specimens used for validation had similar geometries. For cylindrical specimens, two-dimensional axisymmetric FE models were created (see **Fig. 28**(a)). For flat specimens, one-eighth of the full models were created, assuming symmetric boundary conditions in all three planes, i.e., X_1-X_2, X_1-

X_3, and X_2-X_3, as shown in **Fig. 28**(b). The FE models for cylindrical specimens were meshed using CAX6M, 6-node modified quadratic axisymmetric triangle elements, while C3D10, 10-node quadratic tetrahedron elements, were used for flat specimens. For each model, a mesh convergence study was performed, resulting in the smallest element size of ~0.5 μm at the notch root. The converged meshes for each of the FE models are presented in **Figs. 28**(c-f). A remote displacement of 100 μm was applied, as indicated using black arrows in **Figs. 28**(c-f). The resulting normal stresses, along the loading direction, σ_{33}, were extracted from seven different heights relative to the notch root plane, i.e., h_{center}/h_0, where h_{center} is the distance of the crack initiation site from the notch root plane and h_0 is the total height of the notch geometry, schematically shown in **Fig. 28**(g). For flat specimens, normal stresses from both center and lateral planes (schematically shown in **Fig. 28**(h)) were extracted. The extracted normal stresses, σ_{33}, were normalized using the nominal stress, σ_0, at the notch root plane to obtain the local stress concentration factor, i.e., $K_{t(local)} = \sigma_{33}/\sigma_0$.

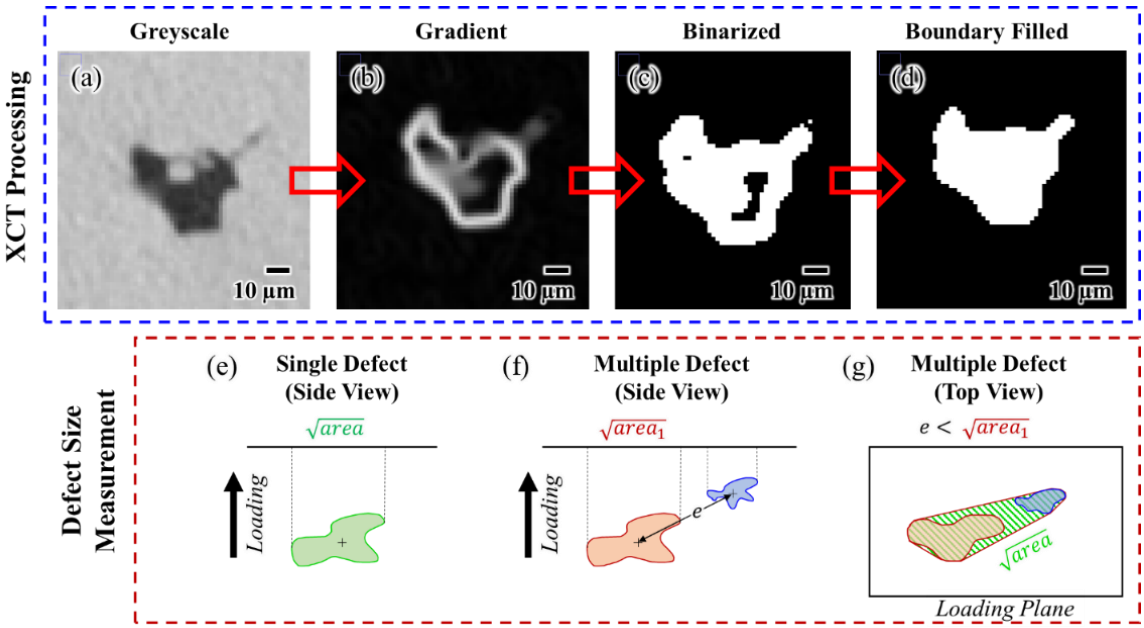

Fig. 27 Different stages of XCT data post-processing: (a) greyscale, (b) gradient, (c) binarized, and (d) boundary filled. Schematic illustration of defect size measurement in the case of (e) single and (f, g) multiple (two) nearby defects.

Third, Mode-I SIF for every volumetric defect within the XCT scan volume was calculated using LEFM, i.e., Murakami's approach. Assuming a defect-crack equivalency, the Mode-I SIF for a volumetric defect under the intended cyclic loading was calculated using:

$$K_{I(Max.)} = Y\sigma_{Max.}K_{t(local)}\sqrt{\pi\sqrt{area}}\,, \tag{1}$$

where $K_{I(Max.)}$ is the maximum Mode-I SIF during a loading cycle, Y is Murakami's location-dependent factor (0.5 for internal and 0.65 for surface defects [180]), $\sigma_{Max.}$ is the maximum applied nominal stress, $K_{t(local)}$ is the local stress concentration factor at the defect's location [181,182], and $\sqrt{area}$ is the defect size. During XCT processing, the defect's size was measured in accordance with Murakami's approach, i.e., the square root of the area of a convex hull around the projected shape of the defect onto the loading plane [15]. Additionally, the combined influence of a cluster of defects on the fatigue behavior was accounted for by calculating the $\sqrt{area}$ of the

convex hull surrounding the cluster, again based on Murakami's approach. For any defect, if the centroidal distance to its smaller neighbor is less than its own size, then the neighbor is included in the cluster with the defect as schematically shown in **Figs. 2**(f & g). Note that, for a cluster, the calculated SIF was assigned to all of its defects. The obtained SIF was used to represent the fatigue criticality of volumetric defects in notched specimens (see **Fig. 26**(c)), i.e., defects with higher SIF were assumed to possess higher probability to initiate fatigue cracks. Finally, validation of the approach was performed by comparing the top ranked defects having the highest SIF with the ones observed via fractography (see **Fig. 26**(d)).

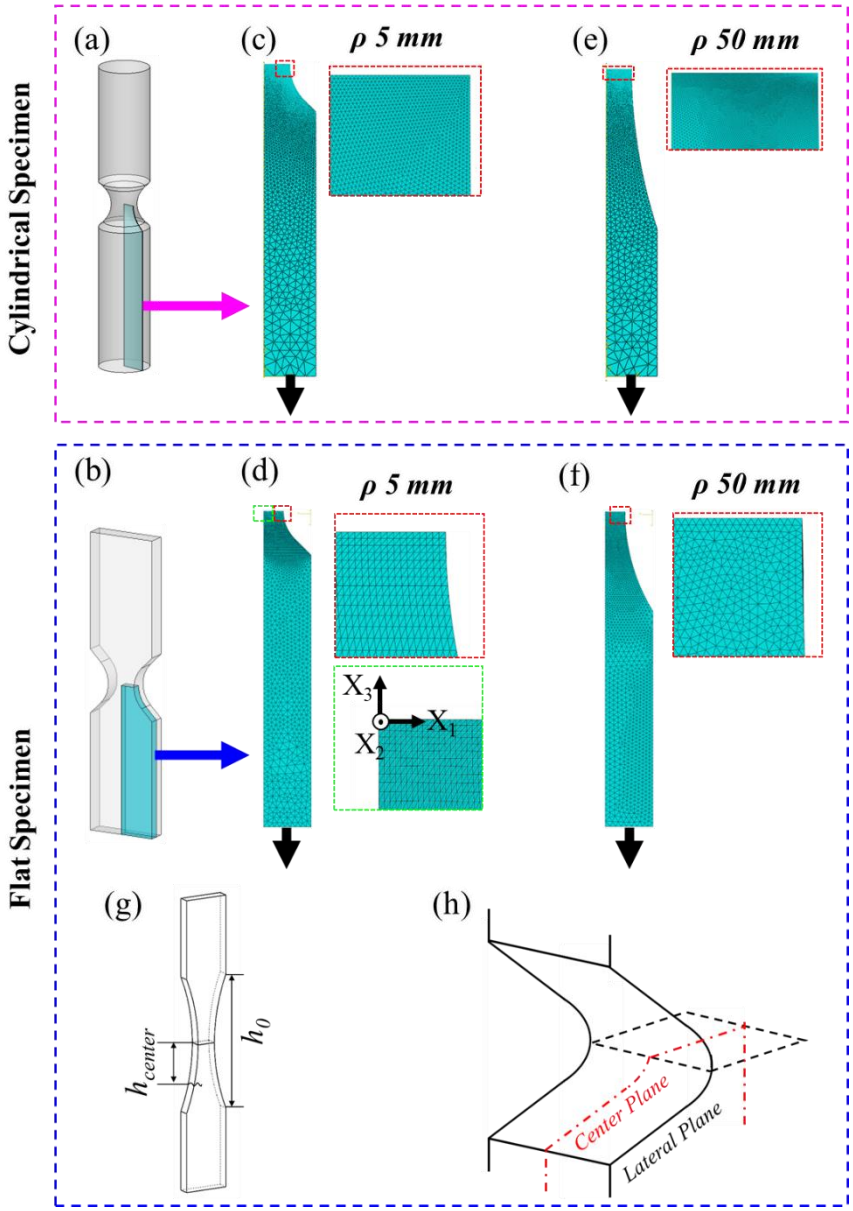

Fig. 28 (a, b) Geometries and FE meshes for (c, d) *ρ 5 mm* and (e, f) *ρ 50 mm* cylindrical and flat notched specimens. Schematics showing (g) relative height of crack initiation (h_{center}/h_0), and (h) center and lateral planes in the flat specimen.

The procedure illustrated in **Fig. 26** was applied to the notched fatigue specimens fabricated and tested for some earlier works [181,182], which included both flat and cylindrical ones with different notch root radii and were made from both AlSi10Mg and 17-4 PH SS. The cylindrical and flat specimens (whose geometries are shown in **Fig. 29**) were machined, respectively, from bars and rectangular blocks fabricated from two different L-PBF machines, and

their axial directions were aligned with the build directions. AlSi10Mg was fabricated using Renishaw RenAM 500Q Flex, and 17-4 PH SS using 3D SYSTEMS DMP Flex 350B. To vary the defect content within notched specimens, both the manufacturer recommended process parameters (referred to as the R specimens) and the modified ones to induce underheated condition (referred to as the U specimens) were used for fabrication.

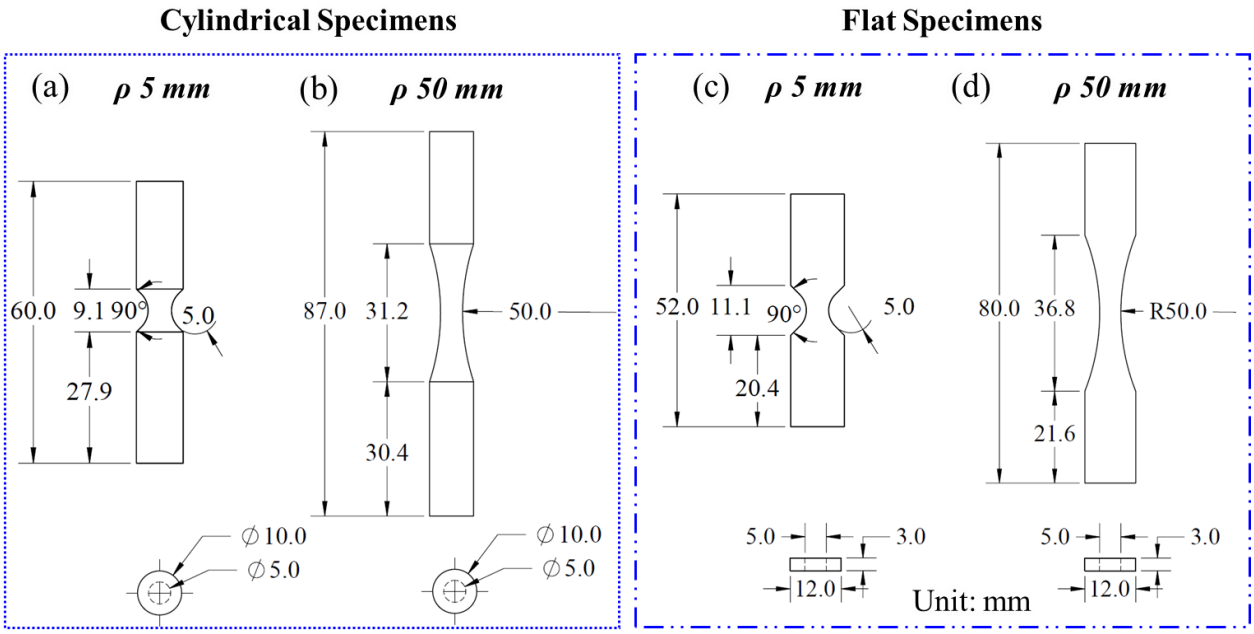

Fig. 29 Geometries and dimensions of (a, b) cylindrical and (c, d) flat notched specimens with notch root radii of 5 mm and 50 mm.

Prior to machining, AlSi10Mg parts were stress-relieved (SR) at 285 °C for 2 hours in accordance with AMS 2771 standard [103], while 17-4 PH SS parts were SR at 700 °C for an hour, followed by CA-H1025, in accordance with ASTM A693 standard [104]. For convenience, specimens with notch root radii of 5 mm and 50 mm will be referred to as *ρ 5 mm* and *ρ 50 mm* in the remaining sections of this article. After machining, the specimens were ground and polished using sandpapers with grits ranging from P240 to P1200. These specimens were scanned using an XCT technique on a ZEISS Xradia 620 Versa machine with a voxel size of 6.5 µm. To avoid false detection from noise, any defects/features smaller than 20 µm were not considered for analysis.

The notched specimens were subjected to force-controlled fatigue tests and after failure, fractography was performed to identify the crack initiating defect. AlSi10Mg specimens were subjected to maximum nominal stresses ranging from 100 to 150 MPa, and 17-4 PH SS from 800 to 1200 MPa at a stress ratio of 0.1. Considering sixteen different configurations, i.e., 2 materials × 2 fabrication conditions × 4 notch geometries, 32 specimens (2 per configuration) were analyzed and tested. Out of 32 specimens, 15 specimens showed fatigue crack initiation from volumetric defects within the scan volume. The remaining specimens either showed crack initiation from microstructural features, defects outside the scan volume, or reached run-out during fatigue testing.

4.4 Results and discussion

4.4.1 Local stress concentrations in cylindrical and flat notched specimens

The local stress concentration factors, $K_{t(local)}$, for ρ *5 mm* and ρ *50 mm* cylindrical and flat notched specimens, obtained via LEFEA, are plotted against the normalized distance ahead of the notch surface, i.e., l/l_0, where l is the distance ahead of the notch surface and l_0 is the distance from the notch surface to the symmetric axis, in **Fig. 30**. For both cylindrical and flat specimens, ρ *5 mm* showed higher stress concentration factor compared to ρ *50 mm*, at the notch root. Ahead of the notch root, $K_{t(local)}$ for ρ *5 mm* decreased at a higher rate compared to ρ *50 mm* (see **Fig. 30**), indicating a higher rate of stress field decay in sharper notches. Due to the variation in the notch stress field, the $K_{t(local)}$ trends ahead of the notch surface shifted from a decreasing trend, near the notch root plane, to an increasing trend at higher relative heights (h_{center}/h_0), especially for ρ *5 mm* specimens. For flat specimens, ρ *5 mm* showed slightly lower $K_{t(local)}$ at the lateral plane compared to the center plane, likely due to the influence of plane stress condition in the lateral free surfaces. For ρ *50 mm*, $K_{t(local)}$ in both center and lateral planes were near identical

(see **Fig. 30**(c)). The $K_{t(local)}$, presented in **Figs. 30**(a-c), was utilized to calculate the SIF of volumetric defects at different locations within the notched specimens, using Eq. 1.

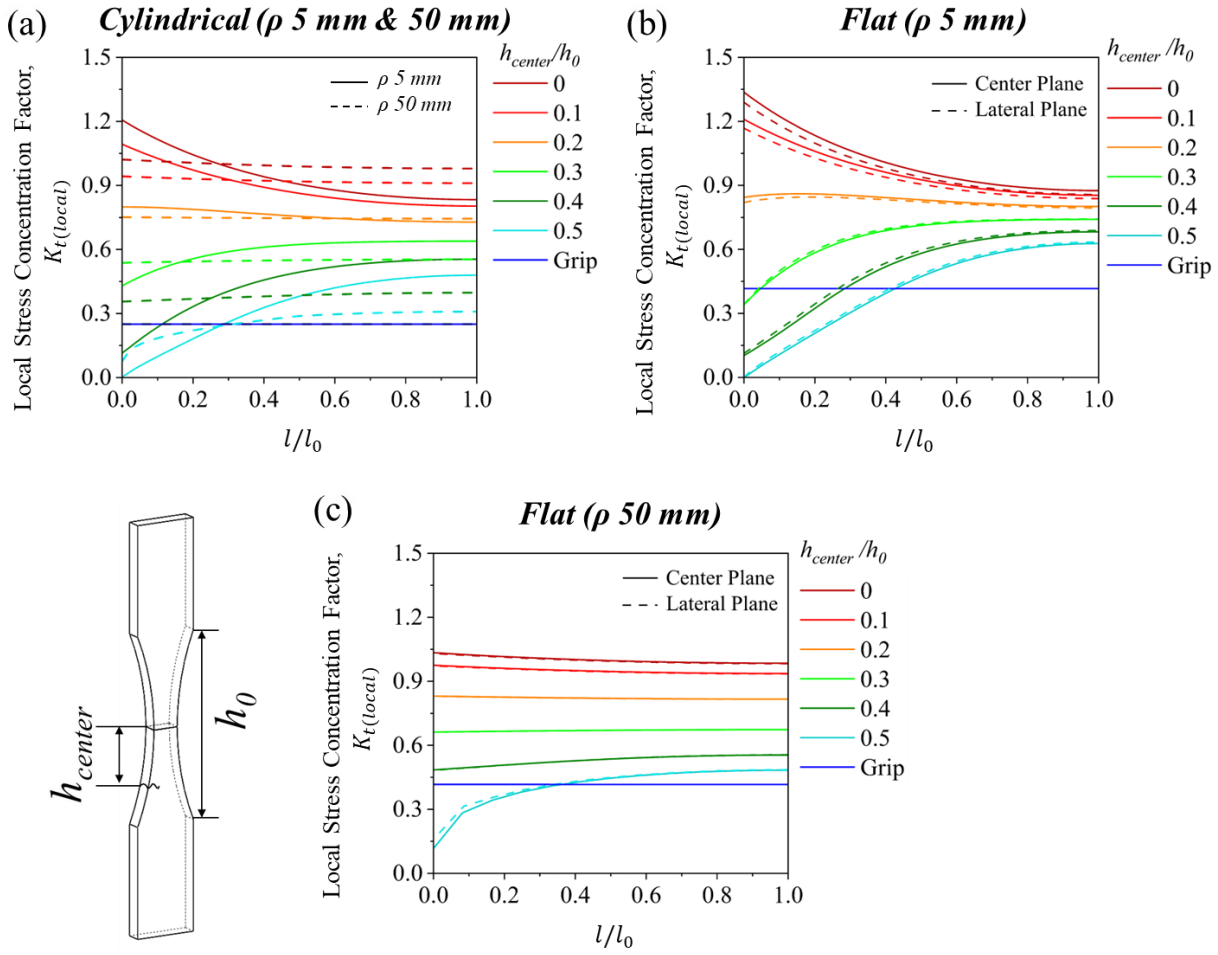

Fig. 30 Local stress concentration factors at different heights relative to the notch root plane and distances away from the notch surface, for *ρ 5 mm* and *ρ 50 mm* (a) cylindrical and (b, c) flat notched specimens.

4.4.2 Effectiveness of the NDI-based approach

Based on the SIF calculated according to the procedure outlined in **Fig. 26**, the fatigue criticality of volumetric defects within AlSi10Mg and 17-4 PH SS notched specimens could be quantitatively represented. To be exact, the SIF should signify the tendency of a volumetric defect to initiate a fatigue crack, e.g., the defect with the highest SIF in a specimen should be responsible for the initiation of the fatigue failure. Realizing this, the efficacy of the utilized NDI-based

approach can be validated by comparing top ranked defects from the XCT analysis with the fatigue critical defects identified from fractography after fatigue tests. The critical defects within the XCT scan volume were identified by utilizing their location information (both in and out of the fracture plane) obtained from the fractured specimens.

Fig. 31 demonstrates the efficacy of the NDI-based approach using *ρ 5 mm* and *ρ 50 mm* AlSi10Mg cylindrical notched specimens that were subjected to 125 MPa and 150 MPa maximum nominal stresses as examples. Implementing the procedure outlined in **Fig. 26**, SIF for all volumetric defects within the scan volumes were calculated and visualized in **Figs. 31**(a & b). Furthermore, the defects with the highest SIF were identified (pointed using arrows in greyscale images in **Figs. 31**(c & d)) and compared to the critical defects in the fracture surface of the respective specimens, **Figs. 31**(e & f). Volumetric defects with the highest SIF were found to initiate critical fatigue cracks in both *ρ 5 mm* and *ρ 50 mm* AlSi10Mg specimens. Interestingly, the two crack initiating defects in both *ρ 5 mm* and *ρ 50 mm* (see **Figs. 31**(e & f)) had the highest and the second highest SIF among all defects within the specimen.

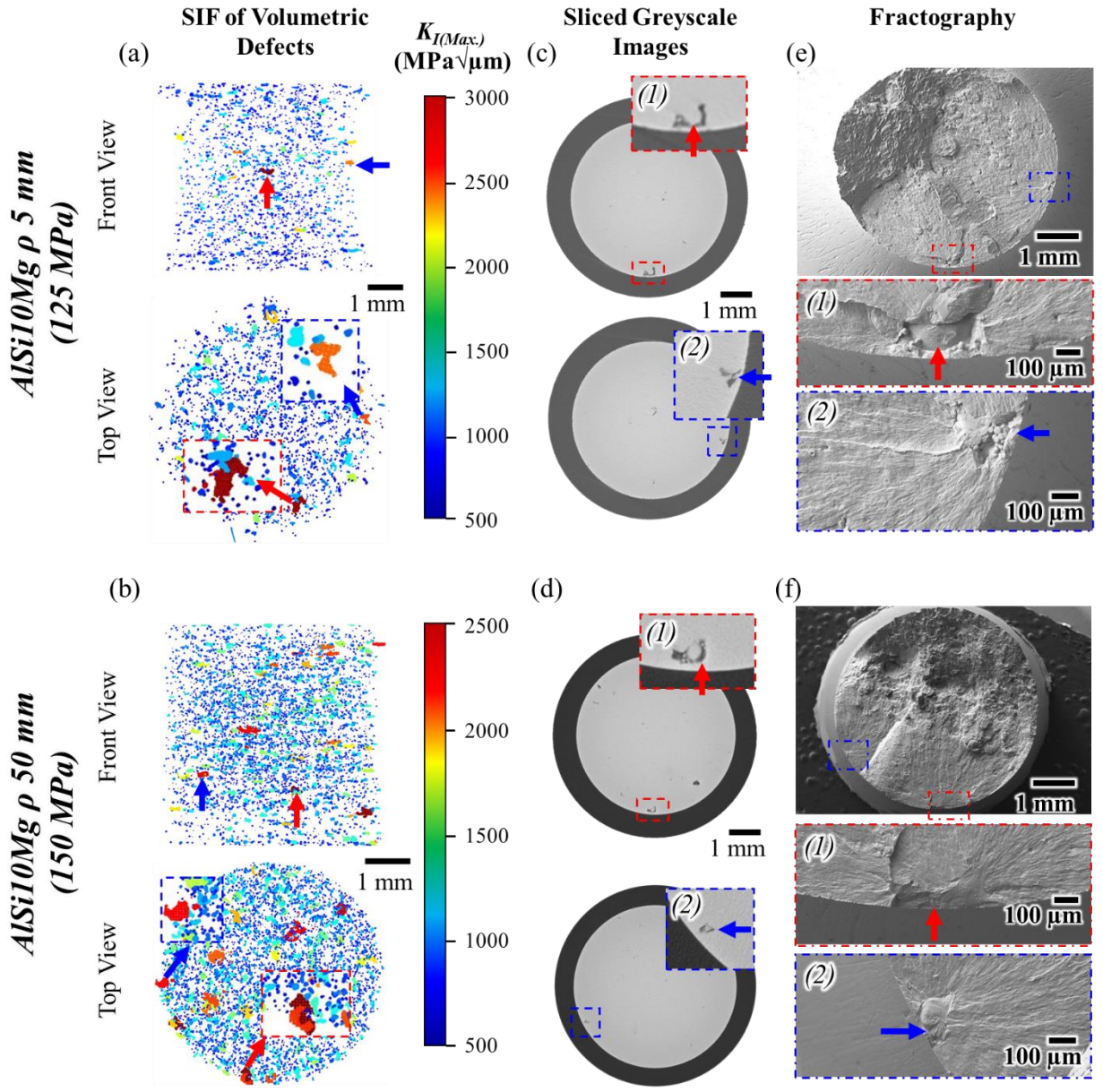

Fig. 31 (a, b) Visualization of volumetric defects, colored according to their SIF, within the XCT scan volume, (c, d) sliced greyscale images showing the critical defects, and (e, f) fractography images showing the fatigue crack initiation sites in *ρ 5 mm* and *ρ 50 mm* AlSi10Mg cylindrical specimens.

Similarly, **Fig. 32** shows additional examples demonstrating the efficacy of the NDI-based approach using *ρ 5 mm* and *ρ 50 mm* AlSi10Mg flat notched specimens subjected to 150 MPa and 125 MPa maximum nominal stresses. Fractography images show the presence of critical defects at the corner and the faces of notches for *ρ 5 mm* and *ρ 50 mm* specimens, respectively (see **Figs.**

32(e & f)). The critical defect that initiated the crack and caused fatigue failure had the highest SIF among all defects for both *ρ 5 mm* and *ρ 50 mm* flat notched specimens. In addition to what's shown in **Fig. 32**, fatigue cracks were also found, in other specimens, to initiate from lateral surfaces, i.e., the flat side surfaces. Given the lesser degree of stress concentration, the crack initiating defects from lateral surfaces were typically larger. Regardless, the approach was robust enough to address the complex stress environment imposed by the flat notched specimens. Similar confirmation on the efficacy of the NDI-based approach using cylindrical and flat 17-4 PH SS notched specimens was obtained, as shown in **Fig. 33**.

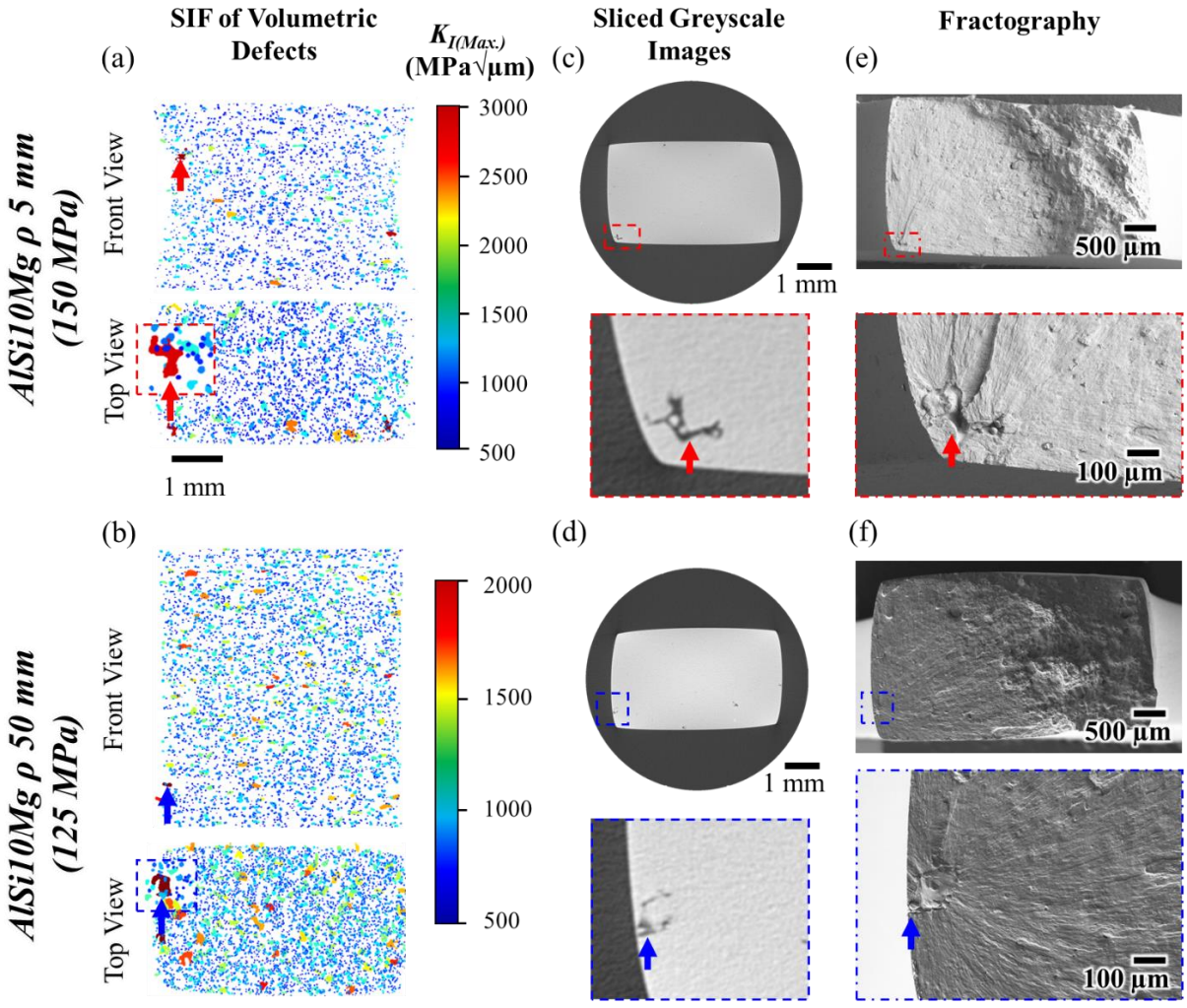

Fig. 32 (a, b) Visualization of volumetric defects, colored according to their SIF, within the XCT scan volume, (c, d) sliced greyscale images showing the critical defects, and (e, f) fractography

images showing the fatigue crack initiation sites in *ρ 5 mm* and *ρ 50 mm* AlSi10Mg flat notched specimens.

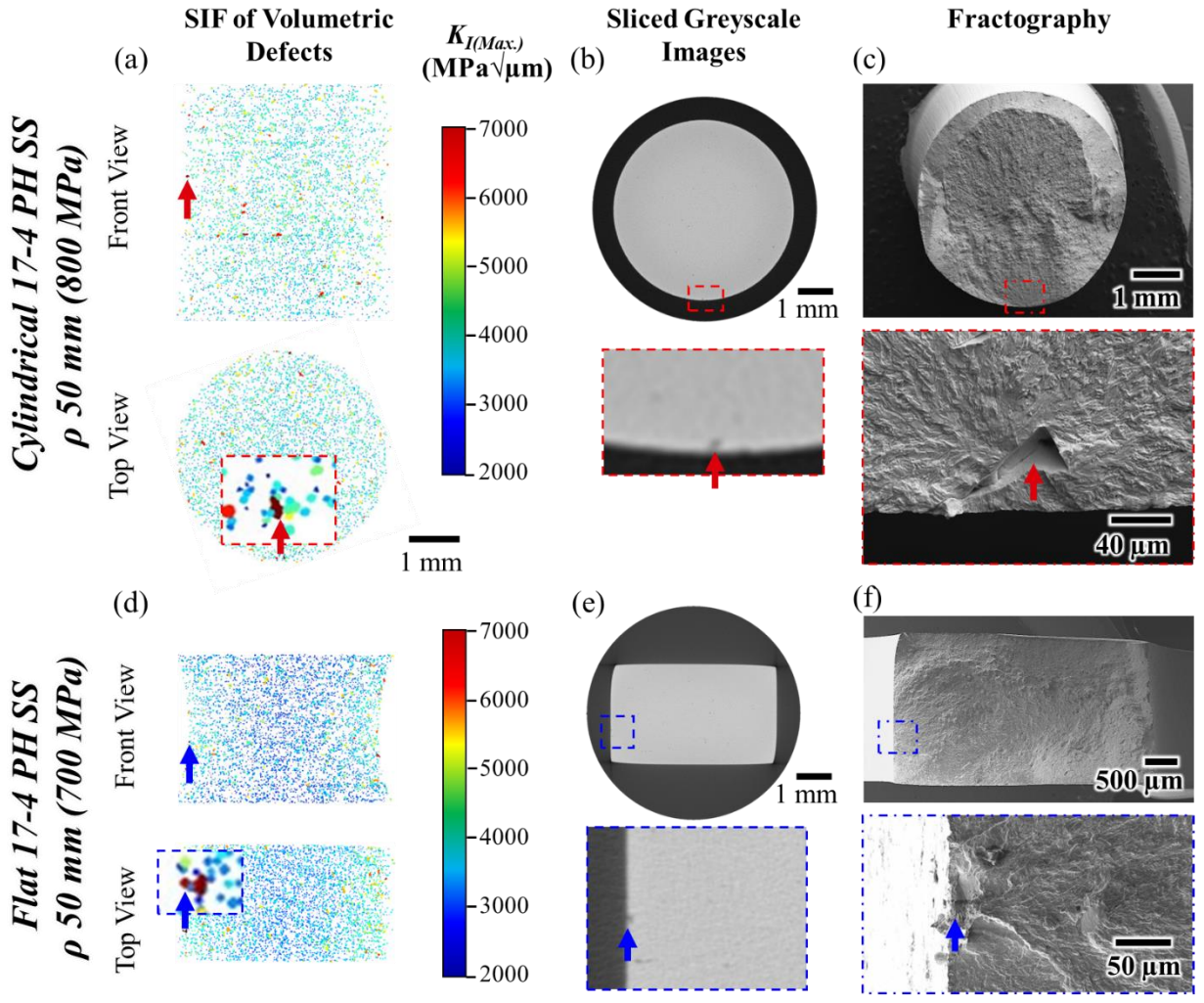

Fig. 33 (a, b) Visualization of volumetric defects, colored according to their SIF, within the XCT scan volume, (c, d) sliced greyscale images showing the critical defects, and (e, f) fractography images showing the fatigue crack initiation sites in cylindrical *ρ 50 mm* and flat *ρ 5 mm* 17-4 PH SS specimens.

Overall, the NDI-based approach performed well in assessing the fatigue criticality of volumetric defects in notched specimens. **Table 9** lists the information of all 17 fatigue critical defects observed in this study (i.e., from the 15 specimens that experienced fatigue crack initiation from volumetric defects) including their size measured via both XCT and fractography, normalized SIF (calculated with size measured via XCT), and the corresponding rankings in SIF among other

defects in the same specimens. For completeness, the details of the specimens including the material, the geometry type, and the notch root radius are also provided. It is worth mentioning that the critical defect size obtained via fractography was measured in accordance with Murakami's $\sqrt{area}$ approach. All crack initiating defects were found to be within the 99.3 percentile of the defects with the highest stress intensity factor in the respective notched specimens. Additionally, the NDI-based approach showed critical defects in ten specimens out of fifteen to have the top rank, i.e., the highest SIF according to Eq. (1), among all other defects in the respective notched specimens.

Table 9 Information of all 17 fatigue critical defects observed in this study including their sizes measured via both XCT and fractography, normalized SIF, and absolute and relative ranking of critical defects in accordance with their SIF within the respective notched specimens as well as the details of the specimens. It should be noted that the critical defects' information is shown in the increasing order of critical defect sizes (i.e., 1st column) for both materials.

Size via XCT (µm)	Size via fractography (µm)	$K_{I(Max.)}/\sigma_{Max.}$	Abs. rank of critical defects	Relative rank of critical defects (%ile)	Specimen (Crack initiation site) ID	Material	Specimen geometry	ρ (mm)
28	19	6.0	1	99.320	1	17-4 PH SS	Cylindrical	50
45	24	5.9	1	99.457	2	17-4 PH SS	Cylindrical	50
54	50	25.4	1	99.978	3	17-4 PH SS	Flat	5
83	62	12.1	1	99.985	4	17-4 PH SS	Cylindrical	5
98	58	12.9	1	99.989	5	17-4 PH SS	Cylindrical	5
154	79	16.9	17	99.574	6	AlSi10Mg	Flat	5
162	113	14.0	15	99.423	7	AlSi10Mg	Cylindrical	50
179	114	15.6	18	99.377	8	AlSi10Mg	Cylindrical	5
200	149	16.3	1	99.976	9	AlSi10Mg	Flat	50
201	149	19.3	2	99.918	10	AlSi10Mg	Flat	5
222	181	17.5	1	99.973	11	AlSi10Mg	Flat	50
251	186	17.8	14	99.405	12	AlSi10Mg	Flat	50
257	141	21.8	1	99.965	13	AlSi10Mg	Flat	5
291	187	21.6	1	99.952	14 (Site 1)	AlSi10Mg	Cylindrical	5

346	244	25.4	1	99.952	14 (Site 2)	AlSi10Mg	Cylindrical	5
371	140	20.9	1	99.979	15 (Site 1)	AlSi10Mg	Cylindrical	50
377	194	20.7	1	99.979	15 (Site 2)	AlSi10Mg	Cylindrical	50

The SIF of the top rank defects, obtained utilizing the NDI-based approach and XCT data, were compared with the SIF of the experimentally observed fatigue critical defects from fractography, using Gumbel's largest extreme value statistics (LEVS). The SIF of the fatigue critical defects were calculated using Eq. (1) but with two different measures of size, namely via fractography and XCT. The obtained SIF were normalized using the maximum nominal stresses, i.e., making them independent of the applied nominal stress, during the fatigue testing for respective specimens, i.e., $K_{I(Max.)}/\sigma_{Max.}$. The reduced variate and the corresponding cumulative and probability density functions (CDF and PDF) for the normalized SIF of top rank defects according to the NDI-based approach and the actual fatigue critical defects are plotted in **Fig. 34**. The reduced variate measure, *V,* was calculated using:

$$V_i = -ln\,(-\,ln(i/\,N+1))\,, \tag{2}$$

where *i* and *N* are the rank and the total number of critical volumetric defects whose SIF were being analyzed [183]. The coefficient of determination, R^2, in all cases, was found to be higher than 0.8 (see **Fig. 34**(a)), indicating that the normalized SIF of top rank and fatigue critical defects followed a Gumbel distribution.

The CDF and PDF curves, shown in **Fig. 34**(b), show similarities between the normalized SIF of top rank and fatigue critical defects (defect sizes measured via both fractography and XCT). Such correlation between the top rank and the experimentally observed fatigue critical defects suggests the efficacy of the NDI-based approach to assess fatigue criticality of volumetric defects.

Note, the distribution of the normalized SIF for the top rank defects (magenta curve in **Fig. 34**(b)) was much closer to the critical defects (blue curve in **Fig. 34**(b)) whose sizes were measured via XCT than to the critical defects measured via fractography (green curve in **Fig. 34**(b)). The normalized SIF of critical defects whose sizes were measured via fractography skewed towards smaller sizes. This is likely due to the overestimation of defect sizes by XCT. The methodology implemented to post-process the XCT data to extract defects, shown in **Figs. 27**(a-d), including gradient operation followed by binarization (thresholding), likely resulted in an overestimation of the defect morphology detected via XCT.

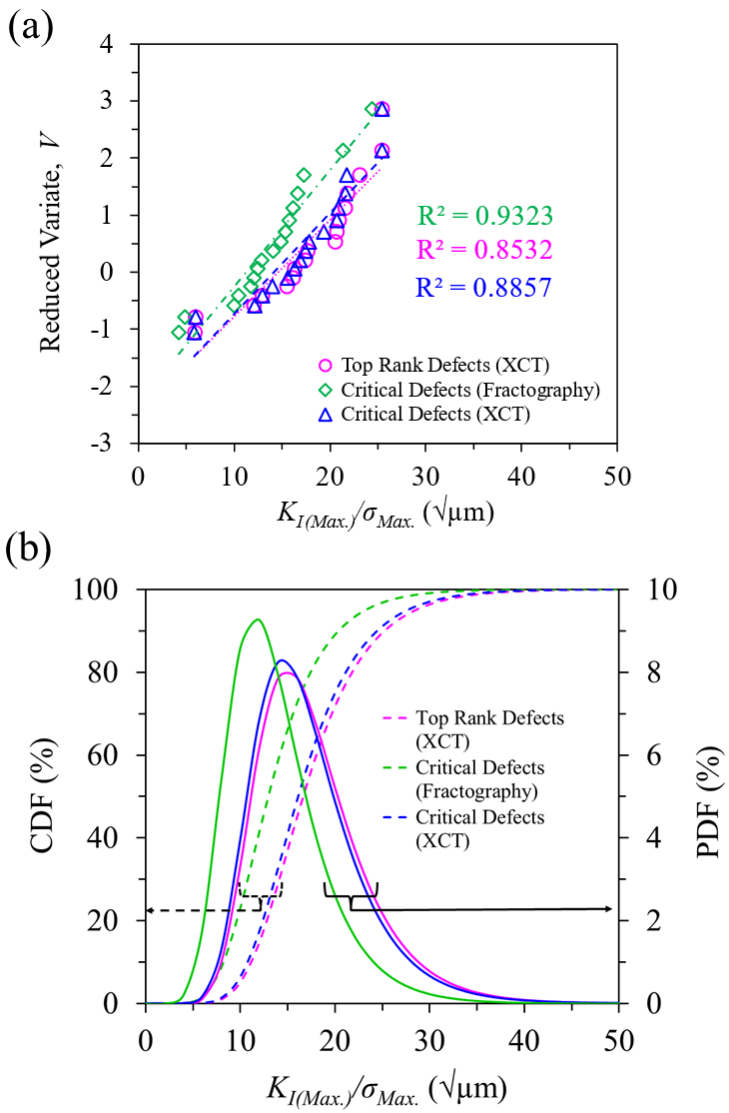

Fig. 34 (a) Reduced variate, (b) CDF, and PDF plots, according to LEVS [183], for normalized SIF of top rank defects obtained via the NDI-based approach, and the actual fatigue critical defects whose sizes were measured via fractography and XCT.

4.4.3 Limitations of the NDI-based approach

Out of the 17 fatigue critical defects (in 15 specimens) analyzed, 5 did not rank the highest SIF among the volumetric defects in their respective specimens. These unusual critical defects were examined to understand the limitations of the approach. For these critical defects, XCT was unable to detect its true morphology, thus mischaracterizing their sizes and fatigue criticality. As examples, **Fig. 35** illustrates the use of the NDI-based approach in two such specimens. One such

instance of XCT not being able to fully capture the critical defect's features occurred in the *ρ 5 mm* cylindrical AlSi10Mg specimen tested at 150 MPa. As shown in **Figs. 35**(a - c), XCT did not detect the fine intricate features of the critical LoF defect. This error caused the critical defect to be measured smaller than its true size which led to the mischaracterization of its fatigue criticality; the critical defect's SIF was lower than seventeen other volumetric defects within the notched specimen. Similarly, in **Figs. 35**(d - f), XCT could not detect the fine features of two nearby critical LoF defects. Despite these defects showing the highest SIF among other defects within the specimen, only partial morphologies were detected via XCT. Therefore, the resolution used during the XCT posed a limitation to the NDI-based approach to assess fatigue criticality of volumetric defects for these specimens.

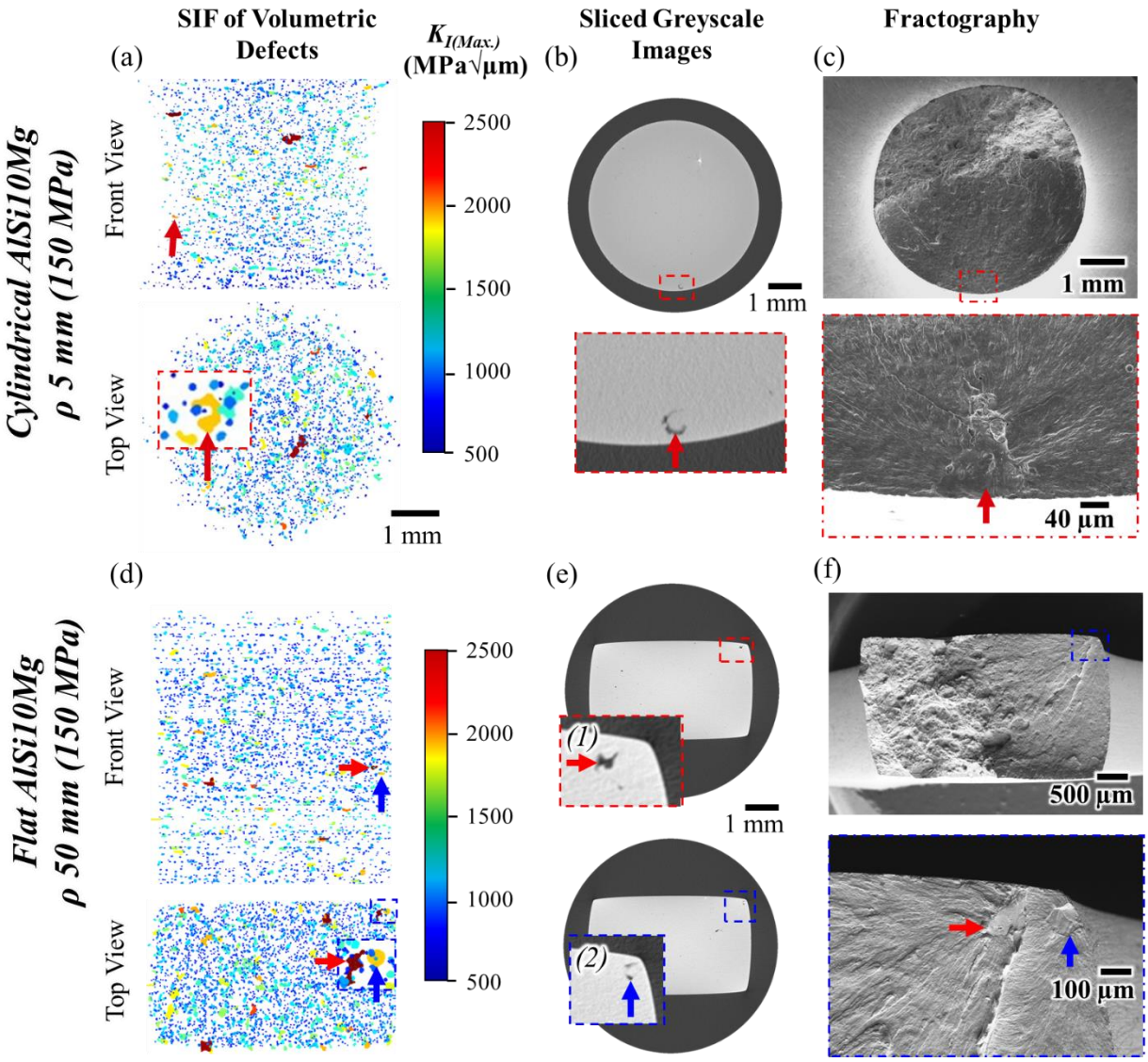

Fig. 35 (a, b) Visualization of volumetric defects, colored according to their SIF, within the XCT scan volume, (c, d) sliced greyscale XCT images showing the critical defects, and (e, f) fractography images showing the fatigue crack initiation sites in cylindrical and flat *ρ 5 mm* AlSi10Mg specimens.

Lastly, since the NDI-based approach was intended for techniques that can at least reveal the spatial and size information of volumetric defects, it cannot account for the fatigue crack initiation from only microstructural features (such as delta-ferrites (δ-Fe) in CA-H1025 17-4 PH SS). Out of 32 specimens that were analyzed and tested, 6 17-4 PH SS specimens showed fatigue crack initiation from δ-Fe precipitates. In the absence of large enough volumetric defects acting as

stress concentrators, these precipitates acted as weak points in the microstructure [55,184] and likely promoted fatigue crack initiation and growth along the δ-Fe-martensite interfaces to form crystallographic facets. As examples, the presence of crystallographic facets in the fatigue crack initiation sites for two 17-4 PH SS flat notched specimens from R batch with ρ *5 mm* and ρ *50 mm* is shown in **Fig. 36**.

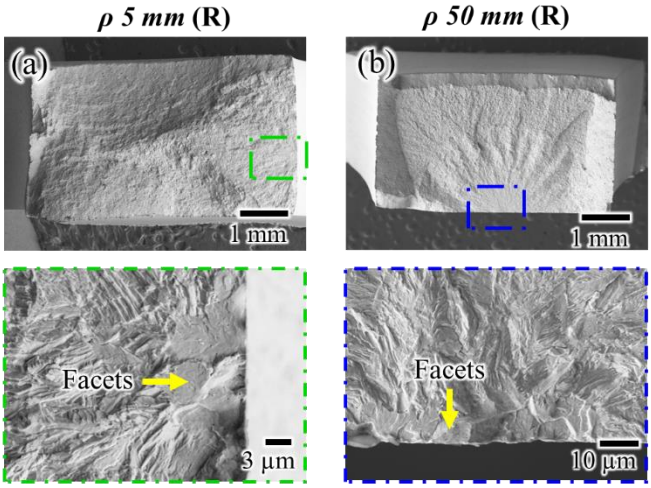

Fig. 36 Fractography images showing crystallographic facets in the fatigue crack initiation sites for (a) ρ *5 mm* and (b) ρ *50 mm* 17-4 PH SS flat notched specimens from R batch.

4.5 Conclusions

This study utilized linear elastic fracture mechanics to assess the fatigue criticality of volumetric defects in notched specimens detected via non-destructive inspection (NDI) techniques, specifically X-ray computed tomography. Assuming a defect-crack equivalency based on Murakami's approach, Mode-I stress intensity factor (SIF) of volumetric defects was calculated to represent their fatigue criticality. The linear elastic fracture mechanics approach, ($K_{I(Max.)} = Y\sigma_{Max.}K_{t(local)}\sqrt{\pi\sqrt{area}}$), accounted for defects' size and location as well as the local stresses due to the notch geometry, to calculate the SIF. Defects with higher SIF were considered as critical defects to initiate critical fatigue cracks. This behavior was validated using laser powder bed fused AlSi10Mg and 17-4 precipitation hardening stainless steel cylindrical and flat notched specimens

with varying notch root radii (5 mm and 50 mm). All critical defects fell within the 99.3 percentile of the defects with the highest stress intensity factor in the respective specimen, demonstrating the efficacy of the NDI-based approach. Despite the general success of the fatigue criticality assessment, some limitations were noted. These limitations included critical defects with features that were obscured by the resolution of the XCT and cases where defects did not contribute to critical crack formation.

5 Modeling the Short Fatigue Crack Growth in Additively Manufactured Notched Parts

5.1 Abstract

This work investigated the synergistic effects of volumetric defects and macroscopic notches on the short fatigue crack growth behavior in metallic materials. The effective stress intensity factor (SIF), proposed by El-Haddad to quantify a crack's driving force, was utilized to assess the tendency of crack arrest for short cracks initiating from defects in notched specimens. Notch-defect configurations with defects of varying shapes and sizes at different locations (notch-surface, corner, sub-surface, and lateral-surface) were analyzed using linear elastic finite element analysis. Features such as notch root radii, defect's size, shape, and location (proximity to notch and free lateral surfaces) influenced the effective SIF of cracks. A fatigue notch factor-based approach, incorporating the effective SIF of cracks, was employed to predict the fatigue lives of notched specimens. Validation was performed using additively manufactured AlSi10Mg and 17-4 precipitation hardening (PH) stainless steel (SS) flat notched specimens with varying geometries. For AlSi10Mg, 95% of all fatigue life predictions fell within the scatter band of 3, and 100% fell within the same scatter band for 17-4 PH SS.

Keywords

Laser-powder bed fusion (L-PBF/LB-PBF); Fatigue modeling; Short crack growth behavior; Crack arrest/non-propagating cracks; Effective stress intensity factor; Flat notched specimens

5.2 Introduction

Notch fatigue is a class of engineering problems that have been extensively investigated for the past few decades for conventionally manufactured (CM) parts [82,185–188]. Under loading, macroscopic notches or notch-like features in mechanical components, such as shaft shoulders/grooves/key slots, fastener holes, weldments, and gear tooth roots, etc., exert stress concentration and are often fatigue critical [121–124]. Fatigue design approaches typically employ a fatigue notch factor concept to estimate the stress-life (S-N) behavior of a notched member by "knocking down" the reference fatigue data of notch-free specimens with a fatigue stress concentration factor that accounts for the effects of both notch geometry and the materials' notch-sensitivity [82,189]. The fatigue stress concentration factor is commonly calculated using 2D elastic stress solutions (e.g., according to classical Neuber's formula or theory of critical distance) and assuming the crack front runs in the root plane along the third dimension (e.g., circumferential cracks in cylindrical notches and through-the-thickness cracks in edge notches). While these approaches have been effective for notches in CM parts, the current notch treatments have not been adequate when applied to additively manufactured (AM) ones. Specifically, significant fatigue scatters have been exhibited by notched members which cannot be explained by the state-of-art understandings of CM notches [135,190].

One of the most significant and persisting differences between the AM metallic materials with their CM counterparts is the ubiquitous presence of process-induced volumetric defects [69]. Because of the use of hard-to-dissolve shield gases (such as argon) during additive manufacturing (AM) processes, these volumetric defects are almost impossible to completely remove [191]. The volumetric defects generate their own stress fields [160] under load and, when appearing near notches, can initiate fatigue cracks, introduce significant fatigue scatter given the uncertainties in

the defects' location, size, and shape [29,152,153]. Accordingly, the presence of defects violates the assumptions of the prevailing treatments of CM notches that the fatigue cracks always initiate from the notch root surface thereby rendering them ineffective. A defect of a given size and shape can exert significantly different degrees of criticality to fatigue depending on its location with respect to notches. Assuming the placement of a fatigue critical defect on the root plane (i.e., the plane of maximum principal stress) of an edge notch, **Fig. 37** depicts four scenarios. Among the four locations indicated, Locations 1 and 2 can give defects more criticality since they are at the notch root and experience higher stresses than Locations 3 and 4. At Locations 2 and 4, due to less material constraints in the presence of the lateral, free surface (indicated in **Fig. 37**), the initiation and subsequent growth of fatigue cracks from volumetric defects are easier (corner and lateral surface fatigue cracks in these cases tend to exhibit higher stress intensity factor (SIF)), giving the defects heightened criticality than at Location 1 and 3.

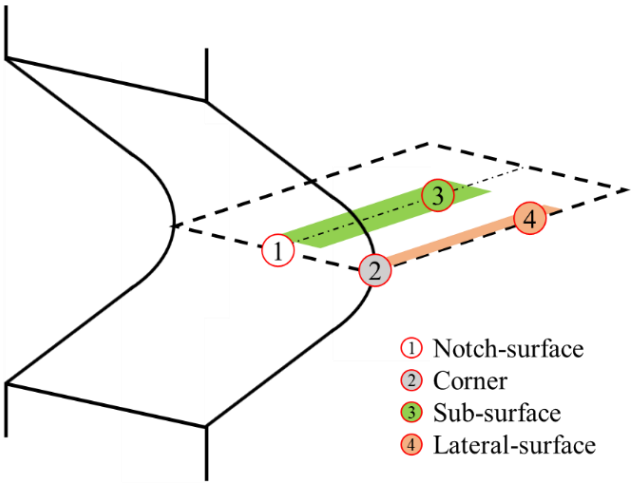

Fig. 37 Schematic showing potential placements of fatigue critical volumetric defects in an edge notch geometry: (1) notch-surface, (2) corner, (3) sub-surface, and (4) lateral-surface.

In an isolated environment (i.e., in the absence of surface notches, roughness, or the proximity of other defects), volumetric defects themselves behave like microscopic notches [192]. Based on the knowledge of small, surface notches, although volumetric defects can accelerate

fatigue crack nucleation, the driving force they can exert on the nucleated cracks is often limited because of the defects' small sizes. Specifically, the rapidly decaying stress fields, especially those from the flat and sharp defects, can lead to a temporary reduction in the effective SIF of short cracks, and potentially crack arrest [149]. Consequently, addressing the influence of the volumetric defects, therefore, should not only consider the degree of their elastic stress concentration but also their propensity to crack arrest due to their steep stress gradient. Indeed, the author's recent work has shown that short fatigue cracks nucleated from lack-of-fusion defects, which are flatter and with sharper edges, tend to experience an initial reduction in effective SIF [149]. Using a fatigue notch factor approach incorporating Murakami's $\sqrt{area}$ and the minimum effective SIF of cracks at arrest, the detrimental effects of volumetric defects in surface machined, notch-free parts could be quantified. However, near macroscopic notches, the coupling of the stress fields of the notches and volumetric defects severely influences the growth and arrest behaviors of the short cracks, and the understandings in this regard have been lacking.

This work addresses the synergistic effects of macroscopic notches and volumetric defects on the short fatigue crack growth behavior in AM metallic materials. Using linear elastic finite element analysis (LEFEA), the combined influence of notch geometry and defects' size, shape, and location on the driving force, i.e., SIF, of short cracks is quantified. The driving force of short cracks, calculated using effective SIF by El-Haddad et al. (1979), initiating from volumetric defects of various sizes, morphologies, and locations, residing near notches of different radii are assessed and compared to gain insights into the factors governing the short cracks' growth behavior. Using the minimum effective SIF for each defect-notch configuration, the corresponding fatigue stress concentration factor is determined, which can be used for fatigue life prediction using a fatigue notch factor-based framework if information regarding the fatigue critical defect is

known. This prediction scheme is validated using experimental fatigue data for laser-powder bed fused (L-PBF) AlSi10Mg and 17-4 precipitation hardening (PH) stainless steel (SS), published previously by the authors [182]. These materials are selected due to the differences in their tensile strengths leading to different sensitivity of fatigue crack initiation to volumetric defects and notch geometry [110,140,193].

5.3 Methodology

5.3.1 Design of simulations

A parametric LEFEA, using models of flat V-notch specimens containing cracks initiating from singular volumetric defects, was performed to quantify the effects of notch geometry, defects' size, shape, and location on the SIF of cracks. Flat V-notch specimens with an opening angle of 90°, notch depth of d = 3.5 mm, semi-width of w = 2.5 mm, and thickness of t = 3 mm were modeled (see **Figs. 38**(a and b)). Four defect configurations based on location (notch-surface, corner, sub-surface, and lateral-surface) were modeled, as shown in **Figs. 38**(c-f). For each configuration, the notch root radius, ρ, defect's size, r, and shape, h/r, and (for sub-surface and lateral-surface configurations only) the defect's distance from the notch surface, l, were varied individually, resulting in 540 cases, as detailed in **Table 10**. For each case, crack fronts were modeled, initiating from the defect, and the mode-I SIF of cracks was calculated as a function of crack length, a, up to 250 µm. The modeled crack fronts were circular and concentric with the defects in the modeled geometries (blue shaded bodies in **Figs. 38**); they were quarter circular in notch-surface and corner (see **Figs. 38**(c and d)) and semi-circular in sub-surface and lateral-surface configurations (see **Figs. 38**(e and f)). Note that, geometrically, the cases where a crack of size a is extending from a flat defect (h/r = 0) would be equivalent to those of a pure crack of size $a + r$.

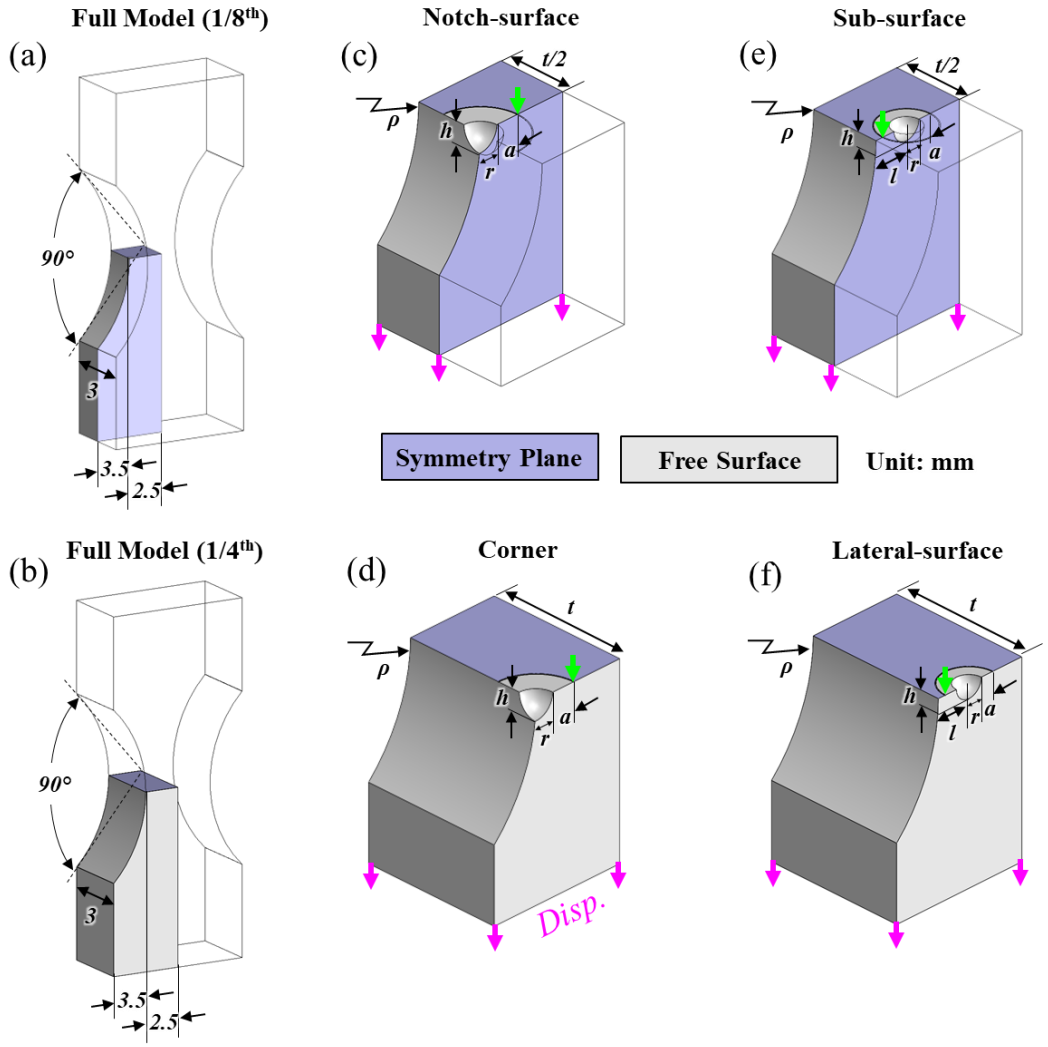

Fig. 38 Schematics showing different notch configurations with crack initiating defects at different locations (dimensions not to scale): modeled geometries (blue shaded bodies) being (a) one-eighth and (b) one-fourth of the simulated full specimens (wireframes), (c) notch-surface, (d) corner, (e) sub-surface, and (f) lateral-surface configurations. Symmetric and free surface boundary conditions in each configuration are color-coded.

Table 10 Geometric parameters and their ranges.

Parameter	Designation	Values
Normalized notch root radius	ρ/d	0.25, 0.5, 1, 1.5, 2, 2.5, 3, 7, and 15
Defect size (μm)	r	10.5, 52.5, and 105
Defect shape	h/r	0 and 1

Normalized distance from notch surface to defect	*l/w*	0.006, 0.012, 0.02, 0.032, 0.046, 0.1, 0.2, 0.3, 0.4, and 0.6
Crack length (μm)	*a*	0.2 to 250

5.3.2 Execution of simulations

The finite element (FE) simulations were performed using the ABAQUS® software. Utilizing the symmetry of the notch configurations, FE models representing a portion of the specimens were created and applied with appropriate boundary conditions, as shown in **Fig. 38**. The FE models comprised $1/8^{th}$ of the full model for notch-surface and sub-surface, and $1/4^{th}$ of the model for corner and lateral-surface configurations. Two element types were used for meshing (see **Fig. 39**). 20 node isoparametric quadratic brick elements (C3D20R) [194] were used in the crack front region with collapsed elements at the crack tip to model the singularity; the crack fronts are shown using yellow dashed lines in **Fig. 39**. On the other hand, quadratic tetrahedron elements (C3D10) were used to mesh the remaining regions of the FE models [194]. Mesh convergence studies were performed for each configuration until the SIF value at the crack front (at locations indicated by yellow arrows in **Fig. 39**) remained within 0.05% between successive mesh refinements. Upon convergence, the refined crack front element size was approximately 0.3 μm.

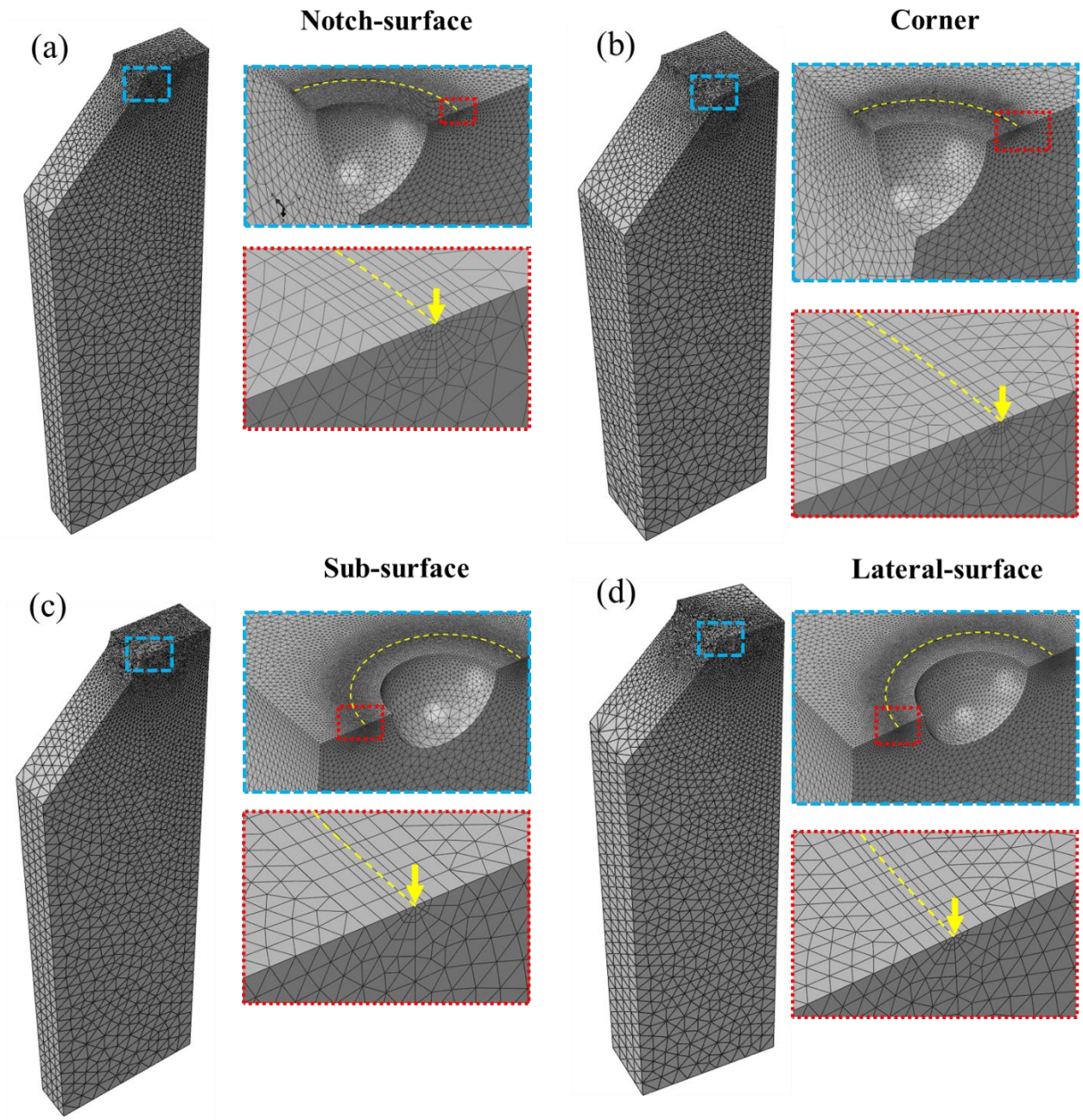

Fig. 39 FE meshes for different notch configurations: (a) notch-surface, (b) corner, (c) sub-surface, and (d) lateral-surface. Yellow arrows point to a location on the crack front in each configuration.

A remote displacement of 100 μm, along the direction of magenta arrows at the grip section, as shown in **Fig. 38**, was applied. The resulting SIFs along the crack front, calculated using the contour integral method implemented in ABAQUS® [194], were extracted. From each simulation, SIFs from three coaxial contours around the crack front were obtained; however, only

the converged SIF value from the second contour, where the stress field was more stable, was used. In addition to the SIF, nominal stresses, based on the cross sectional area at the notch root plane, were also estimated.

5.3.3 Analysis and validation of results

The obtained mode-I SIFs, K_I, were normalized with nominal stress, σ_{nom}, i.e., K_I/σ_{nom}, to make them independent of the applied load. For this reason, although the LEFEA was with static loads, the resulting normalized SIF, K_I/σ_{nom}, represents the normalized SIF range of cracks under cyclic loading, $\Delta K_I/\Delta\sigma_{nom}$. In general, the SIFs varied along the crack front due to the heterogeneous stress field of notches and defects as well as the proximity of the crack front to the free surface. Nevertheless, only the SIF at specific points as indicated by the green arrows in **Fig. 38** were of interest. These locations, i.e., at the base of the crack front for notch-surface and corner (**Figs. 38**(c and d)) and at the point on the crack front closest to the notch surface for sub-surface and lateral-surface configurations (**Figs. 38**(e and f)), were selected to capture the influence of decaying stress field of both the notch and the defect. The decay in the stress field due to the notch geometry is more prominent/significant along the ligament width direction than in the specimen thickness direction.

To account for the influence of small-scale cyclic plasticity, due to the stress concentration of defects and notches, on crack initiation behavior, El Haddad's effective SIF incorporating a material parameter a_0 was adopted [177,195]. This approach has previously been shown to be effective in the authors' earlier work to treat the effect of volumetric defects in notch-free condition [149]. The effective SIF of cracks is expressed as,

$$\left(\Delta K_{eff}\right)_{norm} = \frac{\Delta K_I}{\Delta\sigma_{nom}}\sqrt{1 + a_0/a}\ , \qquad (1)$$

where $\left(\Delta K_{eff}\right)_{norm}$ is the normalized effective SIF range, ΔK_I is the elastic mode-I SIF range and $\Delta\sigma_{nom}$ is the nominal stress range [177,195]. Utilizing Eq. (1) and LEFEA results, i.e., expressions for $\Delta K_I/\Delta\sigma_{nom}$, the effective SIF of cracks were calculated for different notch configurations.

The normalized effective SIF, capable of assessing the non-propagating condition of the initiated crack, can be used to predict the fatigue life of a notched specimen, given that geometrical information of the critical defect is known. For this, a fatigue notch factor (K_f)-based approach is often adopted [82,189]. The K_f behaves as a knock-down factor or a fatigue stress concentration factor, that knocks down or divides the fatigue limit of the reference stress-life relation to obtain the fatigue behavior of a defective/notched specimen. In a stress-life plot, given the fatigue life point at a high stress level and the fatigue limit of the defective/notched specimen, its corresponding fatigue life can be calculated based on Basquin's equation at desired stress levels [149].

In this study, the K_f was calculated as a ratio of the minimum effective SIF of cracks initiating from a critical defect in the notched specimen to that of a crack initiating from a microstructural discontinuity in defect-free, reference specimens, i.e., $K_f = \min\left(\left(\Delta K_{eff}\right)_{norm}\right)_{Defect} / \min\left(\left(\Delta K_{eff}\right)_{norm}\right)_{Ref.}$. The microstructural discontinuity can be persistent slip bands (PSBs) or other features that are responsible for fatigue crack initiation, e.g., delta-ferrites in the CA-H1025 treated microstructure [182]. As a note, these microstructural features were treated as defects with flat geometries (h/r = 0).

In this work, the fatigue data generated from laser powder bed fused (L-PBF) flat notched AlSi10Mg and 17-4 PH SS specimens with varying notch root radii (5 mm and 50 mm) [182] were

leveraged and the lives of the specimens were correlated with the geometrical features of the critical volumetric defects and notches via the fatigue notch factor-based framework outline above. The geometries and dimensions, which are the same as the ones being modeled in this work, of the flat notched specimens are shown in **Fig. S1** of the Supplemental Material. Details on the experimental setup including fabrication, heat treatment, and fatigue testing procedure are provided in **Section S1** of the Supplemental Material.

Furthermore, as a comparison, additional fatigue life-defect correlations were also made with the classical Murakami's defect sensitive fatigue model [114]. The prediction scheme was also fatigue notch factor-based, and the fatigue limit of a defective material, σ_e^{defect}, according to Murakami was,

$$\sigma_e^{\text{defect}} = C_2 \frac{(HV+120)}{(\sqrt{area})^{1/6}} \left(\frac{1-R}{2}\right)^{\alpha}, \quad (2)$$

where $\sqrt{area}$ is the square root of the projected area of the critical defect onto the plane normal to the loading direction, *HV* is the Vickers hardness, and *R* is the stress ratio. The fitting constants C_2 and α of values 1.43 and 0.226 + HV×10^{-4}, were used [114]. For L-PBF AlSi10Mg and 17-4 PH SS, *HV* values of 135 and 361 were used [196,197]. For the fatigue life predictions, the local stress concentration factor, $K_{t(local)}$ due to the notch geometry was also taken into account [198]. For each specimen, $K_{t(local)}$ was obtained at the location of the critical defect and was used to elevate the applied nominal stress.

5.4 Results

5.4.1 LEFEA results for different notch configurations

The normalized mode-I SIF, K_I/σ_{nom}, of pure cracks and cracks initiating from flat and spherical defects of varying sizes in notched geometries of different root radii are presented in **Fig. 40** for notch-surface and corner, and in **Fig. 41** for sub-surface and lateral-surface configurations. **Figure 4** only presents the normalized SIF for extreme and intermediate notch root radii, i.e., ρ/d of 0.25, 1, and 15. The plots containing the complete dataset of SIF for all notch root radii, listed in **Table 1**, are presented in **Section S2** of the Supplemental Material. In general, the SIF increased with increasing crack length for both notch-surface and corner configurations (see **Fig. 40**). For cracks initiating from spherical defects (indicated using dotted lines in **Fig. 40**), their SIF exhibited a brief period of rapid increase before approaching the pure crack cases. The SIF of cracks initiating from smaller defects merged with the pure crack cases at shorter crack lengths, likely due to the influence of its smaller stress field, diminishing at shorter distances, on the crack front. In contrast, the SIF of cracks initiating from a perfectly flat defect, i.e., $h/r = 0$, first vertically approached then followed the pure cracks' SIF curves. Note that the intermediate scenarios of flat and spherical defects, i.e., the ones with $0 < h/r < 1$, were not modeled explicitly in this work. Nevertheless, based on the authors' earlier work [149], the SIF curves for such cases should be the intermediate of spherical (see dotted lines in **Fig. 40**) and perfectly flat (see dashed lines in **Fig. 40**) defect cases. Among notches with different ρ/d, sharper notches resulted in higher SIF of pure cracks as well as cracks initiating from defects, for both notch-surface and corner configurations.

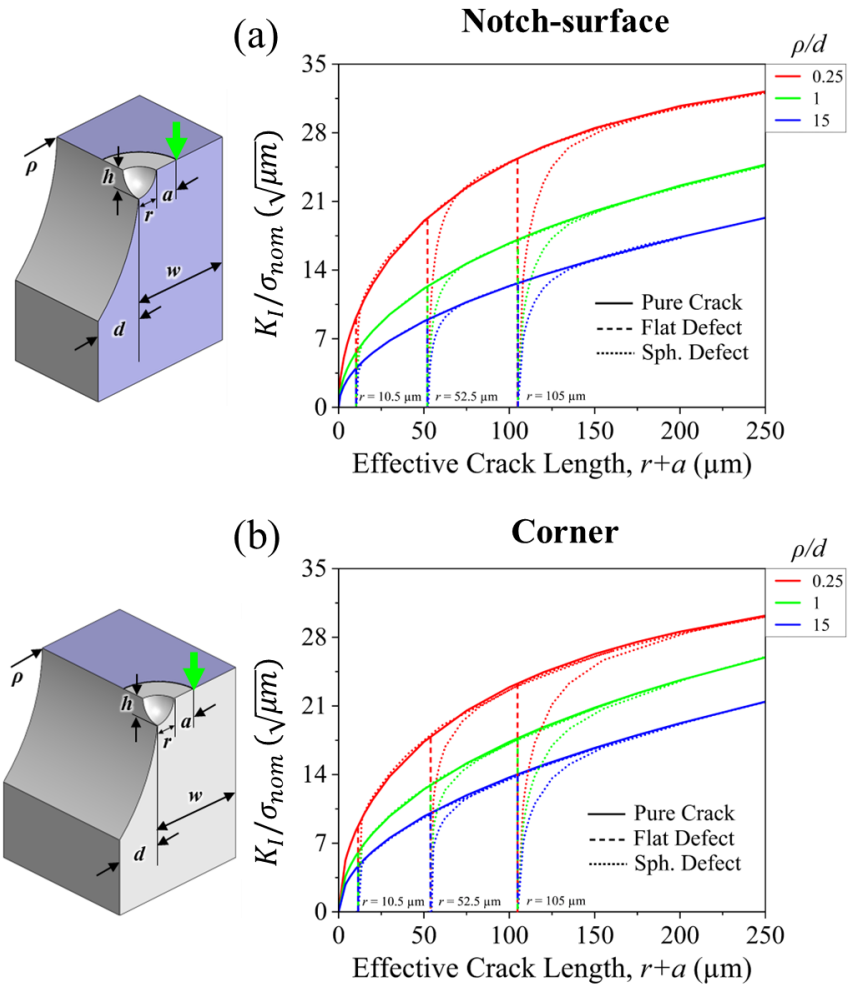

Fig. 40 Normalized mode-I SIF of pure cracks and cracks initiating from flat and spherical defects of different sizes in (a) notch-surface and (b) corner configurations. Green arrows in the schematics point to the location on the crack front where the SIFs were measured.

For sub-surface and lateral-surface configurations, **Fig. 41** presents the normalized SIF of pure cracks and cracks initiating from flat and spherical defects, located at different distances, *l*/*w*, away from the notch root, in notches with extreme notch root radii, i.e., *ρ/d* of 0.25 and 15. The complete dataset of SIF of cracks for all notch root radii, listed in **Table 10**, for sub-surface and lateral-surface configurations, is presented in **Section S3** of the Supplemental Material. For both configurations, the SIF increased with increasing crack length; however, when cracks approached the free surface, the SIF approached infinity, as shown in **Fig. 41**. The positions of the free surface

relative to the defect are shown using dash-dotted vertical lines of the corresponding colors in **Fig. 41**. A similar behavior in the mode-I SIF of cracks due to its proximity to the free surface has previously been reported for a center-crack in a fixed-width flat plate [199]. Similar to notch-surface and corner configurations (see **Fig. 40**), cracks initiating from flat defects vertically approached and followed the pure crack cases (dashed lines in **Fig. 41)**, while the spherical defect ones showed a brief period of rapid increase before approaching the pure crack cases (dotted lines in **Fig. 41)**. Between notches with ρ/d of 0.25 and 15, there was a clear difference in the SIF trends for cracks initiating at different l/w. The sharp notch (ρ/d = 0.25) illustrated a wider variation in the SIF of cracks for different l/w compared to the blunt notch (ρ/d =15), as shown in **Fig. 41**. It was attributed to the higher stress concentration and the higher stress gradient of the sharper notch, resulting in larger differences in the local stresses, and thus larger variation in the SIF of cracks, at different distances ahead of the notch root.

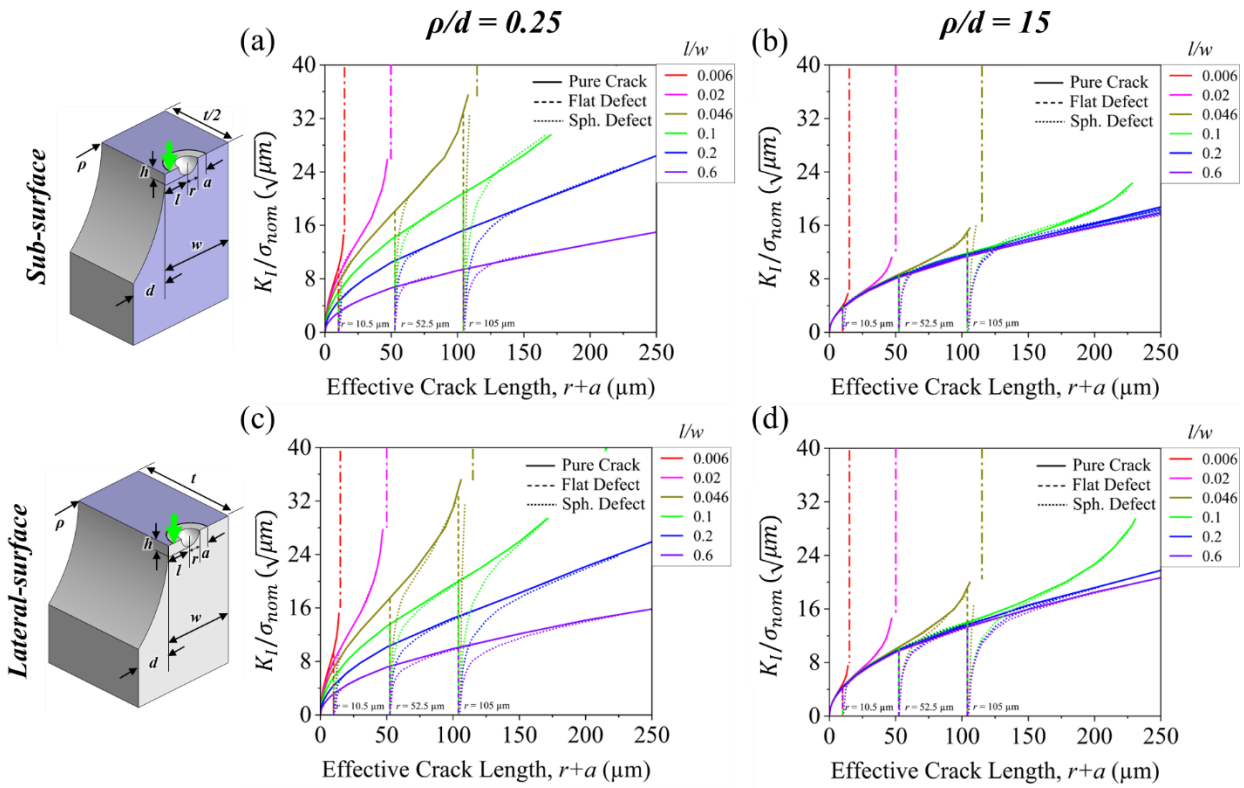

Fig. 41 Normalized mode-I SIF of pure cracks and cracks initiating from different sizes flat and spherical defects in (a and b) sub-surface and (c and d) lateral-surface configurations, for sharp (ρ/d = 0.25) and blunt (ρ/d = 15) notches. The color-coded dash-dotted vertical lines represent the free surface for the corresponding l/w. Green arrows in the schematics point to the location on the crack front where the SIFs were measured.

5.4.2 Expressions for elastic mode-I SIF in different notch configurations

In notch-surface and corner configurations (**Figs. 38**(c and d)), as the circular crack grows, their deepest points (indicated by the green arrows in the figures) propagate along the notch stress gradient, which is similar to the growth behavior of through-the-thickness cracks. Accordingly, the variation of SIF for the two crack geometries as a function of crack size is expected to be similar. By blending the SIF of shallow and deep, through-the-thickness cracks, which are respectively under and free of the influence of notches, Härkegård introduced a semi-empirical form for SIF for notch cracks as a function of crack length [200]. Following this approach, this work expressed the normalized mode-I SIF of shallow and deep pure circular cracks using

$$\frac{\Delta K_I}{\Delta\sigma_{nom}} = F_\alpha \left(\frac{2}{\pi}\right) K_t \sqrt{\pi a} \text{ and} \quad (3)$$

$$\frac{\Delta K_I}{\Delta\sigma_{nom}} = F_\alpha \left(\frac{2}{\pi}\right) \sqrt{\pi a}\,, \quad (4)$$

where F_α is the crack geometry factor depending on the notch configuration, i.e., 1.025 for notch-surface and 1.122 for corner, and K_t is the associated elastic stress concentration factor at the notch root. A shallow crack, in notch-surface and corner configurations, experiences the local stress concentration at the notch root; however, for a sufficiently deep crack, the stress field due to the notch geometry decays and reaches minimum, i.e., $K_t = 1$. Introducing a transition function, θ, to interpolate between Eqs. (3), and (4), where $\theta \sim 0$ for shallow and $\theta \sim 1$ for deep cracks, yields

$$\frac{\Delta K_I}{\Delta\sigma_{nom}} = F_\alpha \left(\frac{2}{\pi}\right) \sqrt{\pi a + \frac{(1-\theta)K_t^n a}{\pi}}\,, \quad (5)$$

where $\theta = 1 - e^{-a/a^*}$, and n and a^* are the fitting parameters. The fitting parameters vary with the notch geometry and are provided in **Figs. S3**(b and c) in the Supplemental Material.

For flat defects, due to the fast-approaching nature of the SIF of cracks initiating from them to that of pure cracks (see **Fig. 40**), Eq. (5) was utilized by substituting the pure crack's length, a, with $r+a$, i.e., crack of length a initiating from a flat defect of size r. However, at crack length, $a = 0$, the effective SIF of cracks initiating from flat defects approached infinity. Such trends of effective SIF of cracks initiating from different configurations of flat defects in the notch-surface configuration are discussed in more detail in **Section 4.1**. In the case of spherical defects, an additional transition function, γ, was introduced. Based on θ, γ, Eqs. (3), and (4), a generalized expression for the normalized mode-I SIF range for an arbitrary length crack, with $a < 250$ μm, initiating from a spherical defect, in notch-surface and corner configurations, was expressed as

$$\frac{\Delta K_I}{\Delta \sigma_{nom}} = F_\alpha \left(\frac{2}{\pi}\right) \sqrt{\pi \gamma \left((r+a) + \frac{(1-\theta) K_t^n (r+a)}{\pi^2}\right)}, \quad (6)$$

where $\theta = 1 - e^{-(r+a)/a^*}$, $\gamma = 1 - e^{-a/b^*}$, and b^* is the fitting parameter. b^* varies with the defect size, as shown in **Fig. S4**(d) in the Supplemental Material.

For sub-surface and lateral-surface configurations (**Fig. 41**), the normalized elastic mode-I SIF range of cracks was expressed using

$$\frac{\Delta K_I}{\Delta \sigma_{nom}} = F\sqrt{\pi a}\ , \quad (7)$$

where *F* is the crack geometry factor. Utilizing the LEFEA results, *F* for pure cracks initiating at different distances, *l/w*, in notches of different root radii, i.e., *ρ/d* = 0.25, 0.5, 1, 1.5, 2, 2.5, 3, 7, and 15, was calculated and the calculated *F* for notches with *ρ/d* of 0.25 and 15 are presented in **Figs. S6**(a and b) of the Supplemental Material. *F* approached infinity as cracks approached the free surface, i.e., *a/l*~1, (see **Fig. S6**). During the LEFEA, crack lengths only up to 250 μm were assessed; this caused the near notch surface SIF of pure cracks with *l/w* > 0.1 not to be captured. For pure cracks with *l/w* < 0.1, *F* was a function of the following form

$$F = \left[sec\left(\frac{\pi a}{2l}\right)^{1/2}\right]\left[1 + A\left(\frac{a}{l}\right)^2 + B\left(\frac{a}{l}\right)^4\right] + C, \text{ for } l/w < 0.1, \quad (8)$$

where *A*, *B*, and *C* are the fitting parameters. These fitting parameters vary with *l/w* and *ρ/d*, and are provided in **Fig. S7** of the Supplemental Material, for sub-surface and lateral-surface configurations. For *l/w* > 0.1, *F* was near constant for crack lengths up to 250 μm. The near constant *F* for different *l/w* and *ρ/d* is presented in **Figs. S6**(c and d), respectively, for sub-surface

and lateral-surface configurations. An approximation function of F for pure cracks with $l/w > 0.1$ was expressed as

$$F = A_1 e^{-\left(\frac{l/w}{A_2}\right)^{A_3}} + A_4, \text{ for } l/w > 0.1, \quad (9)$$

where A_1, A_2, A_3, and A_4 are the fitting parameters, and their values, influenced by ρ/d, are presented in **Section S3** of the Supplemental Material, for both sub-surface and lateral-surface configurations.

Similar to notch-surface and corner configurations, for flat defects, the expressions of pure cracks, shown in Eqs. (7-9), were utilized by substituting the pure crack's length, a, with $r+a$, i.e., crack of length a initiating from a flat defect of size r. Such trends of effective SIF of cracks initiating from flat defects at different distances ahead of the notch surface, are presented in **Fig. 43**, and discussed in **Section 4.1**. In the case of spherical defects, a transition function, γ, was used and the generalized expression for mode-I SIF was expressed as

$$\frac{\Delta K_I}{\Delta \sigma_{nom}} = F\sqrt{\pi\, a\, \gamma}\,, \quad (10)$$

where F was obtained using Eqs. (8) and (9), for defects with $l/w < 0.1$ and $l/w > 0.1$, respectively.

5.5 Discussion

5.5.1 Short crack growth behavior in different notch configurations

Following the approach outlined in **Section 2.3**, the elastic mode-I SIF presented in **Section 3** was used to calculate the effective mode-I SIF of cracks initiating from defects. As examples for the notch-surface configuration, the effective SIF of pure cracks and cracks initiating from flat and spherical defects have been calculated using Eqs. (1), (5), and (6), and selected results are plotted

in **Fig. 42**. Specifically, only the effective SIF of cracks initiating from defects with sizes, r =10.5 µm and 105 µm, in notched specimens with extreme notch root radii, ρ/d = 0.25 and 15, are shown. Sizes of 10.5 µm and 105 µm represent the range of typical defect sizes in AM metallic materials [69]. It is worth mentioning that similar effective SIF behavior was observed for the corner configuration (see **Fig. S4** of the Supplemental Material) and not shown in the main text. For the effective SIF calculations plotted in **Fig. 42** and **Fig. 43**, a material characteristic length, a_0, of 10 µm was used for illustrative purposes. The a_0 of 10 µm represented the microstructure of AlSi10Mg specimens used for the validation of the proposed life assessment approach—together with 17-4 PH SS specimens. Similar observations would be expected to result if a characteristic length scale for 17-4 PH SS (a_0 of 8 µm) was used.

In the notch-surface configuration, the effective SIF of cracks initiating from a flat defect dropped rapidly ahead of the defect and then showed a gradual increase with increasing crack length (see **Figs. 42**(a, b, e, and f)). In addition, cracks initiating from larger defects (r = 105 µm) showed higher effective SIF, illustrating higher detrimental effects on the fatigue behavior; higher minimum effective SIF results in a higher crack growth rate and a lower likelihood of crack arrest. For cracks initiating from spherical defects with r =10.5 µm, the effective SIF decreased, reached minimum, and then gradually increased with increasing crack length (see **Figs. 42**(c and d)). On the other hand, for spherical defects with r =105 µm, the effective SIF increased gradually with increasing crack length, without an initial reduction. This resulted in the defect with r =10.5 µm to have higher effective SIF at shorter crack lengths; however, as the crack advanced, it became lower than for the defect with r =105 µm. This suggests a higher likelihood for cracks initiating from small defect (r =10.5 µm) to get arrested. Such an initial reduction in the effective SIF of cracks initiating from smaller defects is likely due to the influence of their own stress fields, which

decay at shorter crack lengths, producing a higher gradient stress field. This rapid decay in the stress field ahead of the defect influences the SIF of cracks, and thus the crack arrest behavior. Between the two notch root radius cases presented in **Fig. 42**, the effective SIF of cracks for ρ/d =0.25 was higher than ρ/d =15, likely due to higher stress concentration at the notch root. Additionally, the variation in the minimum effective SIF of cracks between defects with r =10.5 µm and r =105 µm was wider for ρ/d =0.25 than ρ/d =15 (**Figs. 42**(e and f)). This is likely due to the smaller defect's proximity to the notch root, experiencing a higher gradient notch stress field, resulting in a larger dip/reduction in the effective SIF of cracks for the shaper notch.

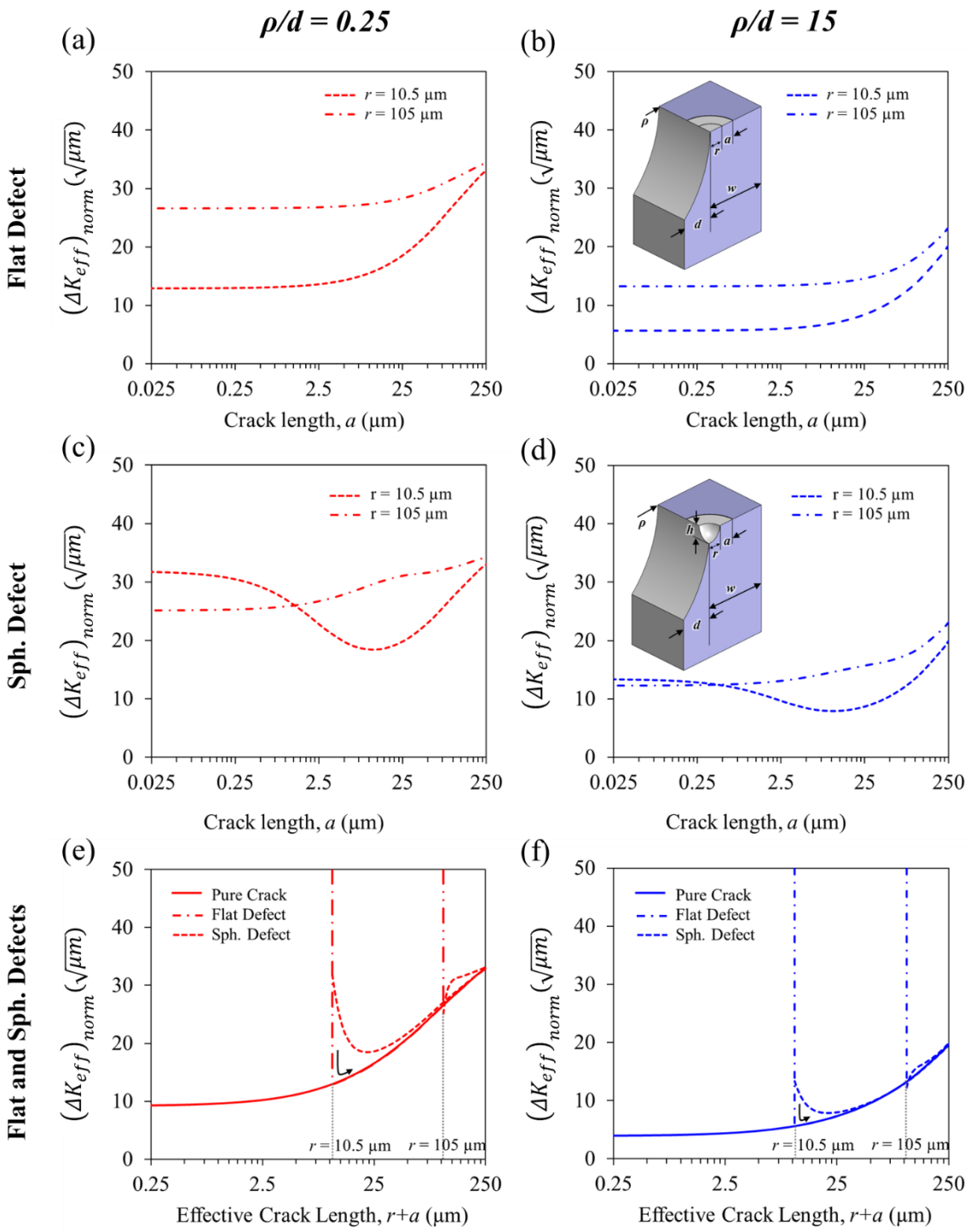

Fig. 42 Effective SIF of cracks initiating from (a and b) flat defect, (c and d) spherical defect, and (e and f) comparison between pure cracks and cracks initiating from both flat and spherical defects, in notches with ρ/d of 0.25 and 15, for notch-surface configuration.

For comparison among pure cracks, and cracks initiating from flat and spherical defects, their effective SIF, for different defect sizes, are plotted against the effective crack length (r+a) in

Figs. 42(e and f). For the notch-surface configuration, the effective SIF of cracks initiating from flat defects dropped rapidly (**Figs. 42**(e and f)), then showed a gradual increase with increasing crack length, and merged with their corresponding pure crack cases. Such a sudden decrease in the effective SIF is likely due to a very high stress gradient ahead of the flat defect. For cracks initiating from spherical defects, effective SIF showed a gradual decrease for defect with r = 10.5 μm. This caused cracks initiating from spherical defects with r = 10.5 μm to have higher minimum effective SIFs than flat defects. Such initial decrease in the effective SIF, reaching minimum, and then increasing with increasing crack lengths, has previously been observed for cracks initiating from the notch roots of ductile cast iron specimens [50]. At sufficiently low stress levels, there can exist a condition when the effective SIF becomes lower than the threshold SIF, and consequently, the propagating crack ceases its growth, i.e., crack arrest, [177,195]. A lower minimum effective SIF of cracks initiating from flat defects suggested a higher likelihood of crack arrest compared to cracks initiating from spherical defects [149]. However, for cracks initiating from spherical defects with r = 105 μm, there was no initial decrease in the effective SIF. Here, the minimum effective SIF for flat defects was higher than for spherical ones.

For the sub-surface configuration, the effective SIF of pure cracks and cracks initiating from flat and spherical defects, located at different distances, l/w, from the notch surface, is presented in **Fig. 43**. The lateral-surface configuration showed similar effective SIF behavior to the sub-surface configuration, as shown in **Fig. S5** of the Supplemental Material. **Figure 7** shows the effective SIF of cracks initiating from defects at extreme and intermediate locations, l/w of 0.012, 0.1, and 0.6, in notches with extreme notch root radii, ρ/d = 0.25 and 15, as a function of crack length. Cracks initiating from flat defects, with increasing crack length, showed a sudden initial decrease in the effective SIF and later approached the pure crack cases, for all l/w (see **Figs.**

43(a and b)). When cracks approached the free surface, effective SIF increased rapidly and approached infinity. The position of the free surface is indicated using dash-dotted green lines in **Figs. 43**(a and b) for l/w = 0.012 (the position of the free surface for the other two l/w ratios are outside the axis limits and are not shown in the figure). For spherical defects, similar to flat defects, the effective SIF initially decreased and then merged with the pure crack cases. However, spherical defects showed a more gradual initial decrease (see **Figs. 43**(c and d)), likely due to the influence of their lower gradient stress field, compared to flat defects.

Among different l/w, cracks initiating from defects closer to the notch surface (smaller l/w) showed higher effective SIF at all crack lengths, $r+a$. This behavior was more pronounced for the sharp notch (ρ/d = 0.25), where l/w = 0.012 showed significantly higher effective SIF than l/w = 0.6, compared to the blunt notch (ρ/d = 15). For the blunt notch, the effective SIF was comparable among different l/w (see **Figs. 43**(b and d)). This is likely due to the prevalence of a lower gradient stress field ahead of the blunt notch, resulting in a smaller variation in the local stresses at different l/w. Among different defect sizes, smaller defects showed lower minimum effective SIF, suggesting a higher likelihood of crack arrest. For defects with r = 10.5 µm, an initial decrease in the effective SIF was observed for both flat and spherical defects; however, for r = 105 µm, such an initial dip was observed only for flat defects. A lower minimum effective SIF for smaller defects, and for defects at larger l/w suggested a higher likelihood of crack arrest for cracks emanating from them.

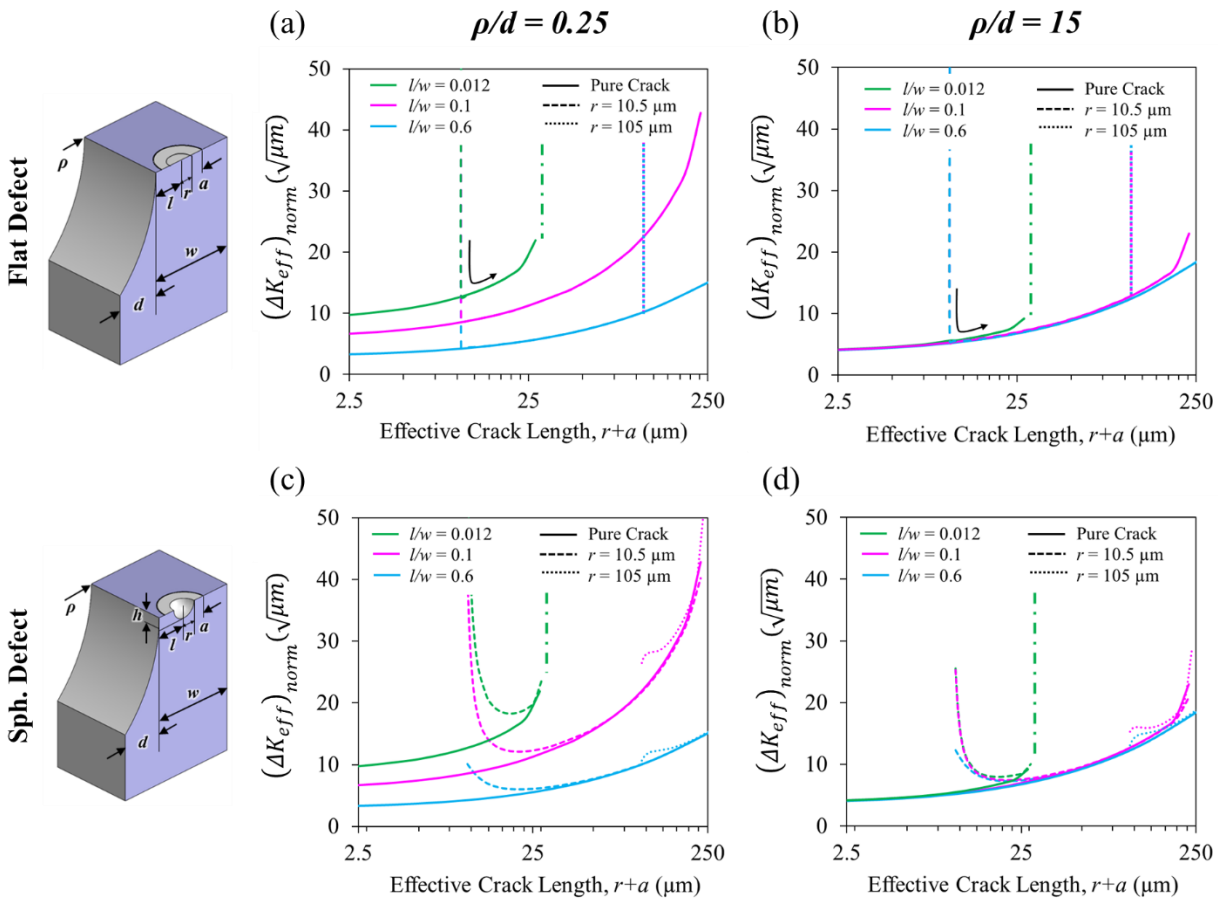

Fig. 43 Effective SIF of pure cracks and cracks initiating from different sizes (a and b) flat and (c and d) spherical defects in notches with ρ/d = 0.25 and ρ/d = 15 in sub-surface configuration. The green dash-dotted vertical lines represent the free surface for l/w = 0.012 (the position of the free surfaces for the other two l/w ratios are outside the axis limits and are not shown).

5.5.2 Fatigue life prediction and validation

Following the fatigue notch factor-based framework outlined in **Section 2.3**, the fatigue lives of flat, edge-notched specimens tested by Poudel et al. [182] were predicted using the defect information obtained via fractography. These experimentally tested specimens showed fatigue critical crack initiations from volumetric defects of different sizes at different locations. Experimentally obtained stress-life plots for *ρ5* and *ρ50* specimens are shown in **Figs. 44**(a and b) with colored markers. These specimens showed critical crack initiation from lack-of-fusion (LoF) volumetric defects located either at/near notch-surface, corner, or lateral-surface (see **Figs. 44**(c-

f)). Utilizing the size, i.e., equivalent radius, *r*, calculated using $\sqrt{area/\pi}$ where $\sqrt{area}$ is measured in accordance with Murakami's approach [176], and the location of the critical defect, the effective SIF of cracks initiating from them were calculated using Eq. (1). In the case of multiple crack initiation, the size and location of the largest crack initiating defect was used in the analysis. During the calculations, the material characteristic length, a_0, of 10 µm and 8 µm were used, respectively, for AlSi10Mg and 17-4 PH SS. For AlSi10Mg, a_0 was estimated by measuring the average grain size in the radial plane, i.e., the direction of the crack propagation [182]. For 17-4 PH SS, it was the average size of the delta-ferrites in the CA-H1025 treated microstructure [182]. It is worth noting that, during the effective SIF calculation, the critical LoF defects, due to similarities in morphology and short crack growth behavior [149], were treated as flat defects.

Following the methodology mentioned in **Section 2.3**, the knock-down factor, K_f, for each of the experimentally tested flat notched specimens was calculated by dividing the minimum effective SIF of cracks initiating from the critical defect to that from a critical microstructural discontinuity in defect-free, reference specimens. The reference stress-life behavior should correspond to notch-free specimens whose crack initiation is not influenced by volumetric defects and is instead driven by the largest weak microstructural features, which can be the largest persistent slip bands (PSBs) in FCC alloys (such as Inconel 718 and AlSi10Mg) and the largest delta ferrite in martensitic stainless steels (such as 17-4 PH SS) [54,55,151,201]. It has been shown that microstructure-driven fatigue crack initiation can out-compete volumetric defect-driven initiation when the largest microstructural features are larger than the most critical volumetric defects [54]. In Poudel et al, the largest grain size (which is proportional to the largest PSBs' size) for AlSi10Mg was ~15 µm and the largest delta-ferrite for 17-4 PH SS was ~12 µm (Poudel et al.,

2025). With these lengths, the fatigue limit for the reference stress-life curve can be obtained from the Shiozawa curves [202] constructed for the *ρ50* AlSi10Mg and 17-4 PH SS specimens.

For AlSi10Mg and 17-4 PH SS, the Shiozawa curve was generated, respectively, using 7 out of 22 and 9 out of 18 specimens; these specimens are labeled as *ρ 50 mm* (Shiozawa) in **Figs. 44**(a and b). The remaining *ρ 50 mm* specimens, together with all *ρ 5 mm* ones, were used for validation. In order to plot the Shiozawa curve, a classical linear elastic fracture mechanics (LEFM), proposed by Murakami [114] was modified, i.e., by incorporating the local stress concentration factor near notches, and used to estimate the mode-I SIF of crack initiating defects. Assuming a defect-crack equivalence, $K_{I(Max)} = YK_{t(local)}\sigma_{Nom}\sqrt{\pi\sqrt{area}}$, where $K_{I(Max)}$ is the equivalent mode-I SIF of a defect, *Y* is the crack geometry factor (0.65 for surface and 0.5 for internal locations), and $K_{t(local)}$ is the local stress concentration factor at the location of the crack initiation site, was used. $K_{t(local)}$accounts for the stress concentration due to the notch geometry at different locations within the cross-section as well as at different heights relative to the notch root plane (Poudel et al., 2024a), was used. The obtained SIF for critical defects of *ρ50* specimens were plotted against the defect-related fatigue life, $N_f/\sqrt{area}$, to generate Shiozawa curves for AlSi10Mg and 17-4 PH SS (see **Figs. 44**(g and h)). The use of Shiozawa's curve, derived from the Paris crack growth relationship, can be rationalized due to the ease of fatigue crack initiation in the presence of both notch and defect's stress field, suggesting a greater fraction of the fatigue life is spent on crack growth [180,203,204].

For the construction of the reference stress-life behavior (Basquin's equations as indicated by the black dashed lines in **Figs. 44**(a and b)), the stress-life information corresponding to two points, one at a higher stress level and another at a lower stress level, was needed. The life

corresponding to the fatigue limit was considered to be 10^7 reversals. The reference fatigue limits were read from the Shiozawa curves by treating the sizes of the largest microstructural features (15 μm for AlSi10Mg and 12 μm for 17-4 PH SS) as the critical sizes. Since linear elastic assumptions are no longer valid at low cycle life regimes, Shiozawa's approach is not suitable for estimating the nominal stresses at higher stress levels. For the points at the higher stress level, the max. nominal stresses were calculated by multiplying the fatigue strength fraction, *f*, by the materials' ultimate tensile strength (UTS). For AlSi10Mg and 17-4 PH SS, *f* of 0.9 and 0.78 [205] were used. The UTS of AlSi10Mg and 17-4 PH SS were 295 MPa and 1260 MPa, respectively [198]. The fatigue lives at the points of higher stress levels were simply the extrapolation of Basquin's fits (magenta dashed lines in **Figs. 44**(a and b)) to $\rho 50$ data points at $f \times$UTS. The calculated stress-life points, shown as hollow black triangles in **Figs. 44**(a and b), were used to determine the reference Basquin's equation for both AlSi10Mg and 17-4 PH SS.

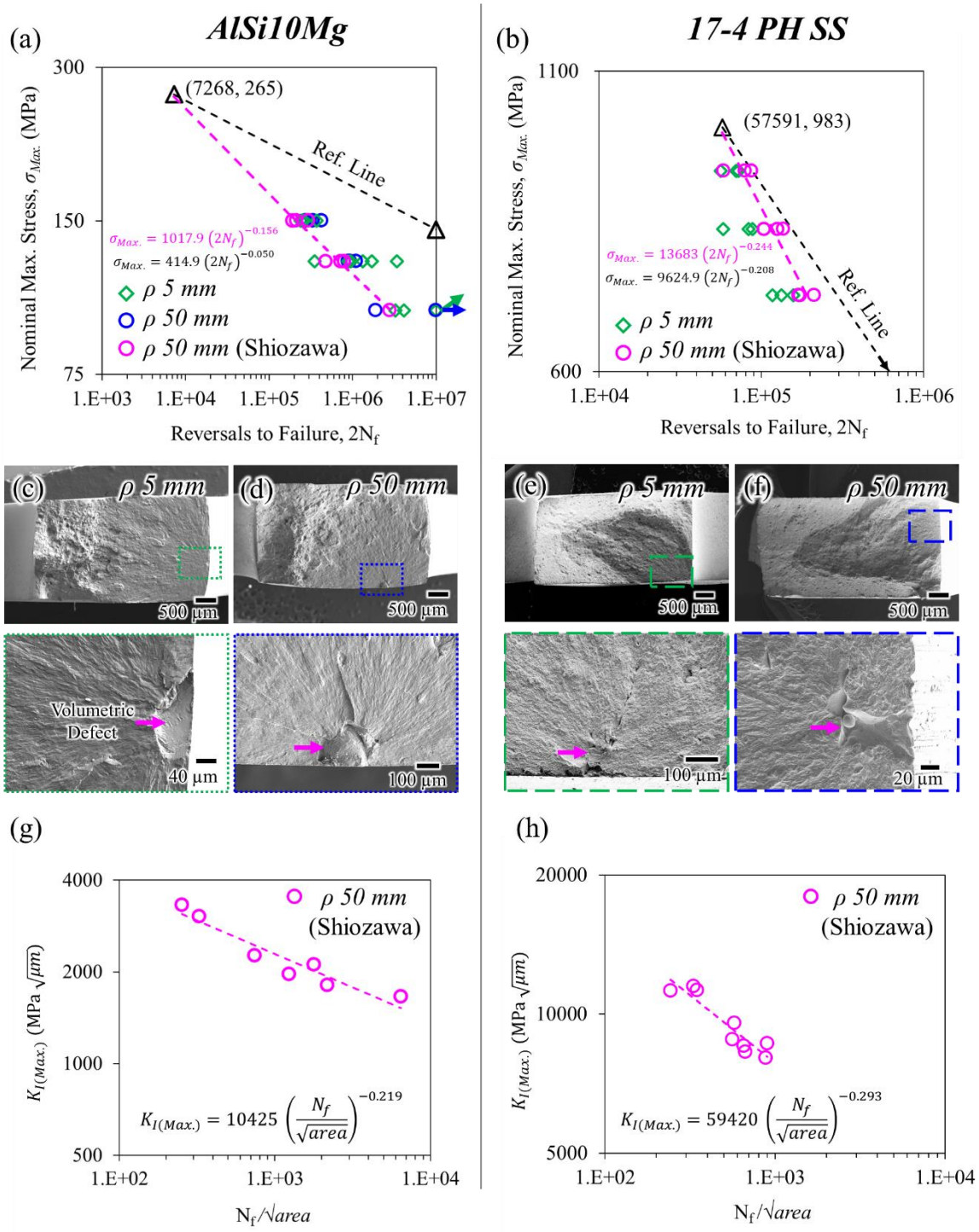

Fig. 44 Stress-life plots for *ρ5* and *ρ50* (a) AlSi10Mg and (b) 17-4 PH SS flat specimens [198]. Fractography images for (c and d) AlSi10Mg and (e and f) 17-4 PH SS specimens. Shiozawa curves for *ρ50* (g) AlSi10Mg and (h) 17-4 PH SS specimens.

For *ρ5* and *ρ50* specimens (excluding the *ρ 50 mm* (Shiozawa) specimens), the fatigue lives were predicted using the fatigue notch factor-based framework and plotted against their experimental fatigue lives, as shown in **Figs. 45**(a and b) for AlSi10Mg and 17-4 PH SS. In general, this study predicted the fatigue lives of notched specimens reasonably well, with a slightly conservative prediction for AlSi10Mg. For AlSi10Mg, 95% of the predictions fell within the scatter band of 3 while it was 100% for 17-4 PH SS. The efficacy of the approach proposed in this study was further analyzed by comparing the predicted fatigue lives with those from the existing approach, i.e., Murakami's approach given by Eq. (2). The predicted fatigue lives using the existing approach for AlSi10Mg and 17-4 PH SS specimens are shown in **Figs. 45**(c and d). For AlSi10Mg, 36% of the predictions fell within the scatter band of 3, while 54% fell within the scatter band of 5; the majority of the predictions were non-conservative. For 17-4 PH SS, all 100% of the predictions fell within the scatter band of 3. However, in comparison between the two prediction approaches, the scatter in the predicted fatigue lives of 17-4 PH SS specimens was significantly higher for Murakami's approach (see **Figs. 45**(b and d). Such predictions using the existing approach showcase its limitation to account for the short fatigue crack growth behavior in metallic notches. In the case of AlSi10Mg, such a large deviation in the predicted fatigue lives is likely due to the use of material constants in Eq. (2) that was originally developed for steels [15].

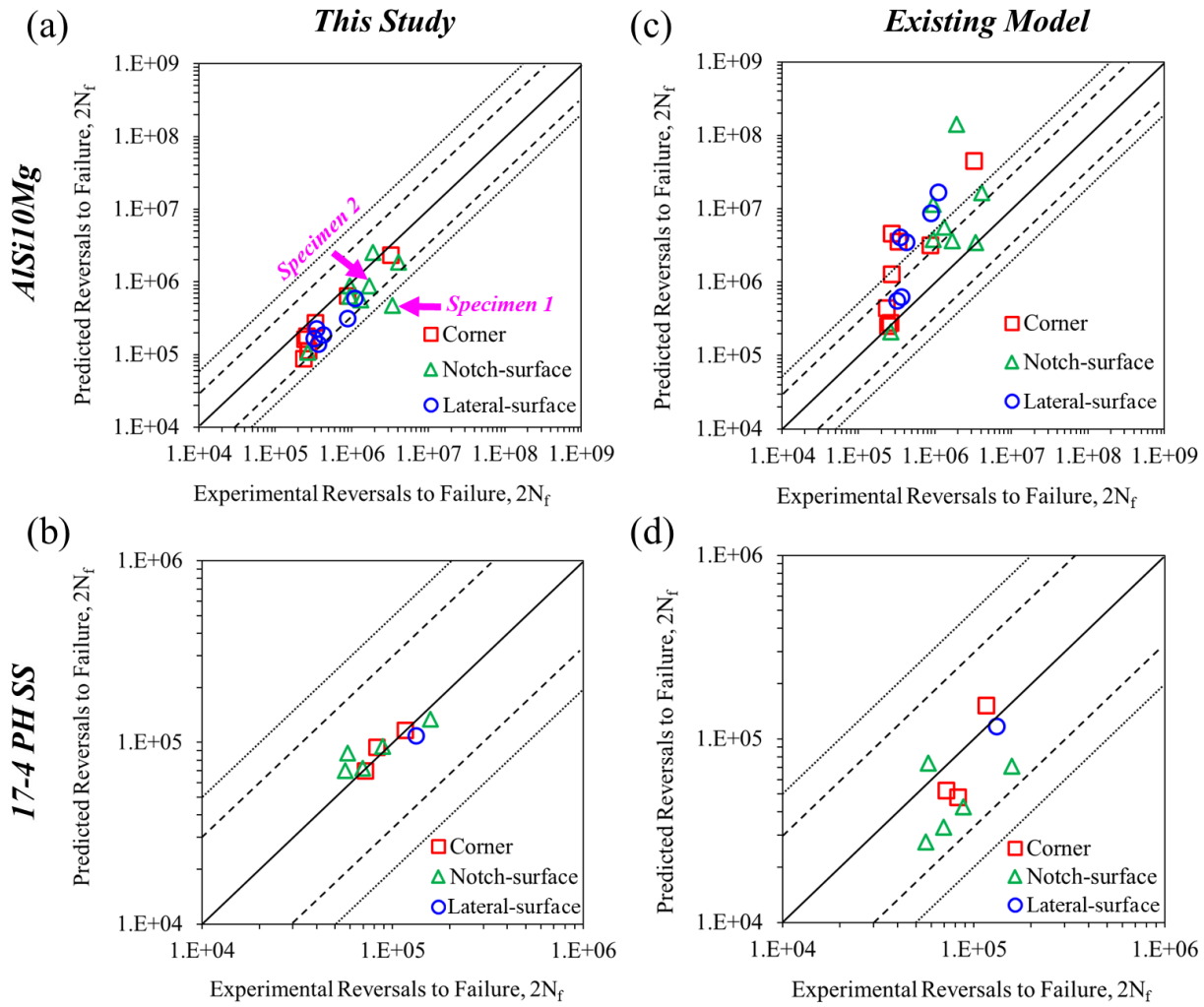

Fig. 45 Fatigue life predictions performed (a and b) in this study and (c and d) following an existing model for AlSi10Mg and 17-4 PH SS flat notched specimens. Magenta arrows point to two specimens, one with conservative and another with slightly better predictions.

While the predictions performed in this study were better than the existing approach, they still contain some scatter in the predicted fatigue lives of AlSi10Mg specimens (see **Fig. 45**(a)). Specimens pointed using magenta arrows in **Fig. 45**(a) were further investigated to identify the additional features influencing the fatigue behavior. Fractographs for these specimens (Specimens 1 and 2), along with their stress levels, fatigue lives, and critical defect sizes are shown in **Fig. 46**(a), and their corresponding effective SIF trends ahead of critical defects in **Fig. 46**(b). Specimen 1, despite having a larger critical defect, showed twice the fatigue life of specimen 2. Fractographs

showed both critical defects near the notch surface; however, their morphologies were found to vary significantly. Specimen 1 had an irregular shape critical defect, with several arms-like thin features, compared to the defect of circular shape in Specimen 2. This variation in defect morphology likely caused the discrepancy in the minimum effective SIF of cracks ahead of critical defects (see **Fig. 46**(b)). The model proposed in this study assumes circular or semi-circular, depending on the location, projected shape defects onto the loading plane, for the calculation of effective SIF. The additional effect of irregular shaped defects, thus could not be captured, resulting in a conservative prediction for Specimen 1, where the arms-like features of the large critical defect (**Fig. 46**(a)) had been shown to be less detrimental [120].

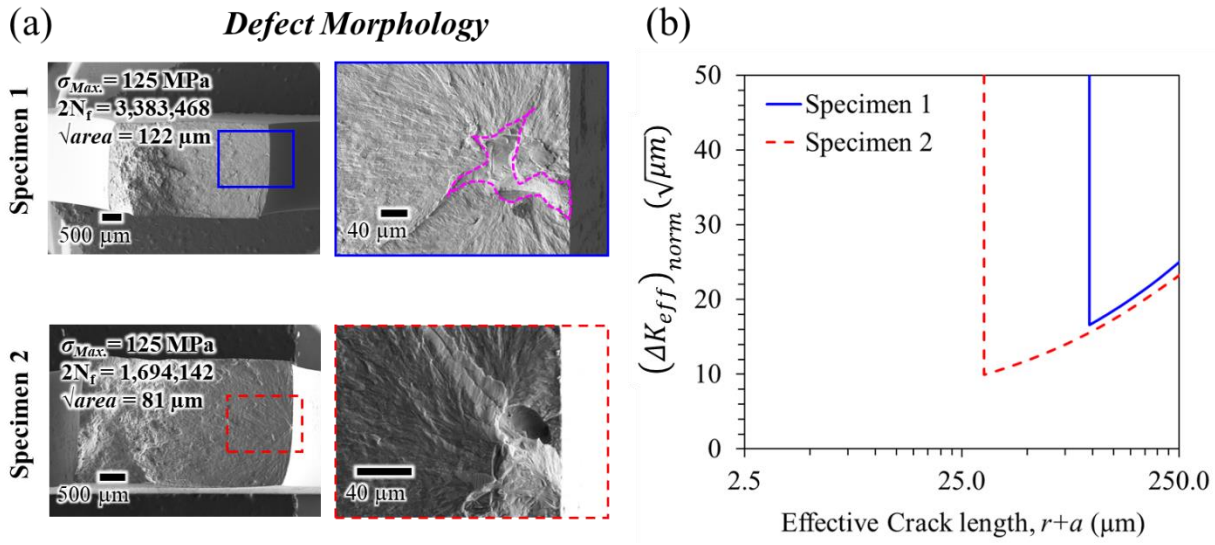

Fig. 46 (a) Fractography images and (b) effective SIF of cracks ahead of the critical defect in Specimens 1 and 2.

5.6 Conclusion

This work modeled the synergistic effects of notch geometry, volumetric defect's size, shape, and location, on the short fatigue crack growth behavior in metallic materials. El-Haddad's effective stress intensity factor of cracks initiating from defects in different notch configurations, which represent their driving force for growth, were assessed. With the critical defect information

such as size and location identified from fractography, the fatigue lives of flat notched specimens with varying notch root radii and for two materials (AlSi10Mg and 17-4 precipitation hardening (PH) stainless steel (SS)) were estimated via a fatigue notch factor-based framework and validated with the experimentally measured lives. In this study, the following major conclusions were drawn.

1. The expressions for elastic mode-I stress intensity factor (SIF) for pure cracks and cracks initiating from flat and spherical defects in notch-surface, corner, sub-surface, and lateral-surface configurations were determined.
2. Notch geometry, volumetric defects' shape, size, and location influenced the effective SIF of cracks initiating from volumetric defects, and thus the crack arrest and short crack growth behavior.
3. In notched specimens, cracks initiating from flat defects experienced a much sharper initial decline in the effective SIF, resulting in lower minimum values, compared to spherical defects. This hinted at a higher likelihood for cracks initiating from flat defects to be arrested than the ones from spherical defects.
4. In notch-surface and corner configurations, smaller defects due to their high gradient stress fields tended to result in an initial decline in the effective SIF of cracks with increasing crack length. This decline became more prominent in sharper notches, due to the additional influence of the higher gradient notch stress field.
5. In sub-surface and lateral-surface configurations, the notch stress field influenced the SIF of cracks initiating from defects at different distances away from the notch root. Smaller defects closer to the notch root experienced a much steeper initial decline in effective SIF than larger defects that were farther away.

6. The fatigue notch factor, obtained by utilizing the minimum effective SIF of cracks, predicted the fatigue lives of flat, edge-notched AlSi10Mg and 17-4 PH SS specimens reasonably well. For AlSi10Mg, 95% of all fatigue life predictions fell within the scatter band of 3, while it was 100% for 17-4 PH SS.

This study accounted for the influence of notch geometry, and volumetric defects' shape, size, and location on the short fatigue crack growth behavior in metallic notches. The approach proposed in this study is expected to work for other defect-sensitive materials as well where the localized fatigue crack initiation is observed within the notched specimens.

6 Summary and potential future work

6.1 Summary

This dissertation investigated the synergistic effects of volumetric defects and notch geometry on the fatigue behavior of additively manufactured metallic materials. Different features influencing the fatigue behavior, especially crack initiation and short crack growth behavior, were identified and their fatigue criticality were assessed. This work contributes toward the qualification of complex AM parts with notch-like features, for fatigue-critical applications. This was achieved by dividing the overall goal into multiple objectives.

The **first objective** was identifying the factors influencing the fatigue behavior of cylindrical & flat notched specimens with varying notch root radii & ligament widths. AlSi10Mg and 17-4 PH SS cylindrical and flat notched specimens with varying notch root radii, ligament widths, and defect contents, were used. The specimens were subjected to uniaxial fatigue testing, and after failure, fractography was performed to identify the crack initiation sites and investigate the failure mechanisms. Irrespective of the material, *ρ0.1* specimens had the shortest fatigue lives with the lowest scatter compared to *ρ5* and *ρ50*, and showed critical crack initiations from the notch root. For cylindrical AlSi10Mg specimens, *ρ5* and *ρ50* showed comparable fatigue lives and had volumetric defects as their crack initiation sites. For 17-4 PH SS, despite having critical cracks initiation from volumetric defects similar to AlSi10Mg, *ρ50* showed slightly superior fatigue performance than *ρ5*. This was attributed to the wider range of critical defect features, such as defect size, in AlSi10Mg than in 17-4 PH SS specimens. All critical cracks in *ρ5* and *ρ50* cylindrical specimens initiated from volumetric defects located either at the surface or near surface **(*Confirmation of Hypothesis 1a*)**. Features such as notch root radii, critical defects' size, and location (within the cross-section and height relative to the notch root plane) influenced the fatigue

behavior of cylindrical notched specimens. For flat specimens, there was an additional influence from the microstructural features; δ-Fe acted as weak points in the microstructure for near defect-free 17-4 PH SS specimens. Furthermore, larger ligament width resulted in shorter fatigue lives for *ρ0.1* and *ρ5* specimens for both AlSi10Mg and 17-4 PH SS **(*Confirmation of Hypothesis 1b*)**. Chapter 2 and Chapter 3 identified the features influencing the fatigue behavior of cylindrical and flat notched specimens. Furthermore, the fatigue criticality of notch geometry and volumetric defect features were assessed and correlated with the experimental fatigue lives. For specimens with minimal plasticity at the notch root, mode-I SIF calculated using LEFM correlated with fatigue lives. However, for specimens with significant plasticity at the notch root, equivalent plastic strain correlated with experimental fatigue lives.

The **second objective** was assessing the fatigue criticality of volumetric defects in notched specimens via a non-destructive approach. Assuming defect-crack equivalency, mode-I SIF for volumetric defects was calculated using LEFM (Murakami's approach) and used to represent their fatigue criticality. The approach utilized LEFEA to account for the notch stress field at different locations within the specimen. The cylindrical and flat notched specimens from Chapters 2 and 3 were XCT scanned and processed to calculate the SIF for every defect observed within the scan volume. The volumetric defect with the highest SIF was deemed the most fatigue critical and compared with the critical defect observed via fractography. Utilizing this approach, all critical defects fell within the 99.3 percentile of defects with the highest SIF in the respective specimens. This showed the applicability of mode-I SIF, calculated by correcting for the notch stress field, to rank the fatigue criticality of volumetric defects in notched specimens **(*Confirmation of Hypothesis 2a*)**. Due to the influence of the notch stress field, a smaller defect closer to the notch

root plane was observed to have higher SIF, i.e., higher fatigue criticality, compared to a larger defect away from it **(*Confirmation of Hypothesis 2b*)**.

The **third objective** was modeling the synergistic effects of volumetric defects and notch geometry on the short crack growth behavior of metallic materials. The approach assessed the effects of notch geometry and volumetric defect features (size, shape, and location) on the crack arrest behavior. Numerical modeling involving LEFEA was utilized to calculate the effective SIF of cracks initiating from defects in different notch configurations. During LEFEA, four different notch configurations with defects at different locations: notch-surface, corner, sub-surface, and front-surface, were used. As a result, notch root radius, defects' size, shape, and location were found to influence the SIF of cracks, and ultimately the effective SIF ahead of the critical defect **(*Confirmation of Hypothesis 3a*)**. Smaller defects, due to their higher gradient stress fields, showed a rapid initial decline in the effective SIF of cracks ahead of the defect with increasing crack lengths. Regarding defect shape, flat defect showed a much sharper decline in the effective SIF compared to the spherical one, suggesting a higher likelihood for their crack arrest and superior fatigue performance. In addition, sharper notches, with a higher gradient stress field ahead of the notch root, resulted in a sharper decline in the effective SIF of cracks. The minimum effective SIF, at crack arrest, was utilized to obtain the fatigue notch factor **(*Confirmation of Hypothesis 3b*)**. The obtained factor was used to predict the fatigue lives of flat notched specimens via a fatigue notch factor-based framework. The proposed approach predicted the fatigue lives of AlSi10Mg and 17-4 PH SS flat notched specimens reasonably well. For AlSi10Mg, 95% of all fatigue life predictions fell within the scatter band of 3, while it was 100% for 17-4 PH SS.

6.2 Potential future work

Throughout this research work, only the key/primary factors influencing the fatigue behavior of AM cylindrical and flat notched specimens were identified and assessed. These factors include notch geometry, critical defects' size, and location (within the cross-section, and at different heights relative to the notch root plane). The combined criticality posed by these features on the fatigue behavior was quantified using different numerical approaches. However, there were several other factors that impacted the fatigue behavior of notched specimens but fell outside the scope of this work. One such factor is defect interaction; stress field interaction between two nearby defects promotes fatigue crack initiation and leads to early fatigue failure. Several instances were seen for both AlSi10Mg and 17-4 PH SS where specimens with two nearby critical defects had shorter fatigue lives compared to the ones with a single critical defect of an equivalent size.

Additionally, multiple crack initiation, defects being away from each other with minimal interaction between their stress fields, is another factor influencing the fatigue behavior of notched specimens. The presence of two or more independent crack initiation sites in the same specimen led to shorter fatigue lives, especially when the crack initiation planes were different, compared to a specimen with a single critical defect. Another feature influencing the fatigue behavior of notched specimens is the defect morphology. Critical LoF defects with arms-like features but with relatively smaller core regions were found to be less detrimental as compared to spherical defects of the same size; size was obtained using Murakami's $\sqrt{area}$ approach. In this work, the effects of defects interaction, multiple crack initiation, defect morphology, etc., were found to influence the fatigue behavior of AlSi10Mg and 17-4 PH SS notched specimens. However, these features have not been formally accounted for while assessing/quantifying the criticality of different features on fatigue behavior. Since the occurrence of these features is very probable in complex AM parts,

these features need to be investigated and incorporated into the approaches developed in this work. While utilizing the approaches developed in this work, limitations might arise due to the use of only mode-I loading conditions, while investigating the crack arrest and the short crack growth behavior. However, in applications, mode-I, mode-II, mode-III, mixed mode, and multi-axial loading conditions exist. To ensure the industrywide adoption of complex AM parts with notch-like features, the fatigue behavior of notched specimens with inherent AM features under different loading conditions needs to be investigated.

7 Supplement Material for Chapter 2

S1: Methodology for linear elastic finite element analysis

Linear elastic-finite element analysis (LE-FEA) was performed to analyze the stress fields in different configurations of notched specimens, i.e., ρ of 0.1 mm, 5 mm, and 50 mm, using ABAQUS® software. For each configuration, a two-dimensional finite element model was created using geometries indicated by magenta arrows in **Fig. S1** and dimensions shown in **Fig. 2** in the main manuscript. Both symmetric and axisymmetric boundary conditions were used during the analysis. Symmetric boundary condition (BC) was applied on X_1-X_2 plane at the notch root and axisymmetric BC along the central loading axis, i.e., along X_3. A displacement of 100 µm was applied on the grip of specimens as shown by black arrows in **Fig. S1**. Material constants, modulus of elasticity of 200,000 MPa and Poisson's ratio of 0.33, were used. For meshing, CAX6M—6-node modified quadratic axisymmetric triangle—elements were used, and a mesh convergence study was performed for each notch configuration. Converged meshes for each configuration are shown in **Figs. S1**(b, d, & f).

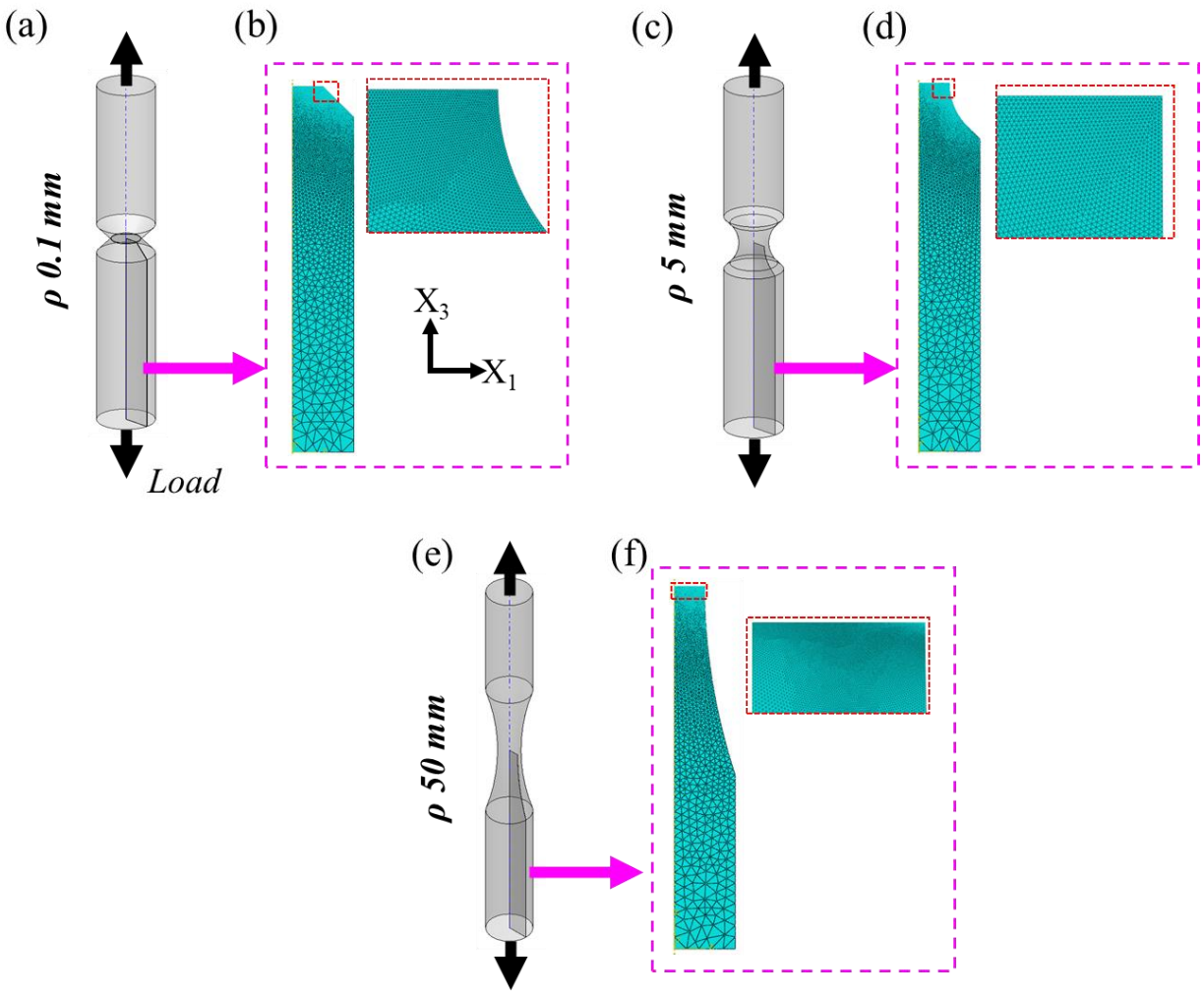

Fig. S1 Geometries and meshes in finite element models for notch configurations with ρ of (a & b) 0.1 mm, (c & d) 5 mm, and (e & f) 50 mm, respectively.

Local stresses at seven different heights relative to the notch root plane were extracted and shown in **Figs. 10**(d-f) in the main manuscript. Normalized local stress (σ_{33}/σ_0) trends ahead of the notch surface varied among different relative heights (h_{center}/h_0). At the notch root plane, the σ_{33}/σ_0 showed a decreasing trend ahead of the notch surface; however, it changed into an increasing trend for larger relative heights. Hence, only the normalized stress data for ρ 5 mm and 50 mm configurations with relative heights less than or equal to 0.3, with a similar decreasing trend, were fitted using an exponential decay function,

$$\frac{\sigma_{33}}{\sigma_0} = M_1 + M_2 e^{-l/(l_0 M_3)}, \quad \text{(S1)}$$

where σ_{33}/σ_0 is the local elastic stress concentration factor ($K_{t(local)}$), l is the distance of a crack initiation site from the notch surface, l_0 is the distance from the notch surface to the axisymmetric axis, and M_1, M_2, and M_3 are the fitting parameters. Each of these fitting parameters can be calculated using,

$$M_i = A_{i1}x^2 + A_{i2}x + A_{i3}, \quad \text{(S2)}$$

where $x = h_{center}/h_0$, and the constants, A_{i1}, A_{i2}, and A_{i3} are provided in **Table S1** and **Table S2**, respectively, for ρ 5 mm and 50 mm configurations.

Table S1 Constants used in Eq. (S1) for ρ 5 mm configuration.

i	A_{i1}	A_{i2}	A_{i3}
1	-1.323	-0.104	0.794
2	-5.155	-0.604	0.422
3	-4.625	0.859	0.377

Table S2 Constants used in Eq. (S2) for ρ 50 mm configuration.

i	A_{i1}	A_{i2}	A_{i3}
1	-2.981	-0.511	0.974
2	-0.386	-0.126	0.053
3	-4.282	1.329	0.474

8 Supplement Material for Chapter 3

S1: Dimensions of AlSi10Mg and 17-4 precipitation hardening (PH) stainless steel (SS) notched specimens

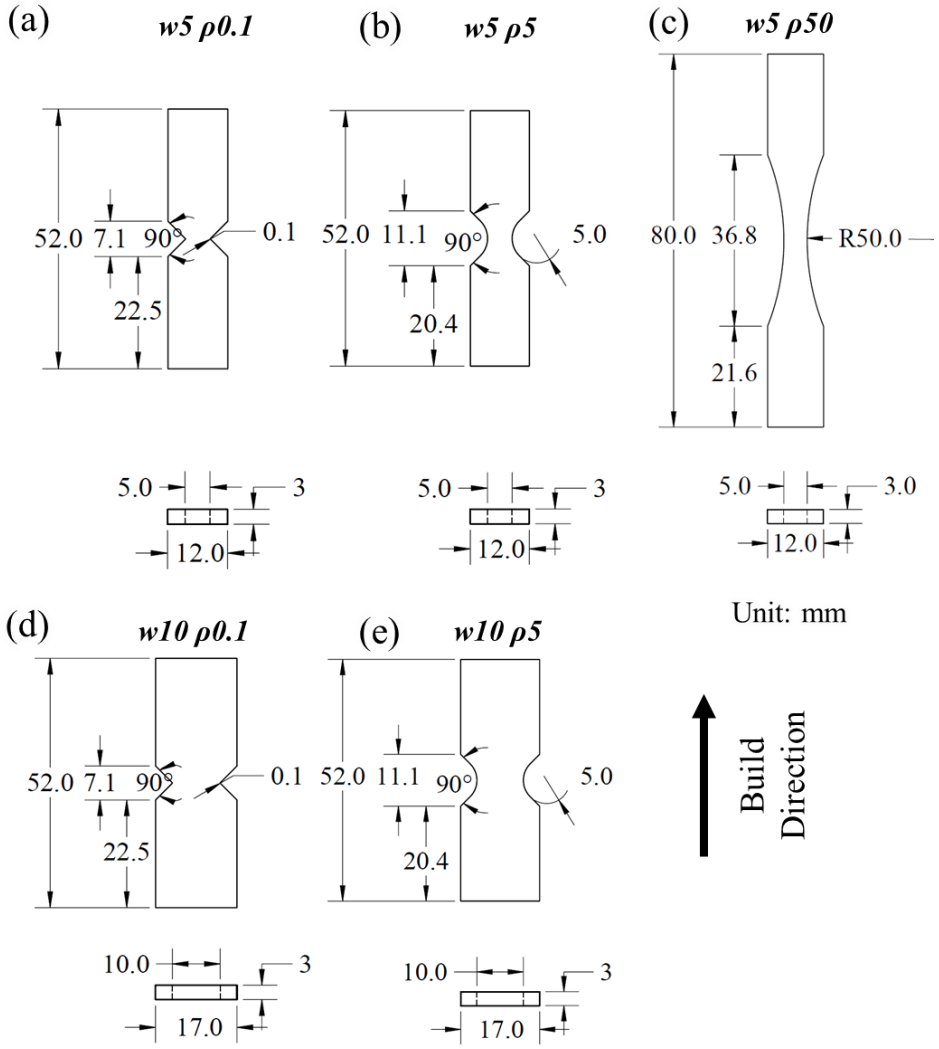

Fig. S1 Geometries and dimensions of flat notched specimens with different ligament widths, *w*, and notch root radii, *ρ*: (a) *w5 ρ0.1*, (b) *w5 ρ5*, (c) *w5 ρ50*, (d) *w10 ρ0.1*, and (e) *w10 ρ5*.

S2: Microstructure and defect content in heat treated AlSi10Mg and 17-4 PH SS

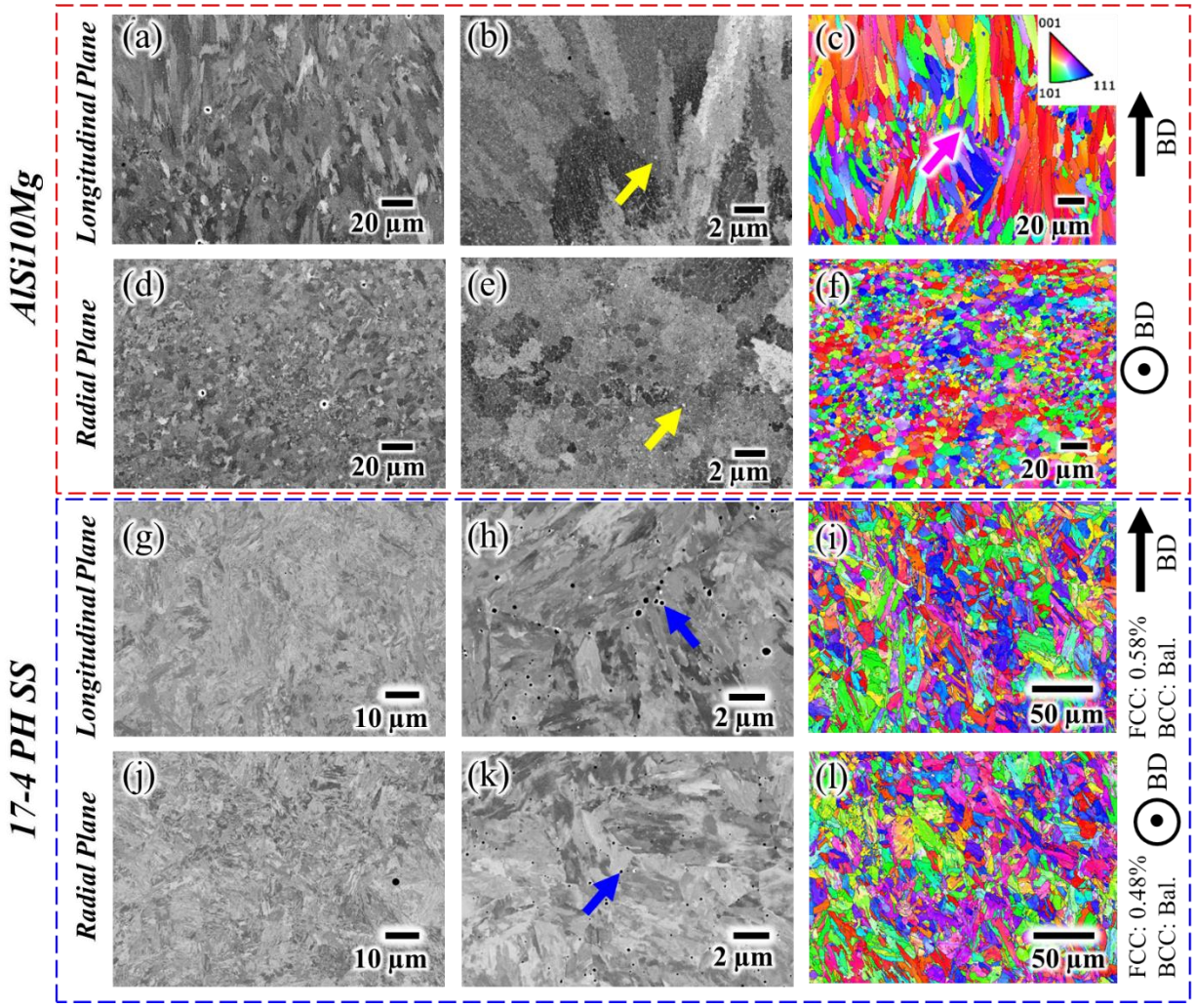

Fig. S2 BSE images and IPF maps of (a-c) AlSi10Mg (LP), (d-f) AlSi10Mg (RP), (g-i) 17-4 PH SS (LP), and (j-l) 17-4 PH SS (RP). Yellow, magenta, and blue arrows, respectively, point to Si-rich precipitates, fine grains near the melt pool boundaries in AlSi10Mg, and Nb, Cu, Si, and S-rich precipitates in 17-4 PH SS. As a note, BD stands for build direction.

For AlSi10Mg, BSE images show the presence of a vast Si-network in both longitudinal plane (LP), i.e., plane parallel to the build direction, and radial plane (RP), i.e., plane perpendicular to the build direction (see **Figs. S2**(a, b, d & e)). For 17-4 PH SS, BSE images show the presence of fine laths grouped together, commonly referred to as lath packets, in **Figs. S2**(h & k). Globular precipitates rich in Nb, S, Si, and Cu, indicated using blue arrows in **Figs. 2**(h & k), were present

throughout the microstructure. The EDS elemental maps for these precipitates are shown in **Fig. S3**.

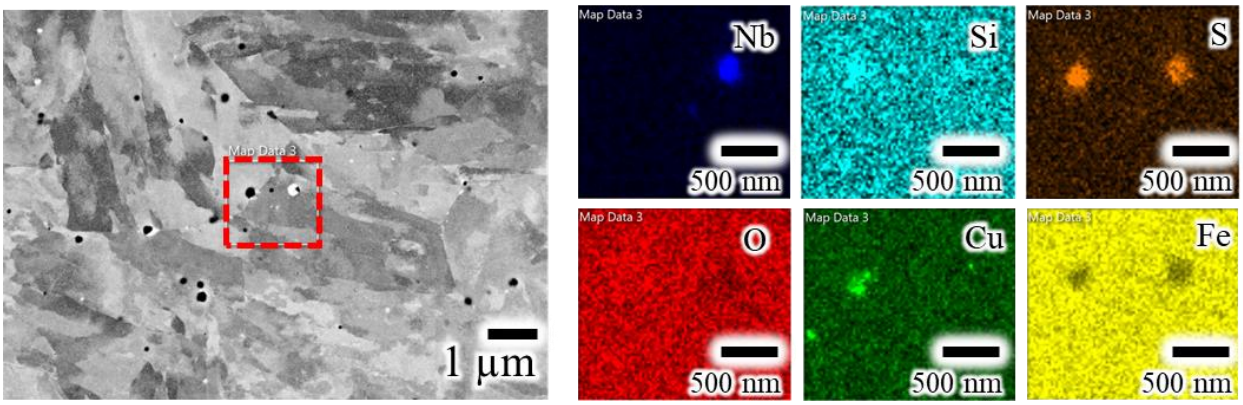

Fig. S3 EDS elemental maps for precipitates in CA-H1025 treated L-PBF 17-4 PH SS.

Table S1 Defect content quantified in terms of relative density, number of defects larger than 50 µm, 90th percentile size, and maximum defect size for specimens shown in **Fig. 3** in the main manuscript.

AlSi10Mg	REC	UH
Relative Density, %	99.833	99.771
No. of Defects > 50 µm	328	369
90th Percentile Size, µm	56	57
Max. Defect Size, µm	163	209
17-4 PH SS	REC	UH
Relative Density, %	99.998	99.844
No. of Defects > 50 µm	2	787
90th Percentile Size, µm	44	63
Max. Defect Size, µm	55	84

S3: Methodology for elastic plastic finite element analysis (EPFEA)

During EPFEA, two-dimensional finite element (FE) models for *w5 ρ0.1, w5 ρ5, w10 ρ0.1,* and *w10 ρ5* configurations were created in ABAQUS® software and analyzed under plane stress conditions. One-fourth of the model (see **Fig. S4**(a)) was used with symmetric boundary conditions

along X_1 and X_2. CPS6M, a 6-node modified quadratic plane stress triangle element, was used and mesh convergence studies were conducted for all notch configurations. The final meshes for *w5 ρ0.1, w5 ρ5, w10 ρ0.1,* and *w10 ρ5* configurations are shown in **Fig. S4**. Considering the smallest cross-sectional area in the specimen, remote force/load equivalent to the nominal stresses of 100 MPa, 125 MPa, and 150 MPa, were applied on the FE models for AlSi10Mg and 700 MPa, 800 MPa, and 900 MPa, for 17-4 PH SS. The material parameters, i.e., modulus of elasticity and true stress-plastic strain data, for AlSi10Mg and 17-4 PH SS were obtained from the tensile tests conducted in accordance with ASTM E8 standard. During the tests, the extensometer was removed at 0.015 mm/mm strain level to prevent any damage to it. To obtain the true stress measures at higher strain levels for both AlSi10Mg and 17-4 PH SS, the post-yield stress-strain data (shown in **Fig. S5**) were fitted using, $\sigma_{true} = K(\varepsilon_p)^n$, where *K* and *n* are the strain hardening coefficient and strain hardening exponent, respectively. The obtained *K* and *n* were used to extrapolate the true stress-plastic strain data up to the plastic strain level of 2 mm/mm.

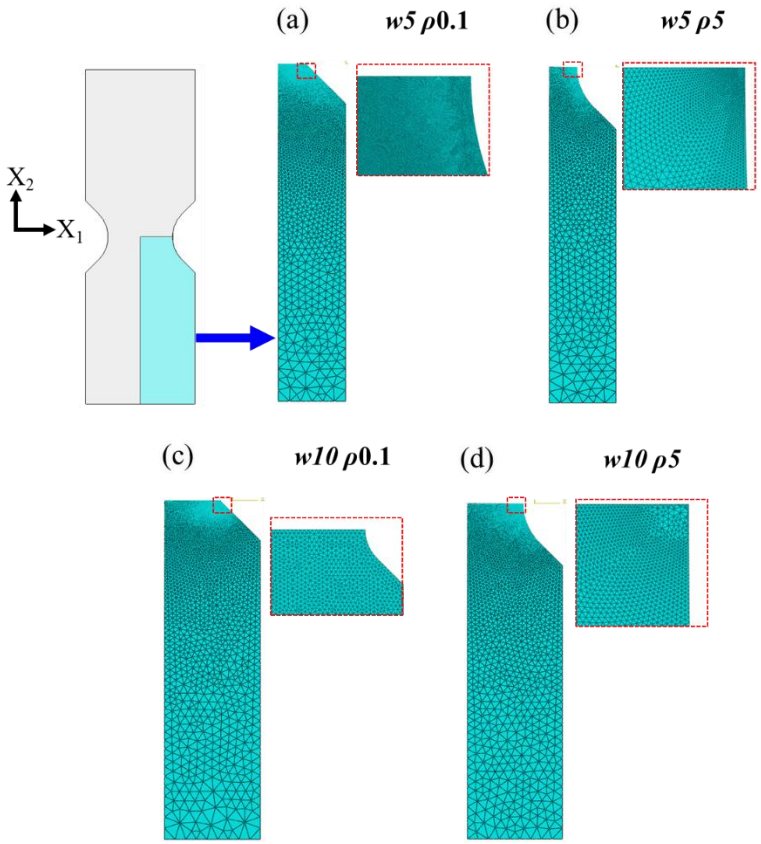

Fig. S4 2D finite element meshes for (a) *w5 ρ0.1*, (b) *w5 ρ5*, (c) *w10 ρ0.1*, and (d) *w10 ρ5* configurations.

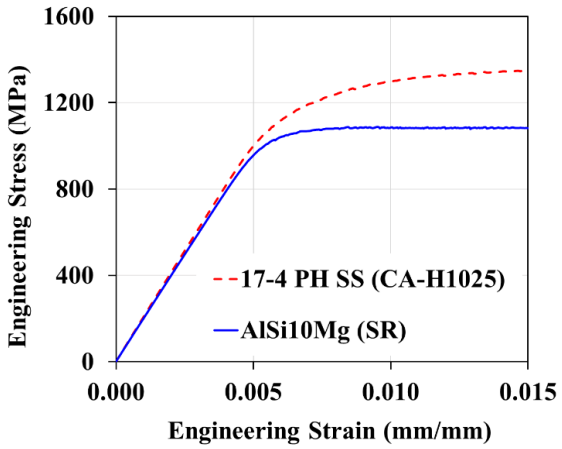

Fig. S5 Engineering stress-strain curves for stress relieved AlSi10Mg and CA-H1025 treated 17-4 PH SS.

S4: Fractography and critical defect features for different notch configurations

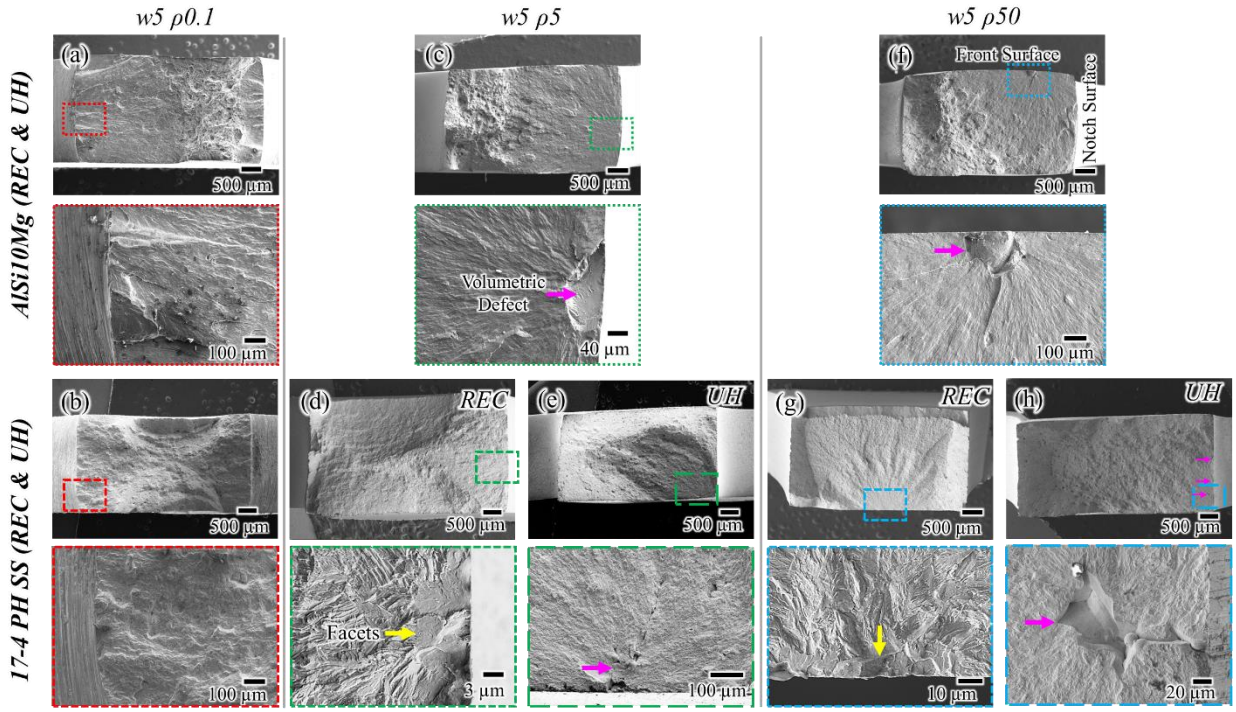

Fig. S6 Fractography images showing the fatigue crack initiation sites in specimens with notch root radii of (a & b) 0.1 mm, (c-e) 5 mm, and (f-h) 50 mm, respectively, for AlSi10Mg (REC and UH) and 17-4 PH SS (REC & UH). Magenta and yellow arrows point to the crack initiating volumetric defects and δ-Fe leading to the formation of facets, respectively.

Fractography was conducted to investigate the fatigue failure mechanisms in different notch configurations; representative images from each configuration of specimens with *w* of 5 mm are shown in **Fig. S6**. Irrespective of the material or the fabrication condition, fatigue cracks in *ρ0.1* specimens initiated from the notch roots (see **Figs. S6**(a & b)). For *ρ5* and *ρ50* AlSi10Mg specimens, all fatigue cracks initiated from either surface-exposed or near-surface volumetric defects for both REC and UH batches. For AlSi10Mg, all crack initiating defects were irregularly shaped LoF defects. Additionally, cracks did not solely initiate from defects near the notch surfaces but also close to the lateral surfaces. For 17-4 PH SS, critical fatigue cracks initiated from δ-Fe, leading to the formation of crystallographic facets, for near defect-free REC batch and from volumetric defects for UH batch *ρ5* and *ρ50* specimens (see **Figs. S6**(d-e, g-h)).

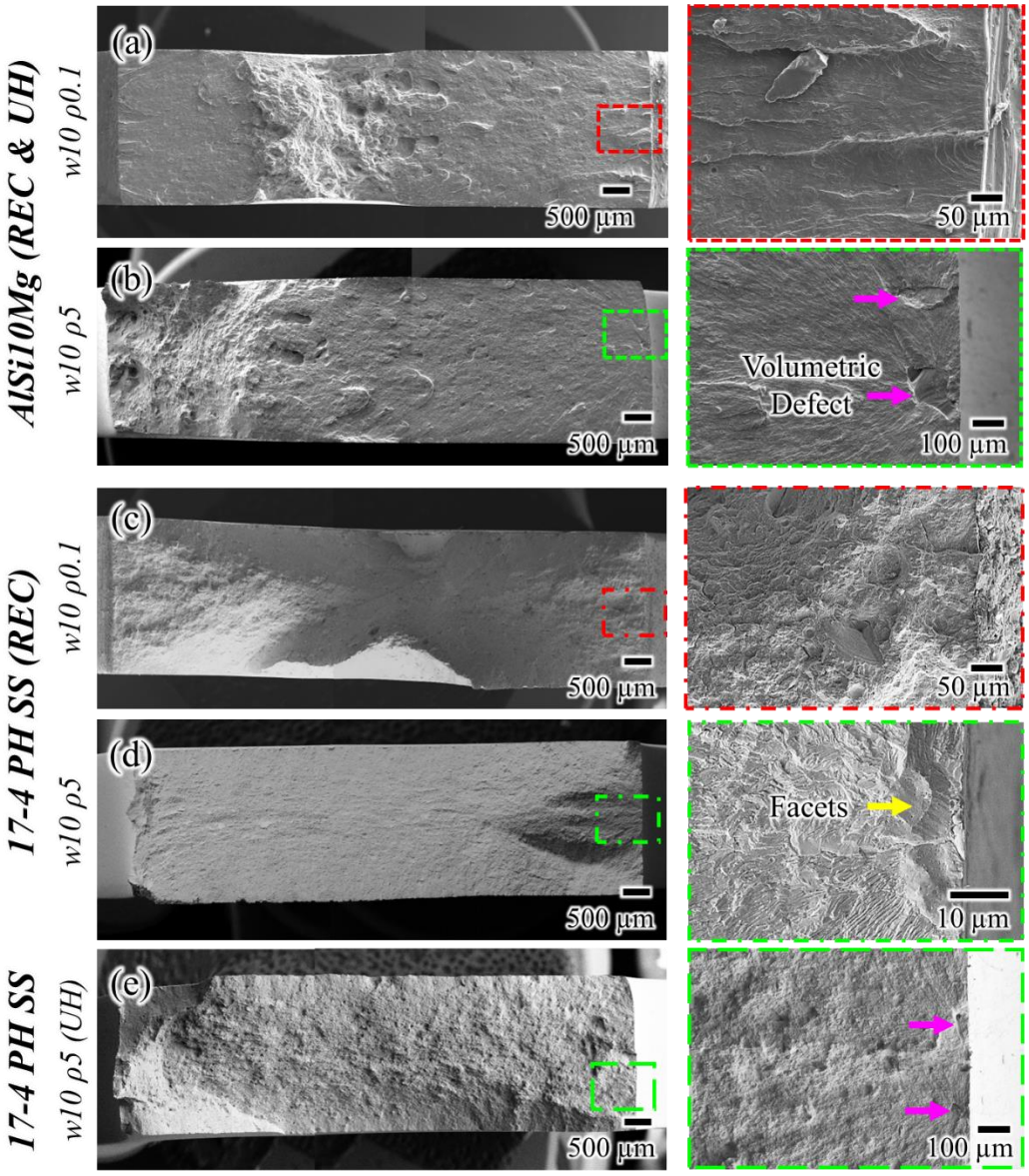

Fig. S7 Fractography images showing the fatigue crack initiation sites in (a) *w10 ρ0.1* and (b) *w10 ρ5* AlSi10Mg (REC and UH), (c) *w10 ρ0.1* and (d) *w10 ρ5* 17-4 PH SS (REC), and (d) *w10 ρ5* 17-4 PH SS (UH) specimens. Magenta and yellow arrows point toward the crack initiating volumetric defects and δ-Fe, respectively.

The fatigue crack initiation sites for *w10* specimens were similar to *w5*, as shown in **Fig. S7**. Fractography images showed fatigue crack initiation from the notch roots for *w10 ρ0.1* AlSi10Mg and 17-4 PH SS specimens. For *w10 ρ5* AlSi10Mg specimens, all fatigue cracks initiated from either the surface-exposed or the near-surface volumetric defects for both REC and UH batches. On the other hand, for 17-4 PH SS, similar to *w5*, critical fatigue cracks in *w10 ρ5*

initiated from δ-Fe for the REC batch and from multiple volumetric defects for the UH batch specimens.

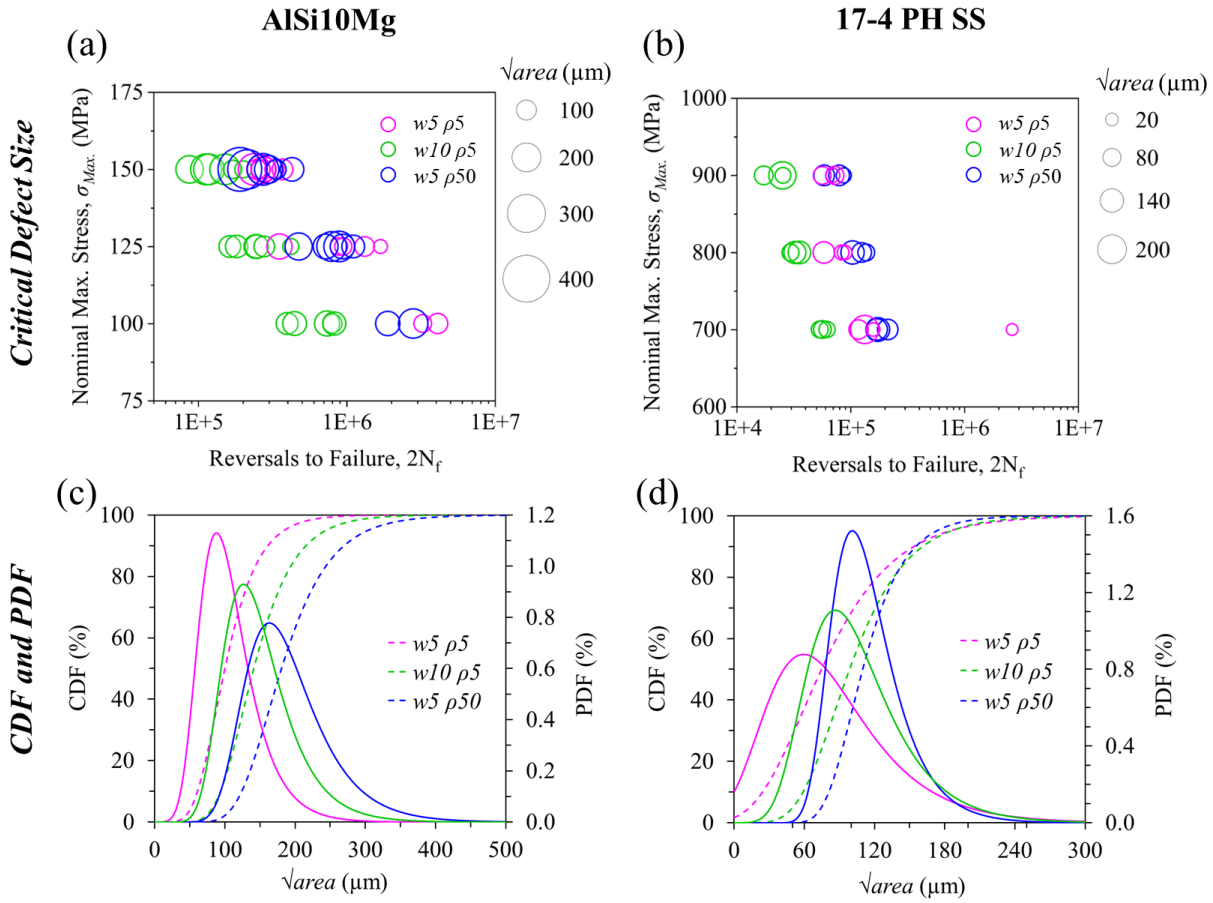

Fig. S8 (a & b) Stress-life plots with markers scaled according to the critical defect sizes, (c & d) CDF and PDF curves obtained using the largest extreme value statistics (LEVS) for critical defect sizes in AlSi10Mg and 17-4 PH SS.

To identify features of volumetric defects that influenced the fatigue crack initiation behavior, and to establish a correlation with the experimental fatigue lives, the size of critical volumetric defects was analyzed/quantified. The quantified critical defect sizes ($\sqrt{area}$ [114] measured in accordance with Murakami's approach) for different notch root radii and ligament widths AlSi10Mg and 17-4 PH SS specimens are shown as marker sizes in **Figs. S8**(a & b). The trend showing shorter fatigue lives with larger critical defects is unclear for both AlSi10Mg and 17-4 PH SS; several anomalies are observed at all stress levels. Similarly, in the case of varying

ligament width specimens, the trend was uncertain and contained many anomalies (see **Figs. S8**(a & b). This suggests the influence of features other than only critical defect sizes on the fatigue behavior. The critical defect sizes in AlSi10Mg and 17-4 PH SS specimens were further evaluated using the largest extreme value statistics (LEVS) in accordance with the ASTM E2283 standard [206]. Upon analysis, the defect sizes were found to follow the Gumbel distribution, and the corresponding probability and cumulative density function (PDF and CDF) curves are shown in **Figs. S8**(c & d), respectively, for AlSi10Mg and 17-4 PH SS. Among the notch configurations where cracks initiated from volumetric defects, the mean critical defect size for *w5 ρ5* was the smallest, followed by *w10 ρ5*, and *w5 ρ50* for both AlSi10Mg and 17-4 PH SS. This was likely due to the differences in the region/volume with elevated stress at the notch root of these specimens. Between *w5 ρ5* and *w5 ρ50*, a larger volume of elevated stress at the notch root of the latter increased the likelihood of having larger critical defects. Similarly, the larger volume of elevated stress at the notch root of *w10 ρ5* specimens increased the likelihood of having larger critical defects than *w5 ρ5*.

S5: Linear elastic finite element analysis (LEFEA) of flat notched specimens

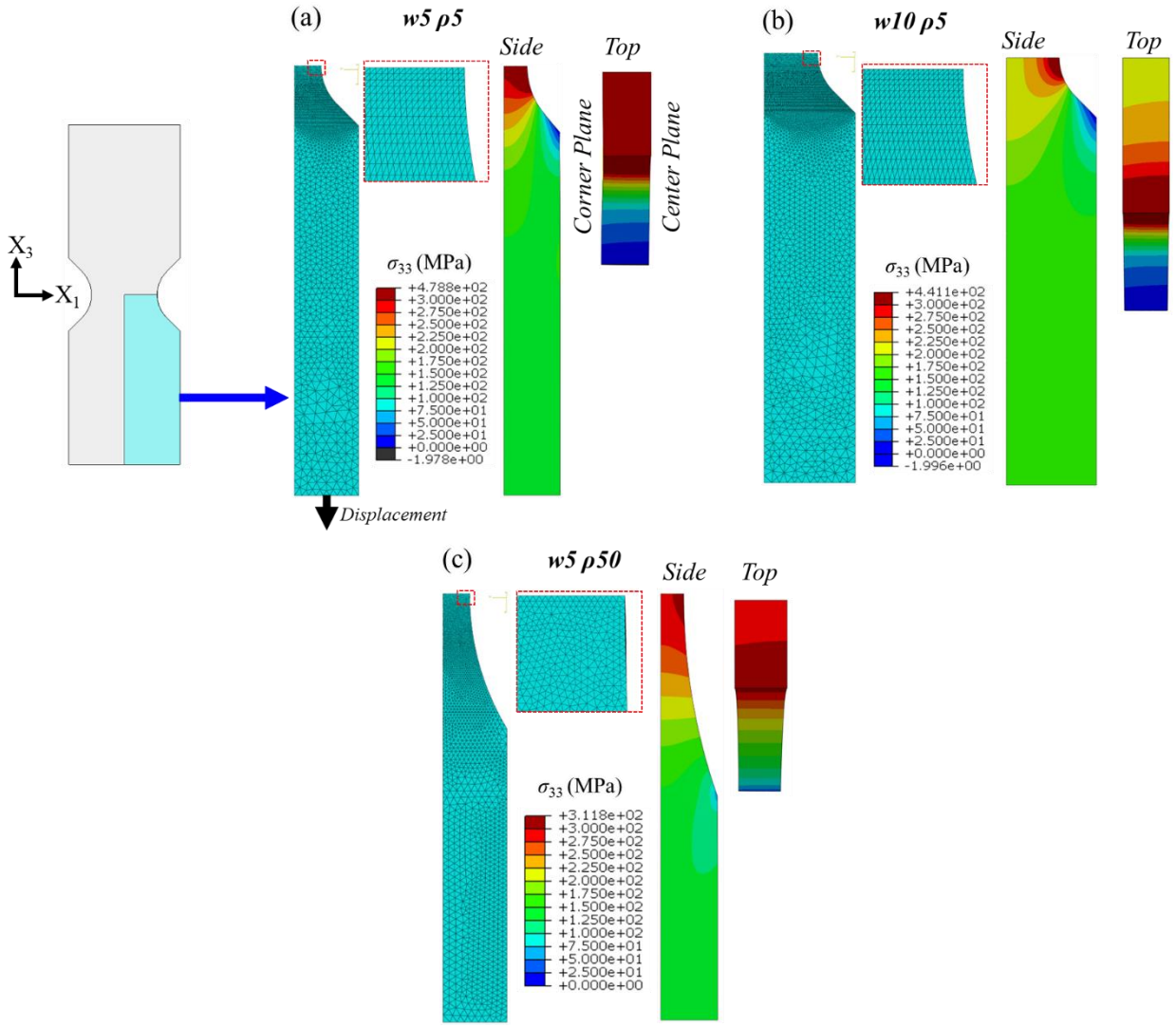

Fig. S9 Finite element meshes and stress contour plots for (a) *w5 ρ5*, (c) *w10 ρ5*, and (e) *w5 ρ50* configurations. For stress contour plots, both side and top views of the FE models are shown.

During LEFEA, one-eighth of the full model (see **Fig. S9**) was used to create three-dimensional FE models for *w5 ρ5*, *w10 ρ5*, and *w5 ρ50* configurations. The thickness of the FE models was 1.5 mm, i.e., half the specimens' thickness. Symmetric boundary conditions were applied on all three planes, i.e., X_1-X_2, X_1-X_3, and X_2-X_3, and a remote displacement of 100 µm was applied along X_3 (shown using a black arrow in **Fig. S9**(a)). Mesh convergence studies were performed, and the final meshes for all configurations are shown in **Fig. S9**. C3D10, 10-node

quadratic tetrahedron elements, were used in the models. The resulting normal stresses along the loading direction for each configuration are shown in **Fig. S9**.

The normal stresses (σ_{33}) at different relative heights were normalized using the nominal stress (σ_0) and presented in **Figs. 7**(a-c) of the main manuscript for *w5 ρ5*, *w10 ρ5*, *w5 ρ50* configurations. The normalized stress trends in **Figs. 7**(a-c) with relative heights (h_{center}/h_0) ≤ 0.3 were fitted using an exponential decay function,

$$\frac{\sigma_{33}}{\sigma_0} = M_1 + M_2 e^{-l/(l_0 M_3)} \quad \text{(S1)}$$

where σ_{33}/σ_0 is the local elastic stress concentration factor ($K_{t(local)}$), l is the distance of the crack initiation site from the notch surface, l_0 is the distance from the notch surface to the central axis, and M_1, M_2, and M_3 are the fitting parameters. The fitting parameters can be calculated using

$$M_i = A_{i1}x^2 + A_{i2}x + A_{i3}, \quad \text{(S2)}$$

where $x = h_{center}/h_0$, and the constants, A_{i1}, A_{i2}, and A_{i3} are provided in **Table S2**.

Table S2 Constants used in Eq. (S2).

Center Plane	***w5 ρ5***			***w10 ρ5***		
i	A_{i1}	A_{i2}	A_{i3}	A_{i1}	A_{i2}	A_{i3}
1	-0.875	0.016	0.825	-7.670	0.697	0.792
2	-8.690	-0.541	0.522	-5.315	-1.021	0.851
3	-2.425	0.109	0.389	37.575	-3.418	0.256
Lateral Plane	***w5 ρ5***			***w10 ρ5***		
i	A_{i1}	A_{i2}	A_{i3}	A_{i1}	A_{i2}	A_{i3}
1	-0.655	-0.016	0.825	-1.531	0.083	0.787
2	-8.313	-0.512	0.485	-7.265	-0.733	0.793
3	-8.547	2.155	0.346	11.075	-0.727	0.255

Center and Lateral Plane: w5 ρ50				
i	A_{i1}	A_{i2}	A_{i3}	
1	-2.180	-0.358	0.977	
2	-0.514	-0.098	0.060	
3	-0.842	0.556	0.481	

9 Supplement Material for Chapter 5

S1: Experimental details

AlSi10Mg and 17-4 precipitation hardening (PH) stainless steel (SS) blocks of dimensions 90 mm×60 mm×38 mm were fabricated using laser powder bed fusion (L-PBF) additive manufacturing (AM) machines in a vertical orientation perpendicular to the build plate. AlSi10Mg blocks were fabricated using Renishaw RenAM 500Q Flex and 17-4 PH SS using 3D SYSTEMS DMP Flex 350B. After fabrication, the AlSi10Mg blocks being attached to the build plates were stress relieved (SR) at 285 °C for 2 hours followed by air cooling and at 700 °C for an hour followed by furnace cooling for 17-4 PH SS. The notched specimens of dimensions, shown in **Fig. S1**, were extracted using electrical discharge machining (EDM). These specimens were then ground and polished using sandpapers of reducing grits from P240 to P1200. Uniaxial load-controlled fatigue tests, at a stress ratio of 0.1, were performed on these specimens using MTS servohydraulic test frames with a load cell of 25 kN for AlSi10Mg and 100 kN for 17-4 PH SS. After failure, fractography was performed using a Zeiss Crossbeam 550 scanning electron microscope (SEM).

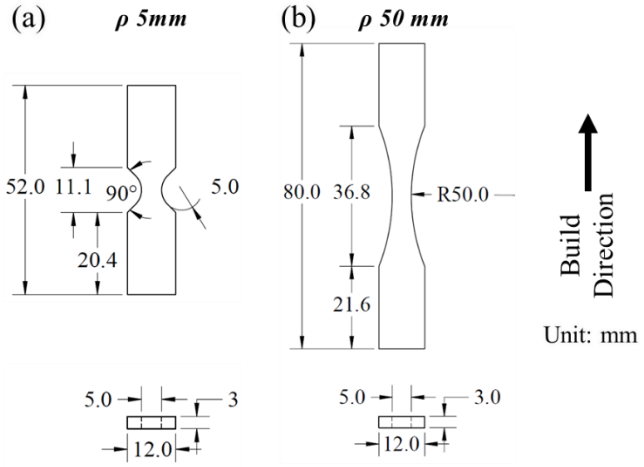

Fig. S1. Geometries and dimensions of flat notched specimens with notch root radii of (a) 5 mm and (b) 50 mm. All units are in mm.

S2: Mathematical fittings for notch-surface and corner configurations

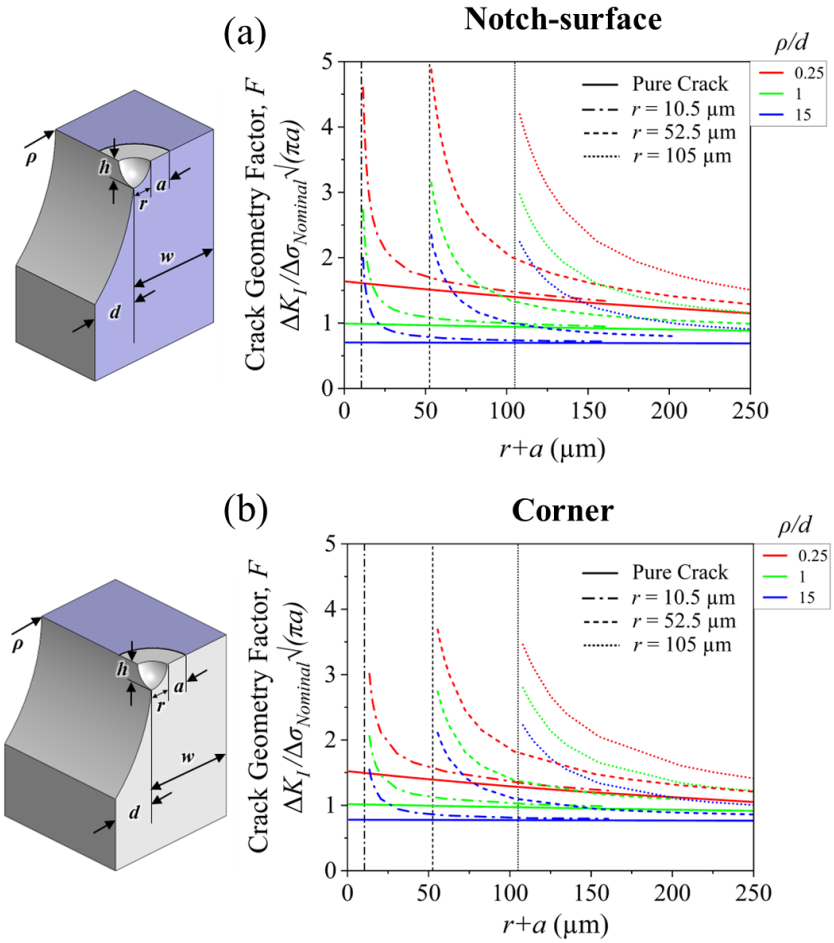

Fig. S2. Crack geometry factor (F) or normalized SIF of pure cracks and cracks initiating from different sizes spherical defects in (a) notch-surface and (b) corner configurations.

The crack geometry factor (F) for pure cracks and cracks initiating from the spherical defects in notch-surface and corner configurations were calculated using

$$F = \frac{K_I}{\sigma_{Nominal}\sqrt{\pi a}}, \quad (3)$$

and plotted in **Fig. S2** of the Supplemental Material. As expected, higher stress concentrations at the notch roots of sharper notches resulted in larger F. Among different defect sizes, smaller ones showed a steeper decline in the F with increasing crack lengths than the bigger defects.

The crack geometry factors (F) for cracks initiating from defects, shown using dotted lines in **Fig. S2**, were higher than for pure crack cases and showed rapid decline ahead of the defect tip. Among different notch geometries, notches with smaller ρ/d showed higher F. Among different sizes of spherical defects, smaller defects showed a higher gradient for the decrease of F with the increase in crack length. It is worth mentioning that the geometrical limitations during modeling resulted in higher F at the defect tip for r of 52.5 µm compared to 10.5 µm. Between notch-surface and corner configurations, the latter showed lower F likely due to the lower constraints experienced by the material in that location.

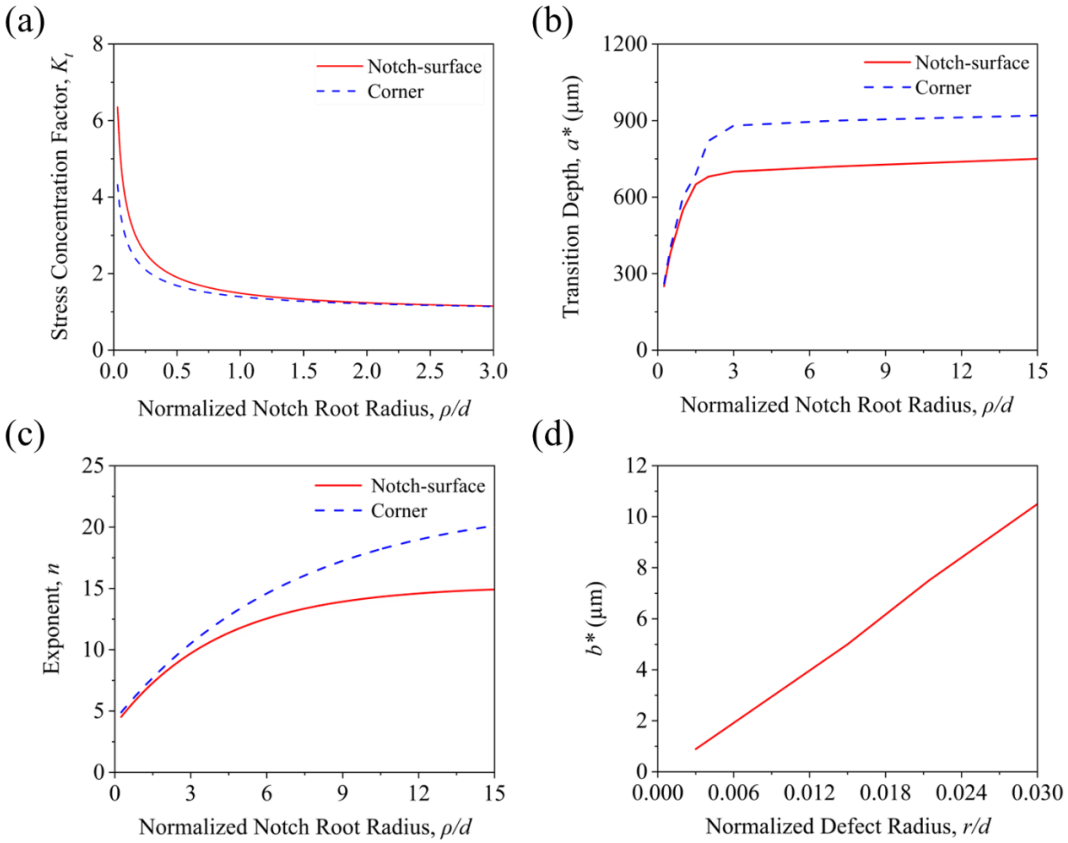

Fig. S3. Variation of (a) K_t, (b) a^*, and (c) n with the notch geometry and b^* with defect size.

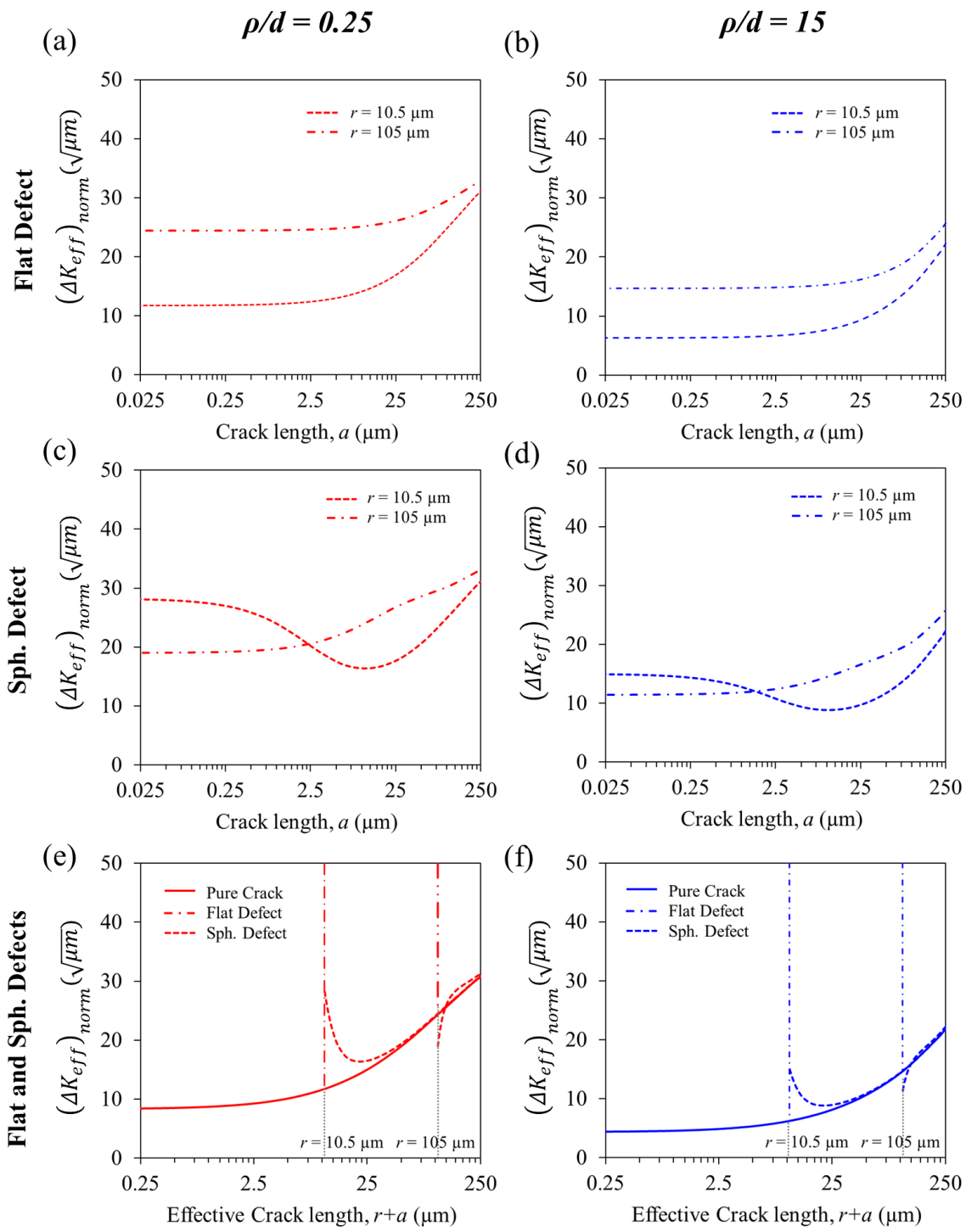

Fig. S4. Variation in the effective SIF of cracks initiating from (a and b) flat defects, (c and d) spherical defects, and (e and f) comparison between pure cracks and cracks initiating from both flat and spherical defects for corner configuration with ρ/d of 0.25 and 15, respectively.

S3: Mathematical fittings for sub-surface and lateral-surface configurations

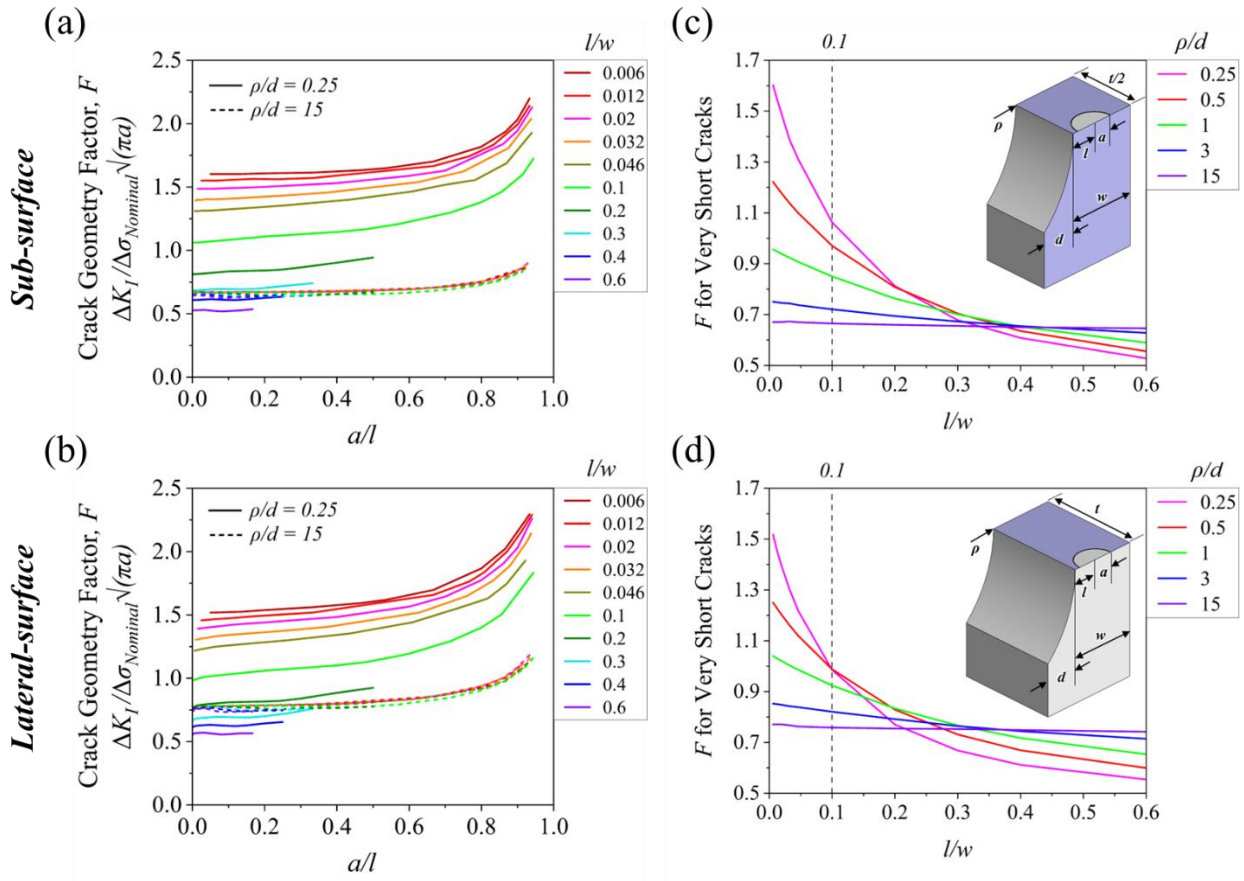

Fig. S6. Crack geometry factor *F* for pure cracks initiating at different distances from the notch surface in (a) sub-surface and (b) lateral-surface configurations. Also, *F* for very short cracks in different root radii notches for (c).

The crack geometry factors for pure cracks at different distances from the notch surface (*l*/*w*) in sub-surface and lateral-surface configurations are shown in **Fig. S6**. A higher *F* was observed for pure cracks closer to the notch surfaces. Among different notch geometries, sharp notches showed higher *F* likely due to their ability for higher stress concentration near the notch root. For $l/w \leq 0.1$, *F* increased asymptotically when the crack modeled the free surface. However, for $l/w > 0.1$, this behavior was not observed since a crack length of only up to 250 μm was analyzed. For configurations with $l/w > 0.1$, near-constant *F* for crack lengths up to 250 μm is

plotted in **Fig. S6**(c and d), respectively, for sub-surface and lateral-surface configurations. An approximation function of F for $l/w > 0.1$ is written as

$$F = \frac{K_{I(Max.)}}{\sigma_{Nominal}\sqrt{\pi a}} = A_1 e^{-\left(\frac{l/w}{A_2}\right)^{A_3}} + A_4, \quad \text{(S1)}$$

where A_1, A_2, A_3, and A_4 are the fitting constants and can be calculated using Eqs. (S2-S5) and (S6-S9) for sub-surface and lateral-surface configurations, respectively.

$$A_1 = 0.332 + 4.709e^{-(\rho/d)/0.151} + 2.187e^{-(\rho/d)/0.961} \quad \text{(S2)}$$

$$A_2 = 0.509 - 0.481e^{-(\rho/d)/0.895} \quad \text{(S3)}$$

$$A_3 = 1.025 - 0.423e^{-(\rho/d)/0.378} \quad \text{(S4)}$$

$$A_4 = 1.12 + 0.107\left(\frac{\rho}{d}\right) - 0.0063\left(\frac{\rho}{d}\right)^2 \quad \text{(S5)}$$

$$A_1 = 0.156 + 0.748e^{-(\rho/d)/0.0.624} + 0.748e^{-(\rho/d)/0.762} \quad \text{(S6)}$$

$$A_2 = 0.510 - 0.483e^{-(\rho/d)/0.896} \quad \text{(S7)}$$

$$A_3 = 1.022 - 0.359e^{-(\rho/d)/0.365} \quad \text{(S8)}$$

$$A_4 = 0.474 + 0.035\left(\frac{\rho}{d}\right) \quad \text{(S9)}$$

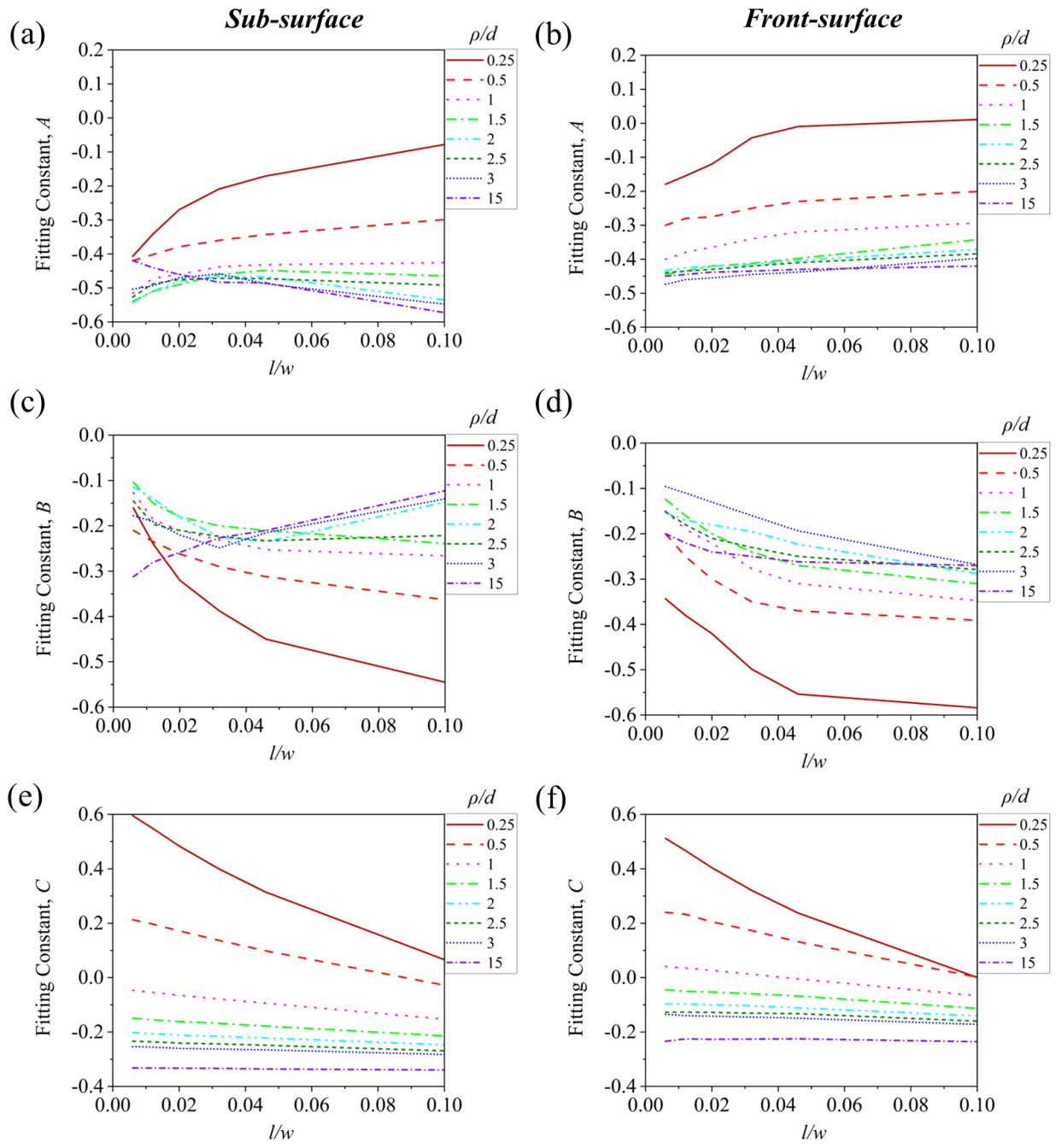

Fig. S7. Variation of fitting constants (a and b) *A*, (c and d) *B*, and (e and f) *C* with varying *l/w* and *ρ/d* in sub-surface and lateral-surface configurations, respectively.

10 References

[1] S. Ford, M. Despeisse, Additive manufacturing and sustainability: an exploratory study of the advantages and challenges, J Clean Prod 137 (2016) 1573–1587. https://doi.org/10.1016/J.JCLEPRO.2016.04.150.

[2] M. Attaran, The rise of 3-D printing: The advantages of additive manufacturing over traditional manufacturing, Bus Horiz 60 (2017) 677–688. https://doi.org/10.1016/J.BUSHOR.2017.05.011.

[3] L. Bian, N. Shamsaei, J. Usher, Laser-based additive manufacturing of metal parts: modeling, optimization, and control of mechanical properties, 2017.

[4] A. Walter, C.L. Marcham, Environmental Advantages in Additive Manufacturing, Prof Saf 65 (2020) 34–38. https://dx.doi.org/ (accessed October 7, 2024).

[5] M. Javaid, A. Haleem, R.P. Singh, R. Suman, S. Rab, Role of additive manufacturing applications towards environmental sustainability, Advanced Industrial and Engineering Polymer Research 4 (2021) 312–322. https://doi.org/10.1016/j.aiepr.2021.07.005.

[6] S.S. Babu, L. Love, R. Dehoff, W. Peter, T.R. Watkins, S. Pannala, Additive manufacturing of materials: Opportunities and challenges, MRS Bull (2015). https://doi.org/10.1557/mrs.2015.234.

[7] S.A.M. Tofail, E.P. Koumoulos, A. Bandyopadhyay, S. Bose, L. O'Donoghue, C. Charitidis, Additive manufacturing: scientific and technological challenges, market uptake and opportunities, Materials Today 21 (2018) 22–37. https://doi.org/10.1016/j.mattod.2017.07.001.

[8] A. Yadollahi, N. Shamsaei, Additive manufacturing of fatigue resistant materials: Challenges and opportunities, Int J Fatigue 98 (2017) 14–31. https://doi.org/10.1016/J.IJFATIGUE.2017.01.001.

[9] J.J. Lewandowski, M. Seifi, Metal Additive Manufacturing: A Review of Mechanical Properties, Annu Rev Mater Res 46 (2016) 151–186. https://doi.org/10.1146/annurev-matsci-070115-032024.

[10] J.J. Wang, M. Zhang, X. Tan, W. Jing, E.J. Liu, S.B. Tor, H. Li, Impact and fatigue characteristics of additively manufactured steel materials: A review, Proceedings of the International Conference on Progress in Additive Manufacturing 2018-May (2018) 487–492. https://doi.org/10.25341/D4T881.

[11] L. Dowling, J. Kennedy, S. O'Shaughnessy, D. Trimble, A review of critical repeatability and reproducibility issues in powder bed fusion, Mater Des 186 (2019) 108346. https://doi.org/10.1016/j.matdes.2019.108346.

[12] D. Greitemeier, C. Dalle Donne, F. Syassen, J. Eufinger, T. Melz, Effect of surface roughness on fatigue performance of additive manufactured Ti–6Al–4V, Materials Science

and Technology (United Kingdom) 32 (2016) 629–634. https://doi.org/10.1179/1743284715Y.0000000053.

[13] J. Pegues, M. Roach, R. Scott Williamson, N. Shamsaei, Surface roughness effects on the fatigue strength of additively manufactured Ti-6Al-4V, Int J Fatigue 116 (2018) 543–552. https://doi.org/10.1016/j.ijfatigue.2018.07.013.

[14] J. Zhang, A. Fatemi, Surface roughness effect on multiaxial fatigue behavior of additive manufactured metals and its modeling, Theoretical and Applied Fracture Mechanics 103 (2019) 102260. https://doi.org/10.1016/j.tafmec.2019.102260.

[15] Y. Murakami, M. Endo, Effects of defects, inclusions and inhomogeneities on fatigue strength, Int J Fatigue 16 (1994) 163–182. https://doi.org/10.1016/0142-1123(94)90001-9.

[16] A. Mostafaei, C. Zhao, Y. He, S. Reza Ghiaasiaan, B. Shi, S. Shao, N. Shamsaei, Z. Wu, N. Kouraytem, T. Sun, J. Pauza, J. V. Gordon, B. Webler, N.D. Parab, M. Asherloo, Q. Guo, L. Chen, A.D. Rollett, Defects and anomalies in powder bed fusion metal additive manufacturing, Curr Opin Solid State Mater Sci 26 (2022) 100974. https://doi.org/10.1016/J.COSSMS.2021.100974.

[17] G. Nicoletto, Directional and notch effects on the fatigue behavior of as-built DMLS Ti6Al4V, Int J Fatigue 106 (2018) 124–131. https://doi.org/10.1016/J.IJFATIGUE.2017.10.004.

[18] B.E. Carroll, T.A. Palmer, A.M. Beese, Anisotropic tensile behavior of Ti–6Al–4V components fabricated with directed energy deposition additive manufacturing, Acta Mater 87 (2015) 309–320. https://doi.org/10.1016/j.actamat.2014.12.054.

[19] Microstructural evolution and anisotropic mechanical properties of Inconel 625 superalloy fabricated by directed energy deposition | Elsevier Enhanced Reader, (n.d.). https://reader.elsevier.com/reader/sd/pii/S0925838821008355?token=1030C3460D7EE9F0A7F0DBA59765436D48017410C2FAE0ACF6C3C75A49F82FFC661DCB8D3450F0CFB9C11E7504A3B642 (accessed March 8, 2021).

[20] E. Maleki, N. Shamsaei, A comprehensive study on the effects of surface post-processing on fatigue performance of additively manufactured AlSi10Mg: An augmented machine learning perspective on experimental observations, Addit Manuf 86 (2024) 104179. https://doi.org/10.1016/j.addma.2024.104179.

[21] E. Maleki, S. Bagherifard, F. Sabouri, M. Guagliano, Effects of hybrid post-treatments on fatigue behaviour of notched LPBF AlSi10Mg: experimental and deep learning approaches, Procedia Structural Integrity 34 (2021) 141–153. https://doi.org/10.1016/J.PROSTR.2021.12.021.

[22] E. Maleki, S. Bagherifard, F. Sabouri, M. Guagliano, Effects of hybrid post-treatments on fatigue behaviour of notched LPBF AlSi10Mg: experimental and deep learning approaches,

Procedia Structural Integrity 34 (2021) 141–153. https://doi.org/10.1016/J.PROSTR.2021.12.021.

[23] E. Maleki, S. Bagherifard, F. Sabouri, M. Bandini, M. Guagliano, Hybrid thermal, mechanical and chemical surface post-treatments for improved fatigue behavior of laser powder bed fusion AlSi10Mg notched samples, Surf Coat Technol 430 (2022) 127962. https://doi.org/10.1016/J.SURFCOAT.2021.127962.

[24] E. Maleki, S. Bagherifard, S.M.J. Razavi, M. Riccio, M. Bandini, A. du Plessis, F. Berto, M. Guagliano, Fatigue behaviour of notched laser powder bed fusion AlSi10Mg after thermal and mechanical surface post-processing, Materials Science and Engineering: A 829 (2022) 142145. https://doi.org/10.1016/J.MSEA.2021.142145.

[25] C. Li, Z.Y. Liu, X.Y. Fang, Y.B. Guo, Residual Stress in Metal Additive Manufacturing, Procedia CIRP 71 (2018) 348–353. https://doi.org/10.1016/j.procir.2018.05.039.

[26] N. Kalentics, E. Boillat, P. Peyre, S. Ćirić-Kostić, N. Bogojević, R.E. Logé, Tailoring residual stress profile of selective laser melted parts by laser shock peening, Addit Manuf 16 (2017) 90–97.

[27] S.J. Park, S.H. Jo, J.G. Kim, J. Kim, R. Lee, Y.S. Oh, S.J. Kim, H.W. Lee, S.H. Kang, J. Jung, Evolution of Microstructure, Mechanical Properties and Residual Stress of a Cold Rolled Invar Sheet Due to Heat Treatment, Metals 2022, Vol. 12, Page 110 12 (2022) 110. https://doi.org/10.3390/MET12010110.

[28] M. Benedetti, C. Santus, Notch fatigue and crack growth resistance of Ti-6Al-4V ELI additively manufactured via selective laser melting: A critical distance approach to defect sensitivity, Int J Fatigue 121 (2019) 281–292. https://doi.org/10.1016/J.IJFATIGUE.2018.12.020.

[29] F. Brenne, T. Niendorf, Effect of notches on the deformation behavior and damage evolution of additively manufactured 316L specimens under uniaxial quasi-static and cyclic loading, Int J Fatigue 127 (2019) 175–189. https://doi.org/10.1016/J.IJFATIGUE.2019.05.018.

[30] B. Gillham, A. Yankin, F. McNamara, C. Tomonto, C. Huang, J. Soete, G. O'Donnell, D. Trimble, S. Yin, D. Taylor, R. Lupoi, Tailoring the theory of critical distances to better assess the combined effect of complex geometries and process-inherent defects during the fatigue assessment of SLM Ti-6Al-4V, Int J Fatigue 172 (2023) 107602. https://doi.org/10.1016/J.IJFATIGUE.2023.107602.

[31] N.A. Noda, Y. Takase, Stress concentration formula useful for all notch shape in a round bar (comparison between torsion, tension and bending), Int J Fatigue 28 (2006) 151–163. https://doi.org/10.1016/J.IJFATIGUE.2005.04.015.

[32] S. Romano, P.D. Nezhadfar, N. Shamsaei, M. Seifi, S. Beretta, High cycle fatigue behavior and life prediction for additively manufactured 17-4 PH stainless steel: Effect of sub-surface

porosity and surface roughness, Theoretical and Applied Fracture Mechanics 106 (2020) 102477. https://doi.org/10.1016/j.tafmec.2020.102477.

[33] S. Romano, A. Brückner-Foit, A. Brandão, J. Gumpinger, T. Ghidini, S. Beretta, Fatigue properties of AlSi10Mg obtained by additive manufacturing: Defect-based modelling and prediction of fatigue strength, Eng Fract Mech 187 (2018) 165–189. https://doi.org/10.1016/j.engfracmech.2017.11.002.

[34] N. Shamsaei, J. Simsiriwong, Fatigue behaviour of additively-manufactured metallic parts, Procedia Structural Integrity 7 (2017) 3–10. https://doi.org/10.1016/J.PROSTR.2017.11.053.

[35] N. Sanaei, A. Fatemi, Defects in additive manufactured metals and their effect on fatigue performance: A state-of-the-art review, Prog Mater Sci 117 (2021) 100724. https://doi.org/10.1016/j.pmatsci.2020.100724.

[36] R. Russell, D. Wells, J. Waller, B. Poorganji, E. Ott, T. Nakagawa, H. Sandoval, N. Shamsaei, M. Seifi, Qualification and certification of metal additive manufactured hardware for aerospace applications, Additive Manufacturing for the Aerospace Industry (2019) 33–66. https://doi.org/10.1016/B978-0-12-814062-8.00003-0.

[37] S. Romano, A. Brandão, J. Gumpinger, M. Gschweitl, S. Beretta, Qualification of AM parts: Extreme value statistics applied to tomographic measurements, Mater Des 131 (2017) 32–48. https://doi.org/10.1016/J.MATDES.2017.05.091.

[38] K. Solberg, F. Berto, The effect of defects and notches in quasi-static and fatigue loading of Inconel 718 specimens produced by selective laser melting, Int J Fatigue 137 (2020) 105637. https://doi.org/10.1016/J.IJFATIGUE.2020.105637.

[39] E. Maleki, S. Bagherifard, S.M.J. Razavi, M. Riccio, M. Bandini, A. du Plessis, F. Berto, M. Guagliano, Fatigue behaviour of notched laser powder bed fusion AlSi10Mg after thermal and mechanical surface post-processing, Materials Science and Engineering: A 829 (2022) 142145. https://doi.org/10.1016/J.MSEA.2021.142145.

[40] S. Afkhami, E. Dabiri, K. Lipiäinen, H. Piili, T. Björk, Effects of notch-load interactions on the mechanical performance of 3D printed tool steel 18Ni300, Addit Manuf 47 (2021) 102260. https://doi.org/10.1016/J.ADDMA.2021.102260.

[41] K. Solberg, F. Berto, A diagram for capturing and predicting failure locations in notch geometries produced by additive manufacturing, Int J Fatigue 134 (2020) 105428. https://doi.org/10.1016/J.IJFATIGUE.2019.105428.

[42] G. Nicoletto, R. Konečna, M. Frkan, E. Riva, Influence of layer-wise fabrication and surface orientation on the notch fatigue behavior of as-built additively manufactured Ti6Al4V, Int J Fatigue 134 (2020) 105483. https://doi.org/10.1016/J.IJFATIGUE.2020.105483.

[43] E. Maleki, S. Bagherifard, F. Sabouri, M. Guagliano, Effects of hybrid post-treatments on fatigue behaviour of notched LPBF AlSi10Mg: experimental and deep learning approaches,

Procedia Structural Integrity 34 (2021) 141–153. https://doi.org/10.1016/J.PROSTR.2021.12.021.

[44] S.M.J. Razavi, P. Ferro, F. Berto, Fatigue Assessment of Ti–6Al–4V Circular Notched Specimens Produced by Selective Laser Melting, Metals 2017, Vol. 7, Page 291 7 (2017) 291. https://doi.org/10.3390/MET7080291.

[45] S.M.J. Razavi, A. Avanzini, G. Cornacchia, L. Giorleo, F. Berto, Effect of heat treatment on fatigue behavior of as-built notched Co-Cr-Mo parts produced by Selective Laser Melting, Int J Fatigue 142 (2021) 105926. https://doi.org/10.1016/J.IJFATIGUE.2020.105926.

[46] S.M.J. Razavi, H. Askes, F. Berto, L. Susmel, Length scale parameters to estimate fatigue lifetime of 3D-printed titanium alloy Ti6Al4V containing notches in the as-manufactured condition, Int J Fatigue 167 (2023) 107348. https://doi.org/10.1016/J.IJFATIGUE.2022.107348.

[47] A.S. Cruces, A. Exposito, R. Branco, L.P. Borrego, F. V. Antunes, P. Lopez-Crespo, Study of the notch fatigue behaviour under biaxial conditions of maraging steel produced by selective laser melting, Theoretical and Applied Fracture Mechanics 121 (2022) 103469. https://doi.org/10.1016/J.TAFMEC.2022.103469.

[48] D.B. Witkin, | D N Patel, | G E Bean, Notched fatigue testing of Inconel 718 prepared by selective laser melting, Fatigue Fract Eng Mater Struct 42 (2019) 166–177. https://doi.org/10.1111/FFE.12880.

[49] M. Kahlin, H. Ansell, J.J. Moverare, Fatigue Behaviour of Notched Additive Manufactured Ti6Al4V with As-Built Surfaces, Int J Fatigue 101 (2017) 51–60.

[50] H.R. Zambrano, G. Härkegård, Self-arresting cracks at notches in ductile cast iron, Eng Fract Mech 102 (2013) 146–155. https://doi.org/10.1016/J.ENGFRACMECH.2012.11.008.

[51] M. Benedetti, C. Santus, Building the Kitagawa-Takahashi diagram of flawed materials and components using an optimized V-notched cylindrical specimen, Eng Fract Mech 224 (2020) 106810. https://doi.org/10.1016/J.ENGFRACMECH.2019.106810.

[52] K. Solberg, F. Berto, Notch-defect interaction in additively manufactured Inconel 718, Int J Fatigue 122 (2019) 35–45. https://doi.org/10.1016/j.ijfatigue.2018.12.021.

[53] L.P. Borrego, J.A.M. Ferreira, J.D.M. Costa, C. Capela, J. De Jesus, A study of fatigue notch sensibility on titanium alloy TiAl6V4 parts manufactured by selective laser melting, Procedia Structural Integrity 13 (2018) 1000–1005. https://doi.org/10.1016/J.PROSTR.2018.12.186.

[54] M.S. Dodaran, M. Muhammad, N. Shamsaei, S. Shao, Synergistic effect of microstructure and defects on the initiation of fatigue cracks in additively manufactured Inconel 718, Int J Fatigue 162 (2022) 107002. https://doi.org/10.1016/J.IJFATIGUE.2022.107002.

[55] R. Bussoloti, G.E. Totten, L.L.M. Albano, L.C.F. Canale, Delta Ferrite: Cracking of Steel Fasteners, in: Encyclopedia of Iron, Steel, and Their Alloys, CRC Press, 2016: pp. 1070–1081. https://doi.org/10.1081/e-eisa-120049491.

[56] S.M.J. Razavi, F. Berto, Directed Energy Deposition versus Wrought Ti-6Al-4V: A Comparison of Microstructure, Fatigue Behavior, and Notch Sensitivity, Adv Eng Mater 21 (2019) 1900220. https://doi.org/10.1002/ADEM.201900220.

[57] P. Lazzarin, R. Zambardi, A finite-volume-energy based approach to predict the static and fatigue behavior of components with sharp V-shaped notches, Int J Fract 112 (2001) 275–298. https://doi.org/10.1023/A:1013595930617.

[58] M. Benedetti, C. Santus, F. Berto, Inverse determination of the fatigue Strain Energy Density control radius for conventionally and additively manufactured rounded V-notches, Int J Fatigue 126 (2019) 306–318. https://doi.org/10.1016/J.IJFATIGUE.2019.04.040.

[59] I. Al Zamzami, S.M.J. Razavi, F. Berto, L. Susmel, The Critical Distance Method to estimate the fatigue strength of notched additively manufactured titanium alloys, Procedia Structural Integrity 28 (2020) 994–1001. https://doi.org/10.1016/J.PROSTR.2020.11.114.

[60] K. Solberg, D. Wan, F. Berto, Fatigue assessment of as-built and heat-treated Inconel 718 specimens produced by additive manufacturing including notch effects, Fatigue Fract Eng Mater Struct 43 (2020) 2326–2336. https://doi.org/10.1111/FFE.13300.

[61] D.B. Witkin, | D N Patel, | G E Bean, Notched fatigue testing of Inconel 718 prepared by selective laser melting, Fatigue Fract Eng Mater Struct 42 (2019) 166–177. https://doi.org/10.1111/FFE.12880.

[62] S. Ford, M. Despeisse, Additive manufacturing and sustainability: an exploratory study of the advantages and challenges, J Clean Prod 137 (2016) 1573–1587. https://doi.org/10.1016/J.JCLEPRO.2016.04.150.

[63] M. Attaran, The rise of 3-D printing: The advantages of additive manufacturing over traditional manufacturing, Bus Horiz 60 (2017) 677–688. https://doi.org/10.1016/J.BUSHOR.2017.05.011.

[64] L. Bian, N. Shamsaei, J. Usher, Laser-based additive manufacturing of metal parts: modeling, optimization, and control of mechanical properties, 2017.

[65] A. Walter, C.L. Marcham, Environmental Advantages in Additive Manufacturing, Prof Saf 65 (2020) 34–38.

[66] F. Venturi, R. Taylor, Additive Manufacturing in the Context of Repeatability and Reliability, J Mater Eng Perform 32 (2023) 6589–6609. https://doi.org/10.1007/s11665-023-07897-3.

[67] N. Shamsaei, A. Yadollahi, L. Bian, S.M. Thompson, An overview of Direct Laser Deposition for additive manufacturing; Part II: Mechanical behavior, process parameter

optimization and control, Addit Manuf 8 (2015) 12–35. https://doi.org/10.1016/j.addma.2015.07.002.

[68] S.M. Wajeeh Shah, S. Khushbash, H.A. Khan, T. Niaz, Investigating the failure mechanism of an aircraft longeron fitting and devising the mitigation techniques, Eng Fail Anal 168 (2025) 109115. https://doi.org/10.1016/J.ENGFAILANAL.2024.109115.

[69] A. Poudel, M.S. Yasin, J. Ye, J. Liu, A. Vinel, S. Shao, N. Shamsaei, Feature-based volumetric defect classification in metal additive manufacturing, Nat Commun 13 (2022) 1–12. https://doi.org/10.1038/s41467-022-34122-x.

[70] T.M. Mower, M.J. Long, Mechanical behavior of additive manufactured, powder-bed laser-fused materials, Materials Science and Engineering A 651 (2016) 198–213. https://doi.org/10.1016/j.msea.2015.10.068.

[71] R. Russell, D. Wells, J. Waller, B. Poorganji, E. Ott, T. Nakagawa, H. Sandoval, N. Shamsaei, M. Seifi, Qualification and certification of metal additive manufactured hardware for aerospace applications, Additive Manufacturing for the Aerospace Industry (2019) 33–66. https://doi.org/10.1016/B978-0-12-814062-8.00003-0.

[72] A. du Plessis, S. Beretta, Killer notches: The effect of as-built surface roughness on fatigue failure in AlSi10Mg produced by laser powder bed fusion, Addit Manuf 35 (2020) 101424. https://doi.org/10.1016/J.ADDMA.2020.101424.

[73] K.S. Stopka, M. Yaghoobi, J.E. Allison, D.L. McDowell, Microstructure-Sensitive modeling of surface roughness and notch effects on extreme value fatigue response, Int J Fatigue 166 (2023) 107295. https://doi.org/10.1016/J.IJFATIGUE.2022.107295.

[74] S. Lee, J.W. Pegues, N. Shamsaei, Fatigue behavior and modeling for additive manufactured 304L stainless steel: The effect of surface roughness, Int J Fatigue 141 (2020) 105856. https://doi.org/10.1016/j.ijfatigue.2020.105856.

[75] E. Maleki, N. Shamsaei, A comprehensive study on the effects of surface post-processing on fatigue performance of additively manufactured AlSi10Mg: An augmented machine learning perspective on experimental observations, Addit Manuf 86 (2024) 104179. https://doi.org/10.1016/j.addma.2024.104179.

[76] M.P. Nascimento, R.C. Souza, W.L. Pigatin, H.J.C. Voorwald, Effects of surface treatments on the fatigue strength of AISI 4340 aeronautical steel, Int J Fatigue 23 (2001) 607–618. https://doi.org/https://doi.org/10.1016/S0142-1123(01)00015-9.

[77] N.E. Uzan, S. Ramati, R. Shneck, N. Frage, O. Yeheskel, On the effect of shot-peening on fatigue resistance of AlSi10Mg specimens fabricated by additive manufacturing using selective laser melting (AM-SLM), Addit Manuf 21 (2018) 458–464. https://doi.org/10.1016/j.addma.2018.03.030.

[78] R.F. Fernandes, J.S. Jesus, R. Branco, L.P. Borrego, J.D. Costa, J.A.M. Ferreira, Effect of low-temperature stress relieving heat treatments on fatigue behaviour and failure

mechanisms of L-PBF AlSi10Mg aluminium alloy, Eng Fail Anal 169 (2025) 109210. https://doi.org/10.1016/J.ENGFAILANAL.2024.109210.

[79] S. Siddique, M. Imran, F. Walther, Very high cycle fatigue and fatigue crack propagation behavior of selective laser melted AlSi12 alloy, Int J Fatigue 94 (2017) 246–254. https://doi.org/10.1016/j.ijfatigue.2016.06.003.

[80] J. Günther, D. Krewerth, T. Lippmann, S. Leuders, T. Tröster, A. Weidner, H. Biermann, T. Niendorf, Fatigue life of additively manufactured Ti–6Al–4V in the very high cycle fatigue regime, Int J Fatigue 94 (2017) 236–245. https://doi.org/10.1016/j.ijfatigue.2016.05.018.

[81] K. Solberg, F. Berto, Notch-defect interaction in additively manufactured Inconel 718, Int J Fatigue 122 (2019) 35–45. https://doi.org/10.1016/j.ijfatigue.2018.12.021.

[82] H. Neuber, Translation Theory of Notched Stresses, Springer (1958).

[83] M.H. El Haddad, K.N. Smith, and T. H Topper, E. Haddad, A. Strain, A Strain Based Intensity Factor Solution for Short Fatigue Cracks Initiating from Notches, 1979.

[84] R.A. Smith, K.J. Miller, Prediction of fatigue regimes in notched components, Int J Mech Sci 20 (1978) 201–206. https://doi.org/10.1016/0020-7403(78)90082-6.

[85] A. Mostafaei, C. Zhao, Y. He, S. Reza Ghiaasiaan, B. Shi, S. Shao, N. Shamsaei, Z. Wu, N. Kouraytem, T. Sun, J. Pauza, J. V. Gordon, B. Webler, N.D. Parab, M. Asherloo, Q. Guo, L. Chen, A.D. Rollett, Defects and anomalies in powder bed fusion metal additive manufacturing, Curr Opin Solid State Mater Sci 26 (2022) 100974. https://doi.org/10.1016/J.COSSMS.2021.100974.

[86] M. Yukitaka, E. Masahiro, Quantitative evaluation of fatigue strength of metals containing various small defects or cracks, Eng Fract Mech 17 (1983) 1–15. https://doi.org/10.1016/0013-7944(83)90018-8.

[87] G. Nicoletto, INFLUENCE OF ROUGH AS-BUILT SURFACES ON SMOOTH AND NOTCHED FATIGUE BEHAVIOR OF L-PBF AlSi10Mg, Addit Manuf 34 (2020) 101251. https://doi.org/10.1016/J.ADDMA.2020.101251.

[88] L. Emanuelli, A. Molinari, L. Facchini, E. Sbettega, S. Carmignato, M. Bandini, M. Benedetti, Effect of heat treatment temperature and turning residual stresses on the plain and notch fatigue strength of Ti-6Al-4V additively manufactured via laser powder bed fusion, Int J Fatigue 162 (2022) 107009. https://doi.org/10.1016/J.IJFATIGUE.2022.107009.

[89] S. Afkhami, E. Dabiri, K. Lipiäinen, H. Piili, T. Björk, Effects of notch-load interactions on the mechanical performance of 3D printed tool steel 18Ni300, Addit Manuf 47 (2021) 102260. https://doi.org/10.1016/J.ADDMA.2021.102260.

[90] R. Branco, P.A. Prates, J.D. Costa, J.A. Martins Ferreira, C. Capela, F. Berto, Notch fatigue analysis and crack initiation life estimation of maraging steel fabricated by laser beam powder bed fusion under multiaxial loading, Int J Fatigue 153 (2021) 106468. https://doi.org/10.1016/J.IJFATIGUE.2021.106468.

[91] H.K. Srivastava, V. Balasubramanian, S. Malarvizhi, A.G. Rao, Notch fatigue behaviour of friction stir welded AA6061-T651 aluminium alloy joints: Role of microstructure, and residual stresses, Eng Fail Anal 167 (2025) 109058. https://doi.org/10.1016/J.ENGFAILANAL.2024.109058.

[92] J. Nafar Dastgerdi, M. Lotf Yasouri, H. Remes, Process-induced defects and failure mechanisms in metal additive manufacturing: A mesoscale coupled damage and plasticity modeling and X-ray computed tomography approach, Eng Fail Anal 168 (2025) 109123. https://doi.org/10.1016/J.ENGFAILANAL.2024.109123.

[93] L. Susmel, Notches, nominal stresses, fatigue strength reduction factors and constant/variable amplitude multiaxial fatigue loading, Int J Fatigue 162 (2022) 106941. https://doi.org/10.1016/J.IJFATIGUE.2022.106941.

[94] B. Torries, A. Imandoust, S. Beretta, S. Shao, N. Shamsaei, Overview on Microstructure- and Defect-Sensitive Fatigue Modeling of Additively Manufactured Materials, Jom 70 (2018) 1853–1862. https://doi.org/10.1007/s11837-018-2987-9.

[95] S. Shao, A. Poudel, N. Shamsaei, A linear elastic finite element approach to fatigue life estimation for defect laden materials, Eng Fract Mech 285 (2023) 109298. https://doi.org/10.1016/J.ENGFRACMECH.2023.109298.

[96] K. V. Yang, P. Rometsch, T. Jarvis, J. Rao, S. Cao, C. Davies, X. Wu, Porosity formation mechanisms and fatigue response in Al-Si-Mg alloys made by selective laser melting, Materials Science and Engineering A 712 (2018) 166–174. https://doi.org/10.1016/j.msea.2017.11.078.

[97] B. Atzori, P. Lazzarin, Notch sensitivity and defect sensitivity under fatigue loading: Two sides of the same medal, Int J Fract 107 (2000) 1–10. https://doi.org/10.1023/A:1007686727207.

[98] M. Benedetti, V. Fontanari, M. Bandini, F. Zanini, S. Carmignato, Low-and high-cycle fatigue resistance of Ti-6Al-4V ELI additively manufactured via selective laser melting: Mean stress and defect sensitivity, Int J Fatigue 107 (2018) 96–109.

[99] P. Lukáš, L. Kunz, Small cracks - Nucleation, growth and implication to fatigue life, Int J Fatigue 25 (2003) 855–862. https://doi.org/10.1016/S0142-1123(03)00133-6.

[100] P. Rambabu, N. Eswara Prasad, V. V Kutumbarao, R.J.H. Wanhill, Aluminium Alloys for Aerospace Applications, in: N.E. Prasad, R.J.H. Wanhill (Eds.), Aerospace Materials and Material Technologies : Volume 1: Aerospace Materials, Springer Singapore, Singapore, 2017: pp. 29–52. https://doi.org/10.1007/978-981-10-2134-3_2.

[101] C. Garcia-Cabezon, C.G. Hernández, M.A. Castro-Sastre, A.I. Fernandez-Abia, M.L. Rodriguez-Mendez, F. Martin-Pedrosa, Heat treatments of 17-4 PH SS processed by SLM to improve its strength and biocompatibility in biomedical applications, Journal of Materials Research and Technology 26 (2023) 3524–3543. https://doi.org/10.1016/J.JMRT.2023.08.104.

[102] S.I. Shakil, A. Hadadzadeh, B. Shalchi Amirkhiz, H. Pirgazi, M. Mohammadi, M. Haghshenas, Additive manufactured versus cast AlSi10Mg alloy: Microstructure and micromechanics, Results in Materials 10 (2021) 100178. https://doi.org/10.1016/J.RINMA.2021.100178.

[103] A.D.N.A. Committee, AMS2771: Heat Treatment of Aluminum Alloy Castings - SAE International, SAE International (n.d.). https://doi.org/https://doi.org/10.4271/AMS2771.

[104] Standard Specification for Precipitation-Hardening Stainless and Heat-Resisting Steel Plate, Sheet, and Strip, (n.d.). https://www.astm.org/a0693-06.html (accessed March 8, 2022).

[105] ASTM E3, Standard Guide for Preparation of Metallographic Specimens, ASTM International (2017).

[106] S. Baig, R. Ghiaasiaan, S. Shao, N. Shamsaei, Tensile and fatigue behaviors of additively manufactured AlSi10Mg: Effect of solutionizing and aging heat treatments, Fatigue Fract Eng Mater Struct 46 (2023) 2662–2680. https://doi.org/10.1111/FFE.14024.

[107] M. Muhammad, P.D. Nezhadfar, S. Thompson, A. Saharan, N. Phan, N. Shamsaei, A comparative investigation on the microstructure and mechanical properties of additively manufactured aluminum alloys, Int J Fatigue 146 (2021) 106165. https://doi.org/10.1016/j.ijfatigue.2021.106165.

[108] L. Růžičková, J. Sobotová, L. Beránek, L. Pelikán, J. Šimota, Influence of Stress Relief Annealing Parameters on Mechanical Properties and Decomposition of Eutectic Si Network of L-PBF Additive Manufactured Alloy AlSi10Mg, Metals 2022, Vol. 12, Page 1497 12 (2022) 1497. https://doi.org/10.3390/MET12091497.

[109] P.D. Nezhadfar, K. Anderson-Wedge, S.R. Daniewicz, N. Phan, S. Shao, N. Shamsaei, Improved high cycle fatigue performance of additively manufactured 17-4 PH stainless steel via in-process refining micro-/defect-structure, Addit Manuf 36 (2020) 101604. https://doi.org/10.1016/j.addma.2020.101604.

[110] P.D. Nezhadfar, P.R. Gradl, S. Shao, N. Shamsaei, Microstructure and Deformation Behavior of Additively Manufactured 17–4 Stainless Steel: Laser Powder Bed Fusion vs. Laser Powder Directed Energy Deposition, JOM 74 (2022) 1136–1148. https://doi.org/10.1007/S11837-021-05032-Y/FIGURES/9.

[111] P.D. Nezhadfar, R. Shrestha, N. Phan, N. Shamsaei, Fatigue behavior of additively manufactured 17-4 PH stainless steel: Synergistic effects of surface roughness and heat

treatment, Int J Fatigue 124 (2019) 188–204. https://doi.org/10.1016/j.ijfatigue.2019.02.039.

[112] A. Shibata, G. Miyamoto, S. Morito, A. Nakamura, T. Moronaga, H. Kitano, I. Gutierrez-Urrutia, T. Hara, K. Tsuzaki, Substructure and crystallography of lath martensite in as-quenched interstitial-free steel and low-carbon steel, Acta Mater 246 (2023) 118675. https://doi.org/10.1016/j.actamat.2023.118675.

[113] M.L. Lobanov, G.M. Rusakov, A.A. Redikul'tsev, S. V. Belikov, M.S. Karabanalov, E.R. Struina, A.M. Gervas'ev, Investigation of Special Misorientations in Lath Martensite of Low-Carbon Steel Using the Method of Orientation Microscopy, Physics of Metals and Metallography 117 (2016) 254–259. https://doi.org/10.1134/S0031918X1603008X.

[114] Y. Murakami, T. Endo, Effects of small defects on fatigue strength of metals, Int J Fatigue 2 (1980) 23–30. https://doi.org/10.1016/0142-1123(80)90024-9.

[115] Y. Murakami, Metal Fatigue: Effects of Small Defects and Nonmetallic Inclusions, Elsevier, 2019. https://doi.org/10.1016/C2016-0-05272-5.

[116] S. Beretta, C. Anderson, Y. Murakami, Extreme value models for the assessment of steels containing multiple types of inclusion, (2006). https://doi.org/10.1016/j.actamat.2006.01.016.

[117] T. Wegrzyn, Delta ferrite in stainless steel weld metals, Welding International 6 (1992) 690–694. https://doi.org/10.1080/09507119209548267.

[118] B. Arh, F. Tehovnik, F. Vode, Transformation of the δ-ferrite in ss2343 austenitic stainless steel upon annealing at 1050◦c, 1150◦c and 1250◦c, Metals (Basel) 11 (2021). https://doi.org/10.3390/met11060935.

[119] D. Taylor, Geometrical effects in fatigue: a unifying theoretical model, Int J Fatigue 21 (1999) 413–420. https://doi.org/10.1016/S0142-1123(99)00007-9.

[120] M. Muhammad, M.S. Yasin, S. Soman, S. Shao, N. Shamsaei, Defect features critical to the fatigue of additively manufactured Ti-6Al-4V (Unpublished), Theoretical and Applied Fracture Mechanics (2025).

[121] R. Fleury, Investigation of fretting fatigue in turbine fir tree blade to disc joints at high temperature, (2015).

[122] B. Lee, G. Nygren, R.L. Karkkainen, J. Lee, Failure investigation of pure titanium bleed air ducts in jet fighters, Eng Fract Mech 188 (2018) 381–392. https://doi.org/10.1016/J.ENGFRACMECH.2017.09.008.

[123] C.B. Meher-Homji, G. Gabriles, Gas Turbine Blade Failures - Causes, Avoidance, And Troubleshooting., (1998). https://doi.org/10.21423/R1RD4R.

[124] Y. Zhang, F. Ye, T. Qian, J. Yan, K. Chen, G. Cheng, Y. Wang, The fatigue fracture of mounting bracket: A microstructure characterization, Int J Mod Phys B 36 (2022). https://doi.org/10.1142/S0217979222400550.

[125] Z. Yang, C.B. Kim, C. Cho, H.G. Beom, The concentration of stress and strain in finite thickness elastic plate containing a circular hole, Int J Solids Struct 45 (2008) 713–731.

[126] M. Li, A. Gupta, C.J. Bennett, Z.F. Yue, W. Sun, S.T. Tu, Cyclic plasticity of additively manufactured Ti-6Al-4V bracket for aeroengine application, Int J Mech Sci 258 (2023) 108567. https://doi.org/10.1016/J.IJMECSCI.2023.108567.

[127] L. Huang, H. Wan, Q. Han, J. Wang, X. Yi, Mitigating surface notches for enhanced fatigue performance of metallic gyroid structures via contour scanning, Int J Mech Sci 286 (2025) 109913. https://doi.org/10.1016/J.IJMECSCI.2024.109913.

[128] F.J. Gómez, M. Elices, F. Berto, P. Lazzarin, A generalised notch stress intensity factor for U-notched components loaded under mixed mode, Eng Fract Mech 75 (2008) 4819–4833. https://doi.org/10.1016/J.ENGFRACMECH.2008.07.001.

[129] Y. Murakami, L.M. Keer, Stress Intensity Factors Handbook, Vol. 3, J Appl Mech 60 (1993) 1063–1063. https://doi.org/10.1115/1.2900983.

[130] L.S. Teh, F.P. Brennan, Evaluation of mode I stress intensity factors for edge cracks from 2-D V-notches using composition of constituent SIF weight functions, Int J Fatigue 29 (2007) 1253–1268. https://doi.org/10.1016/J.IJFATIGUE.2006.10.012.

[131] Y. Hou, S. Kench, T. Wauters, R. Talemi, Numerical framework for predicting fatigue scatter in additively manufactured parts, Int J Mech Sci 281 (2024) 109562. https://doi.org/10.1016/J.IJMECSCI.2024.109562.

[132] J.A. Sow, J.H. Crews, R.J. Exton, FATIGUE-CRACK INITIATION AND GROWTH IN NOTCHED 2024-T3 SPECIMENS MONITORED BY A VIDEO TAPE SYSTEM, n.d.

[133] J. Toribio, B. González, J.C. Matos, Ó. Mulas, Stress intensity factors for embedded, surface, and corner cracks in finite-thickness plates subjected to tensile loading, Materials 14 (2021). https://doi.org/10.3390/ma14112807.

[134] P.W. Tan, J.C. Newman, C.A. Bigelow, Three-dimensional finite-element analyses of corner cracks at stress concentrations, Eng Fract Mech 55 (1996) 505–512. https://doi.org/10.1016/0013-7944(94)00231-2.

[135] R.F. Fernandes, J.S. Jesus, L.P. Borrego, J.A.M. Ferreira, D. Neto, R. Branco, J.D. Costa, Notch sensitivity and heat treatment effect on the fatigue behaviour of AlSi10Mg aluminium alloy processed by additive manufacturing, Theoretical and Applied Fracture Mechanics 133 (2024) 104553. https://doi.org/10.1016/J.TAFMEC.2024.104553.

[136] W. Li, R. Sun, T. Hu, X. Li, C. Li, Y. Zhang, X. Ding, P. Wang, Effect of elevated temperature on high-cycle and very-high-cycle fatigue properties of Ni-based superalloy

manufactured by selective laser melting, Int J Fatigue 148 (2021) 106250. https://doi.org/10.1016/j.ijfatigue.2021.106250.

[137] J.M. Alegre, A. Díaz, R. García, L.B. Peral, I.I. Cuesta, Effect of HIP post-processing at 850 °C/200 MPa in the fatigue behavior of Ti-6Al-4V alloy fabricated by Selective Laser Melting, Int J Fatigue 163 (2022) 107097. https://doi.org/10.1016/J.IJFATIGUE.2022.107097.

[138] D.J. Morrison, J.C. Moosbrugger, Effects of grain size on cyclic plasticity and fatigue crack initiation in nickel, Int J Fatigue 19 (1997) 51–59. https://doi.org/10.1016/S0142-1123(97)00034-0.

[139] M. Gabriela Galvão Camarinha, L. Contri Campanelli, M. Justino Ribeiro Barboza, L. Reis, A. Augusto Couto, D. Aparecida Pereira Reis, Fatigue behavior of notched and unnotched 7075-T6 aluminum alloy subjected to retrogression and re-aging (RRA) heat treatment and plasma nitriding, Theoretical and Applied Fracture Mechanics 127 (2023) 104051. https://doi.org/10.1016/J.TAFMEC.2023.104051.

[140] S. Beretta, S. Romano, A comparison of fatigue strength sensitivity to defects for materials manufactured by AM or traditional processes, Int J Fatigue 94 (2017) 178–191. https://doi.org/10.1016/j.ijfatigue.2016.06.020.

[141] B. Atzori, P. Lazzarin, Notch sensitivity and defect sensitivity under fatigue loading: Two sides of the same medal, Int J Fract 107 (2000) 1–10. https://doi.org/10.1023/A:1007686727207.

[142] F. Sausto, P.E. Carrion, N. Shamsaei, S. Beretta, Fatigue failure mechanisms for AlSi10Mg manufactured by L-PBF under axial and torsional loads: The role of defects and residual stresses, Int J Fatigue 162 (2022) 106903. https://doi.org/10.1016/J.IJFATIGUE.2022.106903.

[143] P.D. Nezhadfar, K. Anderson-Wedge, S.R. Daniewicz, N. Phan, S. Shao, N. Shamsaei, Improved high cycle fatigue performance of additively manufactured 17-4 PH stainless steel via in-process refining micro-/defect-structure, Addit Manuf 36 (2020) 101604. https://doi.org/10.1016/j.addma.2020.101604.

[144] A. Poudel, P.R. Gradl, S. Shao, N. Shamsaei, Tensile deformation behavior of laser powder direct energy deposited Inconel 625: Cryogenic to elevated temperatures, Materials Science and Engineering: A 889 (2024) 145826. https://doi.org/10.1016/J.MSEA.2023.145826.

[145] A. Hadadzadeh, B.S. Amirkhiz, B. Langelier, J. Li, M. Mohammadi, Microstructural consistency in the additive manufactured metallic materials: A study on the laser powder bed fusion of AlSi10Mg, Addit Manuf 46 (2021) 102166. https://doi.org/10.1016/J.ADDMA.2021.102166.

[146] L.C. Araújo, A.H.G. Gabriel, E.B. da Fonseca, J.A. Avila, A.L. Jardini, R. Seno Junior, É.S.N. Lopes, Effects of build orientation and heat treatments on the tensile and fracture

toughness properties of additively manufactured AlSi10Mg, Int J Mech Sci 213 (2022) 106868. https://doi.org/10.1016/J.IJMECSCI.2021.106868.

[147] P.D. Nezhadfar, R. Shrestha, N. Phan, N. Shamsaei, Fatigue data for laser beam powder bed fused 17-4 PH stainless steel specimens in different heat treatment and surface roughness conditions, Data Brief 25 (2019) 104215. https://doi.org/10.1016/j.dib.2019.104215.

[148] ASTM International, E8/E8M Standard Test Methods for Tension Testing of Metallic Materials, West Conshohocken, PA; ASTM International (2016). https://doi.org/https://doi.org/10.1520/E0008_E0008M-13.

[149] S. Shao, A. Poudel, N. Shamsaei, A linear elastic finite element approach to fatigue life estimation for defect laden materials, Eng Fract Mech 285 (2023) 109298. https://doi.org/10.1016/J.ENGFRACMECH.2023.109298.

[150] R.G. (Richard G. Budynas, J.Keith. Nisbett, J.Edward. Shigley, Shigley's mechanical engineering design, 9th ed., McGraw-Hill, New York SE - xxi, 1082 pages : illustrations ; 27 cm., 2011.

[151] P.D. Nezhadfar, P.R. Gradl, S. Shao, N. Shamsaei, Microstructure and Deformation Behavior of Additively Manufactured 17–4 Stainless Steel: Laser Powder Bed Fusion vs. Laser Powder Directed Energy Deposition, JOM 74 (2022) 1136–1148. https://doi.org/10.1007/S11837-021-05032-Y/FIGURES/9.

[152] M. Benedetti, C. Santus, Building the Kitagawa-Takahashi diagram of flawed materials and components using an optimized V-notched cylindrical specimen, Eng Fract Mech 224 (2020) 106810. https://doi.org/10.1016/J.ENGFRACMECH.2019.106810.

[153] M. Kahlin, H. Ansell, J.J. Moverare, Fatigue behaviour of notched additive manufactured Ti6Al4V with as-built surfaces, Int J Fatigue 101 (2017) 51–60. https://doi.org/10.1016/J.IJFATIGUE.2017.04.009.

[154] J.C. Sobotka, M.P. Enright, R.C. McClung, Application of critical distances to fatigue at pores, Fatigue Fract Eng Mater Struct 42 (2019) 1646–1661. https://doi.org/10.1111/ffe.13004.

[155] S. Afazov, A. Serjouei, G.J. Hickman, R. Mahal, D. Goy, I. Mitchell, Defect-based fatigue model for additive manufacturing, Progress in Additive Manufacturing (2022). https://doi.org/10.1007/s40964-022-00376-6.

[156] R. Molaei, A. Fatemi, N. Sanaei, J. Pegues, N. Shamsaei, S. Shao, P. Li, D.H. Warner, N. Phan, Fatigue of additive manufactured Ti-6Al-4V, Part II: The relationship between microstructure, material cyclic properties, and component performance, Int J Fatigue 132 (2020) 105363. https://doi.org/10.1016/j.ijfatigue.2019.105363.

[157] A. Fatemi, R. Molaei, J. Simsiriwong, N. Sanaei, J. Pegues, B. Torries, N. Phan, N. Shamsaei, Fatigue behaviour of additive manufactured materials: An overview of some recent experimental studies on Ti-6Al-4V considering various processing and loading

direction effects, Fatigue Fract Eng Mater Struct 42 (2019) 991–1009. https://doi.org/10.1111/ffe.13000.

[158] A. Soltani-Tehrani, R. Shrestha, N. Phan, M. Seifi, N. Shamsaei, Establishing Specimen Property to Part Performance Relationships for Laser Beam Powder Bed Fusion Additive Manufacturing, Int J Fatigue (2021).

[159] N. Sanaei, A. Fatemi, N. Phan, Defect characteristics and analysis of their variability in metal L-PBF additive manufacturing, Mater Des 182 (2019) 108091. https://doi.org/10.1016/j.matdes.2019.108091.

[160] A. du Plessis, I. Yadroitsava, I. Yadroitsev, Effects of defects on mechanical properties in metal additive manufacturing: A review focusing on X-ray tomography insights, Mater Des 187 (2020) 108385. https://doi.org/10.1016/j.matdes.2019.108385.

[161] M. Seifi, M. Gorelik, J. Waller, N. Hrabe, N. Shamsaei, S. Daniewicz, J.J. Lewandowski, Progress Towards Metal Additive Manufacturing Standardization to Support Qualification and Certification, JOM 69 (2017) 439–455. https://doi.org/10.1007/s11837-017-2265-2.

[162] L. Levine, B. Lane, E. Glaessgen, M. Gorelik, Providing a Rigorous Benchmark Measurement Foundation for Modeling-Informed Qualification and Certification of Metal Additive Manufactured Components, JOM 76 (2024) 1897–1904. https://doi.org/10.1007/S11837-024-06388-7/FIGURES/2.

[163] W.E. Frazier, Metal additive manufacturing: A review, J Mater Eng Perform 23 (2014) 1917–1928. https://doi.org/10.1007/s11665-014-0958-z.

[164] J. Ferchow, D. Kälin, G. Englberger, M. Schlüssel, C. Klahn, M. Meboldt, Design and validation of integrated clamping interfaces for post-processing and robotic handling in additive manufacturing, International Journal of Advanced Manufacturing Technology 118 (2022) 3761–3787. https://doi.org/10.1007/S00170-021-08065-4/FIGURES/34.

[165] D. Arola, C.L. Williams, Estimating the fatigue stress concentration factor of machined surfaces, Int J Fatigue 24 (2002) 923–930. https://doi.org/10.1016/S0142-1123(02)00012-9.

[166] M. Åman, Y. Tanaka, Y. Murakami, H. Remes, G. Marquis, Fatigue strength evaluation of small defect at stress concentration, Procedia Structural Integrity 7 (2017) 351–358. https://doi.org/10.1016/J.PROSTR.2017.11.099.

[167] P. Livieri, R. Tovo, Fatigue limit evaluation of notches, small cracks and defects: an engineering approach, Fatigue Fract Eng Mater Struct 27 (2004) 1037–1049. https://doi.org/10.1111/J.1460-2695.2004.00816.X.

[168] B. Atzori, P. Lazzarin, G. Meneghetti, Fracture mechanics and notch sensitivity, Fatigue Fract Eng Mater Struct 26 (2003) 257–267. https://doi.org/10.1046/J.1460-2695.2003.00633.X.

[169] H. Villarraga-Gómez, C.M. Peitsch, A. Ramsey, S.T. Smith, The role of computed tomography in additive manufacturing, Proceedings - 2018 ASPE and Euspen Summer Topical Meeting: Advancing Precision in Additive Manufacturing (2018) 201–210.

[170] A. Du Plessis, I. Yadroitsev, I. Yadroitsava, S.G. Le Roux, X-Ray Microcomputed Tomography in Additive Manufacturing: A Review of the Current Technology and Applications, 3D Print Addit Manuf 5 (2018) 227–247. https://doi.org/10.1089/3DP.2018.0060/ASSET/IMAGES/LARGE/FIGURE13.JPEG.

[171] Z. Wu, Z. He, S. Wu, X. Gao, L. Lei, C. Liu, B. Chen, C. Dong, Rotating bending fatigue mechanisms of L-PBF manufactured Ti-6Al-4V alloys using in situ X-ray tomography, Int J Fatigue 176 (2023) 107876. https://doi.org/10.1016/J.IJFATIGUE.2023.107876.

[172] A. Tawfik, P. Bills, L. Blunt, R. Racasan, Development of an Additive Manufactured Artifact to Characterize Unfused Powder Using Computed Tomography, International Journal of Automation Technology 14 (2020) 439–446. https://doi.org/10.20965/IJAT.2020.P0439.

[173] X. Cai, A.A. Malcolm, B.S. Wong, Z. Fan, Measurement and characterization of porosity in aluminium selective laser melting parts using X-ray CT, Virtual Phys Prototyp 10 (2015) 195–206. https://doi.org/10.1080/17452759.2015.1112412.

[174] A. Du Plessis, S.G. Le Roux, G. Booysen, J. Els, Quality Control of a Laser Additive Manufactured Medical Implant by X-Ray Tomography, 3D Print Addit Manuf 3 (2016) 175–182. https://doi.org/10.1089/3DP.2016.0012/ASSET/IMAGES/LARGE/FIGURE8.JPEG.

[175] X. Gao, C. Tao, S. Wu, B. Chen, S. Wu, X-ray imaging of defect population and the effect on high cycle fatigue life of laser additive manufactured Ti6Al4V alloys, Int J Fatigue 162 (2022) 106979. https://doi.org/10.1016/J.IJFATIGUE.2022.106979.

[176] Y. Murakami, Metal Fatigue. Effects of Small Defects and Nonmetallic Inclusions, 2002.

[177] M.H. El Haddad, T.H. Topper, K.N. Smith, Prediction of non propagating cracks, Eng Fract Mech 11 (1979) 573–584. https://doi.org/10.1016/0013-7944(79)90081-X.

[178] M.D. Chapetti, Fracture mechanics models for short crack growth estimation and fatigue strength assessment, Matéria (Rio de Janeiro) 27 (2022). https://doi.org/10.1590/1517-7076-RMAT-2022-0030.

[179] M.H. El Haddad, K.N. Smith, and T. H Topper, E. Haddad, A. Strain, A Strain Based Intensity Factor Solution for Short Fatigue Cracks Initiating from Notches, 1979.

[180] R.A. Smith, K.J. Miller, FATIGUE CRACKS AT NOTCHES, Pergamon Press, 1977.

[181] A. Poudel, J. Pegues, M. Kelly, S. Shao, N. Shamsaei, Fatigue Behavior of Additively Manufactured Cylindrical Notched Specimens: The Effect of Volumetric Defects (Submitted), Eng Fail Anal (2025).

[182] A. Poudel, J. Pegues, M. Kelly, S. Shao, N. Shamsaei, Edge Notches in Additive Manufacturing: Effects of Volumetric Defects and Microstructure on the Fatigue Behavior (Submitted), Int J Mech Sci (2025).

[183] A. E2283-08, Standard Practice for Extreme Value Analysis of Nonmetallic Inclusions in Steel, 08 (2015) 1–11. https://doi.org/10.1520/E2283-08R19.1.

[184] T. Wegrzyn, Delta ferrite in stainless steel weld metals, Welding International 6 (1992) 690–694. https://doi.org/10.1080/09507119209548267.

[185] D. Tay, D. Taylor, A mechanistic approach to critical-distance methods in notch fatigue, Fatigue Fract Eng Mater Struct 24 (2001) 215–224. https://doi.org/10.1046/J.1460-2695.2001.00401.X.

[186] M.T. Yu, D.L. DuQuesnay, T.H. Topper, Notch fatigue behaviour of SAE1045 steel, Int J Fatigue 10 (1988) 109–116. https://doi.org/10.1016/0142-1123(88)90038-2.

[187] D. Liao, S.P. Zhu, J.A.F.O. Correia, A.M.P. De Jesus, F. Berto, Recent advances on notch effects in metal fatigue: A review, Fatigue Fract Eng Mater Struct 43 (2020) 637–659. https://doi.org/10.1111/FFE.13195.

[188] K. Tanaka, Y. Nakai, Prediction of Fatigue Threshold of Notched Components, J Eng Mater Technol 106 (1984) 192–199. https://doi.org/10.1115/1.3225698.

[189] R.E. Peterson, Notch sensitivity, Metal Fatigue, McGraw-Hill, New York, 1959.

[190] M. Benedetti, M. Dallago, C. Santus, Statistical significance of notch fatigue prognoses based on the strain-energy–density method: Application to conventionally and additively manufactured materials, Theoretical and Applied Fracture Mechanics 109 (2020) 102720. https://doi.org/10.1016/J.TAFMEC.2020.102720.

[191] S. Shao, M.J. Mahtabi, N. Shamsaei, S.M. Thompson, Solubility of argon in laser additive manufactured α-titanium under hot isostatic pressing condition, Comput Mater Sci C (2017) 209–219. https://doi.org/10.1016/J.COMMATSCI.2017.01.040.

[192] F. Morel, A. Morel, Y. Nadot, Comparison between defects and micro-notches in multiaxial fatigue – The size effect and the gradient effect, Int J Fatigue 31 (2009) 263–275. https://doi.org/10.1016/J.IJFATIGUE.2008.09.005.

[193] S. Baig, R. Ghiaasiaan, S. Shao, N. Shamsaei, Tensile and fatigue behaviors of additively manufactured AlSi10Mg: Effect of solutionizing and aging heat treatments, Fatigue Fract Eng Mater Struct 46 (2023) 2662–2680. https://doi.org/10.1111/FFE.14024.

[194] Dassault Systèmes Simulia, Abaqus 6.14 CAE User Guide, (2024) 1146.

[195] M.H. El Haddad, K.N. Smith, T.H. Topper, Fatigue crack propagation of short cracks, Journal of Engineering Materials and Technology, Transactions of the ASME 101 (1979) 42–46. https://doi.org/10.1115/1.3443647.

[196] P. Wei, Z. Chen, S. Zhang, X. Fang, B. Lu, L. Zhang, Z. Wei, Effect of T6 heat treatment on the surface tribological and corrosion properties of AlSi10Mg samples produced by selective laser melting, Mater Charact 171 (2021) 110769. https://doi.org/10.1016/J.MATCHAR.2020.110769.

[197] ATI, Precipitation Hardening Stainless Steel, (2014). www.ATImetals.com (accessed July 16, 2024).

[198] A. Poudel, J. Pegues, M. Kelly, S. Shao, N. Shamsaei, Fatigue Behavior of Additively Manufactured Flat Notched Specimens: Effect of Microstructure and Volumetric Defects (Submitted), Eng Fract Mech (2024).

[199] T.L. Anderson, Fracture Mechanics, Fundamentals and Applications, 2nd Editio, CRC Press, Washington DC, 1994.

[200] G. Härkegård, Intrinsic-crack modelling of the notch fatigue limit of a solid with an elliptical-cylindrical or a spheroidal cavity, Eng Fract Mech 279 (2023) 109057. https://doi.org/10.1016/J.ENGFRACMECH.2023.109057.

[201] C.Y. Ou, C.R. Liu, The Effects of Grain Size and Strain Amplitude on Persistent Slip Band Formation and Fatigue Crack Initiation, Metall Mater Trans A Phys Metall Mater Sci 50 (2019) 5056–5065. https://doi.org/10.1007/S11661-019-05423-6/TABLES/7.

[202] K. Shiozawa, L. Lu, Effect of Non-Metallic Inclusion Size and Residual Stresses on Gigacycle Fatigue Properties in High Strength Steel, in: Materials and Product Technologies, Trans Tech Publications Ltd, 2008: pp. 33–42. https://doi.org/10.4028/www.scientific.net/AMR.44-46.33.

[203] R.I. Stephens, A. Fatemi, R.R. Stephens, H.O. Fuchs, Metal Fatigue in Engineering, 2nd ed., John Wiley & Sons, 2000.

[204] C.S. Shin, R.A. Smith, Fatigue crack growth from sharp notches, 1985.

[205] R.G. (Richard G. Budynas, J.Keith. Nisbett, J.Edward. Shigley, Shigley's mechanical engineering design, 9th ed., McGraw-Hill, New York SE - xxi, 1082 pages : illustrations ; 27 cm., 2011.

[206] A. E2283-08, Standard Practice for Extreme Value Analysis of Nonmetallic Inclusions in Steel, 08 (2015) 1–11. https://doi.org/10.1520/E2283-08R19.1.